PH.D. DISSERTATION / TESIS DOCTORAL

ATMOSPHERIC VERTICAL PROFILING BY RAMAN LIDAR

FRANCISCO JESÚS NAVAS GUZMÁN

Grupo Física de la Atmósfera

Universidad de Granada   Centro Andaluz de Medio Ambiente

UNIVERSIDAD DE GRANADA

DEPARTAMENTO DE FÍSICA APLICADA

GRUPO DE FÍSICA DE LA ATMÓSFERA

TESIS DOCTORAL

ATMOSPHERIC VERTICAL PROFILING BY

RAMAN LIDAR

Tesis presentada por Francisco Jesús Navas Guzmán para optar al grado de Doctor.

Directores de Tesis:

Dr. Lucas Alados Arboledas
Catedrático de la Univ. de Granada
Departamento de Física Aplicada
Universidad de Granada

Dr. Juan Luis Guerrero Rascado
Investigador de la Univ. de Granada
Departamento de Física Aplicada
Universidad de Granada

Granada, Junio de 2011

El trabajo de investigación que se expone en la presente memoria, titulada: **ATMOSPHERIC VERTICAL PROFILING BY RAMAN LIDAR**, que para aspirar al grado de Doctor en Física presenta Francisco Navas Guzmán, ha sido realizado en la Universidad de Granada gracias a la beca concedida por el Ministerio de Educación "Formación de Profesorado Universitario (convocatoria 2008)", bajo la dirección de:

VºBº

Los Directores:

Dr. LUCAS ALADOS ARBOLEDAS   Dr. JUAN LUIS GUERRERO RASCADO

Aspirante a grado de Doctor

Ldo. FRANCISCO NAVAS GUZMÁN

Abstract

This PhD thesis reports on the study of atmospheric aerosol particles and the characterization of the vertical structure of the atmosphere using the lidar technique. The advantages of this active remote sensing technique include its non-invasive nature, in contrast to *in situ* measurements or chemical analyses, as well as the ability to depict the structure of the atmosphere with high vertical and temporal resolution. The multiwavelength Raman lidar used in this thesis is routinely operated by the Atmospheric Physics Group in Granada. This instrument is part of the European Aerosol Research Lidar Network (EARLINET) whose main aim is the observation of the temporal and spatial distributions of atmospheric aerosol particles at the continental scale. The main advances presented in this thesis are the implementation and application of an appropriate methodology to characterize profiles of aerosol optical and microphysical properties and water vapour. The following paragraphs briefly present the main issues discussed in this thesis.

The thesis includes a summary presentation of key concepts of aerosol theory and the active optical remote sensing used in the thesis. Following this is the presentation of the primary instrument used in this thesis, namely the multiwavelength Raman lidar. Basic information on other instruments used in the development of this thesis, such as the sun- and star-photometers and microwave radiometer, is also included.

Concerning methodological aspects, the thesis includes a detailed description of the pre-processing steps to be applied to raw lidar signals before using the inversion algorithms. Next, the two most important inversion algorithms (elastic and inelastic) are introduced. The thesis includes the implementation of some improvements in lidar data processing: the derivation of the lidar overlap function and two alternative procedures

for calibrating the lidar infrared channel. Results of the validation exercise for the elastic algorithm are also presented.

The Planetary Boundary Layer (PBL) height has been analyzed using an algorithm based on the Wavelet Covariance Transform of the lidar range-corrected signal. The algorithm has been implemented and optimized against an independent set of radiosonde profiles. The performance of the algorithm has been tested using a coincident set of microwave radiometer profiles. In addition, the seasonal evolution of the Convective Boundary Layer has been studied.

The thesis includes a statistical study of aerosol optical properties retrieved from the Raman lidar in the urban environment of Granada. Three years of measurements acquired in coincidence with the CALIPSO satellite overpasses are analyzed. Mean values and variances of the aerosol extinction (AE) and backscatter coefficients in the troposphere have been calculated. Monthly mean AE values have been calculated in the PBL and in the free troposphere during day- and night-time. Moreover, monthly mean lidar ratio (LR) values at 532 nm have been retrieved from Raman profiles during night-time.

The retrieval of water vapour mixing ratio profiles from Raman lidar also has been addressed. Simultaneous and co-located radiosonde data are used to calibrate the lidar water vapour measurements for experiments performed during summer and autumn 2011. The chapter includes the study of total precipitable water using the Raman lidar and the star-photometer. Finally, the retrieval of relative humidity profiles from the combination of simultaneous profiles of temperature (retrieved from the microwave radiometer) and water vapour mixing ratio (from the Raman lidar) is presented.

Retrieval of aerosol microphysical properties from multiwavelength Raman lidar measurements is a topic of current interest that has been studied in this thesis. The application of multiwavelength Raman lidars can be used to quantify the main particle microphysical parameters with few *a priori* assumptions. Information on the particle extinction and backscatter coefficients at multiple wavelengths is produced by such lidars and, with this information, microphysical properties of aerosol particles can be retrieved through mathematical inversion. The retrieval procedure is applied to special situations like an episode of fresh biomass burning and a volcanic plume detected in the lower troposphere.

Abstract

Abstract

iv

Resumen

Esta tesis doctoral trata sobre el estudio del aerosol atmosférico y la caracterización de la estructura vertical de la atmósfera usando la técnica lidar. Las principales ventajas de esta técnica de teledetección activa son su naturaleza no invasiva, en contraste con las medidas in situ o análisis químicos, y la capacidad de caracterizar la estructura de la atmósfera con una alta resolución vertical y temporal. El Grupo de Física de la Atmósfera de la Universida de Granada opera rutinariamente el sistema lidar Raman multiespectral utilizado en esta tesis. Este instrumento forma parte de la red EARLINET (European Aerosol Research Lidar Network) cuyo principal objetivo es la observación de la distribución espacial y temporal del aerosol atmosférico a escala continental. Los principales avances presentados en esta tesis han sido la implementación y aplicación de la metodología apropiada para caracterizar verticalmente las propiedades ópticas y microfísica del aerosol atmosférico y del vapor de agua. En los siguientes párrafos se indican brevemente los principales temas tratados en esta tesis.

La tesis incluye un resumen de los conceptos clave de la teoría del aerosol atmosférico y de las técnicas de teledetección activa que se han usado. Se presenta una descripción detallada del instrumento principal usado en la tesis, es decir del sistema lidar Raman multiespectral. Además se describe las características básicas de otros instrumentos que han complementado las medias realizadas, como son un fotómetro solar, un fotómetro estelar y un radiómetro de microondas.

En lo referente a aspectos metodológicos, la tesis incluye una descripción detallada de los pasos previos que son necesarios aplicar a las señales lidar medidas antes de usar los algoritmos de inversión. Se presentan los dos algoritmos de inversión más importantes (elástico e inelástico). La tesis incluye la implementación de algunas mejoras en el procesado de los datos lidar como son la obtención de la función de

solapamiento y el desarrollo de dos métodos alternativos para calibrar el canal infrarrojo del sistema lidar. Además se presentan los resultados de un ejercicio de validación del algoritmo elástico.

Se ha realizado un estudio de la altura de la Capa Límite Planetaria usando un algoritmo basado en la transformada de covarianza wavelet de la señal lidar corregida de rango. El algoritmo ha sido implementado y optimizado a partir de un conjunto independiente de perfiles obtenidos a partir de radiosondeos. Los resultados del algoritmo han sido validados con perfiles obtenidos con un radiómetro de microondas coincidentes tanto temporal como espacialmente. Además, se ha estudiado la evolución de la Capa Límite Convectiva.

La tesis incluye un estudio estadístico de las propiedades ópticas del aerosol atmosférico obtenidas mediante el sistema lidar Raman en el entorno urbano de Granada. Se han analizado tres años de medidas que fueron realizadas en coincidencia con las pasadas del satélite CALIPSO. A partir de estas medidas se han obtenido valores medios y varianzas de los coeficientes de extinción y retrodispersión en la troposfera. También se han obtenido valores medios mensuales de los exponentes de Angström en la Capa Límite Planetaria y en la troposfera libre durante el día y la noche. Además, se presentan los valores medios mensuales de razón lidar para la longitud a 532 nm obtenidos a partir de las medidas lidar nocturnas.

En esta tesis se aborda también la obtención de perfiles de razón de mezcla de vapor de agua a partir del sistema lidar Raman. Se usa información de radiosondeos lanzados en el mismo lugar y simultáneamente a las medidas lidar para calibrar las medidas lidar de vapor de agua en una campaña que tuvo lugar durante el verano y otoño del 2011. El capítulo incluye el estudio de contenido total de agua precipitable obtenido a partir del lidar Raman y el fotómetro estelar. Finalmente, se presenta una metodología para obtener perfiles de humedad relativa mediante la combinación de perfiles de temperatura (obtenidos con el radiómetro de microondas) y perfiles de razón de mezcla de vapor de agua (obtenidos con el sistema lidar Raman).

Otro aspecto tratado en la tesis, y que actualmente es de gran interés, es la obtención de propiedades microfísicas a partir de un sistema lidar multiespectral. Los sistemas lidar Raman multiespectrales pueden ser usados para cuantificar los principales parámetros microfísicos con pocas hipótesis a priori. A partir de los perfiles de coeficientes extinción y retrodispersión de partículas es posible obtener propiedades

microfísicas del aerosol atmosférico usando inversiones matemáticas. Este método de inversión se ha aplicado a dos eventos especiales como son un episodio de humo reciente y una capa de aerosol volcánico detectada en la baja troposfera.

Contents

Chapter 1

Introduction

Although Earth's atmosphere consists primarily of gases, aerosol particles and clouds play significant roles in shaping conditions at the surface and in the lower atmosphere. Aerosol particles are liquid or solid particles suspended in the air, whose typical diameters range over four orders of magnitude, from a few nanometers to a few tens of micrometers. They exhibit a wide range of compositions and shapes that depend on their origins and subsequent atmospheric processing. For many applications, aerosol particles from about 0.05 to 10 micrometers in diameter are of greatest interest, as particles in this size range dominate aerosol direct interaction with sunlight, and also make up the majority of the aerosol mass. Particles at the small end of this size range play a significant role in interactions with clouds, whereas particles at the large end, though much less numerous, can contribute significantly near dust and volcanic sources.

Aerosol particles participate in the Earth's energy budget directly by scattering and absorbing radiation [*Charlson and Pilat*, 1969; *Coakley et al.*, 1983] (the "direct effect") and indirectly by acting as cloud condensation nuclei (that is by serving as the particles on which cloud droplets form and grow) and, thereby, affecting cloud microphysical and radiative properties [*Twomey*, 1977; *Albrecht*, 1989]. The perturbation of sunlight by aerosol particles is designated aerosol radiative forcing (RF). Aerosol RF, it is characterized by large spatial and temporal heterogeneity due to the wide variety of aerosol sources and types, the spatial non-uniformity and intermittency of these sources, the short atmospheric lifetime of aerosol particles, and the chemical and microphysical processing that occurs in the atmosphere. On a global average basis,

the sum of direct and indirect forcing by anthropogenic particles at the top of the atmosphere (TOA) is almost certainly negative (cooling), and thus almost certainly offsets a fraction of the positive (warming) forcing due to anthropogenic greenhouse gases. However, because of the spatial and temporal non-uniformity of the aerosol RF, and likely differences in the effects of shortwave and longwave forcings, the net effect on Earth's climate is not simply a fractional offset to the effects of forcing by anthropogenic greenhouse gases [*CCSP*, 2009].

Aerosol absorption and scattering are strong functions of the size of particles, the state of mixture, the shape, the wavelength and the relative humidity. A characterization of aerosol absorption is complicated by instrumental errors and modelling inadequacies, as summarized in Bond and Bergstrom [2006]. The global assessment of aerosol absorption represents a major challenge in efforts to quantify the direct forcing and aerosol-cloud interactions.

The potential influences of aerosol particles on climate were proposed and debated at least several decades ago [*Charlson and Pilat*, 1969; *Twomey*, 1977]. However, because of the paucity of aerosol measurements, even the sign of the aerosol effect on global radiation (warming or cooling) was uncertain. Nevertheless, these pioneering studies highlighted the importance of acquiring better information concerning aerosol particles, and thereby inspired substantial research efforts in the intervening decades. Radiative forcing of climate change by anthropogenic particles regained scientific attention in the 1990s [*Charlson et al.*, 1992; *Penner et al.*, 1992] followed by the assessment of Intergovernmental Panel on Climate Change [1995; 1996] that first identified anthropogenic aerosol as a climate forcing agent.

The use of high-quality aerosol measurements from remote sensing and in-situ techniques, along with the improved performance of model simulations in the past decade, has resulted in a new estimate of aerosol climate forcing with reduced uncertainties in IPCC AR4. The aerosol direct climate forcing is estimated to be -0.5±0.4 Wm^{-2} with a medium-low level of scientific understanding. Moreover, the indirect forcing due to the cloud albedo effect for liquid water clouds is estimated to be -0.7 (ranging from -1.1 to +0.4) Wm^{-2}, with a low level of scientific understanding [*Foster et al.*, 2007]. In fact, such progress in quantifying the aerosol direct and indirect forcing plays an exclusively important role in the more definitive assessment of the

global anthropogenic radiative forcing as *virtually certainly positive* and conversely *exceptionally unlikely negative* in IPCC AR4 [*Haywood and Schulz*, 2007].

It is also important to recognize that the global scale aerosol TOA forcing alone is not an adequate metric for climate change [*NCR*, 2005]. Because of aerosol absorption mainly by soot particles, the aerosol direct radiative forcing at the surface could be much greater than the TOA forcing, and the atmospheric radiative heating rate increases. The aerosol climate forcing and radiative effect are characterized by large spatial and temporal heterogeneities due to the wide variety of aerosol sources, the spatial non-uniformity and intermittency of these sources, the short atmospheric lifetime of aerosol particles, and processing (chemical and microphysical) that occurs in the atmosphere. Over heavily polluted regions, the aerosol forcing can be much stronger than the global average and be far more of an offset for the Greenhouse Gases warming effect. By realizing aerosol's climate significance and the challenge of charactering highly variable amount and properties of aerosol particles, the research on atmospheric concentrations and effects of aerosols has become a top priority [*NCR*, 2005].

Despite the substantial progress, several important issues remain, such as measurements of aerosol absorption and vertical profiles. Significant efforts are needed to address them. Current observational capability requires algorithm refinement to improve retrievals of such aerosol properties as size distribution, particle shape, absorption, and vertical distribution. These new measurements are essential to reducing uncertainties associated with the estimate of aerosol climate forcing, in particular the anthropogenic fraction of aerosol, aerosol TOA forcing over land, aerosol forcing at the surface, and aerosol induced increment of atmospheric heating rate profile [*CCSP*, 2009].

Vertical distributions of aerosol particles are crucial to quantifying the aerosol direct effect in the thermal infrared and under cloudy conditions. Due to its large size, mineral dust can cause warming in the thermal infrared, both at the TOA and at the surface. This warming effect could be significant, as suggested by a few observational studies [*Slingo et al.*, 2006]. However, current estimates of the warming effects in the thermal infrared remain highly uncertain, because of lack of observations of vertical distributions of particles in the thermal infrared range [*Sokolik et al.*, 2001]. Calculations of the cloudy-sky aerosol direct effect require an adequate characterization of aerosol vertical distributions and three-dimensional fields of clouds, especially for

absorbing particles. The surface cooling in climatologically cloudy conditions is comparable to that under clear conditions, while the TOA effect could switch from cooling in clear conditions to warming in overcast conditions [*Keil and Haywood*, 2003]. Lidar systems will help improve the understanding of the aerosol direct forcing in cloudy conditions and the thermal infrared range. The lidar measurements can also well constrain the aerosol-induced atmospheric heating rate increment that is essential for assessing atmospheric responses to the aerosol radiative forcing [*Feingold et al.*, 2005; *Yu et al.*, 2006].

For accurate modelling of corresponding radiative forcing, knowledge of the vertical distribution of particle macro- and microphysical parameters is needed. During recent years ground-based and airborne lidar have become important tools for profiling tropospheric aerosol particles using either single or multiple wavelengths [*Kovalev and Eichinger*, 2004]. The advantage of using a lidar is that it can provide relatively continuous altitude resolved measurements of aerosol properties without perturbing the aerosol or its surroundings. For quantitative studies of the optical properties of tropospheric aerosol, Raman lidars have proven to be most useful [*Ansmann et al.*, 1992]. This lidar type measures elastically backscattered light simultaneously with Raman backscattered from molecules (nitrogen or oxygen), thus allowing independent calculation of particle backscatter and extinction coefficients without the need for critical assumptions about atmospheric parameters. Microphysical properties of aerosol particles can be retrieved through mathematical inversion information on the particle extinction and backscatter coefficients at multiple wavelengths obtained by Raman lidars [*Müller et al.*, 1999; *Veselovskii et al.*, 2002; *Alados-Arboledas et al.*, 2011; *Guerrero-Rascado et al.*, 2011].

Besides aerosol, the water vapour plays a key role in the global radiation budget and in energy transport mechanisms in the atmosphere [*Whiteman et al.*, 1992; *Ferrare et al.*, 2000]. It is one of the most important constituents in the Earth's atmosphere and it is characterized by high variability in space and time. It is the most important gaseous source of infrared opacity in the atmosphere, accounting for about 60% of the natural greenhouse effect for clear skies [*Kiehl and Trenberth*, 1997], and providing the largest positive feedback in model projections of climate change [*Held and Soden*, 2000]. It also contributes indirectly to the radiative budget by means of microphysical processes leading to the formation and development of clouds, and by affecting the size, shape and

chemical composition of aerosol particles [*Reichardt et al.*, 1996], thus modifying the aerosol role in the radiative forcing [*De Tomasi and Perrone*, 2003].

Global observations are required to better determine the water vapour and aerosol effect on climate. In this sense ground-based network and satellite represent key tools in the study of the aerosol radiative forcing. In this sense, this thesis has been developed on the framework of existing networks/observatories that are already providing consistent datasets of observations and that are performed using the state-of-the-art measurement technology and data processing. In particular, the thesis is directly linked to the activities that the Atmospheric Physics Group develops in the frame of EARLINET (European Aerosol Research Lidar Network).

The aim of this thesis is contributing to the advancement of the atmospheric aerosol research, in particular on those aspects that require additional improvement like spectral dependence of the atmospheric aerosol properties and to the vertical profiling of aerosol microphysical properties.

The thesis is organized as follows.

Chapter 2 presents key concepts of the aerosol theory and of active optical remote sensing that will be used along this thesis.

Chapter 3, devoted to the instrumentation and the experimental site, covers key aspects about the main instrument used in this thesis, the multiwavelenght Raman lidar. Basic information on other instruments used in the development of this work like sun- and star-photometer, and microwave radiometer is also included.

Chapter 4 focused on methodological aspects presents the algorithms to retrieve optical properties from lidar measurements. A detailed description of the pre-processing steps to be applied to raw lidar signals before using the inversion algorithms is presented. Next the two most important inversion algorithms (elastic and inelastic) are introduced. This chapter includes some improvements in the lidar data processing implemented in this thesis like the derivation of the overlap function of the lidar and two alternative procedures for calibrating the lidar infrared channel. The chapter ends with presentation of the validation exercise of the elastic algorithm.

Chapter 5 presents a study of the Planetary Boundary Layer (PBL) height using an algorithm based on Wavelet Covariance Transform of the lidar range corrected signal. In this sense, the algorithm has been implemented and calibrated against an

independent set of radiosounding profiles. The performance of the algorithm has been tested using a coincident set of microwave radiometer profiles. Finally, the seasonal evolution of the Convective Boundary Layer has been studied.

Chapter 6 presents a statistical study of aerosol optical properties retrieved from Raman lidar in the urban environment of Granada. Three years of measurements acquired in coincidence with CALIPSO satellite overpasses are analyzed. Mean values and variances of the aerosol extinction and backscatter coefficients in the troposphere have been calculated. Monthly mean AE values have been calculated in the PBL and in the free troposphere during day and night-time. Moreover, monthly mean LR values at 532 nm have been retrieved from Raman profiles during night-time.

Chapter 7 is focused on the retrieval of water vapour mixing ratio profiles from Raman lidar. Simultaneous and co-located radiosonde data are used to calibrate the lidar water vapour measurements and the calibration results obtained during six experiments performed during summer and autumn 2011. The chapter includes the study of total precipitable water (TPW) using the Raman lidar and the star-photometer. Finally, the retrieval of relative humidity profiles from the combination of simultaneous profiles of temperature (retrieved from a microwave radiometer) and water vapour mixing ratio (from a Raman lidar) is outlined.

Chapter 8 presents the methodology to retrieve aerosol microphysical properties from Raman lidar measurements. The application of multiwavelength Raman lidar can be used to quantify the main particle microphysical parameters with few *a priori* assumptions. Information on the particle extinction and backscatter coefficients at multiple wavelengths is produced by such lidars and, with this information, microphysical properties of aerosol particles can be retrieved through mathematical inversion. The retrieval procedure is applied to special situations like an episode of fresh biomass burning and a volcanic plume detected in the low troposphere.

Chapter 9 presents a summary of the main conclusion of this work together with an outline of future research activities.

References

Alados-Arboledas, L., D. Muller, J. L. Guerrero-Rascado, F. Navas-Guzman, D. Perez-Ramirez, and F. J. Olmo (2011), Optical and microphysical properties of fresh biomass burning aerosol retrieved by Raman lidar, and star-and sun-photometry, *Geophysical Research Letters*, *38*.

Albrecht, B. A. (1989), Aerosols, cloud microphysics, and fractional cloudiness, *Science*, *245*(4923), 1227-1230.

Ansmann, A., M. Riebesell, U. Wandinger, C. Weitkamp, E. Voss, W. Lahmann, and W. Michaelis (1992), Combined Raman elastic-backscatter lidar for vertical profiling of moisture, aerosol extinction, backscatter, and lidar ratio, *Applied Physics B-Photophysics and Laser Chemistry*, *55*(1), 18-28.

Bond, T. C., and R. W. Bergstrom (2006), Light absorption by carbonaceous particles: An investigative review, *Aerosol Science and Technology*, *40*(1), 27-67.

CCSP (2009), Atmospheric Aerosol Properties and Climate Impacts, A Report. National Aeronautics and Space Administration, *Washington, D.C., USA, 128 pp.*

Coakley, J. J., R. D. Cess, and F. Yurevich (1983), The effect of tropospheric aerosols on the earth's radiation budget: A parameterization for climate models, *J. Atmos. Sci*, *40*, 116-138.

Charlson, R. J., and M. Pilat (1969), Climate: The influence of aerosols, *J. Appl. Meteorol.*, *8*, 1001-1002.

Charlson, R. J., S. E. Schwartz, J. M. Hales, R. D. Cess, J. A. Coakley, J. E. Hansen, and D. J. Hofmann (1992), Climate forcing by anthropogenic aerosols, *Science*, *255*(5043), 423-430.

De Tomasi, F., and M. R. Perrone (2003), Lidar measurements of tropospheric water vapor and aerosol profiles over southeastern Italy, *Journal of Geophysical Research-Atmospheres*, *108*(D9).

Feingold, G., H. L. Jiang, and J. Y. Harrington (2005), On smoke suppression of clouds in Amazonia, *Geophysical Research Letters*, *32*(2).

Ferrare, R., et al. (2000), Comparison of aerosol optical properties and water vapor among ground and airborne lidars and Sun photometers during TARFOX, *Journal of Geophysical Research-Atmospheres*, *105*(D8), 9917-9933.

Foster, P., et al. (2007), Changes in Atmospheric Constituents and in Radiative Forcing. In: Climate Change 2007: The Physical Science Basis. Contribution of Working Group

I to the Fourth Assessment Report of the Intergovernmental Panel on Climate Change, edited by S. Solomon, D. Qin, M. Manning, Z. Chen, M. Marquis, K. B. Averyt, M. Tignor and H. L. Miller, Cambridge University Press, Cambridge, United Kingdom.

Guerrero-Rascado, J. L., D. Muller, F. Navas-Guzman, D. Perez-Ramirez, and L. Alados-Arboledas (2011), FIRST RESULTS OF AEROSOL MICROPHYSICAL PROPERTIES BY 3+2 RAMAN LIDAR AT EARLINET GRANADA STATION, *Romanian Journal of Physics*, *56*(3-4), 467-475.

Haywood, J., and M. Schulz (2007), Causes of the reduction in uncertainty in the anthropogenic radiative forcing of climate between IPCC (2001) and IPCC (2007), *Geophysical Research Letters*, *34*(20).

Held, I. M., and B. J. Soden (2000), Water vapor feedback and global warming, *Annual Review of Energy and the Environment*, *25*, 441-475.

IPCC (1995), : Radiative forcing of climate change and an evaluation of the IPCC IS92 emission scenarios, in Climate Change 1994, Cambridge Univ. Press, New York, Cambridge University Press.

IPCC (1996), Radiative forcing of climate change, in Climate Change 1995, Cambridge Univ. Press, New York, Cambridge University Press.

Keil, A., and J. M. Haywood (2003), Solar radiative forcing by biomass burning aerosol particles during SAFARI 2000: A case study based on measured aerosol and cloud properties, *Journal of Geophysical Research-Atmospheres*, *108*(D13).

Kiehl, J. T., and K. E. Trenberth (1997), Earth's annual global mean energy budget, *Bulletin of the American Meteorological Society*, *78*(2), 197-208.

Kovalev, V. A., and W. E. Eichinger (2004), *Elastic lidar*, John Wiley & Sons, Inc.

Müller, D., U. Wandinger, and A. Ansmann (1999), Microphysical particle parameters from extinction and backscatter lidar data by inversion with regularization: theory, *Applied Optics*, *38*(12), 2346-2357.

NCR (2005), Radiative Forcing of Climate Change: Expanding the Concept and Addessing Uncertainties, National Academy Press, Washington D.C. (Available at http:// www.nap.edu/openbook/0309095069/html).

Penner, J. E., R. E. Dickinson, and C. A. Oneill (1992), Effects of aerosol from biomass burning on the global radiation budget, *Science*, *256*(5062), 1432-1434.

Reichardt, J., U. Wandinger, M. Serwazi, and C. Weitkamp (1996), Combined Raman lidar for aerosol, ozone, and moisture measurements, *Optical Engineering*, *35*(5), 1457-1465.

Slingo, A., et al. (2006), Observations of the impact of a major Saharan dust storm on the atmospheric radiation balance, *Geophysical Research Letters*, *33*(24).

Sokolik, I. N., D. M. Winker, G. Bergametti, D. A. Gillette, G. Carmichael, Y. J. Kaufman, L. Gomes, L. Schuetz, and J. E. Penner (2001), Introduction to special section: Outstanding problems in quantifying the radiative impacts of mineral dust, *Journal of Geophysical Research-Atmospheres*, *106*(D16), 18015-18027.

Twomey, S. (1977), *Introduction to the Mathematics of Inversion in Remote Sensing and Indirect Measurements*, Elsevier ed., Amsterdam.

Veselovskii, I., V. Griaznov, A. Kolgotin, and D. N. Whiteman (2002), Angle- and size-dependent characteristics of incoherent Raman and fluorescent scattering by microspheres. 2. Numerical simulation, *Applied Optics*, *41*(27), 5783-5791.

Whiteman, D. N., S. H. Melfi, and R. A. Ferrare (1992), Raman lidar systems for the measurement of water vapor and aerosols in the Earth's atmosphere, *Applied Optics*, *31*(16), 3068-3082.

Yu, H., et al. (2006), A review of measurement-based assessments of the aerosol direct radiative effect and forcing, *Atmospheric Chemistry and Physics*, *6*, 613-666.

1. Introduction

Chapter 2

Fundamentals

This chapter presents key concepts of the aerosol theory and active optical remote sensing that will be used along this thesis. Firstly, an introduction to the aerosol concept and its effect on climate is presented. Second and third sections introduce the Earth's atmosphere and the fundamentals of scattering and absorption processes. Following sections present a classification and a description of the aerosol physical properties. Finally, the lidar technique is presented and the fundamental lidar equation is derived.

2.1. Aerosol and climate

Atmospheric aerosol is defined as the suspension of solid or liquid particles in the atmospheric air (excluding clouds) [*Horvath*, 1998]. Atmospheric aerosol particles, both natural and anthropogenic, may change climate through their direct and indirect effects on the radiative energy budget of the Earth-atmosphere system.

The direct effect is the mechanism by which aerosol particles scatter and absorb shortwave and longwave radiation, thereby altering the radiative balance of the Earth-atmosphere system [*Foster et al.*, 2007]. Scattering aerosol particles exert a net negative direct radiative forcing. Partially absorbing aerosol particles may exert a negative top-of-the-atmosphere (TOA) direct radiative forcing over dark surfaces such as oceans or dark forest surfaces, and a positive TOA radiative forcing over bright surfaces such as desert, snow and ice, or if the aerosol layer is located above a cloud [*Chylek and Wong*,

1995; *J M Haywood and Shine*, 1995]. Both positive and negative TOA direct radiative forcing mechanisms reduce the shortwave irradiance at the surface. The longwave direct radiative forcing is only substantial if the aerosol particles are large and occur in considerable concentrations at high altitudes [*Tegen et al.*, 1996]. The direct radiative forcing due to tropospheric aerosol particles is most frequently derived at TOA rather than at the tropopause because shortwave radiative transfer calculations have shown a negligible difference between the two [*J M Haywood and Shine*, 1997]. The surface forcing will be approximately the same as the direct radiative forcing at the TOA for scattering aerosol particles, but for partially absorbing aerosol particles the surface forcing may be many times stronger than the TOA direct radiative forcing [*Ramanathan et al.*, 2001].
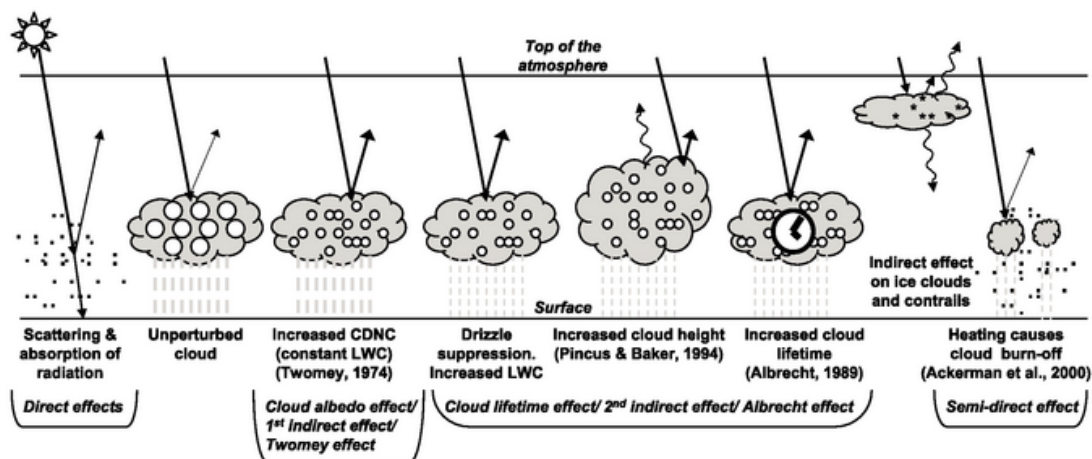
Figure 2.1. Schematic diagram showing the various radiative mechanisms associated with cloud effects that have been identified as significant in relation to aerosol particles (modified from Haywood and Boucher, 2000). The small black dots represent aerosol particles; the larger open circles cloud droplets. Straight lines represent the incident and reflected solar radiation, and wavy lines represent terrestrial radiation. The filled white circles indicate cloud droplet number concentration (CDNC). The unperturbed cloud contains larger cloud drops as only natural aerosol particles are available as cloud condensation nuclei, while the perturbed cloud contains a greater number of smaller cloud drops as both natural and anthropogenic aerosol particles are available as cloud condensation nuclei (CCN). The vertical grey dashes represent rainfall, and LWC refers to the liquid water content. (Source: Foster et al., IPCC, 2007).

The indirect effect is the mechanism by which aerosol particles influence cloud properties through their role as cloud condensation nuclei (CCN) and/or ice forming nuclei. The increase in aerosol particle concentrations may increase the ambient concentration of CCN and/or ice forming nuclei, therefore affecting cloud properties. A CCN increase can lead to more cloud droplets so that, for fixed cloud liquid water

content, the cloud droplet size will decrease. This effect leads to brighter clouds (the so-called "cloud albedo effect", "Twomey effect" or "first indirect effect"). Aerosol particles can also affect clouds by absorbing solar energy and altering the environment in which the cloud develops, thus changing cloud properties without actually serving as CCN. Moreover, the presence of aerosol particles can increase the cloud lifetime and hence increase the amount of solar radiation reflected from clouds. Such effects can change precipitation patterns as well as cloud extent and optical properties. Figure 2.1 shows a schematic diagram showing the different radiative mechanisms associated to the aerosol.

On a global average, the effect of anthropogenic aerosol particles only is comparable in magnitude to the radiative forcing of anthropogenic greenhouse gases. However, the quantification of the aerosol effects is more complex than the quantification of radiative forcing by greenhouse gases because of aerosol particle mass and particle number concentrations are highly variable in space and time, due to their much shorter atmospheric lifetime compared with the important greenhouse gases. Aerosol particles are difficult to measure without instrumental offsets or biases, making difficult to estimate their radiative effects. In fact, radiative forcing induced by aerosol particles has a factor two uncertainty, and may thus have much more importance in the overall energy budget [*Foster et al.*, 2007]. Figure 2.2 shows the main components of the climate radiative forcing. These results highlight the need for a better estimation of the aerosol radiative effects on a planetary scale in order to reduce the uncertainties.

Because the global aerosol distribution is very inhomogeneous, both horizontally and vertically, aerosol particles can have quite large effects in some regions of the Earth, whereas their influence is negligible in others. However, data on the spatial and temporal aerosol distribution are rather sparse. Satellite data cover most parts of the Earth [*Herman et al.*, 1997] but are still of high uncertainty over land, where the main aerosol sources are [*Kaufman and al.*, 1997]. Additionally, most of them suffer from the poor vertical resolution [*Kaufman and al.*, 1997] and the influence of clouds, which can completely prevent the observation of aerosol plumes. Ground-based Sun photometers for the measurement of the total optical depth are now widely spread over the whole globe [*Holben et al.*, 1998], but these measurements cannot deliver vertical resolution either and can only be performed under cloud free conditions. Therefore, winter data in mid-latitudes are not very frequent and definitely there is a ''good weather'' bias of

those measurements. In situ measurements at ground level give only locally representative information on the aerosol variability that cannot be used for the vertical dimension. Aircraft-based aerosol measurements can provide vertically resolved measurements but are very expensive and therefore, are only performed for short time periods during intensive field campaigns.
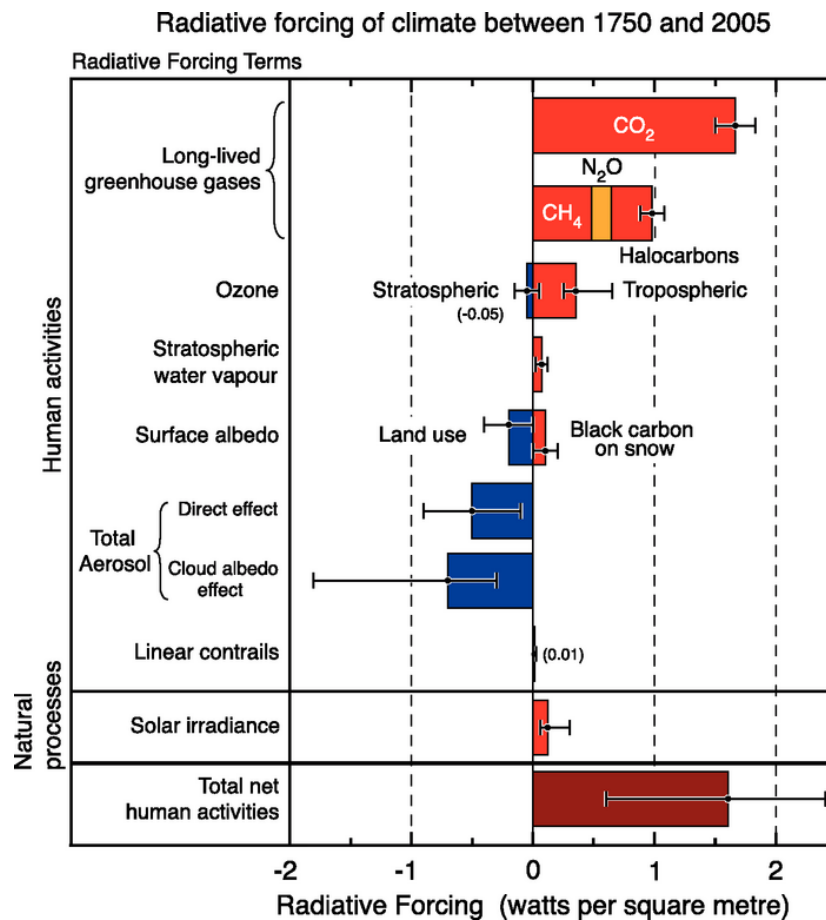
Figure 2.2. Summary of the main components of the climate radiative forcing. All these radiative forcings result from one or more factors that affect climate and are associated to human activities or natural processes. The values represent the forcings in 2005 relative to the start of the industrial era (about 1750). Human activities cause significant changes in long-lived gases, ozone, water vapour, surface albedo, aerosol particles and contrails. The only increase in natural forcing of any significance between 1750 and 2005 occurred in solar irradiance. Positive forcings lead to warming of planet and negative forcings lead to a cooling. The thin black line attached to each coloured bar represents the range of uncertainty for the respective value (Source: Foster et al., IPCC 2007).

2.2. Atmosphere structure and properties

In general terms, the atmosphere is divided into lower and upper regions. The lower atmosphere is generally considered to extend up to the top of the stratosphere (an altitude of about 50 km). The study of the lower atmosphere is known as meteorology, whereas the study of the upper atmosphere is called aeronomy.

The Earth's atmosphere is characterized by temperature and pressure variable with height. In fact, the variation of the average temperature profile with altitude is the basis for distinguishing the atmospheric layers. The regions of the atmosphere, including their key features, are summarized below (Fig. 2.3):
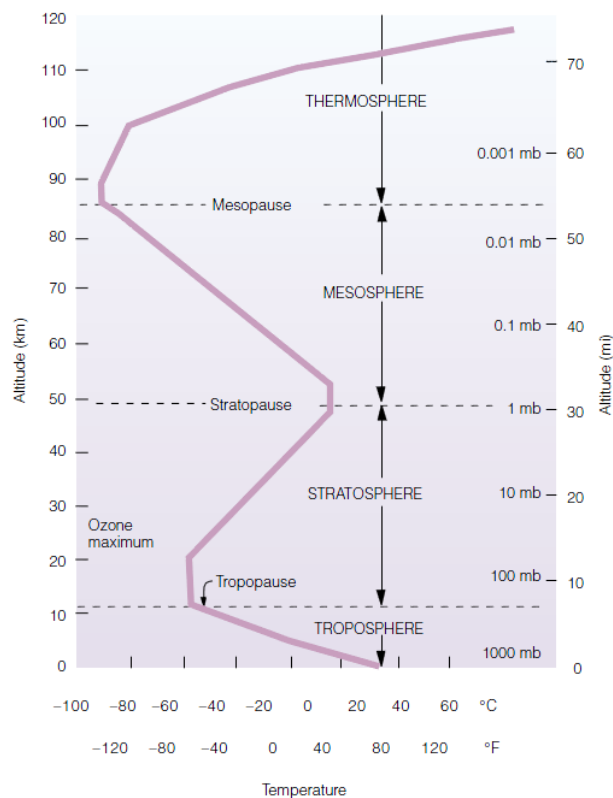
Figure 2.3. Atmospheric layers as related to the average profile of air temperature above the Earths's surface. The thick line illustrates how the average temperature varies in each layer (Adapted from Seinfeld and Pandis, 1998).

Troposphere. The lowest layer of the atmosphere, extending from the Earth's surface up to around 11 km (depending on the latitude and time of year) and characterized by decreasing temperature with height and rapid vertical mixing. The

tropopause is located at the top of the troposphere and the temperature remains fairly constant across this zone.

Stratosphere. Region extending from tropopause up to around 50 km altitude. In this region the temperature increases with altitude, leading to a layer in which vertical mixing is slow. The stratopause is located at the top of the stratosphere and it is the region where a maximum in the temperature occurs.

Mesosphere. Region extending from the stratopause up to around 85 km altitude; In this layer temperature decreases with altitude and a rapid vertical mixing occurs. The top of this layer is called mesopause and it is the coldest region in the atmosphere.

Thermosphere. The region above the mesopause. It is characterized by high temperatures as a result of absorption of short wavelength radiation by N_2 and O_2 and by rapid vertical mixing. The *ionosphere* is a region of the upper mesosphere and lower thermosphere where ions are produced by photoionization.

Exosphere. It is the outermost region of the atmosphere (>500 km altitude) where gas molecules with sufficient energy can escape from the Earth's gravitational attraction.

The atmosphere is composed primarily of nitrogen, oxygen, and several noble gases, with concentrations that have remained remarkably fixed over time. In addition, it also present a certain number of trace gases that occur in relatively small and sometimes highly variable amounts.

In spite of its apparent unchanging nature, the atmosphere is a dynamic system, with its gaseous constituents being continuously exchanged by means of processes related to vegetation, oceans, and biological organisms. The so-called cycles of atmospheric gases involve a number of physical and chemical processes. Gases are produced by chemical processes within the atmosphere itself by biological activity, volcanic exhalation, radioactive decay, and human industrial activities. Gases are removed from the atmosphere by chemical reactions in the atmosphere, by biological activity, physical processes such as particle formation, and deposition and uptake by the oceans and Earth. The average lifetime of a gas molecule introduced into the atmosphere can range from seconds to millions of years, depending on the effectiveness of the involved removal processes. Most of the species considered as air pollutants (in a region in which their concentrations exceed substantially the normal background levels)

have natural as well as anthropogenic sources. Therefore, in order to assess the effect that anthropogenic emissions may have on the atmosphere as a whole, it is essential to understand the atmospheric cycles of trace gases, including natural and anthropogenic sources as well as the predominant removal mechanisms. The important atmospheric gases are listed in Table 2.1.

Permanent		Variable	
Element	**% volume**	**Element**	**% volume**
Nitrogen	78.084	Water vapor	$0 - 4.00$
Oxygen	20.948	Ozone	$0 - 12\text{x}10^{-4}$
Argon	0.934	Sulfur dioxide	$0.001\text{x}10^{-4}$
Carbon dioxide	0.033	Nitrogen dioxide	$0.001\text{x}10^{-4}$
Neon	$18.18\text{x}10^{-4}$	Ammonia	$0.004\text{x}10^{-4}$
Helium	$5.24\text{x}10^{-4}$	Nitric Oxide	$0.0005\text{x}10^{-4}$
Krypton	$1.14\text{x}10^{-4}$	Hydrogen Sulfide	$0.00005\text{x}10^{-4}$
Xenon	$0.089\text{x}10^{-4}$		
Hydrogen	$0.5\text{x}10^{-4}$		
Methane	$1.5\text{x}10^{-4}$		
Nitric oxide	$0.27\text{x}10^{-4}$		
Carbon monoxide	$0.19\text{x}10^{-4}$		

Table 2.1. U.S. Standard Atmosphere (1976) composition.

2.3. Electromagnetic radiation propagation in the atmosphere

In the field of laser remote sensing, the propagation of electromagnetic radiation and the attenuation characteristics of the involved target and media are obviously important issues. In this section, we will give a brief description of the basic radiometric quantities, the scattering and absorption processes and the basic radiative-transfer equation that is used for describing the propagation of a collimated beam of radiation.

2.3.1. Basic radiometric quantities

The measurement of the interaction between radiation and atmosphere requires quantitatively dealing with electromagnetic radiation and defining radiometric quantities. The basis of the radiometric quantities is the monochromatic radiant flux Φ_λ, which is defined as the radiant energy, Q, included in an spectral interval dλ around the wavelength of interest, λ, passing through a control surface per unit time. This quantity does not provide any information about the spatial distribution of the energy. The radiant flux, $d\Phi_\lambda$, received (or emitted) at (from) the unit area on a detector (or source)

without considerations about the direction is denominated as the radiant flux density or irradiance:

$$E_\lambda = \frac{d\Phi_\lambda}{dS} \tag{2.1}$$

In order to characterize the emission of point sources, the radiant intensity I_λ represents the radiant flux $d\Phi_\lambda$, propagated in a solid angle $d\Omega$, defined as

$$I_\lambda = \frac{d\Phi_\lambda}{d\Omega} \tag{2.2}$$

For extended sources the radiance, defined as the flux emitted per unit solid angle and unit area (perpendicular to the considered direction s) is used. If θ is the angle between the normal of the radiating surface and the direction in which the emitted radiant flux is considered, the radiance is given by

$$L_\lambda = \frac{d^2\Phi_\lambda}{dSd\Omega\cos\theta} \tag{2.3}$$

Figure 2.4 shows a schematic diagram of the definition of radiance. Table 2.2 summarizes the different radiometric quantities, including the symbol used and the corresponding units in the International System (IS).
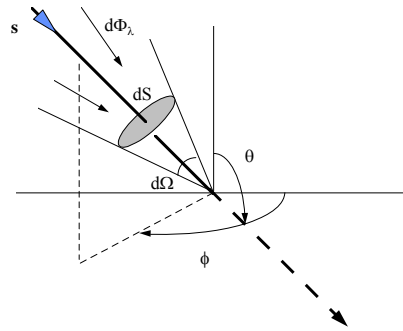
Figure 2.4. Radiance. Zenith angle θ and azimuth angle ϕ define the direction of the radiant flux s.

Radiometric quantity	Symbol	Unit
Radiant energy	Q	J
Radiant flux	Φ_λ	$W\mu m^{-1}$
Radiant flux density (irradiance)	E_λ	$W\,m^{-2}\,\mu m^{-1}$
Radiant intensity	I_λ	$W\,\mu m^{-1}\,sr^{-1}$
Radiance	L_λ	$W\,m^{-2}\,\mu m^{-1}\,sr^{-1}$

Table 2.2. Radiometric symbols and units.

2.3.2. Scattering and absorption processes in the atmosphere

The atmosphere presents basically two scattering phenomena: the first one due to molecules in the air, namely Rayleigh scattering and the second one due to aerosol particles [*Iqbal*, 1983].

Rayleigh's theory describes the scattering by air molecules. This theory, published in 1899, is based on the assumption that the scattering particles are spherical, being their radii less than 0.2 times the wavelength of the incident radiation, it only considers single scattering processes. A key feature of this theory is that the monochromatic optical extinction varies approximately as λ^{-4}, and this has been verified experimentally.

For most scattering of incident radiation by atmospheric molecules the energy and wavelength of the scattered photon are equal to those of the incident photon. This is called elastic scattering. For a very small fraction of scattered radiation a wavelength shift between incident and scattered photon is observed. This inelastic Raman scattering is caused by excitation or decay of the scattering molecule by incident photons changing its vibrational, rotational, and/or vibrational-rotational energy level.

A Raman scatterer molecule absorbs energy by being excited to a higher energy level while the frequency of the scattered photon decreases. The wavelength of the scattered photon is shifted towards higher values and the process is called Stokes Raman scattering with

$$\tilde{\upsilon}_{out} = \tilde{\upsilon}_{in} - \left| \Delta \tilde{\upsilon} \right| \tag{2.5}$$

The frequency of scattered light, $\tilde{\upsilon}_{out}$, compared to the frequency of incident light, $\tilde{\upsilon}_{in}$, is shifted by $\left| \Delta \tilde{\upsilon} \right|$. However, the scattering molecule might also loose energy to the scattered photon and decrease its energy level. The frequency of the scattered photon is now increased and the wavelength is shifted towards lower values. This case is called anti-Stokes Raman scattering with

$$\tilde{\upsilon}_{out} = \tilde{\upsilon}_{in} + \left| \Delta \tilde{\upsilon} \right| \tag{2.6}$$

A molecule is always in a certain state of vibrational-rotational energy. The frequency shift $\left| \Delta \tilde{\upsilon} \right|$ is caused by a change of the vibrational, rotational, and/or

vibrational-rotational energy level of the scattering molecule. It is characteristic for the scattering molecule and can be calculated as

$$\Delta\tilde{\upsilon} = \tilde{\upsilon}_{in} - \tilde{\upsilon}_{out} = \frac{\Delta E}{hc_0} \qquad (2.7)$$

$\tilde{\upsilon} = 1/\lambda = \upsilon/c_0$ in cm^{-1} is the wavenumber (usually used in spectroscopy) of the scattered photon, ΔE is the difference between the rotational-vibrational energy levels of the scattering molecule before and after the scattering process, h is the Planck constant and c_0 the speed of light in vacuum. The frequency (wavelength) shift for changes of the vibrational energy level of the molecule is much larger compared to the one for changes of the rotational energy level. Thus, electromagnetic radiation originating from vibrational-Raman scattering can easier be separated from elastically scattered light. This effect is used in the receiver of the Raman lidar systems. On the other hand, the intensity of the Raman scattered electromagnetic radiation is much lower than the intensity of Rayleigh scattering. Thus, for atmospheric applications, the detection of Raman signals is usually restricted to night-time when background noise is minimized.

On the other hand, Gustav Mie [*Mie*, 1908] solved the Maxwell equations for the interaction between an electromagnetic wave and a spherical particle, assuming that the sphere is homogeneous and isotropic. A deep description of both theories, Mie and Rayleigh, is presented by Bohren and Huffman [1983].The formulation describes two basic optical properties, the absorption and the scattering of solar radiation by a spherical particle.

Both scattering and absorption occur simultaneously, because all materials scatter, at least via their molecules, and absorb. These properties depend on the size parameter (x) defined as the relation between the particle radius and the wavelength of the incident wave ($2\pi r/\lambda$) and also on the refractive index m, that depends on the particle chemical composition. The scattered radiance also depends on the scattering angle, Θ, and the phase function that describes its angular distribution. The attenuation of the radiant energy in a real medium is expressed by the extinction coefficient σ_e, defined by the sum of the scattering (σ_s) and absorption (σ_a) coefficients: $\sigma_e = \sigma_s + \sigma_a$. Mie reached to an expression for σ_e for a suspension of spherical particles of different radii (between r_1 and r_2):

$$\sigma_e = \int_{r_1}^{r_2} \pi r^2 Q_e(x,m)n(r)dr \tag{2.8}$$

where Q_e is the extinction efficiency factor and can be understood as the effectiveness with which the particle interacts with the radiant flux, and *n(r)* is the size distribution of those spherical particles (see section 2.5).

Mie theory is applied when the size of the particles is comparable to the incident wavelength (*x* ~ 1), producing interference patterns with the partial waves emitted by the multipoles of the particles having phase differences. For this reason there is a strong angular dependency, there is an increase in the forward scattering (compared to Rayleigh scattering) and the chromatic dependency of this scattering is smaller. Mie theory converges into Rayleigh theory when *x* decreases, therefore Rayleigh theory can be explained with Mie theory but, due to the simplicity of Rayleigh theory, they usually are applied separately. Figure 2.5 shows the differences in the scattering for both theories. Rayleigh scattering is symmetric respect to the plane perpendicular to the propagation direction and find its minimum at *Θ* = ±90º. On the other hand, Mie scattering presents an asymmetry, with a strong forward scattering.
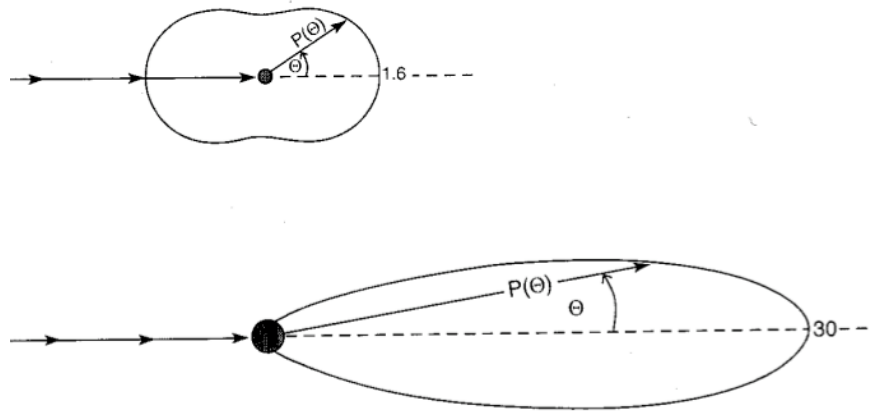
Figure 2.5. (top) Rayleigh scattering and (bottom) Mie scattering.

Electromagnetic radiation is also partially absorbed by the atmospheric components increasing their internal energy and therefore their temperature. The absorption process depends on the energy state of a molecule. The absorbed radiation is used to produce a transition from one energy level to another. Because the energy level associated to some kinds of energy like rotational, vibrational or electronic energies are quantized, the absorption process occurs only at discrete wavelengths and therefore this process is called selective absorption. When the absorption takes place over a number of

wavelengths very close to each other it is possible some overlap and it is called band absorption [*Iqbal*, 1983].

The main molecular absorbers are H_2O (water vapour), CO_2, O_3, N_2O, CO, O_2, CH_4 and N_2. The minor absorbers are oxides of nitrogen NO_2, N_2O_4, N_2O_5; hydrocarbon combinations C_2H_4, C_2H_6, C_3H_8; and sulphurous gas H_2S. Most of these absorbers are active mainly in the near- and far-infrared wavelengths regions (from 0.7 to 100 μm). On the contrary, atomic gases as O and N absorb mainly the maximum UV and shorter wavelengths. Figure 2.6 shows the main molecular absorbers for the solar radiation spectrum.
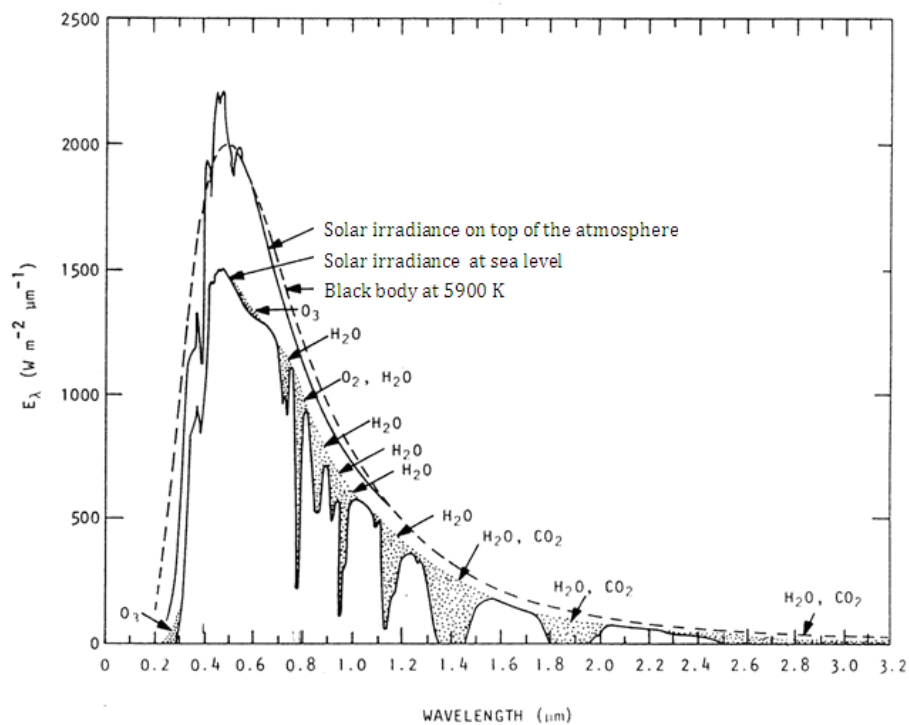
Figure 2.6. Identification of the various molecular absorbers. The graph shows the solar irradiance on top of the atmosphere, at sea level and also the corresponding irradiance for a black body at 5900 K (from Iqbal, 1983).

2.3.3. Radiative transfer equation

The radiative transfer equation mathematically describes the propagation of radiation through a medium, where absorption, emission and scattering processes are present. The radiative transfer equation has application in a wide variety of topics including optics, astrophysics, atmospheric science, and remote sensing. We present a brief derivation of this equation.

Let us consider a volume dV of an isotropic non absorbing medium hit by a radiant flux characterized by the irradiance E. The flux $d^2\Phi$ scattered by dV in the solid angle $d\Omega$ at a given direction Θ respect to the incident direction is

$$d^2\Phi = Ef(\Theta)dVd\Omega \tag{2.9}$$

where $f(\Theta)$ (in m^{-1} sr^{-1}) is the scattering function, that characterizes the angular distribution of scattered photons by the particles in the medium.

The amount of scattered flux is obtained integrating in all directions

$$d\Phi = EdV\int_{4\pi} f(\Theta)d\Omega \tag{2.10}$$

The flux scattered by the volume dV must be equal to the flux lost due to scattering along the thickness of the volume ds. Then, the incident flux in a cross section of the volume is noted EdA and the amount of scattered flux is $d\Phi=\sigma_s EdAds=\sigma_s EdV$. Thus, using equation 2.10 we obtain the relationship between $f(\Theta)$ and the scattering coefficient

$$\sigma_s = \int_{4\pi} f(\Theta)d\Omega \tag{2.11}$$

If we are interested only on the angular dependency of $f(\Theta)$, we define the phase function $P(\Theta)$, related to $f(\Theta)$ by the following expression

$$P(\Theta) = 4\pi\frac{f(\Theta)}{\sigma_s} \tag{2.12}$$

This parameter $P(\Theta)$ represents the fraction of scattered radiation in the direction Θ, per solid angle, respect to the scattered radiation in all directions.

The relative importance of the scattering and absorption is characterized by the single scattering albedo

$$\omega_0 = \frac{\sigma_s}{\sigma_s + \sigma_a} = \frac{\sigma_s}{\sigma_e} \tag{2.13}$$

Let us now consider a radiant flux propagating in a parallel direction to the thickness ds of a medium. The extinction of the radiance along the thickness is defined by means of the optical thickness

$$\tau_\lambda = \int_{s_1}^{s_2} \sigma_e ds \qquad (2.14)$$

In atmospheric science is common the use of the optical depth (OD) or normal optical thickness as the optical thickness measured vertically

$$OD_\lambda = \int_{z_1}^{z_2} \sigma_e dz \qquad (2.15)$$

The relationship between optical thickness and optical depth is

$$\tau_\lambda = OD_\lambda m_0 \qquad (2.16)$$

and m_0 is the relative optical air mass. In equation 2.16 the relative optical air mass m_0 is a function of the solar zenithal angle (θ_0) defined as the angle between the zenith (the vertical direction) and the direct solar irradiance path. Its relation can be approximate with the following expression [*Kasten*, 1966]:

$$m_0 = \frac{1}{\cos(\theta_0)} \ . \qquad (2.17)$$

Equation 2.17 works assuming a uniform atmosphere with refractive index equal to one and considering a plane-parallel atmosphere [*Iqbal*, 1983]. This approximation can be applied for θ_0 smaller than 80º. Otherwise, it has to be used a different approximation (i.e. [*Kasten and Young*, 1989]).

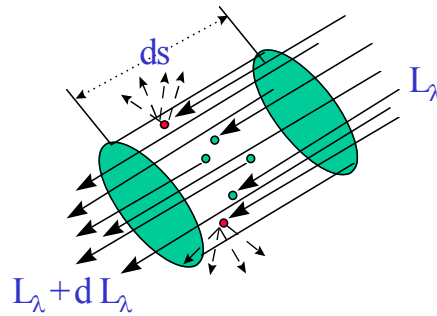**Figure 2.7.** Schematic draw of the radiance variation observed when a radiant flux beam travels through a volume dV.

Based on the principle of energy conservation we present the equation that describes the radiative transfer in a medium. The variation of radiance dL_λ, observed when a radiant flux travels through a volume dV (Fig. 2.7) has two components. On one hand, due to the attenuation

$$dL_\lambda(1) = -\sigma_e L_\lambda ds \qquad (2.18)$$

On the other hand, the radiant flux can be intensified by the emission of the medium and the multiple scattering. This effect is quantified by the coefficient J_λ.

$$dL_\lambda(2) = \sigma_e J_\lambda ds \qquad (2.19)$$

Thus, the total variation in the radiance is $dL_\lambda = dL_\lambda(1) + dL_\lambda(2)$. If we divide this expression by $\sigma_e ds$, the result is the general radiative transfer equation

$$\frac{dL_\lambda}{\sigma_e ds} = -L_\lambda + J_\lambda. \qquad (2.20)$$

If the contribution due to emission is not considered, the source function can be expressed in term of the phase function $P(\Theta)$, and thus the radiative transfer equation presents this form

$$\frac{dL_\lambda}{\sigma_e ds} = -L_\lambda + \frac{\omega_{0\lambda}}{4\pi} \int_\Omega L_\lambda P(\Theta) d\Omega \qquad (2.21)$$

The next step consists on finding a solution to the equation for a medium equivalent to the atmosphere as real as possible. The simplest geometry is a layer limited by two parallel and infinite planes, where the properties are constant and the incident radiation is also constant. This is the case of the plane-parallel atmospheres that constitute a good approximation for the real atmosphere, where the vertical variations are faster than the horizontal variations for all the magnitudes. In this situation is convenient measuring the distance over the vertical direction z, i.e. normal to the stratification plane (figure 2.8).
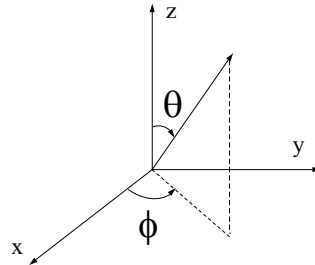

Figure 2.8. Coordinates for defining a point: θ is the zenith angle and ϕ is the azimuth angle.

This geometry allows for approximating the optical mass to $m^{-1} = \mu = cos(\theta)$. Applying the variable change $dz=\mu ds$ in equation 2.20 and using the optical depth (equation 2.15) we obtain

$$\mu \frac{dL_\lambda(\delta_\lambda, \mu, \phi)}{d\delta_\lambda} = -L_\lambda(OD_\lambda, \mu, \phi) + J_\lambda(OD_\lambda, \mu, \phi) \qquad (2.22)$$

Let us assume that the input radiance does not vary with time, does not present horizontal gradients and the atmosphere is isotropic. Multiplying equation 2.22 by $e^{-OD_\lambda/\mu}$ and integrating between $OD_0=0$ (top of the atmosphere) and OD_λ, we obtain the solution for emerging radiance through the atmosphere from the level OD_λ

$$L_\lambda(OD_\lambda, \mu, \phi) = L_\lambda(OD_0, \mu, \phi)e^{\frac{-(OD_0 - OD_\lambda)}{\mu}} + \int_{\delta_\lambda}^{\delta_0} J_\lambda(OD'_0, \mu, \phi)e^{\frac{-(OD_0 - OD_\lambda)}{\mu}} \frac{dOD'_\lambda}{\mu}$$

$$(2.23)$$

The physical interpretation is simple (Fig. 2.9). The radiance that reaches the level OD_λ is equal to the radiance on OD_0 attenuated between both levels, plus the contribution of the medium attenuated by the successive layers OD'.
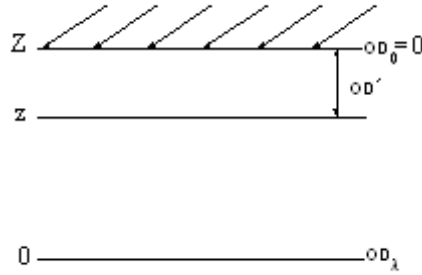
Figure 2.9. Plane-parallel atmosphere irradiated by a solar beam.

In the case of the sun direct irradiance, where the contributions for emission and scattering in directions other than the direct flux can be discarded, the solution to the radiative transfer equation can be reduced to the Beer-Bouguer-Lambert Law:

$$E_\lambda(OD_\lambda, \mu, \phi) = E_\lambda(OD_0, \mu, \phi)e^{\frac{-(OD_0 - OD_\lambda)}{\mu}} \qquad (2.24)$$

This expression tells us that the attenuation of the direct irradiance follows an exponential function.

2.4. Classification of the atmospheric aerosol

The atmospheric aerosol is a complex and dynamic mixture of solid and liquid particles from natural and anthropogenic sources suspended in the air. It can be classified according to different criteria. From the standpoint of its origin, the atmospheric aerosol can be natural or anthropogenic. Considering the mechanism of formation, the aerosol particles are classified as primary when they are emitted as such into the atmosphere and secondary when they are generated through chemical reactions. These chemical reactions can be result of the interaction between precursor gases in the atmosphere to form a new particle by condensation or between a gas and a particle to generate a new particle by adsorption or coagulation [*Penkett*, 1988]. In the next lines we present a brief description of the typical atmospheric aerosols.

2.4.1. Sulphate aerosol

Atmospheric sulphate aerosol may be considered as consisting of sulphuric acid particles that are partly or totally neutralized by ammonia and that are present as liquid droplets or partly crystallized. Sulphate is formed by aqueous phase reactions within cloud droplets, oxidation of SO_2 via gaseous phase reactions with OH, and by condensational growth onto pre-existing particles (e.g., [*Penner and al.*, 2001]). Emission estimates are summarized by Haywood and Boucher [2000]. The main source of sulphate aerosol is via SO_2 emissions from fossil fuel burning (about 72%), with a small contribution from biomass burning (about 2%), while natural sources include dimethyl sulphide emissions by marine phytoplankton (about 19%) and SO_2 emissions from volcanoes (about 7%).

2.4.2. Organic and black carbon aerosol from fossil fuels

Organic aerosols are a complex mixture of chemical compounds containing carbon-carbon bonds produced from fossil fuel and biofuel burning and natural biogenic emissions. Organic aerosols are emitted as primary aerosol particles or formed as secondary aerosol particles from condensation of organic gases considered semi-volatile or having low volatility. Hundreds of different atmospheric organic compounds have been detected in the atmosphere [*Hamilton et al.*, 2004; *Murphy*, 2005], which makes definitive modeling of the direct and indirect effects extremely challenging [*McFiggans et al.*, 2006].

Black carbon (BC) is a primary aerosol emitted directly at the source from incomplete combustion processes such as fossil fuel and biomass burning and therefore much atmospheric BC is from anthropogenic origin. Black carbon aerosol strongly absorbs solar radiation. Electron microscope images of BC particles show that they are emitted as complex chain structures (e.g., [*Posfai et al.*, 2003]), which tend to collapse as the particles age, thereby modifying the optical properties (e.g., [*Abel et al.*, 2003]).

2.4.3. Biomass burning aerosol

Biomass burning describes the burning of living and dead vegetation, including anthropogenic sources, like burning of vegetation for land clearing and land-use, as well as natural induced fires, e.g. from lightning. The human-induced fraction is estimated to be about 90 % [*Andreae*, 1991]. In Africa more biomass is burned (e.g. forest fires and savannas) on an annual basis than anywhere else. But first believed as a regional problem of the tropics, global biomass burning turned out to be more extensive than previously thought, and is increasing with time [*Levine et al.*, 1993]. Therefore biomass burning is an important component in global climate change.

Biomass burning releases particles and gases into the atmosphere. The released gases include greenhouse gases (mainly carbon dioxide (CO_2), methane (CH_4), nitrous oxide (N_2O)) that help warm the Earth (positive radiative forcing). It is also one of the largest sources for small particles [*Reid et al.*, 2005b], which consists of 5 - 10 % of black carbon [*Reid et al.*, 2005a]. Although the contribution of black carbon to the total amount of aerosols is estimated only to 3 - 5% (compared to 21 - 48% of mineral dust) [*Tegen et al.*, 1997], black carbon is the second strongest contribution to current global warming [*Ramanathan and Carmichael*, 2008].

2.4.4. Mineral dust aerosol

Mineral dust is one major component of the Earth's atmosphere. They are created by wind erosion of soil, and a large amount of mineral dust is injected every year into the atmosphere under favorable weather conditions. Since 2001, different studies have reported dust emission estimates from 1000-2150 Tg/yr (with a considerable variation in range) [*Tegen et al.*, 2002; *Luo et al.*, 2003; *Zender et al.*, 2003; *Tegen et al.*, 2004]. The dust emission is assumed to have a significant anthropogenic component mainly originating from agriculture and industrial practices [*Prospero et al.*, 2002; *Rodriguez et al.*, 2011]. Modeling studies have attempted to

constrain the anthropogenic impact on dust emission. Tegen and Fung [1995] estimated the anthropogenic contribution to mineral dust to be 30 to 50% of the total dust burden in the atmosphere.

The main source regions of desert dust are limited to the Northern Hemisphere [*Prospero et al.*, 2002], extending from the west coast of North Africa to Middle and East Asia. The largest source region is the Saharan desert. With 9.000.000 million km^2 it is the largest desert on Earth. Its contribution to the global annual dust emission is about 50 - 70 % [*Washington et al.*, 2003]. Because mineral desert dust can be transported over thousands of kilometers, it is not only a regional phenomenon, but has a global climate effect. Dust is exported from the Saharan desert during the whole year. Once lifted in the air, mineral dust can be transported over several thousands of kilometers [*Hamonou et al.*, 1999; *Goudie and Middleton*, 2001; *Ansmann et al.*, 2003].

The direct aerosol effect of the dust particles is very complex. Due to their large range of size (from about 0.01 μm to about 100 μm, [*Sokolik et al.*, 2001]) and their chemical composition, they not only scatter and absorb the incoming solar light, but also have a significant impact on long-wave terrestrial radiation [*Tanre et al.*, 2003]. The magnitude and sign of the direct aerosol effect of dust strongly depends on the optical properties and the vertical and horizontal distribution of the dust plume, as well as on the albedo of the underlying surface [*Sokolik et al.*, 2001]. A further difficulty in radiative transfer models is the strongly irregular shape of mineral dust particles, which prevents the application of classical Mie theory (section 2.3.2).

2.4.5. Marine aerosol

In addition to mineral dust, sea salt is one major type of aerosols in the atmosphere. Erickson and Duce [1988] estimated the total amount of sea salt emission from ocean to atmosphere to be 1000-3000 Tg per year, Tegen *et al*. [1997] estimated even 5900 Tg per year. In the last IPCC report, a best guess of 3300 Tg per year is given [*Foster et al.*, 2007], therefore the median emission per m^2 ocean surface per year is about 10 g.

Sea salt particles have a large range of sizes from around 0.05 to 10 μm. Their residence time in the atmosphere ranges from a few hours to several days. They are mainly generated by bursting of air bubbles, which is strongly dependent on wind speed. Sea salt particles are very efficient as cloud condensation nuclei. Thus they do

not just scatter the incoming and outgoing radiation, but have also a strong indirect aerosol effect. A small amount of giant particles can significantly change the stratus-cumulus drizzle production and the cloud albedo [*Feingold et al.*, 1999]. Activation of sea-salt particles can significantly increase the number concentration of cloud droplets in marine stratus clouds and therefore enhance the cloud albedo with respect to incoming shortwave radiation [*Latham and Smith*, 1990], leading to a negative radiative forcing and therewith to a cooling effect.

2.5. Physical properties of atmospheric aerosol particles

Aerosol particles are characterized by their shape, size, chemical composition and total content, which determine their radiative properties. A simple way to characterize a set of particles suspended in a fluid is by means of its density that represents the total mass per volume of air, usually expressed in $\mu g\ m^{-3}$ for atmospheric aerosol. It is also widely used the number density of particles N, expressed in inverse volume units.

The particle size in a monodisperse aerosol is completely defined by a single parameter, the particle radius. However, most aerosols are polydisperse and may have particle sizes that range over two or more orders of magnitude. Because of this wide size range and the fact that the physical properties of aerosol particles are strongly dependent on particle size, it is necessary to characterize their size distributions by means of statistical parameters [*Hinds*, 1982]. Considering spherical particles with a radius in the logarithmic interval *[lnr, lnr+dlnr]*, the number of particles in this interval will be *dN* and the mass *dM*. The use of the logarithmic scale is useful due to the large range in particles sizes. Number size distribution is denoted as

$$n(r) = \frac{dN}{d\ln r}$$
(2.25)

and mass size distribution as

$$m(r) = \frac{dM}{d\ln r}$$
(2.26)

In the same way, volume size distribution is defined as

$$v(r) = \frac{dV}{d\ln r}$$
(2.27)

representing the aerosol volume in an air column of unity cross section per logarithmic particle radius unit. The total number of particles (or mass or volume) is obtained integrating between the minimum and maximum particle radius.

$$N = \int_{\min}^{\max} n(r) d \ln r$$

(2.28)

Considering spherical particles, volume and number distributions can be related using the following expression:

$$v(r) = \frac{dV}{d \ln r} = \frac{4\pi}{3} r^3 \frac{dN}{d \ln r}$$

(2.29)

It has been observed that size distributions measured in the atmosphere present certain rules, therefore allowing for their modeling. The general approach is to represent these size distributions using a mathematical expression with some fitting parameters retrieved empirically.

At present, to clarify the number of parameters necessary to define the aerosol radiative features is an open problem; it can be obtained with accuracy using only measurements. A good representation for aerosol particles, specially the smaller particles, in clean and polluted areas, is the log-normal distribution function [*Hegg et al.*, 1993]:

$$v(r) = \frac{dV}{d \ln r} = \frac{V_0}{\sigma \sqrt{2\pi}} \exp\left[-\frac{\ln^2(r/r_m)}{2\sigma^2} \right]$$

(2.30)

Similar functions can describe mass and number size distributions. In eq. 2.30, r_m and σ are the fitting parameters, V_0 represent the volume of particles in an air column of unity cross section. The standard deviation of the logarithm of the radii σ represents the width of the size distribution. The modal radius of the particles r_m provides the position of the maximum in the curve of this distribution.

Atmospheric aerosol size distribution can be represented with the sum of three log-normal distributions, called modes, building a multimodal size distribution function. The nucleation or Aitken mode is formed by particles with diameters between 0.01 and0.1 μm, which are precursors of water vapor condensation. Accumulation mode is constituted by particles from 0.1 to 1 μm of diameter, remaining in the atmosphere around one week, which may lead to condensation or coagulation with nucleation mode

particles. Finally, the coarse mode presents diameter of particles larger than 1 μm. The widespread terminology applied in atmospheric sciences refers as fine particles those of diameter <1 μm and coarse particles with diameters > 1 μm. In epidemiological science the limits of these ranges are different, considering as fine particles those particles with diameters lower than 2.5 μm. Figure 2.10 shows the three modes mentioned above and some examples of aerosol types belonging to each of them.
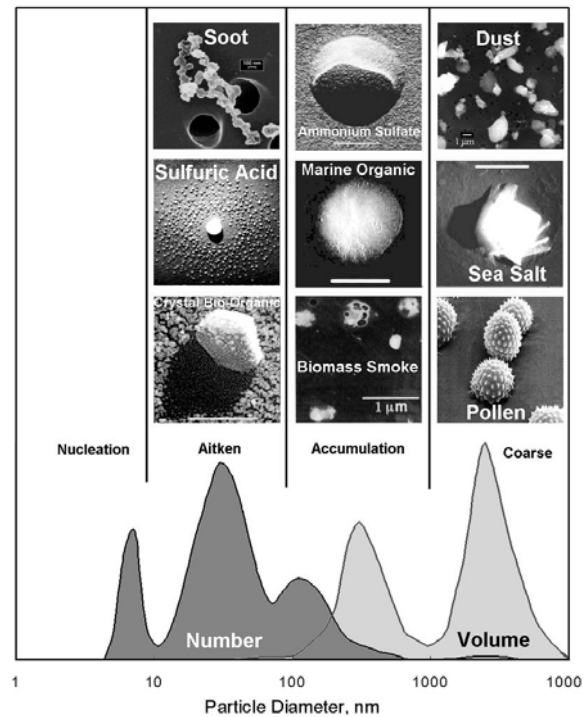
Figure 2.10. Multimodal size distribution for atmospheric aerosols.

2.6. Lidar principle and lidar equation

Lidar is an acronym for light detection and ranging. Lidar is one of the active remote sensing techniques for the environment. It has proven to be an essential tool to monitor the structure, composition and dynamics of the Earth's atmosphere. Lidar has largely contributed to our knowledge of the Earth's atmosphere during the past decades [*Measures*, 1984; *Kovalev and Eichinger*, 2004]. High spatial and temporal resolution of measurements, the possibility of monitoring the atmosphere at ambient conditions, and the potential of covering the height range from the ground to more than 100 km altitude make up the attractiveness of lidar instruments. It is particularly useful for the investigation of some highly variable atmospheric parameters. Simple elastic

backscatter lidars have been used to investigate turbulent processes and the diurnal cycle of the planetary boundary layer (PBL) [*Kovalev and Eichinger*, 2004]. Polarization lidar systems are used to distinguish water droplets from ice crystals in clouds [*Sassen*, 1991]. Rayleigh scatter lidars provide middle atmosphere temperatures and present long-term variability in the thermal structure. Resonance lidars probe the mesospheric region and provide the winds driven metal layer densities. Raman lidars work on the principle of Raman effect and provides an approach to the range resolved measurements of atmospheric trace species [*Weitkamp*, 2005].

Lidar systems are lasers based on systems that operate on principles similar to that of radar (radio detection and ranging) or sodar (sound navigation and ranging). In the case of lidar, a light pulse is emitted into the atmosphere. Light from the beam is scattered in all directions from molecules and particles in the atmosphere. A portion of the light is backscattered to the lidar system. This light is collected by a telescope and focused upon a photodetector that measures the amount of backscattered light as a function of distance from the lidar system. Figure 2.11 is a schematic representation of the major components of a lidar system. A lidar consists of the following basic functional blocks: (1) a laser source of short, intense light pulses, (2) a photoreceiver subsystem, which collects the backscattered light and converts it into an electrical signal, and (3) a computer/recording system, which digitizes the electrical signal as a function of time (or equivalently as a function of the distance from the light source) as well as controlling the other basic functions of the system.
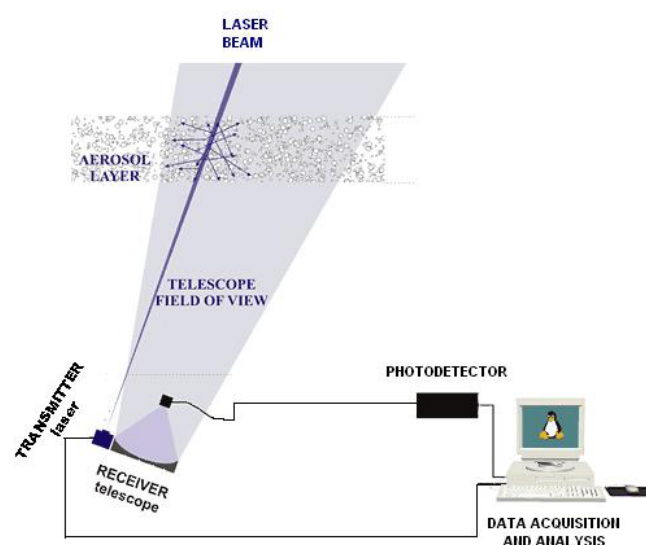
Figure 2.11. Schematic representation of the major parts of a lidar system.

In its simplest form, the detected lidar signal can be written as

$$P(R) = KG(R)\beta(R)T^2(R) \tag{2.31}$$

i.e., the power P received from a distance R is made up of four factors. The first factor, K, summarizes the performance of the lidar system, the second $G(R)$, describes the range-dependent measurement geometry. These two factors are completely determined by the lidar setup and can thus be controlled by the experimentalist. The information on the atmosphere, and thus all the measurable quantities, are contained in the last two factors of Eq. (2.31). The term $\beta(R)$ is the backscatter coefficient at distance R. It stands for the ability of the atmosphere to scatter light back into the direction from which it comes. $T^2(R)$ is the transmission term and describes how much light gets lost on the way from the lidar to distance R and back. Both $\beta(R)$ and $T^2(R)$ are the subjects of investigation and in principle unknown to the experimentalist.

Going into more detail, we can write the system factor as

$$K = P_0 \frac{c\tau}{2} A\eta \tag{2.32}$$

P_0 is the average power of a single laser pulse, and τ is the temporal pulse length. Hence $E_0 = P_0 \tau$ is the pulse energy, and $c\tau$ is the length of the volume illuminated by the laser pulse at a fixed time. The factor 1/2 appears because of an apparent "folding" of the laser pulse through the backscatter process as illustrated in Fig. 2.12. When the lidar signal is detected at an instant time t after the leading edge of the pulse was emitted, backscatter light from the leading edge of the pulse comes from the distance $R_1 = ct/2$. At the same time, light produced by the trailing edge arrives from distance $R_2 = c(t-\tau)/2$. Thus $\Delta R = R_1-R_2 = c\tau/2$ is the length of the volume from which backscatter light is received at an instant time and is called the "effective (spatial) pulse length". A is the area of the receiver optics responsible for the collection of backscattered light, and η is the overall system efficiency. It includes the optical efficiency of all elements that the transmitted and received light has to pass and the detection efficiency. The telescope area A and the laser energy E_0, or, rather, the average laser power $\overline{P} = E_0 f_{rep}$, with the pulse repetition frequency f_{rep}, are primary design parameters of a lidar system.
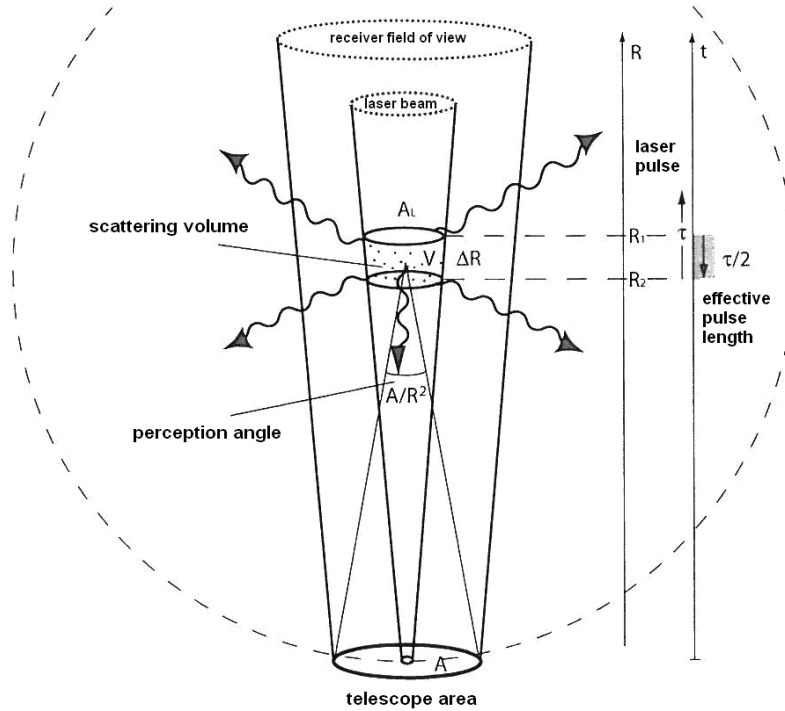
Figure 2.12. Illustration of the lidar geometry (from Weitkamp, 2005).

The geometry factor

$$G(R) = \frac{O(R)}{R^2} \qquad (2.33)$$

includes the overlap function $O(R)$, which described the incomplete overlap between the laser beam and the receiver field of view, and the term R^{-2}. The quadratic decrease of the signal intensity with distance is due to the fact that the receiver telescope area makes up a part of a sphere's surface with radius R that encloses the scattering volume (see Fig. 2.12). If we imagine an isotropic scatterer at distance R, the telescope area A will collect the fraction

$$\frac{I_C}{I_S} = \frac{A}{4\pi R^2} \qquad (2.34)$$

of the overall intensity I_S scattered into the solid angle 4π. In other words, the solid angle A/R^2 is the perception angle of the lidar for light scattered at distance R. The factor 4π does not appear explicitly in the lidar equation because it cancels out by the definition of the backscatter coefficient β as we will see below. It is primarily the R^{-2} dependence that is responsible for the large dynamic range of the lidar signal. If we start

detecting a signal with $O(R) = 1$ at a distance of 10 m, the signal will be 6 orders of magnitude lower at 10 km distance just because of the geometry effect. To what extent lidar is a *range-resolving and remote* measurement technique depends on our ability to compensate for this effect. Geometrical signal compression at short distances is one possibility as can be seen from Fig. 2.13 in which an arbitrary, but realistic overlap function is shown, multiplied with the function R^{-2}. The strong signal in the near field is suppressed by several orders of magnitude.
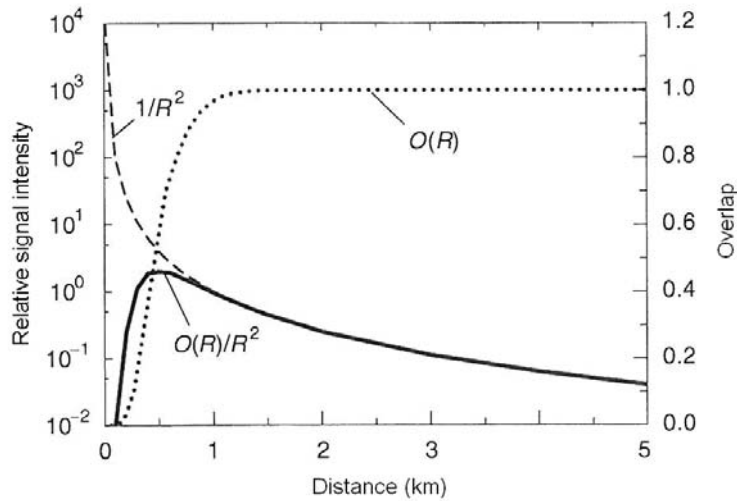
Figure 2.13. Influence of the overlap function on the signal dynamics (from Weitkamp, 2005).

The backscatter coefficient $\beta(R,\lambda)$ is the primary atmospheric parameter that determines the strength of the lidar signal. It describes how much light is scattered into the backward direction, i.e., towards the lidar receiver. The backscatter coefficient is the specific value of the scattering coefficient for the scattering angle $\theta = 180°$. Let N_j be the concentration of scattering particles of kind j in the volume illuminated by the laser pulse, and $d\sigma_{j,sca}(\pi,\lambda)/d\Omega$ the particles' differential scattering cross section for the backward direction at wavelength λ. The backscatter coefficient can then be written as

$$\beta(R,\lambda) = \sum_j N_j(R) \frac{d\sigma_{j,sca}}{d\Omega}(\pi,\lambda) \qquad (2.35)$$

summing over all kinds of scatterers. Since the number concentration is given in units of m^{-3} and the differential scattering cross section in $m^2 sr^{-1}$, the backscatter coefficient has the unit $m^{-1} sr^{-1}$.

If we return to our simplified picture of isotropic scattering and assume that there is only one type of particle in the scattering volume, the relation between the

backscatter coefficient and the isotropic scattering cross section σ_{sca} is $4\pi\beta=N\sigma_{sca}$. The intensity of scattered light from the illuminated volume $V=A_L\Delta R=A_Lc\tau/2$, with the laser-beam cross section A_L, is proportional to the area $A_s=N\sigma_{sca}V$, i.e., the scattering cross section of all particles in the volume V. Thus, the relative intensity of the scattered light is

$$\frac{I_s}{I_0}=\frac{A_S}{A_L}=\frac{N\sigma_{sca}c\tau}{2}=\frac{4\pi\beta c\tau}{2} \qquad (2.36)$$

With Eq. (4.4), we obtain the ratio of the collected to the emitted light intensity

$$\frac{I_c}{I_0}=\frac{A\beta c\tau}{2R^2} \qquad (2.37)$$

The right side of this equation describes that part of the lidar equation that directly refers to the scattering geometry, i.e., it contains the size and the backscatter properties of the scattering volume and the perception angle of the lidar.

In the atmosphere, the laser light is scattered by air molecules and aerosol particles, i.e., $\beta(R,\lambda)$ can be written as

$$\beta(R,\lambda)=\beta_{mol}(R,\lambda)+\beta_{aer}(R,\lambda) \qquad (2.38)$$

Molecular scattering (index mol), mainly occurring from nitrogen and oxygen molecules, primarily depends on air density and thus decreases with height, i.e., backscattering decreases with distance if the observation is made from the ground, but increases in the case of downward-looking system on aircraft or spacecraft. Particle scattering (index aer for aerosol particles) is highly variable in the atmosphere on both spatial and temporal scales. Particles represent a great variety of scatterers: tiny liquid and solid air-pollution particles consisting of, e.g., sulphates, soot and organic compounds, larger mineral dust and sea-salt particles, pollen and other biogenic material, as well as comparably large hydrometeors such as cloud and rain droplets, ice crystals, hail and graupel.

As the final part of the lidar equation, we have to consider the fraction of light that gets lost on the way from the lidar to the scattering volume and back. The transmittance $T(R)$ can take values between 0 and 1 and is given by

$$T^2(R,\lambda)=\exp\left[-2\int_0^R \alpha(r,\lambda)dr\right] \qquad (2.39)$$

This term results from the specific form of the Lambert-Beer-Bouguer law for lidar. The integral considers the path from the lidar to distance R. The factor 2 stands for the two-way transmission path. The sum of all transmission losses is called light extinction, and $\alpha(R,\lambda)$ is the extinction coefficient. It is defined in a similar way as the backscatter coefficient as the product of the number concentration and the extinction cross section $\sigma_{j,ext}$ for each type of scatterer j,

$$\alpha(R,\lambda) = \sum_j N_j(R)\sigma_{j,ext}(\lambda) \tag{2.40}$$

Extinction can occur because of scattering and absorption of light by molecules and particles. The extinction coefficient therefore can be written as the sum of four components,

$$\alpha(R,\lambda) = \alpha_{mol,sca}(R,\lambda) + \alpha_{mol,abs}(R,\lambda) + \alpha_{aer,sca}(R,\lambda) + \alpha_{aer,abs}(R,\lambda) \tag{2.41}$$

where the indexes sca and abs stand for scattering and absorption, respectively. Because scattering into all directions contributes to light extinction, the (integral) scattering cross section σ_{sca}, together with the absorption cross section σ_{abs}, both in m^2, make up the extinction cross section,

$$\sigma_{ext}(\lambda) = \sigma_{sca}(\lambda) + \sigma_{abs}(\lambda) \tag{2.42}$$

Consequently, the extinction coefficient, α, has the unit m^{-1}.

As indicated in the equations above, both β and α depend on the wavelength of the laser light. This wavelength dependence is determined by the size, the refractive index, and the shape of the scatterer particles. We will discuss the consequences in conjunction with the description of the basic lidar techniques below.

Summarizing the discussion of the individual terms, we can now rewrite the lidar equation (2.27) in a more common form as

$$P(R,\lambda) = P_0 \frac{c\tau}{2} A\eta \frac{O(R)}{R^2} \beta(R,\lambda) \exp\left[-2\int_0^R \alpha(r,\lambda)dr\right] \tag{2.43}$$

This equation will be used, in one or other version, in the following chapters as the starting point of the description of the individual lidar techniques. One should mention that the detected signal will always consist of a background contribution P_{bg} in addition to the lidar signal described above. At daytime, the background signal is

dominated by direct or scattered sunlight, whereas at nighttime the moon and the stars as well as artificial light sources contribute to the background light. The detector's noise is another source of undesired signal. The background must be subtracted before a lidar signal can be further evaluated.

2.7. References

Abel, S. J., J. M. Haywood, E. J. Highwood, J. Li, and P. R. Buseck (2003), Evolution of biomass burning aerosol properties from an agricultural fire in southern Africa, *Geophysical Research Letters*, *30*(15).

Andreae, M. O. (1991), *Biomass burning - its history, use, and distribution and its impact on environmental quality and global climate*, Cambridge, MA, MIT Press.

Ansmann, A., et al. (2003), Long-range transport of Saharan dust to northern Europe: The 11-16 October 2001 outbreak observed with EARLINET, *Journal of Geophysical Research-Atmospheres*, *108*(D24).

Bohren, C., and D. R. Huffman (1983), *Absorption and Scattering of Small Particles*, John Wiley and Sons, New York.

Chylek, P., and J. Wong (1995), Effect of absorbing aerosols on global radiation budget, *Geophysical Research Letters*, *22*(8), 929-931.

Erickson, D. J., and R. A. Duce (1988), On the global flux of atmospheric sea salt, *Journal of Geophysical Research-Oceans*, *93*(C11), 14079-14088.

Feingold, G., W. R. Cotton, S. M. Kreidenweis, and J. T. Davis (1999), The impact of giant cloud condensation nuclei on drizzle formation in stratocumulus: Implications for cloud radiative properties, *J. Atmos. Sci.*, *56*(24), 4100-4117.

Foster, P., et al. (2007), Changes in Atmospheric Constituents and in Radiative Forcing. In: Climate Change 2007: The Physical Science Basis. Contribution of Working Group I to the Fourth Assessment Report of the Intergovernmental Panel on Climate Change, edited by S. Solomon, D. Qin, M. Manning, Z. Chen, M. Marquis, K. B. Averyt, M. Tignor and H. L. Miller, Cambridge University Press, Cambridge, United Kingdom.

Goudie, A. S., and N. J. Middleton (2001), Saharan dust storms: nature and consequences, *Earth-Science Reviews*, *56*(1-4), 179-204.

Hamilton, J. F., P. J. Webb, A. C. Lewis, J. R. Hopkins, S. Smith, and P. Davy (2004), Partially oxidised organic components in urban aerosol using GCXGC-TOF/MS, *Atmospheric Chemistry and Physics*, *4*, 1279-1290.

Hamonou, E., P. Chazette, D. Balis, F. Dulac, X. Schneider, E. Galani, G. Ancellet, and A. Papayannis (1999), Characterization of the vertical structure of Saharan dust export to the Mediterranean basin, *Journal of Geophysical Research-Atmospheres*, *104*(D18), 22257-22270.

Haywood, J., and O. Boucher (2000), Estimates of the direct and indirect radiative forcing due to tropospheric aerosols: A review, *Reviews of Geophysics*, *38*(4), 513-543.

Haywood, J. M., and K. P. Shine (1995), The effect of anthropogenic sulfate and soot aerosol on the clear-sky planetary radiation budget, *Geophysical Research Letters*, *22*(5), 603-606.

Haywood, J. M., and K. P. Shine (1997), Multi-spectral calculations of the direct radiative forcing of tropospheric sulphate and soot aerosols using a column model, *Quarterly Journal of the Royal Meteorological Society*, *123*(543), 1907-1930.

Hegg, D. A., R. J. Ferek, and P. V. Hobbs (1993), Aerosol size distributions in the cloudy atmospheric boundary-layer of the North-Atlantic ocean, *Journal of Geophysical Research-Atmospheres*, *98*(D5), 8841-8846.

Herman, M., J. L. Deuze, C. Devaux, P. Goloub, F. M. Breon, and D. Tanre (1997), Remote sensing of aerosols over land surfaces including polarization measurements and application to POLDER measurements, *Journal of Geophysical Research-Atmospheres*, *102*(D14), 17039-17049.

Hinds, W. C. (1982), *Aerosol Technology*, John Wiley & Sons, New York.

Holben, B. N., et al. (1998), AERONET - A federated instrument network and data archive for aerosol characterization, *Remote Sensing of Environment*, *66*(1), 1-16.

Horvath, H. (1998), Influence of atmospheric aerosols upon the global radiation balances, in *Atmospheric particle*, edited by R. M. Harrison and R. van Grieken, pp. 543-596, John Wiley & Sons

Iqbal, M. (1983), *An introduction to solar radiation*, Academic Press Canada

Kasten, F. (1966), A new table and approximate formula for relative optical mass, *Arch. Meteorol. Geophys. Bioclimatol.*, *B14*, 206-223.

Kasten, F., and A. T. Young (1989), Revised optica air-mass tables and approximation formula, *Applied Optics*, *28(22)*, 4735-4738.

Kaufman, Y. J., and e. al. (1997), Operational remote sensing of tropospheric aerosols over the land from EOS-MODIS, *J. Geophy. Res.*, *102(D14)*, 17051-17068.

Kovalev, V. A., and W. E. Eichinger (2004), *Elastic lidar*, John Wiley & Sons, Inc.

Latham, J., and M. H. Smith (1990), Effect on global warming of wind-dependent aerosol generation at the ocean surface, *Nature*, *347*(6291), 372-373.

Levine, J. S., W. R. Cofer, D. R. Cahoon, E. L. Winstead, and B. J. Stocks (1993), Biomass burning and global change, in *World at Risk : Natural Hazards and Climate Change*, edited by R. Bras, pp. 131-139.

Luo, C., N. M. Mahowald, and J. del Corral (2003), Sensitivity study of meteorological parameters on mineral aerosol mobilization, transport, and distribution, *Journal of Geophysical Research-Atmospheres*, *108*(D15).

McFiggans, G., et al. (2006), The effect of physical and chemical aerosol properties on warm cloud droplet activation, *Atmospheric Chemistry and Physics*, *6*, 2593-2649.

Measures, R. M. (1984), *Laser remote-sensing, fundamentals and applications*, John Wiley and Sons, Inc, New York.

Mie, G. (1908), Beiträge zur Optik trüber Medien, speziell kolloidaler Metallösungen, *Annalen der Physik*, *25(3)*, 377-445.

Murphy, D. M. (2005), Something in the air, *Science*, *307*(5717), 1888-1890.

Penkett, S. A. (1988), Chemistry of the natural atmosphere - Warneck,P, *Nature*, *336*(6197), 322-322.

Penner, J. E., and e. al. (2001), Aerosols, their direct and indirect effects. In: Climate Change 2001: The Scientific Basis. Contribution of Working Group I to the Third Assessment Report of the Intergovernmental Panel on Climate Change, edited by J. T. Houghton and e. al., Cambridge University Press, Cambridge.

Posfai, M., R. Simonics, J. Li, P. V. Hobbs, and P. R. Buseck (2003), Individual aerosol particles from biomass burning in southern Africa: 1. Compositions and size distributions of carbonaceous particles, *Journal of Geophysical Research-Atmospheres*, *108*(D13).

Prospero, J. M., P. Ginoux, O. Torres, S. E. Nicholson, and T. E. Gill (2002), Environmental characterization of global sources of atmospheric soil dust identified with the Nimbus 7 Total Ozone Mapping Spectrometer (TOMS) absorbing aerosol product, *Reviews of Geophysics*, *40*(1).

Ramanathan, V., and G. Carmichael (2008), Global and regional climate changes due to black carbon, *Nature Geoscience*, *1*(4), 221-227.

Ramanathan, V., et al. (2001), Indian Ocean Experiment: An integrated analysis of the climate forcing and effects of the great Indo-Asian haze, *Journal of Geophysical Research-Atmospheres*, *106*(D22), 28371-28398.

Reid, J. S., R. Koppmann, T. F. Eck, and D. P. Eleuterio (2005a), A review of biomass burning emissions part II: intensive physical properties of biomass burning particles, *Atmospheric Chemistry and Physics*, *5*, 799-825.

Reid, J. S., T. F. Eck, S. A. Christopher, R. Koppmann, O. Dubovik, D. P. Eleuterio, B. N. Holben, E. A. Reid, and J. Zhang (2005b), A review of biomass burning emissions part III: intensive optical properties of biomass burning particles, *Atmospheric Chemistry and Physics*, *5*, 827-849.

Rodriguez, S., A. Alastuey, S. Alonso-Perez, X. Querol, E. Cuevas, J. Abreu-Afonso, M. Viana, N. Perez, M. Pandolfi, and J. de la Rosa (2011), Transport of desert dust mixed with North African industrial pollutants in the subtropical Saharan Air Layer, *Atmospheric Chemistry and Physics*, *11*(13), 6663-6685.

Sassen, K. (1991), The polarization lidar technique for cloud research - a review and current assessment, *Bulletin of the American Meteorological Society*, *72*(12), 1848-1866.

Sokolik, I. N., D. M. Winker, G. Bergametti, D. A. Gillette, G. Carmichael, Y. J. Kaufman, L. Gomes, L. Schuetz, and J. E. Penner (2001), Introduction to special section: Outstanding problems in quantifying the radiative impacts of mineral dust, *Journal of Geophysical Research-Atmospheres*, *106*(D16), 18015-18027.

Tanre, D., J. Haywood, J. Pelon, J. F. Leon, B. Chatenet, P. Formenti, P. Francis, P. Goloub, E. J. Highwood, and G. Myhre (2003), Measurement and modeling of the Saharan dust radiative impact: Overview of the Saharan Dust Experiment (SHADE), *Journal of Geophysical Research-Atmospheres*, *108*(D18).

Tegen, I., and I. Fung (1995), Contribution to the atmospheric mineral aerosol load from land-surface modification, *Journal of Geophysical Research-Atmospheres*, *100*(D9), 18707-18726.

Tegen, I., A. A. Lacis, and I. Fung (1996), The influence on climate forcing of mineral aerosols from disturbed soils, *Nature*, *380*(6573), 419-422.

Tegen, I., M. Werner, S. P. Harrison, and K. E. Kohfeld (2004), Relative importance of climate and land use in determining present and future global soil dust emission, *Geophysical Research Letters*, *31*(5).

Tegen, I., P. Hollrig, M. Chin, I. Fung, D. Jacob, and J. Penner (1997), Contribution of different aerosol species to the global aerosol extinction optical thickness: Estimates from model results, *Journal of Geophysical Research-Atmospheres*, *102*(D20), 23895-23915.

Tegen, I., S. P. Harrison, K. Kohfeld, I. C. Prentice, M. Coe, and M. Heimann (2002), Impact of vegetation and preferential source areas on global dust aerosol: Results from a model study, *Journal of Geophysical Research-Atmospheres*, *107*(D21).

Washington, R., M. Todd, N. J. Middleton, and A. S. Goudie (2003), Dust-storm source areas determined by the total ozone monitoring spectrometer and surface observations, *Annals of the Association of American Geographers*, *93*(2), 297-313.

Weitkamp, C. (2005), *Lidar: Range-Resolved Optical Remote Sensing of the Atmosphere*, Springer Science + Business Media Inc.

Zender, C. S., H. S. Bian, and D. Newman (2003), Mineral Dust Entrainment and Deposition (DEAD) model: Description and 1990s dust climatology, *Journal of Geophysical Research-Atmospheres*, *108*(D14).

Chapter 3

Instrumentation and experimental site

This chapter presents the instrumentation used in this thesis and the experimental site where the measurements have been registered. In the first section a detailed description of the Raman lidar system is offered. Next, additional instrumentation used to complement the lidar measurements is also described. Finally, a brief description of the study area is presented.

3.1. Raman lidar system

The Raman lidar model LR331D400 (Raymetrics S.A., Greece) is configured in a monostatic-biaxial alignment pointing vertically to the zenith. The lidar consist of a laser, a beam-expanding and transmitter optics, a Cassegrainian receiving telescope, a wavelength separation unit (WSU), photodetectors, and a data acquisition and computer unit. Figure 3.1 shows a picture of this system while the table 3.1 presents its main features. The specific details for each component are explained in the next subsections.

This instrument was incorporated to the European Aerosol Research Lidar Network (EARLINET, http://www.earlinet.org/) in April 2005. EARLINET is the first aerosol lidar network, established in 2000, with the main goal to provide a comprehensive, quantitative, and statistically significant data base for the aerosol

distribution on a continental scale. At present, 27 stations distributed over Europe are part of the network.

Figure 3.1. Raman lidar system operated at the Granada station.

Emitter	
Pulsed laser source (Class IV laser)	Nd:YAG (Quantel CFR Series)
Wavelenght	355, 532 and 1064 nm
Energy/pulse	60, 65, 110 mJ
Pulse duration	8 ns
Repetition rate	1, 2, 5 and 10 Hz
Laser beam diameter	6 mm
Laser beam divergence	<0.1 mrad
Receiver Optics	
Telescope	Cassegrain
Primary mirror diameter (mm)	400
Secondary mirror diameter (mm)	90
Focal lenth (mm)	3998
Telescope-laser axes distance (mm)	320
Detection Unit	
Transient Recorder	LICEL
Detectors	APD (at 1064 nm), PMT (other channels)
Wavelength Separation Unit	Dichroic mirrors, interferencial filtres and polarization cube
Detection mode	Analog and photon counting
Wavelengths (nm)	355, 387, 408, 532p, 532s, 607, 1064
Full Width at Half Maximum (nm)	1.0, 2.7, 1.0, 0.5, 0.5, 2.7, 1.0
1064 nm	Analog acquisition mode. 12 Bit-20 MHz
532, 355 nm	Analog aquisition mode: 12 Bit-20 MHz Photon-counting acquisition mode: 250 MHz
387, 408, 607 nm	Photon-counting acquisition mode: 250 MHz
Range resolution	7.5 m

Table 3.1. Technical characteristics of the Granada lidar system.

3.1.1. Emitter system

The main components of the emitter system are shown in Figure 3.2. The laser source used is a pulsed Nd:YAG (Neodymiun-doped Yttrium Aluminum Garnet) laser with fundamental wavelength at 1064 nm; additional emissions at 532 and 355 nm are obtained by using second and third harmonic generators, respectively. Output energies are 110, 65 and 60 mJ at 1064, 532 and 355 nm, respectively, and pulses of 8 ns can be fired with a pulse repetition frequency (PRF) of 1, 2, 5 and 10 Hz (in this thesis, a PRF of 10 Hz has been used). The laser consists of two major components: the optical head and the power supply.

The laser beam divergence is reduced by means of a beam expander unit (BEXP), allowing for the use of a narrow telescope field, which will help to suppress background light and thus increase the signal-to-noise ratio (SNR). The BEXP unit contains two beam expanders and is designed to provide a factory-set expansion of the laser beam at 355 and 1064/532 nm, respectively. The beam expansion factor is x5 for 355 nm and x4.5 for 1064/532 nm. Beam expansion by a factor n reduces the divergence by the same factor. The expanded laser beams are emitted to the atmosphere through a specially conceived highly transmission window placed on the outer cover box of the lidar system.
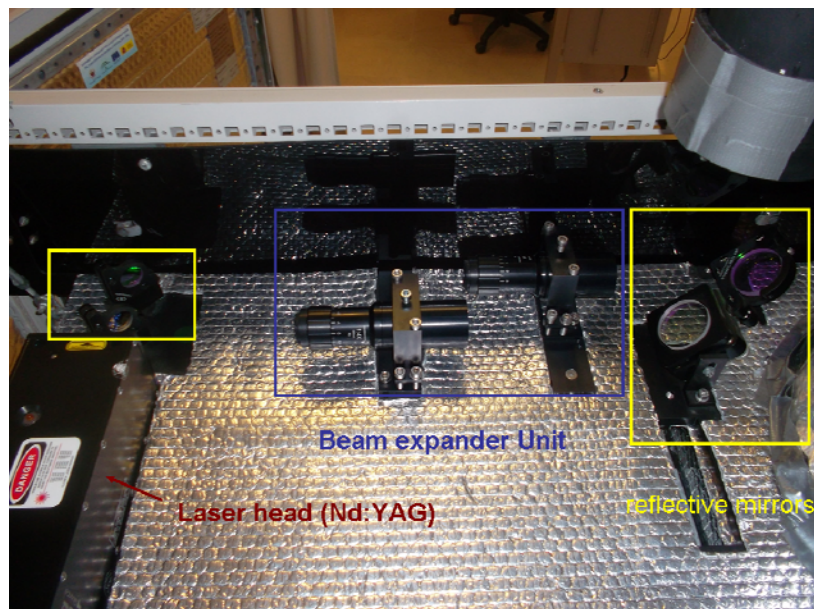

Figure 3.2. Emitter system of the Granada Raman lidar.

The reflective mirrors of the lidar system are conceived to provide a high reflection (> 98%) at the reflected wavelengths (355 and 532/1064 nm). The laser mirrors were carefully selected for their high quality and long-term durability. Both diameters used (25 and 50 mm) match the required specifications of the BEXP unit used. The reflective mirrors are mounted on high quality mirror mounts which permit the alignment of the emitted laser beam with accuracy of the order of several microradians (μrad).

3.1.2. Receiving system

The receiving system consists of two sub-units (Fig 3.3): a receiving telescope and a wavelength separation unit (WSU).

The receiving telescope of the lidar system is based on a Cassegranian design. The primary reflective mirror has a diameter of 400 mm and is coated with a durable high reflective coating suitable for the 350-1100 nm spectral region. The optical material selected shows a very low thermal expansion coefficient. The secondary reflective mirror has a diameter of 90 mm coated in the same way as the primary mirror. The received lidar beams are then collected and focused on an Optical Unit (OU) placed on the telescope's focal point. The OU is equipped with a 7 mm diameter diaphragm (field stop). The field stop in the focal point of the telescope determines the receiver field of view (RFOV) that is normally a factor of 2-10 larger than the laser beam divergence. A compromise must be found between a small RFOV necessary for high background suppression and a larger RFOV for stable adjustment of the laser beam within the RFOV and for sufficient signal intensity from short distances. At the exit of the OU the lidar beams are then collimated.
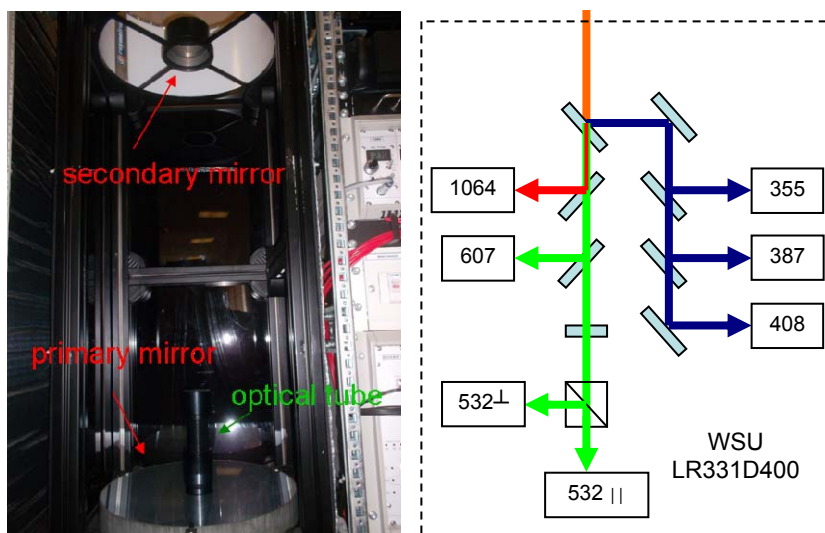
Figure 3.3. Telescope system (right) and wavelength separation unit (left).

At the entrance of the WSU of the lidar system the collected lidar beams are collimated to one parallel beam having a diameter of 15 mm. A series of factory preset custom-made dichroic reflective mirrors and one polarization cube perform the wavelength separation at the various wavelengths and polarizations received [355, 387, 408, 532p (parallel polarization), 532s (cross polarization), 607 and 1064 nm] (Fig. 3.3, left).

For each channel, specially designed interference filters are used to select the lidar wavelength and to reject the atmospheric background radiation. Table 3.2 shows the respective full width at half maximum (FWHM) of the interference filters used at each wavelength.

Wavelength (nm)	FWHM (nm)
355	1.0
387	2.7
408	1.0
532	0.5
607	2.7
1064	1.0

Table 3.2. FWHM values of the interference filters used.

3.1.3. Signal acquisition unit

The signal acquisition unit (SAU) consists of two sub-units (Fig. 3.4): the lidar signals detectors (photomultiplier tubes, PMTs, and avalanche photodiode detector, APD, (Fig. 3.4, left)), and the detection electronics (Fig. 3.4, right), working in analog

(AN) detection mode for the APD and both AN and photon-counting (PC) detection modes for the PMTs.

The spectrally resolved lidar signals inside the WSU are detected by the photomoultiplier tubes (R7400U series, Hamamatsu, www.hamamatsu.com) directly mounted at the respective exits of the WSU. The R7400U series is a subminiature photomultiplier tube with a 16 mm diameter and 12 mm seated length. A precision engineered 8-stage electron multiplier (composed of channel dynodes) is incorporated to produce a noise free gain of 700000 times. These PMTs also features excellent response time with a rise time of 0.78 ns. The PMTs used are selected to be compact and to provide optimum operation in the spectral range 355-607 nm. The PMTs optimum working voltage (for linear operation) is between 750-850 V, depending on the amplitude of the received signal and the atmospheric conditions (background skylight conditions during day-time or night-time conditions and/or cloud presence).

The Si-avalanche photodiode module is based on the EG&G C3095xE series avalanche photodiodes. These Si-diodes are manufactured using a double-diffused "reach through" structure. By using this technique the detectors are designed such that their long wave response (i.e. $\lambda > 900$ nm) has been enhanced without introducing any undesirable properties. At same time, the desirable properties of the double diffused "reach through" structure (such as low noise, low capacitance, and fast rise and fall times) have been retained. The increased sensitivity in the near infrared is a major advantage as compared to photomultipliers. The quantum efficiency at the Nd:YAG fundamental wavelength at 1064 nm is still about 38%.
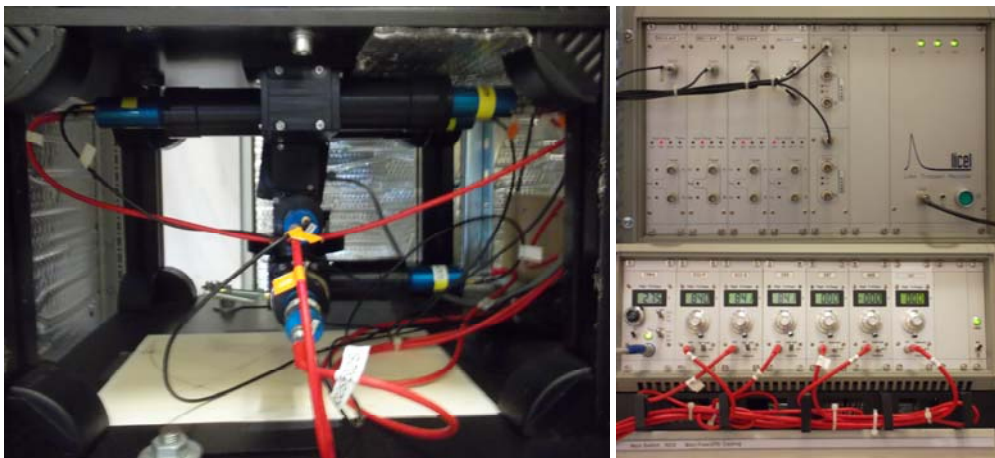

Figure 3.4. Signal acquisition unit: photomultiplier tubes (PMTs) and APD (left) and transient recorders and high-voltage power suppliers of PMTs and APD (right).

The Si-Avalanche Photodiode Module consists of a detector head and a power supply unit. The detector head contains the APD and the preamplifier. The APD is mounted on a temperature stabilized thermoelectric cooler inside a hermetically sealed housing. This detector head is mounted in a XYZ translation stage for easy optical alignment. The power supply unit contains a linear regulated +5V and +/-15V power supply and a 0…+400 V high voltage supply. This provides the voltages for the temperature controller and preamplifier as well as the variable reserve voltage for the APD.

3.1.4. Detection electronics

The Licel transient recorder (www.licel.com) is a powerful data acquisition system, especially designed for remote sensing applications. To meet the demanding requirements of optical signal detection, a new concept was developed to reach the best dynamic range together with high temporal resolution at fast signal repetition rates. The time AN detection of the photomultiplier current and single PC is combined in one acquisition system. The combination of a powerful A/D converter (12 Bit at 40 MHz) with a 250 MHz fast PC system increases the dynamic range of the acquired signal substantially compared to conventional systems. Signal averaging is performed by specially designed ASIC's (Application Specific Integrated Circuit) which outperform any CISC- or Risc-processor based solution. A high speed data interface to the host computer allows readout of the acquired signal even between two laser shots. The implementation of this concept makes the Licel transient recorder the state-of-the-art solution for all applications where fast and accurate detection of photomultiplier, photodiode or other electrical signals is required at high repetition rates.

The Licel transient recorder is comprised of a fast transient digitizer with on board signal averaging, a discriminator for single photon detection and a multichannel scaler combined with preamplifiers for both systems. For AN detection the signal is amplified according to the input range selected and digitized by a 12-Bit-20/40 MHz A/D converter. A hardware adder is used to write the summed signal into a 24-Bit wide RAM.

At the same time the signal part in the high frequency domain is amplified and a 250 MHz fast discriminator detects single photon events above the selected threshold voltage. 64 different discriminator levels and two different setting of the preamplifier

can be selected by using the acquisition software supplied. The PC signal is written to a 16-Bit wide summation RAM which allows averaging of up to 4094 acquisition cycles.

The AN detection mode is used to detect intense lidar signals coming from relatively short distances (typically less than 6-8 km). A transient recorder operating in the AN detection mode is based on an analog-to-digital converter (ADC), which samples and digitizes the lidar signals with a sampling rate of 20-40 MHz (depending on the type of the transient recorder used) with a 12-bit resolution. The memory contains 16000 time bins. Each time bin corresponds to a spatial resolution of 7.5 m.

The PC detection mode is used to detect very low intensity lidar signals coming from relatively large distances (typically higher than 6-8 km). Thus, the PMT is operated under single electron conditions. Flux levels as low as a few tens of photons per second can be measured. In the PC mode the level of the incident flux is such that the cathode emits only single electrons. The individual anode charges due to single photons are integrated to produce proportional voltages pulses, which are passed by a discriminator to a pulse counter, whose output over a pre-set time period is a measure of the incident flux.

3.2. Additional instrumentation

Next we describe the main characteristic of additional instrumentation used in this thesis. Measurements from passive remote sensing presented in this section (sun- and star-photometer and microwave radiometer) were used in some studies presented in this thesis.

3.2.1. Sun-photometer (Cimel CE 318-4)

Daytime, column-integrated characterization of the atmospheric aerosol has been done by means of a sun-photometer CE-318-4 included in the AERONET (Aerosol RObotic NETwork, http://aeronet.gsfc.nasa.gov/). A complete description can be found in Holben *et al*. [1998]. However, a brief description will be given in this section.

The design of the sun photometer CIMEL CE318-4 consists on an optical head with two collimators, a robotic arm for sun tracking and sky positioning and an electronic box (http://www.cimel.fr). Figure 3.5 shows the CIMEL CE318-4.

Figure 3.5. A Cimel CE 318-4 fielded at Sierra Nevada (Granada, Spain)

The automatic tracking sun and sky scanning radiometer made Sun direct measurements with a 1.2° full field of view every 15 min at 340, 380, 440, 500, 675, 870, 940, and 1020 nm (nominal wavelengths). The direct Sun measurements take ~8 s to scan all 8 wavelengths (repeated three times within a minute), with a motor driven filter wheel positioning each filter in front of the detector. These solar extinction measurements are used to compute aerosol optical depth (AOD) at each wavelength except for the 940 nm channel, which is used to retrieve total column water vapour (or precipitable water) in cm. The filters utilized in this instrument were ion assisted deposition interference filters with band pass (full width at half maximum) of 10 nm, except for the 340 and 380 nm channels at 2 nm. The estimated uncertainty in computed AOD, due primarily to calibration uncertainty, is around 0.010–0.021 for field instruments (which is spectrally dependent with the higher errors in the UV) [*Eck et al.*, 1999]. Only AERONET version 2 level 2 AOD data are used in the results presented in this thesis. The spectral AOD data have been screened for clouds following the methodology of Smirnov *et al.* [2000] which relies on the higher temporal frequencies of cloud optical depth versus AOD. The sky radiances measured by the Sun/sky radiometers are calibrated versus frequently characterized integrating spheres at the NASA Goddard Space Flight Center, to an absolute accuracy of ~5% or better [*Holben et al.*, 1998].

The Cimel sky radiance measurements in the almucantar geometry (fixed elevation angle equal to solar elevation and a full 360° azimuthal sweep, see Figure 3.6) at 440, 675, 870, and 1020 nm (nominal wavelengths) in conjunction with the direct

Sun measured AOD at these same wavelengths were used to retrieve optical equivalent, column integrated aerosol size distributions and refractive indices. Using this microphysical information the spectral dependence of single scattering albedo is also calculated. The retrieval of the particle volume size distribution was demonstrated to be adequate in practically all situations [e.g., AOD(440) ≥ 0.05], as demonstrated by Dubovik *et al*. [2000]. These studies show that the error of the retrieved volume density $dV(r)/d \ln r$ changes as a nonlinear function of particle size, aerosol type, and actual values of the size distribution. In particular, for the particle size range $0.1 \leq r \leq 7$ mm, the retrieval errors do not exceed 10% in the maxima of the size distribution and may increase up to about 35% for the points corresponding to the minimum values of $dV(r)/d \ln r$ in this size range. For $0.05 \leq r \leq 0.1$ μm and $7 < r \leq 15$ μm, the accuracy of the size distribution retrieval drops significantly, because of the low sensitivity of the aerosol scattering at 0.44, 0.67, 0.87, and 1.02 μm to particles of these sizes. Correspondingly, the retrieval errors rise up to 80%–100% (and even higher) for the sizes less than 0.1 μm and higher than 7 μm. The high errors at the edges do not significantly affect the derivation of the main features of the particle size distribution (concentration, median and effective radii, etc.), because typically the aerosol particle size distributions [$dV(r)/d \ln r$] have low values at the edges of retrieval size interval. These authors have found that the accuracy levels drop down to 0.05–0.07 for the single scattering albedo, to 80%–100% for the imaginary part of the refractive index, and to 0.05 for the real part of the refractive index.
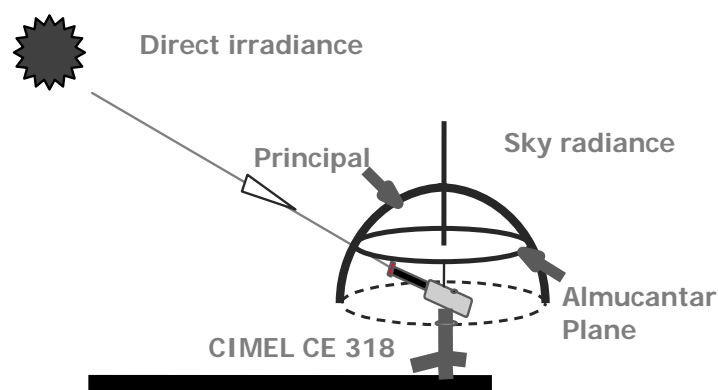

Figure 3.5. Measurements schema for direct irradiance and almucantar and principal planes.

3.2.2. Star-photometer (EXCALIBUR)

Column-integrated characterization of the atmospheric aerosol has been done by means of a star-photometer during night-time. The star-photometer EXCALIBUR (iTec. Astronómica S.L., Spain) allows measurements of direct flux from a given star. Details about this instrument are given in Pérez-Ramírez *et al.* [2008a]. Basically, the instrument consists of a telescope (CELESTRON CGE 1100) that collects the parallel incident light rays from the required star. Later, the starlight passes trough a 10-filter wheel, where six narrow band filters are set up with central wavelengths at 380, 436, 500, 670, 880 and 1020 nm (nominal wavelengths) for aerosol characterization, and an additional filter at 940 nm for retrieving precipitable water vapour. The FWHM ranges between 7.7 and 11.2 nm for the different filters. Once the starlight is spectrally separated, it reaches the CCD camera detector (model SBIG ST8- XME, Santa Barbara, USA), whose linear response and high quantum efficiency makes this device ideal for photometry purposes. On the other hand, an external wide field CCD camera is employed to assure a correct pointing for a given star. The star-photometer EXCALIBUR also has software that is able to minimize errors associated with CCD camera, and also to focus the telescope and to calculate the background light associated with the measurements [*Pérez-Ramírez et al.*, 2008b]. Figure 3.7 shows a picture of EXCALIBUR.
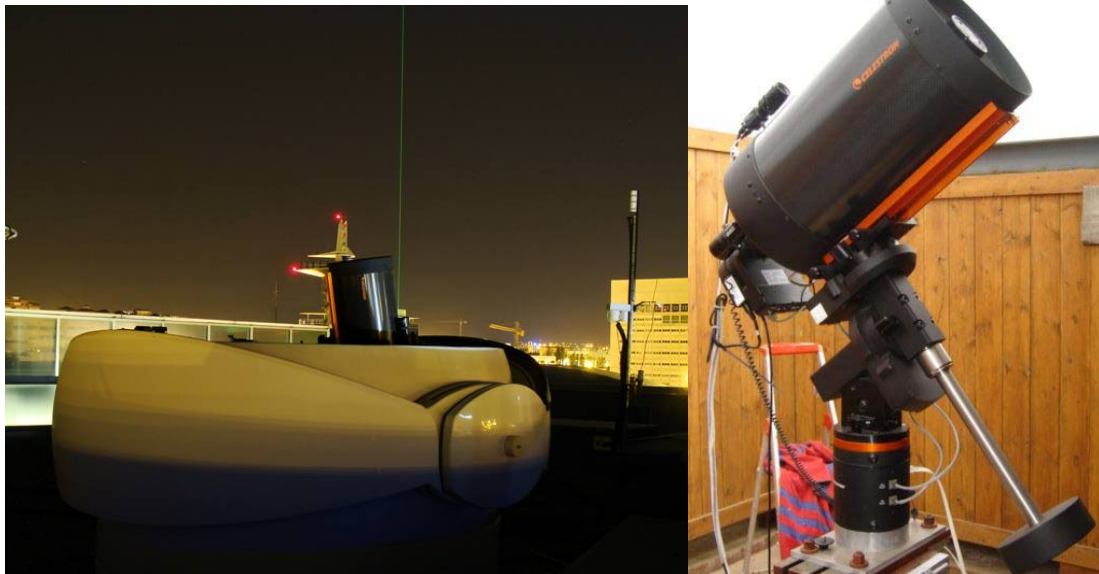

Figure 3.7. Star-photometer EXCALIBUR (iTec. Astronómica S.L., Spain).

Due to the quantum efficiency of the CCD camera and to the different spectral types of stars, the exposure time varies among the different filters and also for different stars. Table 3.3 shows the average exposure time for each filter. In addition, the CCD camera takes approximately 4 s to process one particular measurement (technical specifications of SBIG ST8 CCD are in http://www.sbig.com/ST-8XME-C2.html). As a result, the star photometer EXCALIBUR takes 3-5 minutes approximately to make a sequence of measurements that includes all the filters.

The calibration of the star photometer EXCALIBUR is performed at the high mountain site of Calar Alto (37.2º N, 2.5º W, 2168 m a.s.l.), and it is made once a year [*Perez-Ramirez et al.*, 2011]. AOD(λ) at the selected spectral channels is computed following the methods described in the works of Alados-Arboledas *et al*. [2003] and Pérez-Ramírez *et al*. [2008a]. Uncertainties in AOD(λ) are 0.02 for $\lambda<800$ nm and 0.01 for $\lambda>800$ nm [*Perez-Ramirez et al.*, 2011]. The retrieval of precipitable water vapor (*W*) is based on a look up table using a simplified expression for the water vapour transmittance and the relative optical water vapour air mass. This methodology presents a systematic uncertainty in *W* below 6% [*Perez-Ramirez et al.*, 2012].

Nominal wavelength (nm)	Average exposure time (s)	Minimum exposure time (s)	Maximum exposure time (s)
380	23 ± 30	0.3	124
436	1.42 ± 1.01	0.3	4.9
500	0.7 ± 0.4	0.3	2.5
670	0.5 ± 0.3	0.3	1.7
880	2.5 ± 1.9	0.3	10.3
940	13 ± 11	0.3	62
1020	49 ± 40	0.3	140

Table 3.3. Mean, maximum and minimum exposure times for each filter of the star photometer EXCALIBUR.

3.2.3. Microwave radiometer

The microwave radiometer HATPRO system (HATPRO, Radiometer Physics GmbH, Germany, www.radiometer-physics.de) performs measurements of the sky brightness temperature in a continuous and automatic way, with a radiometric resolution between 0.3 and 0.4 K RMS at 1.0 s integration time. By using inversion algorithms, the microwave radiometer can determine atmospheric temperature and humidity profiles up to 10 km with high vertical resolution in the lower troposphere and high temporal

resolution, of the order of seconds. The spatial vertical resolution ranges from 10 m near the surface to 500 m for higher altitudes. The table 3.4 lists the vertical resolution of the instrument for different heights.

Altitudes (m, agl)	Vertical resolution (m)	Altitudes (m, agl)	Vertical resolution (m)
0-10	10	1600-2200	200
10-50	20	2200-3100	300
50-150	25	3100-3900	400
150-250	50	3900-4400	500
250-700	75	4400-6200	600
700-1000	100	6200-7000	800
1000-1600	150	7000-10000	1000

Table 3.4. Vertical resolution for the microwave radiometer HATPRO system.

It can also provide the liquid water path (LWP), the integrated water vapour and stability indices, together with additional meteorological data from external meteorological sensors incorporated to the system: barometric pressure, surface humidity and temperature. The HATPRO radiometer uses direct detection receivers within two bands: 22-31 GHz and 51-58 GHz. The first band contains seven channels that provide information about the vertical profile of humidity through the pressure broadening of the optically thin 22-23.5 GHz H_2O line and LWP, while the second band contains information about the temperature profile. It has other seven channels and the information results from the homogeneous mixing of O_2 in the atmosphere. In addition to the spectral information, angular information is employed. This provides additional information under the assumption that the atmosphere in the direct horizontal vicinity (3 km) of the microwave profiler is horizontally homogeneous. Only the brightness temperature from the optically thick frequency bands close to 60 GHz are used in these elevation scans. Because the brightness temperatures vary only slightly with elevation angle, the method requires a highly sensitive radiometer [*Lohnert et al.*, 2004]. The precision in temperature profiles used in this thesis is 0.1 K. Figure 3.8 shows the microwave radiometer HATPRO system operated in our station.

Figure 3.8. Microwave radiometer HATPRO system operated at the Granada station.

3.3. Granada station

The station of the Atmospheric Physics Group (GFAT) is located in the Andalusian Center for Enviromental Studies (Centro Andaluz de Medio Ambiente, CEAMA) at Granada, Spain (37.16º N, 3.58ºW, 680 m, asl). The measurements presented in this thesis were registered in this site. Granada, located in south-eastern Spain, is a non-industrialized medium-sized city with a population of 300000 that increases up to 600000 if the whole metropolitan area is considered. The city is situated in a natural basin surrounded by mountains with elevations between 1000 and 3500 m (asl). The near-continental conditions prevailing at this site are responsible for large seasonal temperature differences, providing cool winters and hot summers. The area also experiences periods of a low humidity regime especially at summer time. The study area is also at a short distance, about 200 km away from the African continent and approximately 50 km away from the western Mediterranean basin.

Due to its location in the Mediterranean basin, Granada is influenced by two major aerosol source regions: Europe as a major source of anthropogenic pollutants and North Africa as principal source of natural dust. Furthermore, the Mediterranean area is characterized by a complex meteorology which favours the aging of polluted air masses in the basin and induces high level of airborne particles. Thus, the Mediterranean basin can represent an additional source of atmospheric aerosol for the study area. In summer,

the study area is isolated from travelling lows and associated frontal systems, and the intensification of the Azorean high during the warm season induces a very weak pressure gradient and a strong subsidence that reduces entrainment from the free troposphere. High temperatures and low humidity in summer induce numerous forest fires in the Iberian Peninsula, whose smoke represents an additional source of atmospheric aerosol to our study area [*Alados-Arboledas et al.*, 2011].

3.4. References

Alados-Arboledas, L., H. Lyamani, and F. J. Olmo (2003), Aerosol size properties at Armilla, Granada (Spain), *Quarterly Journal of the Royal Meteorological Society, 129*(590), 1395-1413.

Alados-Arboledas, L., D. Muller, J. L. Guerrero-Rascado, F. Navas-Guzman, D. Perez-Ramirez, and F. J. Olmo (2011), Optical and microphysical properties of fresh biomass burning aerosol retrieved by Raman lidar, and star-and sun-photometry, *Geophysical Research Letters, 38*.

Dubovik, O., A. Smirnov, B. N. Holben, M. D. King, Y. J. Kaufman, T. F. Eck, and I. Slutsker (2000), Accuracy assessments of aerosol optical properties retrieved from Aerosol Robotic Network (AERONET) Sun and sky radiance measurements, *Journal of Geophysical Research-Atmospheres, 105*(D8), 9791-9806.

Eck, T. F., B. N. Holben, J. S. Reid, O. Dubovik, A. Smirnov, N. T. O'Neill, I. Slutsker, and S. Kinne (1999), Wavelength dependence of the optical depth of biomass burning, urban, and desert dust aerosols, *Journal of Geophysical Research-Atmospheres, 104*(D24), 31333-31349.

Holben, B. N., et al. (1998), AERONET - A federated instrument network and data archive for aerosol characterization, *Remote Sensing of Environment, 66*(1), 1-16.

Lohnert, U., S. Crewell, and C. Simmer (2004), An integrated approach toward retrieving physically consistent profiles of temperature, humidity, and cloud liquid water, *Journal of Applied Meteorology, 43*(9), 1295-1307.

Perez-Ramirez, D., H. Lyamani, F. J. Olmo, and L. Alados-Arboledas (2011), Improvements in star photometry for aerosol characterizations, *Journal of Aerosol Science, 42*, 737-745.

Perez-Ramirez, D., F. Navas-Guzman, H. Lyamani, J. Fernandez-Galvez, F. J. Olmo, and L. Alados-Arboledas (2012), Retrievals of precipitable water vapor using star photometry: assessment with Raman lidar and link to sun photometry, *Journal of Geophysical Research-Atmospheres, 117*, D05202.

Pérez-Ramírez, D., J. Aceituno, B. Ruiz, F. J. Olmo, and L. Alados-Arboledas (2008a), Development and calibration of a star photometer to measure the aerosol optical depth: Smoke observations at a high mountain site, *Atmospheric Environment, 42*(11), 2733-2738.

Pérez-Ramírez, D., B. Ruiz, J. Aceituno, F. J. Olmo, and L. Alados-Arboledas (2008b), Application of Sun/star photometry to derive the aerosol optical depth, *International Journal of Remote Sensing*, *29*(17-18), 5113-5132.

Smirnov, A., B. N. Holben, T. F. Eck, O. Dubovik, and I. Slutsker (2000), Cloud-screening and quality control algorithms for the AERONET database, *Remote Sensing of Environment*, *73*(3), 337-349.

Chapter 4

Methodology

In this chapter we present the algorithms that have been implemented in this thesis to retrieve optical properties from lidar measurements. Firstly we describe the previous step (pre-processing) to be applied to the raw lidar signals before using the inversion algorithms. Next the two most important inversion algorithms (elastic and inelastic) are introduced. Improvements for the lidar incomplete overlap and for the infrared channel calibration are also presented. Finally, we present the elastic backscatter algorithm intercomparison developed in the frame of the Spanish and Portuguese Aerosol Lidar Network (SPALINET).

4.1. Lidar data pre-processing

The data pre-processing includes an ensemble of treatments that must be made on the raw lidar signals before applying any inversion algorithm. The sequence used in this work is given below and will be detailed along this section:

i) Dead time correction
ii) Trigger delay correction
iii) Background subtraction (both atmospheric and electronic)
iv) Overlap correction
v) Low and high range signals gluing (for AN/PC systems)
vi) Time averaging

4.1.1. Dead time correction

The first correction applied to the lidar signals in photon-counting mode is called *dead time correction*. This detection mode was described in chapter 3. In any detector system, there is a certain amount of time that is required to discriminate and process an event. If a second event occurs during this time, it will not be counted. The minimum amount of time that allows for separating two events such that both are counted is referred t as "dead time". Because of the random nature of the arrival times of photons, there is always some time with some events that will not be counted. A dead time correction is required to account for those photons that arrive during the time required for the scalar to record a previous photon. When regarding the first photon, the scalar is effectively "dead" or incapable of recording the second photon. In lidar applications, the number of uncounted photons is significant at short height ranges from the lidar and decreases as height range increases. In a non-paralleling detection system, as in our case, a fixed amount of dead time follows a given photon and any photon that arrives during that time is ignored and does not increase the amount of the overall dead time. Thus, two photons that are separated in time by more than the dead time will be both counted. If N_m is the system measured count rate, and t_{dead} is the dead time, the actual (i.e. corrected) count rate N_a is determined by

$$N_a = \frac{N_m}{(1 - N_m t_{dead})} \qquad (4.1)$$

In the case of the photomultiplier tubes (R7400U, Hamamatsu) used in our Raman lidar system the value of the dead time is 4 ns. Therefore, photon-counting channels are corrected by equation 4.1.

4.1.2. Trigger delay correction (zero bin/bin-shift)

An error in the trigger delay between the real laser output and the detection system start (system trigger, zero-bin) can cause large errors in the near height range signal up to about 1 km. Especially the Raman signals can be distorted dramatically, because the signal slope in the near range changes very much when the trigger delay is varied. In general, this delay is different for the AN and PC mode, and it may also be different for each channel.

With the goal of measuring this delay in our lidar system, we have measured the zero position of each signal. For this purpose a target was placed at the output of the laser window in order to produce a strong backscattered radiation. Thus, the first intense peak observed by the detector system should correspond to the zero position of our measurements. This test was only carried out for AN signals, since that saturation suffering in PC mode at close height range could lead to wrong results. The first peak detected for the 532s, 355 and 1064 AN channels was found at position 6, while for 532p was found in position 7. They correspond to distances of 45 m and 52.5 m, respectively, taking into account a spatial resolution of 7.5 m in our system (section 3.1).

For measuring a possible delay between AN and PC signals (bin-shift), which is typical between both detection modes, we used a cloud as target in the far height range. The cloud was selected with a location that guarantees optimal measurements in both modes. Figure 4.1 shows a lidar measurement session on 4th May 2011. The color scale in this plot is proportional to the range corrected signal (RCS), which is defined as the lidar signal multiplied by the square of the distance. As Figure 4.1 shows, low clouds were present at the end of the session. The period selected for the analysis is marked with a red rectangle. Besides the cirrus clouds above 9 km (asl), a thin and white layer (large RCS) identified as a middle-altitude cloud was observed between 3 and 4 km (asl).
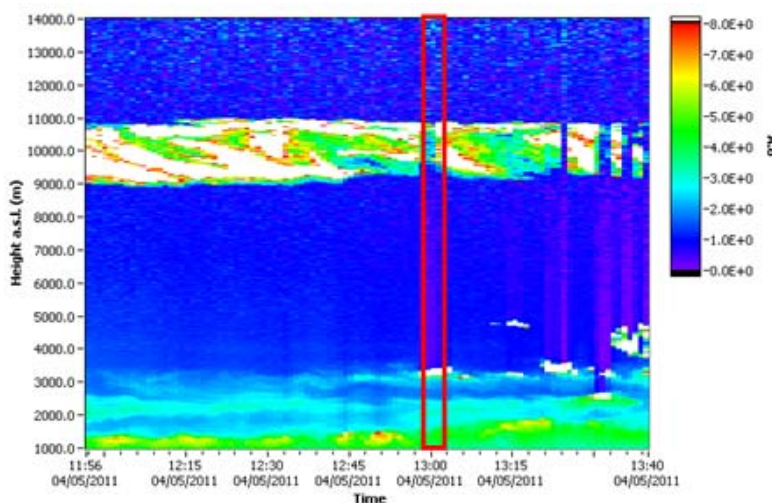

Figure 4.1. Temporal evolution of RCS at 532 nm on 4th May 2011. The selected period is marked as a red rectangle.

In order to measure the bin-shift between both detection modes, we identified the positions of the different peaks at each signal. Figure 4.2a shows the results observed for the 355 nm channel. In figure 4.2b a linear fit between the points where the different peaks are located at both modes is presented. We obtain a perfect fit ($R^2 = 1$), thus indicating that the bin-shift between both modes is perfectly identified in the height range investigated and it is the same in all the points. The interception of the linear fit indicates that the bin-shift between AN and PC signals was 7.5 m (1 bin) at 355 nm. Similar procedure was performed for the other channels. The bin-shift observed for 532p and 532s channels were 15 m (2 bins) and 7.5 m (1 bin), respectively.
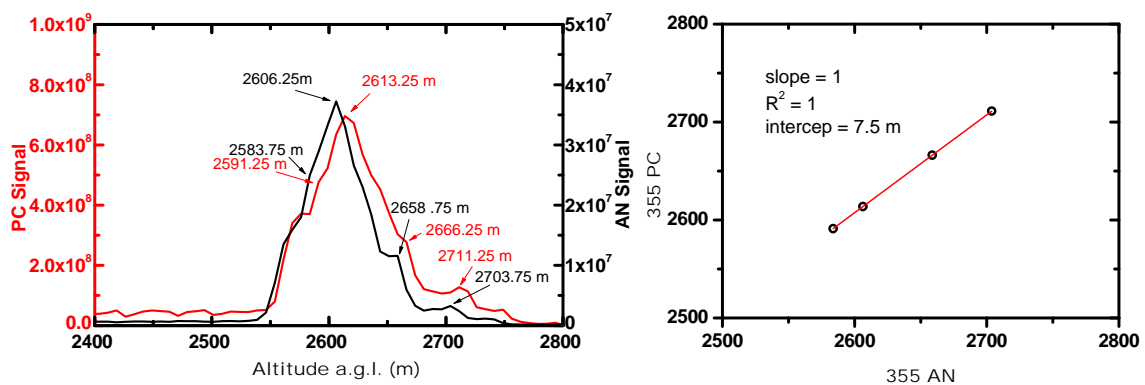
Figure 4.2. a) AN and PC signals observed in a cloud. b) Linear fit between the different points associated to different peaks of the cloud in AN and PC mode.

Taking into account the zero position of AN signals and the bin-shift between AN and PC signals it is possible to obtain the number of bins required to correct each lidar signal from trigger delay (Table 4.1).

Channel	Offset positions
532p (AN)	-6
532p (PC)	-8
532s (AN)	-5
532s (PC)	-6
355 (AN)	-5
355 (PC)	-6
1064 (AN)	-5

Table 4.1. Required shifting for each lidar signals to correct for trigger delay.

4.1.3. Background subtraction (both atmospheric and electronic)

The next correction to be applied to the lidar signals is the background correction due to electronic noise and sky radiation (atmospheric contribution).

In order to measure the dark current in our system, the telescope window is covered after each measurement so that any backscattered radiation from particles or molecules cannot reach the detectors. In this way we are able to measure the signals associated to the noise coming from internal reflections in the instrument that reach the detectors and/or the actual electronic noise that occur inside them. The electronic noise is due to small currents flowing through the detectors even when their surfaces are not illuminated. This current flows because the materials used as photocathodes have low work functions and will emit thermal electrons at the room temperature. The magnitude of the dark current depends on the photocathode material, the temperature of the tube and the applied voltage. This dark current measurement is subtracted from the signals measured by the Raman lidar system.

As mentioned above, it is also necessary to subtract the radiation from the sky (atmospheric background signal). The detection of such kind of signal is inherent to the measurement. To correct the signals for this effect, a region in the far height range, in which the aerosol content is negligible, is defined and in this way the greatest part of the received radiation is due to background sky. We calculate the average value of the lidar signal measured in this height range and this mean value is subtracted to the whole lidar signal profile. A typical range for atmospheric background subtraction in the analysis of this thesis was the interval between 75 and 105 km or, equivalently, a time interval between 250-350 μs after the laser shot.

4.1.4. Overlap correction

The incomplete overlap between the laser beam and the receiver field of view significantly affects lidar observations in the near height range (Fig. 4.3). An appropriate study of the important exchange processes of anthropogenic pollution between the sources and the lowermost layers of the troposphere is not possible without the correction of the range-dependent overlap characteristics.

For our system, a range-dependent overlap function has been retrieved for the 355 and 532 nm channels. A detailed description of the methodology used to retrieve

these functions will be shown in the section 4.3. The overlap correction is applied to the lidar signals as follows:

$$P_{corrected}(R,\lambda) = \frac{1}{O(R,\lambda)}P_{measured}(R,\lambda) \tag{4.2}$$

where $P_{measured}$ is the power received and $O(R,\lambda)$ is the overlap function, both terms were described in chapter 2; and $P_{corrected}$ is the lidar power after the overlap correction.
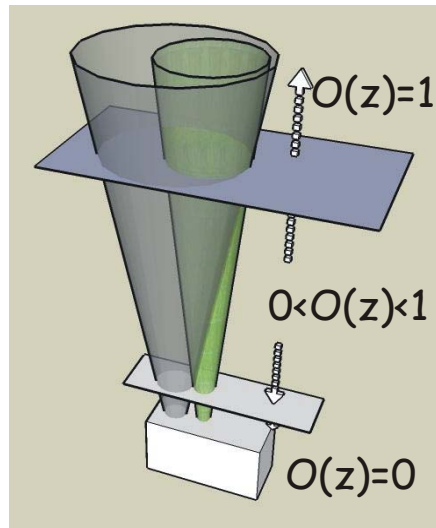
Figure 4.3. Schematic diagram of the incomplete overlapping between a laser beam and the field of view of a receiving telescope.

4.1.5. Low and high range signals gluing (for AN/PC systems)

In remote sensing applications like lidar a photomultiplier looking at a laser pulse sent out into the atmosphere is driven close to saturation by the backscattered light from the vicinity, but a few hundred microseconds later it is required to detect single photons returning from up to around 100 km apart. Such a high dynamic range of up to five orders of magnitude is one of the challenges in detection of lidar signals. The detection systems are usually optimized for measuring low-level light intensities using the single PC technique, but at higher light intensities this approach gives a nonlinear signal response. An AN measurement of the photomultiplier current is therefore necessary to increase the dynamic range.

AN and PC detection techniques require different signal conditioning: a high-speed, high-gain amplification for PC and a strictly linear amplification below the Nyquist frequency of the A/D converter for AN measurements. Only the integration of

two complete acquisition chains from the preamplifier to the summation memory will enable to combine both techniques for increased linear dynamic range.

The main idea of the signal combination is that there is a region where both signals are valid and have a high SNR. For typical PMTs, that region extends from 0.5 to 10 MHz in the PC [Mielke, http://www.licel.com/analogpc.pdf]. However, after several test carried out on our signals, we have found that the upper limit height (which corresponds to the lowest value in PC signals, 0.5 MHz), exceeds the range where the AN has a good dynamic response. For this reason the AN mode is used to determine the maximum height where both detection modes have a linear response. Furthermore, it has been found that in PC mode the detectors have a good response up to values of 20 MHz. Here we summarize the criteria used to select the height range for this linear fitting:

- Lower limit: altitude at which PC signal reaches the value of 20 MHz.

- Upper limit: altitude at which AN signal exceeds 2% the background value. It has been found that this value is the minimum required for a good linear response between both detection modes.

Figure 4.4 shows an example of a linear fit between AN and PC signals for two selected regions. The signals presented here correspond to night-time measurements performed on 7th April, 2011. Figure 4.4a displays the linear fit in the region chosen following the criteria suggested by Mielke (http://www.licel.com/analogpc.pdf), while figure 4.4b shows the fit for the region chosen according to our tests. We can observe that the linear fit is clearly better when the region chosen following the criteria proposed in this thesis is selected (R^2=0.99 vs R^2=0.96).
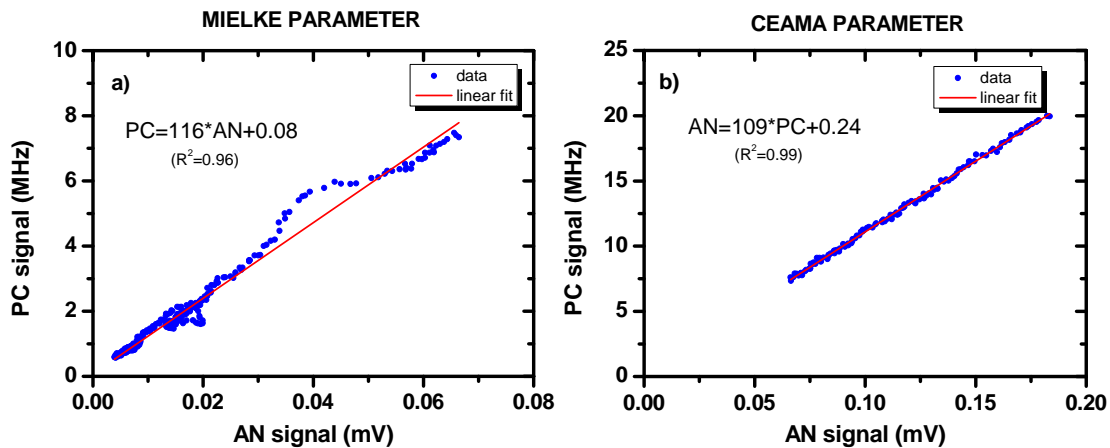

Figure 4.4. Linear fit between AN and PC signals using the region proposed by Mielke (a) and the region proposed in this thesis (b).

In the valid region of both signals one seeks the linear regression coefficients to transfer the AN data into PC data:

$$ScaledAN = a * AN + b; \qquad (4.3)$$

The coefficients *a* and *b* are applied to the AN signal, so that the AN signal is transformed by these coefficients in what we call scaled AN signal.

It must be taken into account that in principle one should glue two signals only if it is necessary. The only scenario when one really need to glue is when the following conditions are fulfilled:

    i)   The peak value of the PC signal is above the maximum frequency of 20 MHz.

    ii)   The background of the PC signal is below the minimum frequency of 0.05 MHz.

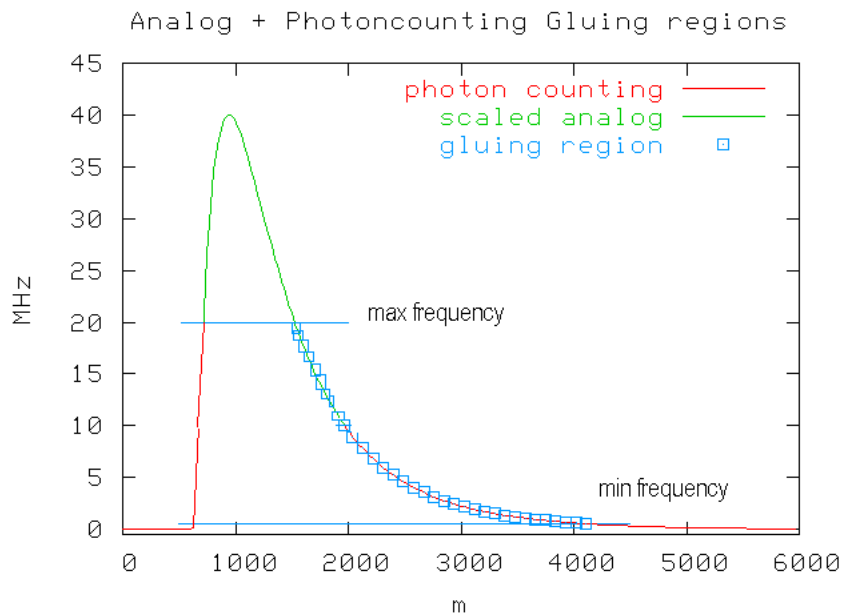This situation is shown below:

Figure 4.5. AN plus PC gluing regions.

If one assumes that the AN signal is valid enough to compute a regression curve then there is no need to compute a regression if the PC background exceeds the minimum frequency (0.05 MHz). In this case one can use the scaled AN signal.

If the peak count rate does not exceed the maximum frequency (20 MHz) there is no need to glue either and the PC signal should be used.

4.1.6. Time averaging

The last step in the pre-processing is the time averaging of the lidar signals. This averaging is performed in order to increase the SNR of our measurements. The time interval to average the signals is selected so that atmospheric variability is minimized. Typical averaging over 30 minutes are usually used in our lidar analysis for aerosol research.

4.2. Lidar inversion algorithms

In this section the two most important methods for the determination of particle optical properties from lidar observations are reviewed. In subsection 4.2.1 we introduce the widely used technique to retrieve backscatter coefficient from the lidar elastic signals. In subsection 4.2.2 the so-called Raman lidar technique that allows for independently determining the particle extinction and backscatter coefficients is presented.

4.2.1. Elastic lidar technique

The basis of any lidar signal analysis is the lidar equation which has been described in detail in chapter 2. The lidar equation in its simplest form is valid for quasi-monochromatic emission of the laser light, instantaneous scattering and negligible multiple scattering and coherence:

$$P(R, \lambda) = K \frac{O(R)}{R^2} \beta(R, \lambda) \exp\left[-2\int_0^R \alpha(r, \lambda) dr\right] \qquad (4.4)$$

where $P(\lambda, R)$ is the backscattered laser power at wavelength λ from the height R. K is the range-independent system constant and $O(z)$ is the overlap function. $\beta(\lambda, R)$ and $\alpha(\lambda, R)$ are the coefficients for backscattering and extinction processes, respectively. Backscattering and extinction are both caused by particles (index aer) and molecules (index mol):

$$\beta(R, \lambda) = \beta_{mol}(R, \lambda) + \beta_{aer}(R, \lambda) \qquad (4.5)$$

$$\alpha(R,\lambda) = \alpha_{mol}(R,\lambda) + \alpha_{aer}(R,\lambda) \tag{4.6}$$

Assuming that the molecular terms in the lidar equation can be calculated by use of standard atmosphere conditions or an atmospheric density profile from radiosondes nearby launched, $\beta_{aer}(\lambda, R)$ and $\alpha_{aer}(\lambda, R)$ remain as the two height-dependent unknowns and only one signal has been measured. One usually solves this problem by assuming an (a priori unknown) relationship between aerosol backscatter and extinction coefficients. This is the extinction-to-backscatter ratio or lidar ratio (LR) of the scattering particles with

$$LR_{aer}(R,\lambda) = \frac{\alpha_{aer}(R,\lambda)}{\beta_{aer}(R,\lambda)} \tag{4.7}$$

Under this assumption, the equation for $\beta_{aer}(R)$ can be solved following the Klett-Fernald-Sasano algorithm [*Fernald et al.*, 1972; *Klett*, 1981; *Fernald*, 1984; *Sasano and Nakane*, 1984; *Klett*, 1985]:

$$\beta_{aer}(R) + \beta_{mol}(R) = \frac{RCS(R)\exp\left\{-2\int_{R_0}^{R}\left[LR_{aer}(r) - LR_{mol}\right]\beta_{mol}(r)dr\right\}}{\dfrac{RCS(R_0)}{\beta_{aer}(R_0) + \beta_{mol}(R_0)} - 2\int_{R_0}^{R}LR_{aer}(r)RCS(r)T(r,R_0)dr} \tag{4.8}$$

with

$$T(r,R_0) = \exp\left\{-2\int_{R_0}^{r}\left[LR_{aer}(r') - LR_{mol}\right]\beta_{mol}(r')dr'\right\} \tag{4.9}$$

where $LR_{mol} = \alpha_{mol}(\lambda,R)/\beta_{mol}(\lambda, R) = 8\pi/3$ and $RCS(R) = P(R){\cdot}R^2$ is the range corrected signal aforementioned.

In order to determine $\beta_{aer}(R)$ from Eq. (4.8-4.9), the aerosol backscatter coefficient has to be estimated at a specific reference height R_0 ($\beta_{aer}(R_0)$). This reference height is usually chosen such that at R_0 the aerosol backscatter coefficient is negligible compared to the known molecular backscatter value. Such clear air conditions are normally given in the upper troposphere.

4.2.2. Inelastic lidar technique

Raman scattering is an inelastic pure molecular scattering that has been successfully used in lidar remote sensing techniques since the late 1960s [*Melfi et al.*, 1969; *Cooney*, 1970]. In a Raman lidar, the wavelength λ_{Ra} of the scattered light is shifted with respect to emitted laser wavelength λ_0, and such a shift depends on the scatterer molecule (such inelastic scattering was described in section 2.3.2). For detection of the Raman scattering of a gas with known atmospheric density, such as nitrogen or oxygen, the backscatter coefficient in the Raman lidar equation is known, and only the aerosol extinction and its wavelength dependence remain as unknowns [*Ansmann et al.*, 1990].

The Raman lidar equation can be written as:

$$P(R, \lambda_{Ra}) = K_{Ra} \frac{O_{Ra}(R, \lambda)}{R^2} \beta_{Ra}(R, \lambda) \times \exp\left\{-\int_0^R [\alpha(r, \lambda_0) + \alpha(r, \lambda_{Ra})] dr\right\} \quad (4.10)$$

where $P(R, \lambda_{Ra})$ is the power received from distance R at Raman wavelength λ_{Ra}, K_{Ra} is a function that depends on all the range-independent system parameters, $\beta_{Ra}(\lambda, R) = N(R)\sigma_{Ra}(\lambda)$ is the Raman backscatter coefficient, where $N(R)$ is the atmospheric number density of the Raman scatterer and $\sigma_{Ra}(\lambda)$ is the Raman backscatter cross section, α is the range-dependent total volume extinction coefficient at wavelengths λ_0 and λ_{Ra}, and r is the range integration variable.

Assuming a wavelength dependence of the aerosol extinction $\alpha_{aer} \propto \lambda^{-k}$, the Raman lidar equation can be solved for the aerosol extinction at the emitted laser wavelength [*Ansmann et al.*, 1990] as:

$$\alpha_{aer}(R, \lambda_0) = \frac{\dfrac{d}{dR} \ln \dfrac{N_{Ra}(R)}{RCS(R, \lambda_{Ra})} - \alpha_{mol}(R, \lambda_0) - \alpha_{mol}(R, \lambda_{Ra})}{1 + \left(\dfrac{\lambda_0}{\lambda_{Ra}}\right)^k} \quad (4.11)$$

where $d\sigma_{Ra}(\lambda)/dR = 0$ has been used. The molecular extinction can be calculated from Rayleigh scattering coefficients and atmospheric number density profiles retrieved from models or radiosonde measurements. From the detection of the Raman scattered light, independent aerosol extinction profiles can be determined. One can also use this information to derive the aerosol backscatter without any assumption about the *LR*,

which is an important parameter because it is directly related to the microphysical properties of the particles.

The aerosol backscatter coefficient $\beta_{aer}(R,\lambda_0)$ at the emitted wavelength λ_0 can be obtained now from the ratio of the received elastically backscattered signal $P(R,\lambda_0)$ (Eq. 4.4) and the Raman signal $P(R, \lambda_{Ra})$ (Eq. 4.10) [*Ansmann et al.*, 1992b]:

$$
\begin{aligned}
\beta_{aer}(R,\lambda_0) + \beta_{mol}(R,\lambda_0) = & \left[\beta_{aer}(R_0,\lambda_0) + \beta_{mol}(R_0,\lambda_0)\right] \\
& \times \frac{P(R_0,\lambda_{Ra})P(R,\lambda_0)}{P(R_0,\lambda_0)P(R,\lambda_{Ra})} \frac{N_{Ra}(R)}{N_{Ra}(R_0)} \\
& \times \frac{\exp\left\{-\int_{R_0}^{R}\left[\alpha_{aer}(r,\lambda_{Ra}) + \alpha_{mol}(r,\lambda_{Ra})\right]dr\right\}}{\exp\left\{-\int_{R_0}^{R}\left[\alpha_{aer}(r,\lambda_0) + \alpha(r,\lambda_0)\right]dr\right\}}
\end{aligned}
\tag{4.12}
$$

Similarly to the Klett method, a reference value $\beta_{aer}(R_0, \lambda_0)$ is needed in order to solve Eq. (4.12). The reference height R_0 is typically set in a region with clear air or at a height where $\beta_{aer}(R_0, \lambda_0)$ is known.

The uncertainties in the optical properties from elastic and inelastic inversions are determined by means of a numerical procedure based on the Monte Carlo technique, commonly used in the EARLINET network . This procedure is based on the random extraction of new lidar signals, each bin of which is considered a sample element of a given probability distribution with the experimentally observed mean value and standard deviation. The extracted lidar signals are then processed with the same algorithm to produce a set of solutions from which the standard deviation is calculated as a function of height [*Guerrero-Rascado*, 2008; *Pappalardo et al.*, 2004].

4.3. Retrieval of the lidar overlap function

In this section we present an iterative method to determine the lidar overlap function. This correction was introduced in section 4.1 and it attempts to correct the incomplete overlap between the laser beam and the receiver field of view. The effect can considerably influence the vertical profiling up to several kilometres in the case of systems with a receiver characterized by a narrow field of view below 0.5 mrad [*Wandinger et al.*, 2002].

Several methods have been suggested to determine the profile of the overlap factor analytically [*Halldorsson and Langerholc*, 1978; *Sassen and Dodd*, 1982; *Ancellet et al.*, 1986; *Kuze et al.*, 1998; *Stelmaszczyk et al.*, 2005], by the application of a ray-tracing model [*Velotta et al.*, 1998], and also experimentally [*Sasano et al.*, 1979; *Tomine et al.*, 1989; *Dho et al.*, 1997]. These techniques present important limitations because they require the knowledge of some technical parameters (not usually available), and the existence of homogeneous aerosol conditions, a situation seldom fulfilled in the lower layers.

Here, we analyze the overlap effect on our system using a simple technique for determination of the overlap function proposed by Wandinger and Ansmann. [2002]. The method is based on the simultaneous measurement of a pure molecular (nitrogen or oxygen Raman) backscattered signal in addition to the elastic backscattered signal performed with an aerosol Raman lidar [*Ansmann et al.*, 1992a; *Whiteman et al.*, 1992]. The method works without the need to know the above-mentioned lidar system parameters and under homogeneous as well as inhomogeneous aerosol conditions. The basic assumption is that the overlap profiles for both the elastic backscatter and the Raman signals are identical. The only input data set that can influence the result significantly is the profile of the particle *LR*. The *LR* effect is minimized using cases with clean atmospheric conditions.

The lidar equations for the elastic and the Raman signals was well described in the sections 2.6 and 4.2.2, and they can be written as follows:

$$P_0(R) = K_0 O_0(R) R^{-2} \left[\beta_{0,aer}(R) + \beta_{0,mol}(R) \right] T_0^2(R) \tag{4.13}$$

$$P_{Ra}(R) = K_{Ra} O_{Ra}(R) R^{-2} \beta_{Ra}(R) T_0(R) T_{Ra}(R) \tag{4.14}$$

where *P* is the received power; the subscripts 0 and *Ra* refer to the laser wavelength λ_0 and the Raman wavelength λ_{Ra}, respectively; K_0 and K_{Ra} are the system constants for the elastic and Raman channels, respectively; and *O(R)* denotes the overlap factor. *O(R)* is zero close to the lidar system (no overlap), and typically reaches 1 (complete overlap) for large distances (Figure 4.3). $O_0(R) = O_{Ra}(R)$ is assumed in this approach [*Wandinger and Ansmann*, 2002].

In Eq. (4.13), $\beta_{0,aer}$ and $\beta_{0,mol}$ represent the elastic backscatter coefficients of aerosols and molecules, respectively, at λ_0, and β_{Ra} in Eq.(4.14) is the Raman

backscatter coefficient at λ_{Ra}. T_0 describes the atmospheric transmission at λ_0 between the lidar and the backscattering region, and T_{Ra} is the atmospheric transmission at λ_{Ra} along the way back to the lidar after Raman scattering.

The iterative approach presented here makes use of the fact that the deviation between the Klett solution for the backscatter coefficient, $\beta_{Klett}(R)$, which is calculated from the elastic backscattered signal, and the Raman solution, $\beta_{Raman}(R)$, contains information about the incomplete overlap [*Wandinger and Ansmann*, 2002]. Here, the *LR* profile is needed as an input for the Klett procedure.

This iterative approach is based on the fact that the elastic backscattered signal, after corrections of range and overlap dependency, is proportional to the total backscatter coefficient [see Eq. (4.13)]:

$$P_0(R)O(R)^{-1}R^2 \propto \beta_{Raman}(R) + \beta_{0,mol}(R) \qquad (4.15)$$

with $\beta_{0,P}(R)=\beta_{Raman}(R)$. In this way we assume that the Raman retrieval procedure provides backscatter coefficients in the near height range, due to the use of the ratio of backscattered signals with similar overlap effects. In contrast, the elastic signal, only corrected for the range dependence, is mainly a function of the combined effect of total backscatter and the range-dependent overlap. This dependency is expressed by means of the Klett solution,

$$P_0(R)R^2 \propto \beta_{Klett}(R) + \beta_{0,mol}(R) \qquad (4.16)$$

The relative difference between the Klett and the Raman lidar solutions,

$$\frac{\beta_{Raman}(R) - \beta_{Klett}(R)}{\beta_{Raman}(R) + \beta_{0,mol}(R)} \propto \frac{P_0(R)O(R)^{-1}R^2 - P_0(R)R^2}{P_0(R)O(R)^{-1}R^2} \propto 1 - O(R) \qquad (4.17)$$

is used iteratively to reduce the overlap effect on the aerosol signal.

In the first step ($i = 1$), the Klett method is applied for the uncorrected elastic backscatter signal. $\beta_{Klett,i=1}(z)$ is used to solve the expression:

$$\Delta O_i(R) = \frac{\beta_{Raman}(R) - \beta_{Klett,i}(R)}{\beta_{Raman}(R) + \beta_{0,mol}(R)} \qquad (4.18)$$

The elastic backscatter signals are corrected with $\Delta O_1(R)$ as follows:

$$P_{0,i+1}(R) = P_{0,i}(R)\left[1 + \Delta O_i(R)\right] \qquad (4.19)$$

By reapplying the Klett method (step $i = 2$), now to the improved signal profile $P_{0,2}(R)$, we obtained an improved backscatter coefficient profile $\beta_{Klett,2}(R)$. After inserting $\beta_{Klett,2}(R)$ into Eq. (4.18) and $\Delta O_2(R)$ into Eq. (4.19) we further correct the signal profile for the overlap effect. Our simulations indicate that approximately 10-12 iterations are sufficient to remove the overlap effect completely. From the comparison of the measured signal profile with the corrected signal profile, we derivate the overlap profile.

This iterative approach has been applied successfully to measurements performed at Granada station. Figure 4.6 shows an example of the application of this method obtained on 1st November 2007. Clean conditions were monitored during night time with the star-photometer EXCALIBUR. This instrument detected a low AOD (0.06 at 380 nm) during the analyzed period. A LR of 40 sr was assumed for the Klett solution. A good agreement is achieved between the Raman solution (red line) and iterative approach solution (blue line) for the backscatter coefficient at 532nm (Fig. 4.6a). The Klett solution (green line) and the solutions for the different iterations (dashed line) are also shown. Twelve iterations were needed in this case. Figure 4.6a shows the importance of the overlap correction. Figure 4.6b presents the corresponding overlap profile determined from Eq. (4.18). This function presents values below one (incomplete overlap) up to 1250 m (agl), being the full overlap reached above this level. As it can be seen, below 500 m (above ground level, agl) the separation from perfect overlap is larger than 50%.
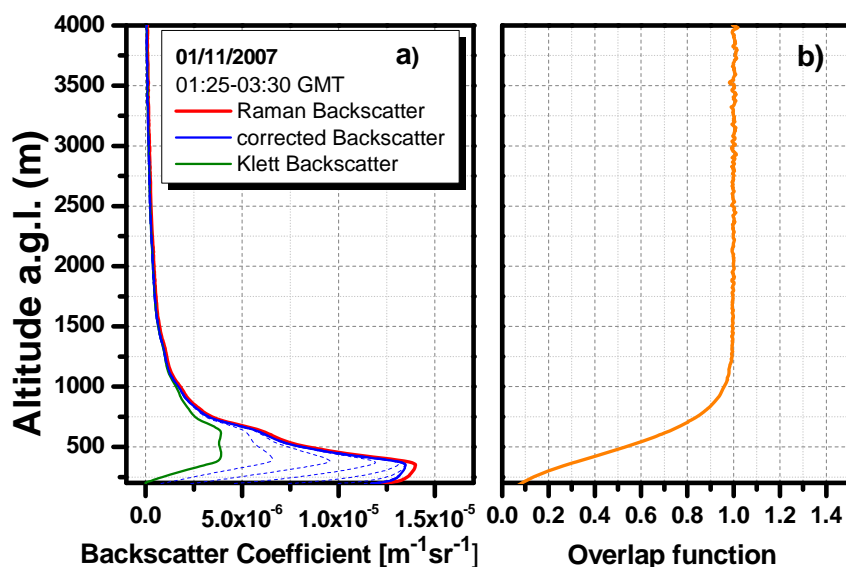

Figure 4.6. a) Backscatter coefficient: Klett solution (green line), Raman solution (red line) and iterative solution (blue lines). b) Overlap function determined by applying the iterative method.

In order to correct our system from the overlap effect, the overlap function has been retrieved periodically for those cases with low aerosol load. A stable solution is found by calculating a mean function. In order to obtain this mean function we retrieve different overlap functions for a period in which the configuration of our system has remained unchanged (same alignment, no change in hardware, etc). Figure 4.7a shows an example of different overlaps and the mean function obtained at 532 nm for the period from September to December 2007. Figure 4.7b shows the relative deviation respect to the mean solution for each case. It can be seen that the relative deviation above 1500 m (asl) is below 5%. The largest deviations are found in the lowest layers but, however, they are below 25%.

These results show the importance of the overlap correction on the lidar signals. This correction has been extensively tested and successfully applied to experimental data obtained in our station. The application has enabled to improve the capabilities of the Raman lidar system operated routinely in the Granada station, allowing for investigating the aerosol optical properties in the lowermost PBL.
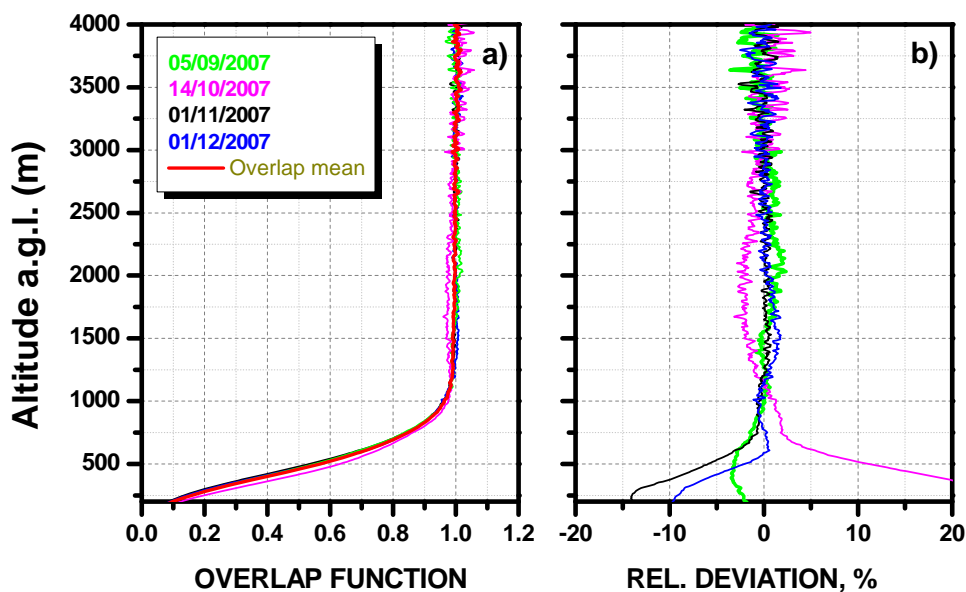

Figure 4.7. a) Overlap functions calculated for 4 days. The mean overlap factor was also obtained (red line). b) Relative deviation for the 4 days respect to mean overlap function.

4.4. Lidar infrared channel calibration

As was seen in section 4.2.1, one of the key parameters to retrieve the backscatter coefficient from elastic lidar signals is its value at a reference height. Traditionally, such a calibration height has fulfilled the criterion that at this altitude the aerosol backscatter coefficient is negligible compared to the molecular backscatter value. Such clean air conditions are normally given in the upper troposphere. However, some signals can show a low SNR in this range, the so called molecular range, and therefore it is not possible to perform such kind of calibration. At 1064 nm the setting of this reference value is more difficult than for the other lidar wavelengths. This is due to the wavelength dependence of the Rayleigh backscattering. At the near-infrared wavelength range the molecular backscatter coefficient is about two orders of magnitude lower than at a visible wavelength [*Heese et al.*, 2010]. Thus, less backscattering from the molecules occurs at the longer wavelengths and from aerosol free levels only very low signals are received by the 1064 nm channel of the lidar. In this section, we present two alternative methods to solve this calibration problem for the infrared channel. The first method is based on the use of a cloud base to calibrate, requiring the presence of cirrus clouds in the lidar profile, [*Navas-Guzmán et al.*, 2011a]; and the second method use the near range, where the contribution of aerosol is not negligible, to calibrate the problematic channel, requiring some estimate of the backscatter at a given height, derived from measurements at other channels (355 and 532 nm) [*Navas-Guzmán et al.*, 2011b].

4.4.1. On the use cirrus clouds for infrared lidar channel calibration

The procedure presented here is based on the presence of cirrus clouds in the lidar profile and the use the cloud base for calibration. The calibration with cirrus clouds have been used previously for satellite lidar measurements [*Reagan et al.*, 2002], achieving uncertainties within 5%. Due to the ice crystal sizes that form cirrus clouds are much larger than the wavelengths used in the lidar technique, it is possible to assume that the process of cirrus-radiation interaction falls in the geometric optics domain. In this domain, assuming the particle backscatter coefficient as essentially independent of the wavelength is a good approximation. The idea is calibrating with a channel with a large SNR in the far height range (above cirrus cloud), where the aerosol component is negligible, and to retrieve the aerosol backscatter profile at this

wavelength. After that, we use the value of the aerosol backscatter coefficient at the cloud base height to calibrate the infrared channel. Finally, substituting this value in the Klett solution (Eq. 4.8) we can retrieve the whole aerosol backscatter profile at 1064 nm.

On the other hand, an important property that describes the spectral slope of the backscatter coefficients $\beta(\lambda,R)$ is the so-called backscatter-related Ångström exponent (β-AE). This parameter is known to be strongly dependent on particle size and shape and is calculated as follows,

$$\beta - AE(532 - 1064) = -\frac{\ln\left[\beta_{aer}(532, R)/\beta_{aer}(1064, R)\right]}{\ln(532/1064)} \qquad (4.20)$$

Inside the cirrus clouds this parameter must be close to zero.

An example of this calibration method is shown next. The measurements were performed during the daytime on 27th February 2008 (12:00-13:00 UTC). Figure 4.8 shows the RCS along the lidar measurement session. We can see cirrus clouds around 12 km (asl) during the measurement and the most aerosol load confined below 3 km (asl), although it is possible to see some aerosol layers between 3 and 4 km (asl).
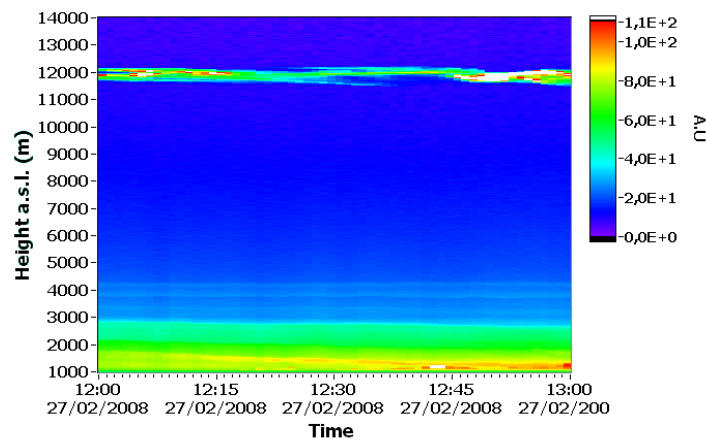

Figure 4.8. RCS on 27th February 2008 during the daytime lidar measurement.

Backward trajectories were calculated with the HYSPLIT model (Hybrid single-particle Lagrangian integrated trajectories model, http://ready.arl.noaa.gov/HYSPLIT_traj.php) [*Draxler and Rolph*, 2003] using GDAS data in order to interpret the different source regions of air masses reaching the study area. Backward trajectories analyses indicated the arrival of air masses coming from North Africa at the lower altitudes. Using a sun-photometer we detected this dust event characterized by low values of AOD-related Ångström exponent (AE) calculated in the

spectral range 440-1020 nm around 0.25 and medium-high aerosol optical depth of 0.17 at 670 nm.

Figure 4.9a shows the aerosol backscatter profiles at 355, 532 and 1064 nm retrieved for this case. The blue and green lines correspond to the backscatter profile at 355 and 532 nm, respectively. The reference range used for the 355 nm channel was 6 km (asl). The reference height for the 532 nm channel was chosen above the cirrus clouds (13 km asl), in order to calibrate the infrared channel. Two profiles at 1064 nm are shown in this figure, corresponding to two different calibration methods. The gray line corresponds to the calibration in the molecular height range, whereas the red line corresponds to the calibration with the cirrus cloud. As can be seen, the backscatter profile at 1064 nm calibrated in the molecular range shows too low values.

Figure 4.9b shows β-AE profiles computed from these lidar profiles. For the spectral range 355-532 nm, the values are around 0.5 below 3 km. This is a typical value for mineral dust particles [*Guerrero-Rascado et al.*, 2009] and it confirms the results expected. If we use the 1064nm-channel calibrated in the molecular height range, the β-AE for the spectral range 532-1064 nm presents larger values, above 1.0 in the whole profile. These values are not typical of mineral dust particles. Moreover, we see large discrepancies between β-AE determined for different spectral ranges. This behaviour can be significantly improved when the 1064 nm profile is calibrated using the cirrus cloud. In fact, after applying this calibration procedure the β-AE for 532-1064 nm presents values around 0.5 in the near height range and a good agreement with the β-AE exponent for 355-532 nm. This example shows an important improvement in the 1064nm-backscatter coefficient profile when the new calibration with cirrus cloud is used.
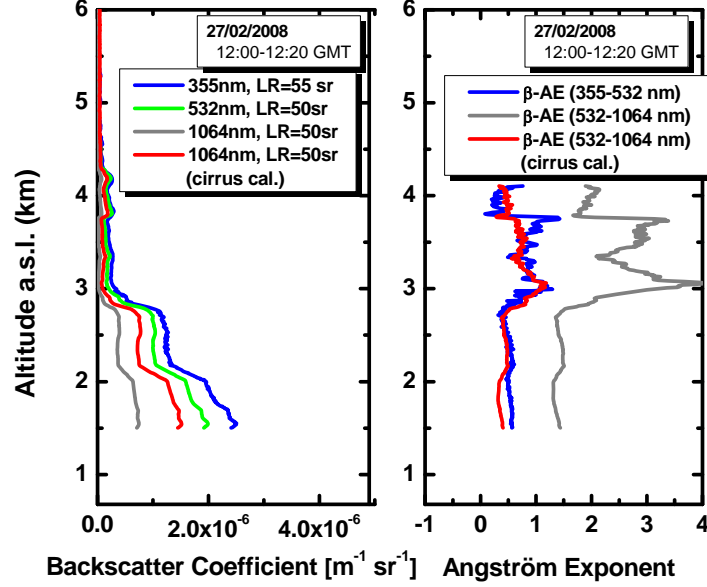
Figure 4.9. a) Aerosol backscatter profiles at 355, 532 nm (blue and green lines) and 1064 nm (gray line: calibration using the molecular height range; red line: calibration using cirrus clouds). b) β-AE derived from 355-532 nm channels (blue line) and 532-1064 channels (gray line: calibration using molecular range; red line: calibration using cirrus clouds).

4.4.2. Infrared lidar channel calibration in the near range

Since the presence of cirrus clouds does not always occur it was necessary to find a new method to calibrate the 1064 nm channel. The alternative calibration method proposed in this section consists in choosing the reference height R_0 in the near height range. As we know, the aerosol backscatter coefficient in the near height range is not negligible. In order to retrieve this parameter at R_0, we use information from other two channels, which can be calibrated in the molecular height range, and we assume the same spectral dependency at this altitude. To that aim we use the Ångström law which relates the backscatter coefficient at different wavelengths:

$$\beta(R,\lambda) = \beta(R,\lambda_0)\left(\frac{\lambda}{\lambda_0}\right)^{-\beta-AE(\lambda-\lambda_0)} \tag{4.21}$$

Considering that at R_0 the *β-AE* determined by different the pairs of backscatter coefficients is the same, we obtain the aerosol backscatter coefficient at λ channel (with low SNR) from the other two retrieved aerosol backscatters (λ_0 and λ_1):

$$\beta^{aer}(R_0,\lambda) = \beta^{aer}(R_0,\lambda_0)\left(\frac{\lambda}{\lambda_0}\right)^{-\beta-AE(\lambda-\lambda_0)} = \beta^{aer}(R_0,\lambda_0)\left(\frac{\lambda}{\lambda_0}\right)^{-\beta-AE(\lambda_0-\lambda_1)} \tag{4.22}$$

84

After computing this parameter, it is possible to retrieve the whole aerosol backscatter profile at the infrared channel from Klett solution (Eq. 4.8). In our case, λ_0 and λ_1 correspond to 355 and 532 nm, respectively; and λ correspond to 1064 nm.

This calibration method has been successfully tested under different conditions. In particular, we present an example corresponding to a Saharan dust outbreak. The measurements were performed during daytime on 5th July 2008 (14:15-14:45 GMT). Figure 4.10 shows the lidar RCS for this measurement session. Although the most important aerosol load is below 2 km (asl), inside the PBL, it is possible to observe the presence of particles up to 4 km (asl). In this case the presence of aerosol at high layers is identified with mineral dust particles.
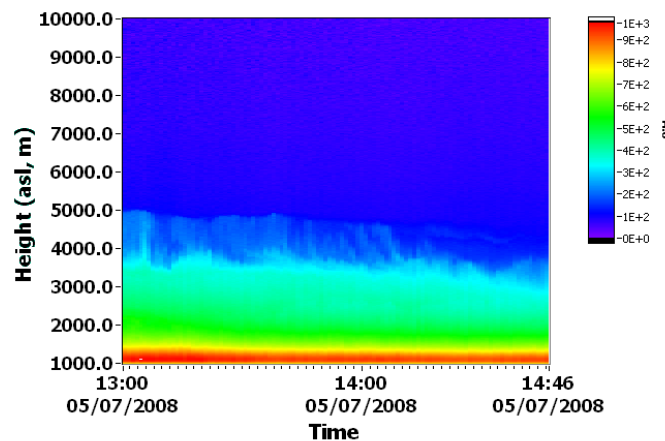

Figure 4.10. Lidar RCS on 5th July 2008 during the daytime measurement.

Backward trajectories analysis calculated with Hysplit model indicated the arrival of air masses coming from North Africa in the lower layers. Sun-photometer co-located with lidar detected mineral dust, with low values of AOD-AE (0.22) in the spectral range of 1020-440 nm and medium AOD (0.17 at 670 nm) that can be associated with a dust event.

Figure 4.11a shows the aerosol backscatter profiles at 355, 532 and 1064 nm retrieved for this case. The blue and green lines correspond to the backscatter profile at 355 and 532 nm, respectively. The reference height used in both cases was 5 km (asl). In addition, two different calibration methods are shown for the 1064 nm channel. The gray line corresponds to the calibration in the molecular height range at 5 km (asl), whereas the red line corresponds to the retrieval when the calibration was performed in the near range at 3.0 km (asl). As can be seen, the profile calibrated for 1064 nm channel in the molecular height range shows unrealistic too low values.
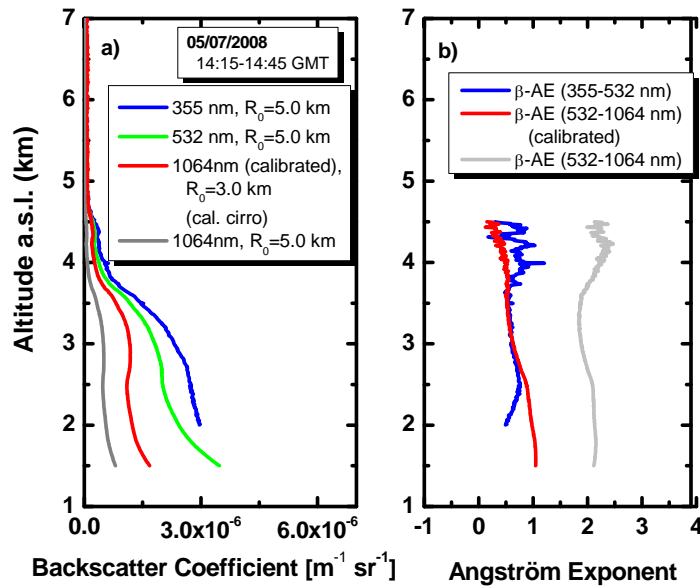
85

Figure 4.11. a) Aerosol backscatter profiles at 355, 532 nm (blue and green line, respectively), and 1064 nm (gray line: calibration using the molecular height range; red line: calibration in the near range). b) β-AE derived from 355-532 nm channels (blue line) and 532-1064 channels (gray line: calibration in molecular range; red line: calibration in near range).

Figure 4.11b shows β-AE computed from the lidar profiles. For the spectral range 355-532 nm, the values are lower than the unity below 4.5 km (asl). This is a typical value for mineral dust particles [*Guerrero-Rascado et al.*, 2009] and it confirms the expected results. If the 1064 nm channel calibrated in the molecular height range is used, the β-AE for 532-1064 nm spectral range presents larger values, above 1.7 for the whole profile. This is not a realistic result respect with the other spectral range and clearly is not coherent taking into account the presence of mineral dust in the atmospheric column. This behaviour can be significantly improved when the 1064 nm profile is calibrated in the near height range. In fact, the β-AE for 532-1064 nm presents values below 1.0 in the whole column and it shows a good agreement with the β-AE for 355-532 nm. This second calibration method for infrared channel shows again an improvement in the aerosol backscatter profile at 1064 nm.

The two methods presented in this section (4.4) have been applied in those cases in which it was not possible to calibrate in the molecular range.

4.5. Backscatter algorithm intercomparison

In the framework of the EARLINET network, intercomparisons of lidar algorithms have been performed in order to assure the quality of the algorithms used by

each member of the network [*Bockmann et al.*, 2004; *Pappalardo et al.*, 2004]. In these intercomparisons a commercial software developed by Raymetrics (Greece) for the elastic algorithm and a software developed by our team for the Raman algorithm were evaluated in the EARLINET network. The intercomparison showed that both algorithms present satisfactory results for the aerosol backscatter and extinction coefficients [*Guerrero Rascado*, 2008].

In order to obtain a greater control on the elastic inversion and thus able to implement all the improvements made during this thesis (e.g. pre-processing, overlap correction, calibrations) this algorithm was also implemented for our team. We also had the opportunity to validate this software during a new intercomparison that took place in the framework of SPALINET.

The mains goals of this network is to extend and reinforce the action of EARLINET, to form nucleus for stimulating the Spanish and Portuguese lidar community and to promote the participation of new groups for improving the spatial coverage of aerosol vertical measurements on the Iberian Peninsula and Canary Islands territories. The Granada station was one of the founding members of this network, which was created in 2007, and now have 10 members distributed in the Iberian Peninsula and the Canary Island [*Sicard et al.*, 2011]. Figure 4.12 shows the geographical distribution of the lidar stations involved in SPALINET.

In this section we present the Klett algorithm intercomparison performed in SPALINET for the Granada elastic algorithm [*Sicard et al.*, 2009]. The procedure for this intercomparison was similar to that performed by EALINET [*Bockmann et al.*, 2004] and it was divided into three stages. Stage 1 is the hardest one because the degree of *a priori* knowledge available before the retrieval is the smallest. The three stages were as follows:

Stage 1: The simulated signals, without any information about the input parameters except the standard atmosphere used, were distributed to all groups. Each group calculated the aerosol backscatter coefficient profiles using its own algorithm.

Stage 2: The prescribed LR profile was provided to all groups. The evaluation was repeated.

Stage 3: The reference value at calibration height was also provided. The evaluation was repeated.

Figure 4.12. Geographical distribution of the lidars involved in SPALINET. Circles and squares indicate transportable and fixed systems, respectively. The black color indicates the systems involved in EARLINET.

For each stage the results were collected and evaluated by Barcelona group (Universidad Politécnica de Cataluña, UPC) that coordinates SPALINET. The first stage was the most difficult but also the most realistic one, because at that stage LR profiles and reference values were unknown. Therefore, not only the correctness and accuracy of the algorithms but also the dependence of the solution on the choice of the LR and on the reference value were tested. In the third and final stage all parameters were known. So the numerical correctness and stability of the algorithms were definitely tested.

Three cases were developed for the major algorithm intercomparison. The three cases with different degrees of difficulty in solving for the backscatter coefficients were calculated with the lidar simulation model of the Institute of Tropospheric Research, Leipzig, Germany [*Bockmann et al.*, 2004]. The Institute of Tropospheric Research's software permits simulation and evaluation, elastically and inelastically, of the dependence of backscattered lidar signals at arbitrary wavelengths on a variety of system parameters for a variable model atmosphere with arbitrary aerosol and cloud layers. Sky background, background noise, and signal noise are considered as well. Atmospheric input parameters are profiles of temperature and pressure used in calculating Rayleigh scattering and profiles of extinction coefficients and lidar ratios for the simulation of aerosol and cloud layers.

In more detail, three different data sets of elastic backscatter signals at wavelengths of 355, 532, and 1064 nm were simulated. A U.S. standard atmosphere

with a ground pressure of 1013 hPa and a ground temperature of 0 °C, a tropopause height of 12.0 km, and the isothermal conditions over this layer was assumed. The signal profiles were simulated without signal noise. An incomplete overlap of laser beam and receiver field of view below 250m was introduced. The simulation of the incomplete overlap should remind the experimenters that one has to take great care when one is working in the nearest range to the lidar, i.e., 100 m to several hundreds of meters, where the overlap function is generally not well known, even if a correction is applied for [*Wandinger and Ansmann*, 2002]. Typical system parameters, e.g., laser power and telescope diameter, were used for the calculations. However, they are not relevant for the algorithm intercomparison.

In all cases, only aerosols at heights below 4.5 km were simulated. Minor particle scattering in the free troposphere and the stratosphere was introduced, and no clouds were considered. The three simulation cases represent different atmospheric conditions with increasing degrees of difficulty in data evaluation:

Case 1: The first case did not represent realistic atmospheric conditions. The extinction coefficient was independent of wavelength and changed stepwise from $3 \cdot 10^{-4}$ m^{-1} below 1500 m to $3.5 \cdot 10^{-4}$ m^{-1} at 1500–2000 m and to $4 \cdot 10^{-4}$ m^{-1} at 2000–2440 m and decreased to values below 10^{-6} m^{-1} over 2440 m. The LR had a constant value of 50 sr for all heights and all wavelengths.

Case 2: In the second case a significant aerosol load up to 4000 m was simulated (Fig. 4.13 a-c). A more realistic, height-dependent extinction coefficient was assumed. In addition, the extinction coefficient changed with wavelength, with highest values for the shortest wavelength. The LR was height independent in the aerosol layer but took values of 64 sr for 355 nm, 62 sr for 532 nm, and 42 sr for 1064 nm. Above 4500 m the LR was 45 sr for all wavelengths.
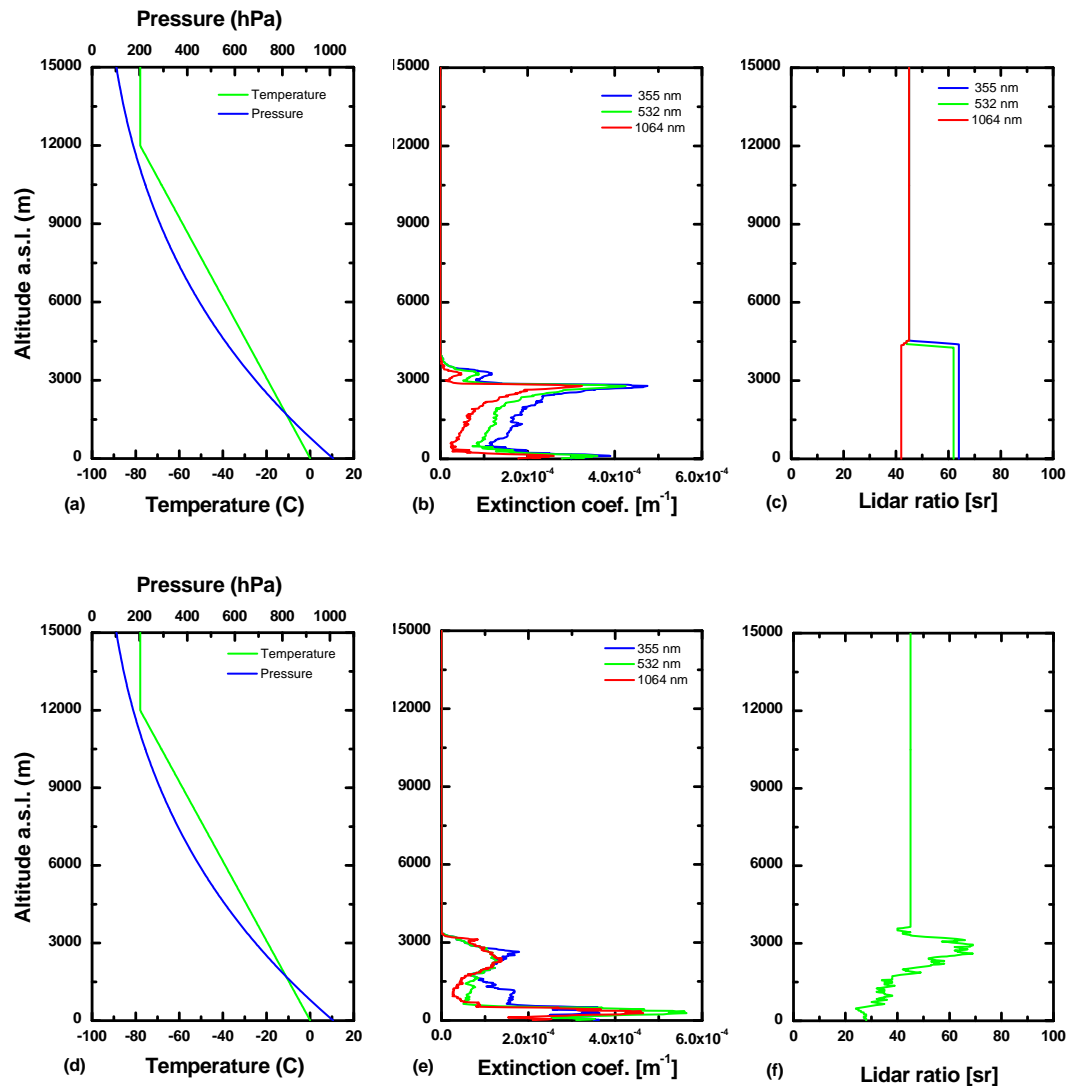
Figure 4.13. Input data for (a)-(c) simulation case 2 and (d)-(f) simulation case 3. In case 3 all wavelengths have the same lidar ratio profile.

Case 3: In case 3 a significant aerosol load up to 3300 m was simulated (Fig. 4.13 d-f). Realistic, height-dependent extinction coefficients and LR were introduced. The extinction coefficient varied widely with wavelength at different heights. The LR took values of 24–69 sr but did not vary with wavelength. Above 3600 m the LR was set to 45 sr for all wavelengths.

Since the conditions in case 3 correspond to the most realistic atmospheric conditions, only the results from that case are presented in this section.

The elastic algorithm comparison presented a low effect of the reference value on the solutions. Similar behavior was observed in EARLINET intercomparison. For

that reason, only the results from stages 1 and 3 are presented next, since the differences between stages 2 and 3 are negligible.
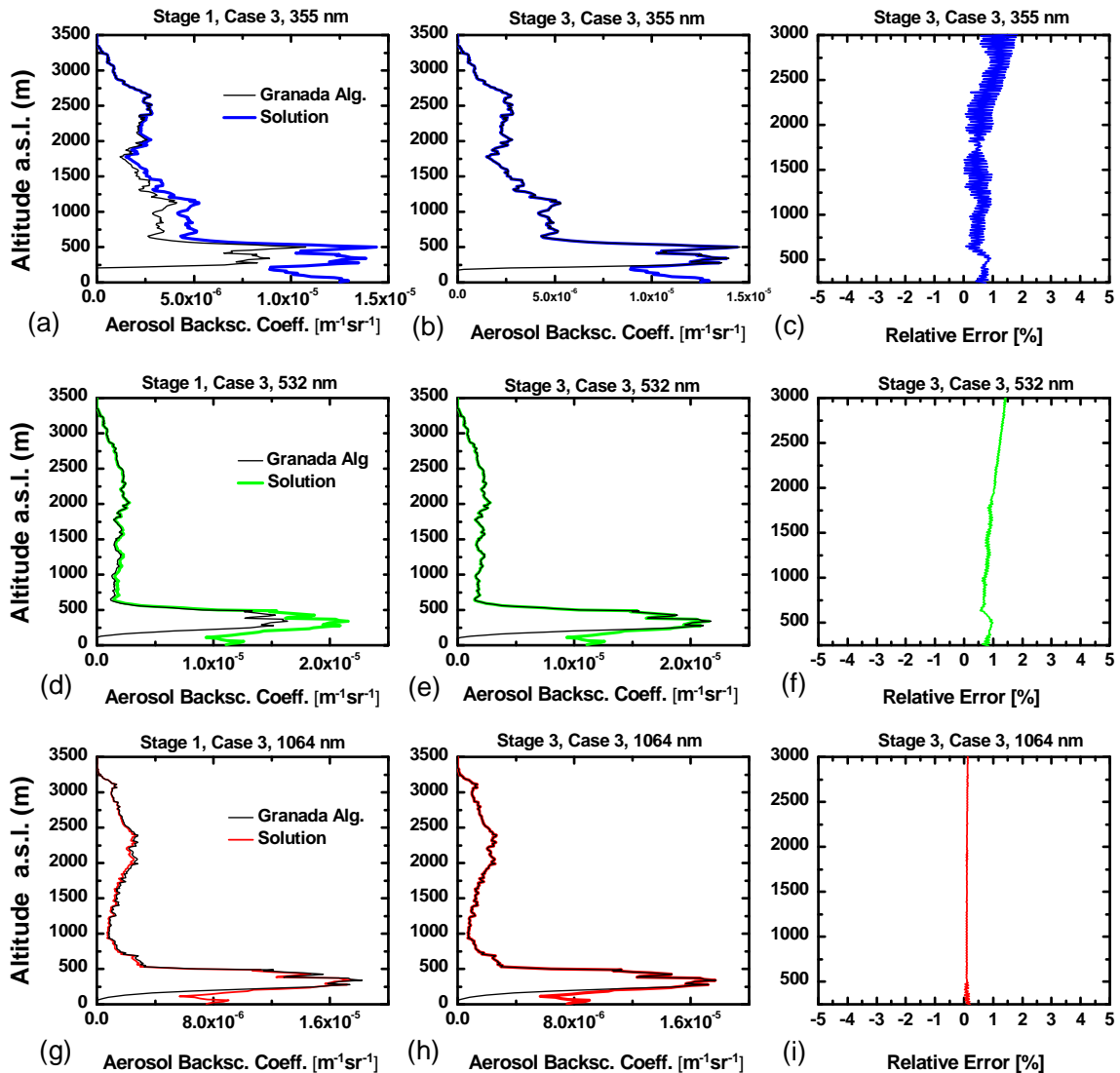

Figure 4.14. Retrieved aerosol backscatter coefficient profiles at all three wavelengths, compared with the simulation input profiles of case 3 for (a), (d), and (g) stage 1 and (b), (e), and (h) stage 3. Relative errors for case 3 and stage 3.

Figure 4.14 shows the aerosol backscatter coefficient profiles retrieved by the Granada team for stages 1 and 3 at all wavelengths. In the aerosol layer (0.6–3.3 km) the difference between stages 1 and 3 is barely visible at 532 and 1064 nm, whereas it is clearly visible at 355 nm. This emphasizes that under low aerosol loading the accuracy of the retrieved backscatter coefficient at 532 and 1064 nm does not strongly depend on the knowledge of the LR used in the inversion. Figure 4(c), (f), and (i) represents the relative errors for stage 3 at 355, 532, and 1064 nm. In detail, the mean relative errors

calculated over the range of 0.3075–3.0075 km for wavelengths of 355, 532, and 1064 nm were approximately 0.7%, 0.9%, and 0.11%, respectively. For stages 1 and 2, the respective mean relative errors were approximately 6.5%, 4.3%, and 3.2%, and 0.8%, 9%, and 0.18%, respectively. As expected, the differences between stages 2 and 3 were very small (< 0.1 %), so the effect of the reference value in the elastic inversion is small. In general, the errors for case 3 are somewhat larger than that for case 2 (not shown here), mainly because the LR is height dependent in case 3. Below the full overlap height (250 m), neither algorithm from Granada nor the algorithms from other stations were able to correctly retrieve the aerosol backscatter [*Sicard et al.*, 2009] because of the lack of information about the overlap function used. In the range of 3.0225–15.0675 km, the mean absolute error for Granada algorithm was smaller than $1 \cdot 10^{-5}$ km^{-1}·sr^{-1}, indicating that the algorithm retrieved the molecular profiles relatively well.

This intercomparison showed that the elastic algorithm developed by Granada team works very well. The discrepancies observed between our retrievals and the solutions were smaller that the obtained for other station in the EARLINET intercomparison [*Bockmann et al.*, 2004].

4.6. References

Ancellet, G. M., M. J. Kavaya, R. T. Menzies, and A. M. Brothers (1986), Lidar telescope overlap function and effects of misalignment for unstable resonator transmitter and coherent receiver, *Applied Optics*, *25*(17), 2886-2890.

Ansmann, A., M. Riebesell, and C. Weitkamp (1990), Measurement of atmospheric aerosol extinction profiles with a raman lidar, *Optics Letters*, *15*(13), 746-748.

Ansmann, A., U. Wandinger, M. Riebesell, C. Weitkamp, and W. Michaelis (1992a), Independent measurement of extinction and backscatter profiles in cirrus clouds by using a combined raman elastic-backscatter lidar, *Applied Optics*, *31*(33), 7113-7131.

Ansmann, A., M. Riebesell, U. Wandinger, C. Weitkamp, E. Voss, W. Lahmann, and W. Michaelis (1992b), Combined Raman elastic-backscatter lidar for vertical profiling of moisture, aerosol extinction, backscatter, and lidar ratio, *Applied Physics B-Photophysics and Laser Chemistry*, *55*(1), 18-28.

Bockmann, C., et al. (2004), Aerosol lidar intercomparison in the framework of the EARLINET project. 2. Aerosol backscatter algorithms, *Applied Optics*, *43*(4), 977-989.

Cooney, J. A. (1970), Remote measurements of atmospheric water vapor profiles using the Raman component of laser backscatter, *J. Appl. Meteorol.*, *9*, 182-184.

Dho, S. W., Y. J. Park, and H. J. Kong (1997), Experimental determination of a geometrical form factor in a lidar equation for an inhomogeneous atmosphere, *Applied Optics*, *36*, 6009-6010.

Draxler, R. R., and G. D. Rolph (2003), http://www.arl.noaa.gov/ready/hysplit4.html*, Silver Spring, MD*.

Fernald, F. G. (1984), Analysis of atmospheric lidar observations - some comments, *Applied Optics*, *23*(5), 652-653.

Fernald, F. G., B. M. Herman, and J. A. Reagan (1972), Determination of aerosol height distribution by lidar, *J. Appl. Meteorol.*, *11*, 482-489.

Guerrero-Rascado, J. L. (2008), PhD Thesis: Técnica lidar para la caracterización atmosférica mediante dispersión elástica y Raman.

Guerrero-Rascado, J. L., F. J. Olmo, I. Aviles-Rodriguez, F. Navas-Guzman, D. Perez-Ramirez, H. Lyamani, and L. A. Arboledas (2009), Extreme Saharan dust event over the southern Iberian Peninsula in september 2007: active and passive remote sensing from surface and satellite, *Atmospheric Chemistry and Physics*, *9*(21), 8453-8469.

Guerrero Rascado, J. L. (2008), Técnica lidar para la caracterización atmosférica mediante dispersión elástica y Raman, *PhD Dissertation*.

Halldorsson, T., and J. Langerholc (1978), Geometrical form-factors for lidar function, *Applied Optics*, *17*(2), 240-244.

Heese, B., H. Flentje, D. Althausen, A. Ansmann, and S. Frey (2010), Ceilometer lidar comparison: backscatter coefficient retrieval and signal-to-noise ratio determination, *Atmospheric Measurement Techniques*, *3*(6), 1763-1770.

Klett, J. D. (1981), Stable Analytical Inversion Solution for Processing Lidar Returns, *Applied Optics*, *20*(2), 211-220.

Klett, J. D. (1985), Lidar Inversion with Variable Backscatter Extinction Ratios, *Applied Optics*, *24*(11), 1638-1643.

Kuze, H., H. Kinjo, Y. Sakurada, and N. Takeuchi (1998), Field-of-view dependence of lidar signals by use of Newtonian and Cassegrainian telescopes, *Applied Optics*, *37*(15), 3128-3132.

Melfi, S. H., J. D. Lawrence, and M. P. McCormick (1969), Observation of Raman scattering by water vapor in the atmosphere, *Applied Physics Letter*, *15*, 295-297.

Navas-Guzmán, F., J. L. Guerrero-Rascado, J. A. Bravo-Aranda, and L. Alados Arboledas (2011a), On the use cirrus clouds for ground-based elastic lidar calibration, *Óptica Pura y Aplicada*, *44 (1)*, 49-53.

Navas-Guzmán, F., J. L. Guerrero-Rascado, J. A. Bravo-Aranda, and L. Alados-Arboledas (2011b), Calibration of 1064 nm-backscatter profiles with a multiwavelength Raman lidar, *Romanian Journal of Physics*, *56*(3-4), 460-466.

Pappalardo, G., et al. (2004), Aerosol lidar intercomparison in the framework of the EARLINET project. 3. Raman lidar algorithm for aerosol extinction, backscatter, and lidar ratio, *Applied Optics*, *43*(28), 5370-5385.

Reagan, J. A., X. Wang, and M. T. Osborn (2002), Spaceborne lidar calibration from cirrus and molecular backscatter returns, *Ieee Transactions on Geoscience and Remote Sensing*, *40*(10), 2285-2290.

Sasano, Y., and H. Nakane (1984), Significance of the extinction backscatter ratio and the boundary-value term in the solution for the 2-component lidar equation, *Applied Optics*, *23*(1), 11-13.

Sasano, Y., H. Shimizu, N. Takeuchi, and M. Okuda (1979), Geometrical form factor in the laser radar equation: experimental determination, *Applied Optics*, *18*(23), 3908-3910.

Sassen, K., and G. C. Dodd (1982), Lidar crossover function and misalignment effects, *Applied Optics*, *21*(17), 3162-3165.

Sicard, M., et al. (2011), SPALINET: The Spanish and Portuguese aerosol lidar network, *Óptica Pura y Aplicada, 44 (1)*, 1-5.

Sicard, M., et al. (2009), Aerosol Lidar Intercomparison in the Framework of SPALINET-The Spanish Lidar Network: Methodology and Results, *Ieee Transactions on Geoscience and Remote Sensing*, *47*(10), 3547-3559.

Stelmaszczyk, K., M. Dell'Aglio, S. Chudzynski, T. Stacewicz, and L. Woste (2005), Analytical function for lidar geometrical compression form-factor calculations, *Applied Optics*, *44*(7), 1323-1331.

Tomine, K., C. Hirayama, K. Michimoto, and N. Takeuchi (1989), Experimental determination of the crossover function in the laser radar equation for days with a light mist, *Applied Optics*, *28*(12), 2194-2195.

Velotta, R., B. Bartoli, R. Capobianco, L. Fiorani, and N. Spinelli (1998), Analysis of the receiver response in lidar measurements, *Applied Optics*, *37*(30), 6999-7007.

Wandinger, U., and A. Ansmann (2002), Experimental determination of the lidar overlap profile with Raman lidar, *Applied Optics*, *41*(3), 511-514.

Wandinger, U., et al. (2002), Optical and microphysical characterization of biomass-burning and industrial-pollution aerosols from multiwavelength lidar and aircraft measurements, *Journal of Geophysical Research-Atmospheres*, *107*(D21).

Whiteman, D. N., S. H. Melfi, and R. A. Ferrare (1992), Raman lidar systems for the measurement of water vapor and aerosols in the Earth's atmosphere, *Applied Optics*, *31*(16), 3068-3082.

Chapter 5

Automatic determination of the Planetary Boundary Layer height using lidar: one-year analysis over South Spain

In this chapter an algorithm based on the wavelet covariance transform (WCT) method applied to lidar data is tested as an automated and non-supervised method to obtain the PBL height. The PBL height is a key variable in atmospheric studies and has an enormous influence on air pollution. The parcel and the Richardson number methods applied to radiosonde data and the parcel method applied to microwave radiometer temperature profiles are used as independent methods to determine the PBL height in order to optimize the algorithm based on the WCT method under different atmospheric conditions. The optimized algorithm has been used to develop a one-year statistical analysis of the Convective Boundary Layer over Granada obtained from lidar data registered in the middle of the day.

5.1. Introduction

The planetary boundary layer (PBL) is the part of the troposphere directly influenced by the Earth's surface and it responds to surface forcings with a time scale of about an hour or less [*Stull*, 1988]. The height of this layer is a fundamental quantity for the description of vertical mixing processes in the lower part of the troposphere and it exerts a strong influence in the environmental state at the surface. The PBL height is highly variable in time and space, ranging from a few hundred meters to several kilometers with diurnal and seasonal cycles. The PBL height and these cycles are key parameters controlling air pollution because they determine the available volume for pollutants dispersion [*Seibert et al.*, 2000] and are crucial for air quality studies, since particles and gases have a different behavior in different atmospheric layers, with longer life time and transport range in the free troposphere (FT) compared to pollutants in the PBL.

Because of its importance in weather forecasting and environmental monitoring, statistical studies of the PBL height provide valuable information. However, most studies have usually focused on local scale and/or short term [*Sicard et al.*, 2006; *Pal et al.*, 2010] primarily due to the complexity of the methodology involved to determine the PBL height. Different methodologies allow estimates of the PBL height depending on the instrumentation and the tracers used. Commonly used methods include the Richardson number method [*Vogelezang and Holstlag*, 1996; *Menut et al.*, 1999] based on radiosounding wind and temperature profile data, the parcel method [*Holzworth*, 1964] using radiosounding temperature profile data, and the derivative and non-derivative methods used for lidar with atmospheric aerosol particles as a tracer [*Baars et al.*, 2008].

Improvements in PBL height determinations include the use of automatic algorithms. Algorithms based on the wavelet covariance transform (WCT) method applied to lidar observations using atmospheric aerosol particles as a tracer represent a promising tool for automatic PBL height detection [*Morille et al.*, 2007; *Baars et al.*, 2008; *Pal et al.*, 2010]. In fact, this methodology has already been used with ceilometers [*Haeffelin et al.*, 2012]. Moreover, automatic PBL height determinations with algorithms based on WCT method will allow for global-scale monitoring of the PBL height from lidar networks such as EARLINET [*Bösenberg et al.*, 2001],

98

MPLNET (Micro-Pulsed Lidar NETwork) [*Welton et al.*, 2001] and ADNET (Asian Dust NETwork) [*Murayama et al.*, 2001].

The aim of this chapter is to step forward on an automatic algorithm for determining the PBL height from lidar measurements based on the WCT method. The algorithm based on the WCT method is optimized using independent PBL height estimates from the parcel and the Richardson number method with radiosounding data as well as the parcel method with atmospheric temperature profiles measured by a co-located passive microwave radiometer. The optimized WCT-based method is used to compute the PBL height from lidar data at midday over the city of Granada during an entire year and the relationship of this height with surface variables is analyzed.

5.2. Methods

There are several methods to determine the PBL height using a lidar system and they are based on the assumption that aerosol particles are much more abundant within the PBL than in the FT. Therefore it is necessary to find the height where aerosol concentration abruptly decreases.

There are mainly two methodologies for lidar system to identify the transition zone where aerosol concentration abruptly decreases and they are known as derivative and non-derivative methods. The variance method [*Hooper and Eloranta*, 1985] is an example of a non-derivative method. On the other hand, derivative methods are widely extended and accepted [*Sicard et al.*, 2006]; some examples are the gradient method and the inflexion point method [*Flamant et al.*, 1997; *Hayden et al.*, 1997; *Menut et al.*, 1999], the fitting method [*Steyn et al.*, 1999] and methods based on WCT [*Cohn and Angevine*, 2000; *Brooks*, 2003; *Baars et al.*, 2008]. WCT-based method is suitable under many meteorological situations and valid for all seasons. Moreover it has the advantage of being less affected by noise than any other method [*Baars et al.*, 2008]. Additionally, it can be easily automated for continuous PBL height detection from lidar data.

The WCT, $W_f(a, b,)$ is defined as:

$$W_f(a,b) = \frac{1}{a}\int_{z_b}^{z_t} RCS(z)\ h\left(\frac{z-b}{a}\right)\ dz \qquad (5.1)$$

where z_b and z_t are the upper and lower limits of the backscattered signal and h is the Haar function (Figure 5.1),

$$h\left(\frac{z-b}{a}\right) = \begin{cases} +1, & b - \dfrac{a}{2} \leq z \leq b \\ -1, & b \leq z \leq b + \dfrac{a}{2} \\ 0, & elsewhere \end{cases} \tag{5.2}$$

a is a parameter called dilation related to the extent of the step function and b is the translation, which indicates the location of the step. Due to the overlap of the lidar system, z_b is limited by the overlap height and therefore the methodology to compute PBL height fails to determine PBL below the overlap height. To overcome this problem an overlap correction can be applied by using the overlap function of the system. Finally, for computing $W_f(a,b)$, the *RCS* is normalized by the maximum value below 1000 m, usually its maximum value within the PBL.

The WCT measures the similarity between the normalized *RCS* and h, presenting its maximum when b coincides with the height at which an abrupt change in *RCS* occurs. Therefore, the PBL height is estimated by the value of b corresponding to the first maximum of the W_f vertical profile above the surface. The uncertainty in the PBL height is of the order of $a/2$, as obtained by a sensitivity analysis.
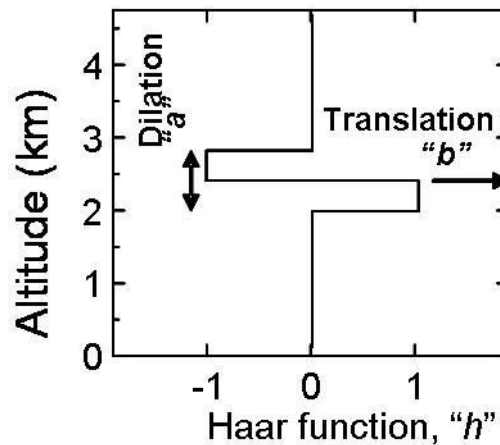

Figure 5.1. Haar function.

The most extended method to determine the PBL height from radiosounding data is based on the Richardson number, but it can only be used under convective conditions. The Richardson number, R_{ib}, is defined as [*Stull*, 1988]:

100

$$R_{ib}(z) = \frac{g(z - z_0)[\theta(z) - \theta(z_0)]}{\theta(z)[u(z)^2 + v(z)^2]} \qquad (5.3)$$

being g the gravity acceleration, z_0 the altitude of measurement location above sea level, θ the potential temperature and $u(z)$ and $v(z)$ the wind zonal and meridional components. The PBL height is obtained as the height where the Richardson number equals the critical Richardson number, 0.21 [*Vogelezang and Holstlag*, 1996; *Menut et al.*, 1999]. At heights where R_{ib} is higher than the critical value the atmosphere is considered to be free of turbulences (FT).

The parcel or Holzworth method [*Holzworth*, 1964] is also widely used for PBL height detection using radiosounding data, with the advantage of no need for wind profile. The PBL height is determined from the intersection between the dry adiabatic starting at the surface temperature and the temperature profile [*Holzworth*, 1964; *Seibert et al.*, 2000]. This height represents the equilibrium level of a hypothetical rising parcel of air representing a thermal. The methodology strongly depends on the surface temperature and a high uncertainty in the estimated height may result in situations without a pronounced inversion at the convective PBL top. Because only temperature profiles are needed to compute the PBL height, this methodology was used for both radiosounding and microwave radiometer profiles.

5.3. Optimization of the WCT-based algorithm for PBL height detection

Lidar system characteristics together with atmospheric conditions may limit the PBL height detection from lidar measurements. Therefore it is important to identify when the detection is possible and then optimize the methodology. For the WCT method, selecting an appropriate dilation parameter, a, is critical; small values result in a noisy WCT profile while large values may overlook some structures. The optimum value would be equal to the depth of the transition zone between the PBL and the FT [*Brooks*, 2003] but this is usually unknown. Baar*s et al.* [2008] proposed to distinguish among strong and weak gradients introducing a threshold value for the WCT profile. Then the PBL height is determined from the lowest height above ground with a local maximum on the WCT profile exceeding this threshold. Dilation values between 200 and 450 m provide good results depending on the lidar vertical resolution [*Baars et al.*,

2008; *Pal et al.*, 2010]. The threshold value for the WCT profile varies with dilation but values between 0.04 and 0.08 are usually satisfactory [*Baars et al.*, 2008].

Based on this range of values, some tests have been carried out in our station in order to establish an optimum fixed pair of values of the dilation a and the WCT-threshold for the automatic detection of the PBL height. To get the optimum combination of these values, lidar derived PBL height results obtained from the WCT applying different dilations and different threshold values were compared with the results obtained from the parcel and the Richardson number methods applied to radiosounding data. The radiosounding data were obtained using a GRAW DFM-06 radiosonde (GRAW Radiosondes, Germany), which is a light-weight weather radiosonde that provides temperature (resolution 0.01 ºC, accuracy 0.2 ºC), pressure (resolution 0.1 hPa, accuracy 0.5 hPa), relative humidity (resolution 1%, accuracy 2%) and wind (accuracy 0.2 m/s). Data acquisition and processing were performed by the Grawmet5 software and a GS-E ground station from the same manufacturer.

From this comparison, we concluded that the automatic detection of the PBL height gets particularly complex in the presence of stratification within the PBL, lofted aerosol layers coupled with the PBL and aerosol vertical gradients larger than the one at the limit with the FT. Under these circumstances the adjustment of the dilation and the WCT-profile threshold becomes critical and not always satisfactory for PBL height detection. A couple of examples are shown in Figure 5.2. Time series of the *RCS* as well as the normalized *RCS* (arbitrary units) at 532 nm on 25th July 2001 from 11:00 to 11:30 UTC are shown in Figure 5.2a including the WCT profile for $a = 300$ m. As it can be observed, several maxima appear in the WCT profile due to stratification within the PBL and a decoupled aerosol layer at 4 km (asl). In this case, it is not easy to determine which one corresponds to the actual PBL height. Independent measurements using radiosounding data with the parcel and the Richardson number methods set the PBL top at 3.1 and 3.2 km a.s.l., respectively. The right combination of dilation and WCT-profile threshold can provide the PBL height with differences of around 100 m compared to the radiosounding (Figure 5.3). Several combinations provided satisfactory results. Nevertheless lower dilations are recommended to improve vertical resolution. Particularly on this date, $a = 225$ m with a 0.04 threshold value and $a = 300$ m and 0.05 threshold were the lower dilations that fulfilled the criteria, providing a PBL height of 3.1 km (asl). On the other hand, an example of those cases when is not possible to

obtain satisfactory results is shown in Figure 5.2b. It corresponds to 25th November 2011 from 12:10 to 12:40 UTC. The PBL height using lidar data is set at 1.2 km (asl) for the whole range of values recommended for *a* and WCT-profile threshold; while 1.6 km (asl) is obtained using the parcel and the Richardson number method using radiosounding data. Therefore, additional information is needed in this case.
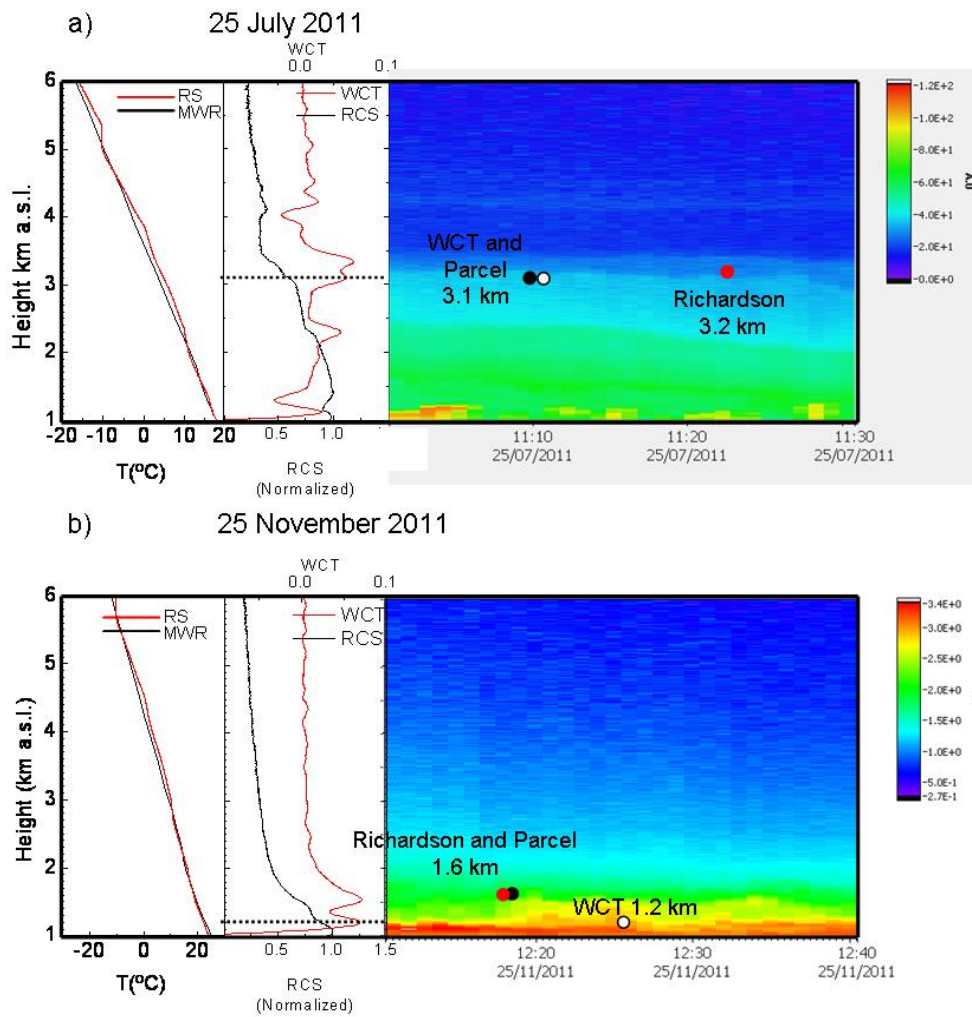

Figure 5.2. a) From left to right, temperature vertical profiles obtained by the radiosounding and the microwave radiometer; WCT and normalized RCS at 532 nm vertical profiles; and time series of the RCS (arbitrary units) for 25th July 2011 between 11:00 and 11:30 UTC. The dot line indicates the maximum of the WCT corresponding to the PBL height. Dots represent the PBL height obtained by the parcel, the Richardson number and the WCT method in black, red and white respectively. b) The same but for 25th November 2011 between 12:10 and 12:40 UTC.

The complete comparison and optimization study was performed with eight radiosounding launched at midday over Granada in spring and autumn 2011. From this comparison *a* = 300 m and 0.05 WCT-profile threshold were chosen as optimum values

for PBL height detection. The agreement between the parcel and the Richardson method from radiosounding profiles where within ±100 m. Comparison of PBL heights using the optimized WCT method and the Richardson method is shown in Figure 5.3.
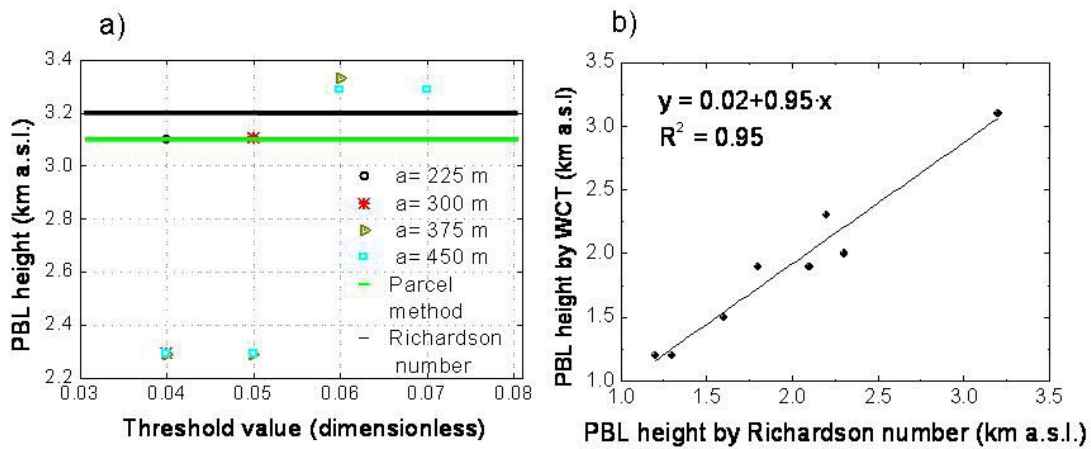

Figure 5.3. a) PBL heights obtained from the WCT method using different dilations and threshold values, from the parcel method (green line) and the Richardson number method (black line) for 25th July 2011. b) Scatter plot of the PBL heights obtained from the Richardson number method applied to radiosounding data and the WCT method applied to lidar data using a dilation of 300 m and 0.05 threshold value for the eight radiosoundings launched over Granada around midday.

To extend the optimization of *a* and WCT-profile threshold, a 3-month period (March-May 2011 from 12:00 to 12:30 UTC) using lidar and temperature profiles from microwave radiometer (described in section 3.2.3) have been used for PBL height detection using the WCT and the parcel method, respectively. The time frame was chosen in order to have high convective activity and a well-mixed PBL. The mean and standard deviation of the PBL height obtained for the microwave radiometer data applying the parcel method was 2.2 ± 0.4 km (asl). In agreement with the results obtained during the comparison of radiosounding and lidar derived PBL heights, the combination of $a = 300$ m and 0.05 WCT-profile threshold provides the best matching between both methods. With these values the automatic PBL height methodology provides a mean PBL height at 2.1 ± 0.7 km (asl) during the same period. Differences in PBL height between the parcel and the WCT methods had a mean value of 0.1 ± 0.6 km. After correcting the results when multilayering within the PBL was detected according to the parcel method applied to the passive microwave radiometer, the mean PBL height was 2.1 ± 0.6 km (asl) and the mean difference 0.1 ± 0.4 km. As obtained from radiosoundings, $a = 225$ m and 0.04 WCT-profile threshold provides good results in most cases. For the lidar data, the mean value obtained with this combination was

equal to 2.0 ± 0.7 km (asl) and the mean value for the differences was 0.2 ± 0.7 km. After correcting the erroneous PBL heights because of multilayering, the mean value was 2.0 ± 0.6 km (asl) and the mean difference 0.2 ± 0.5 km. Statistical results of the comparison analysis are shown in Figure 5.4. Mean values of both combinations are very similar. Nevertheless, the standard deviation is lower when using a = 300 m. An ANOVA (Analysis Of Variance) test applied to the data indicates that the mean differences are not significant at the 99 % level for any of the combinations. However, the variations are significantly different and more significant for a = 225 m and 0.04 WCT-profile threshold.
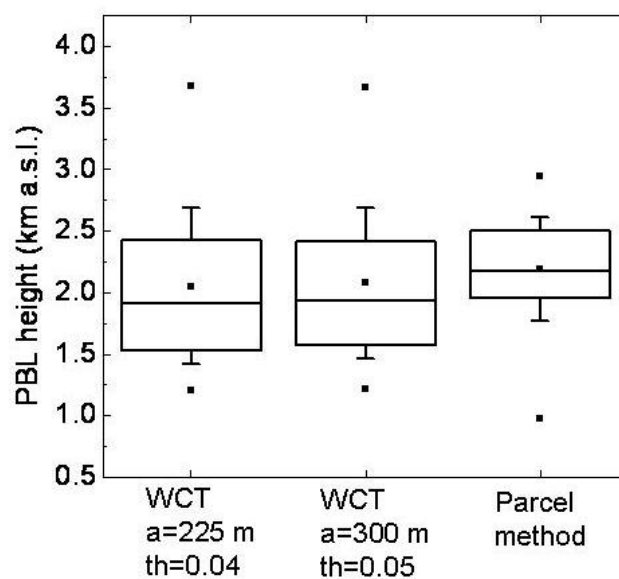

Figure 5.4. Box plot of the PBL heights obtained with different combinations of the dilation and the threshold value and the parcel method. In each box central line indicates the median and the extent of boxes, 25 and 75 percentiles; whiskers represent the standard deviation. The central point is the mean value and the external points are the maximum and minimum.

Therefore, from the comparison of the lidar with the microwave radiometer data, the best combination for the lidar system is again a = 300 m and 0.05 WCT-profile threshold. However, a = 225 m and 0.04 WCT-profile threshold also provide very good results. The pair of values a = 300 m and 0.05 WCT-profile threshold are used from now on in the analysis. Independently of a and the WCT-profile threshold, the PBL height is sometime not detected because the WCT profile does not reach the threshold value at any altitude (5% of the cases). In this study, over 50% of the times it was possible to retrieve a feasible PBL height reducing the threshold value by iterating in steps of 0.005.

From the three-month comparison between the lidar and the microwave radiometer three scenarios are clearly identified depending on the atmospheric conditions and the presence of lofted aerosol layers above the PBL (Fig. 5.5). The reliability of the WCT method from lidar measurements depends on these scenarios. The first scenario corresponds to atmospheric aerosol from local sources and a well-mixed PBL without stratification. This situation was not very often during spring 2011, only occurring 20% of the dates during the monitoring period but quite often in autumn and winter. With a = 300 m and 0.05 WCT-profile threshold, PBL heights from lidar were in agreement (difference lower than 250 m) with the obtained from the parcel method using the temperature profiles from the microwave radiometer. Figure 5.5a shows an example of this scenario on 18th March 2011, where the PBL heights from both methods differ less than 100 m. The WCT profile shows a single maximum at 2.3 km (asl) clearly identifying the PBL height.
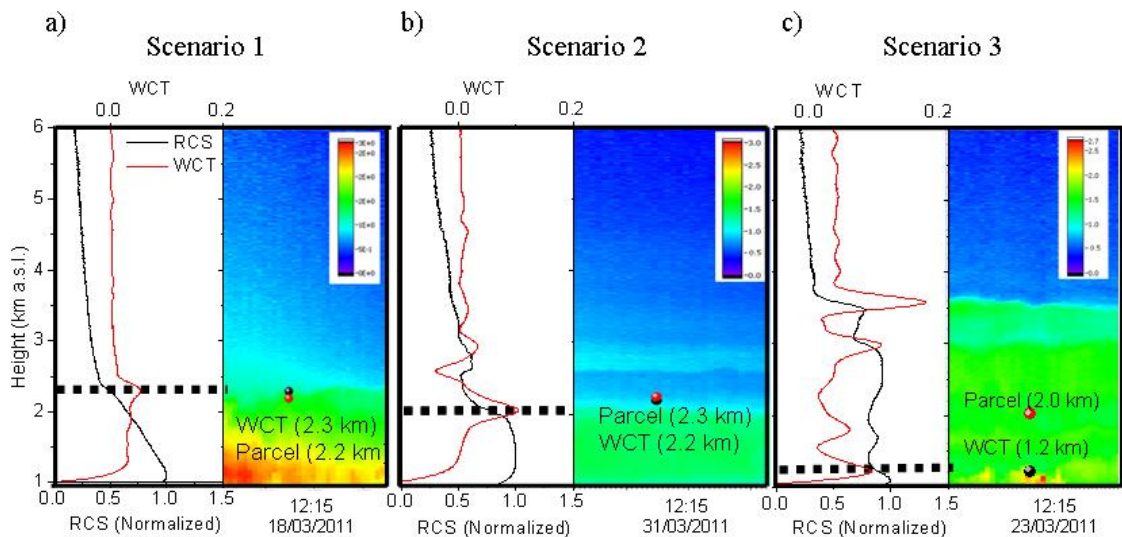

Figure 5.5. a) WCT and normalized RCS (arbitrary units) profiles for 18th March 2011 between 12:00 and 12:30 UTC. The PBL height is indicated by the dot line. Time series of the RCS (arbitrary units) on 18th March between 12:00 and 13:00 UTC. The red and black dots represent the PBL height obtained from the parcel method and the WCT method respectively. b) The same but for 31st March between 12:00 and 12:30 UTC. c) The same but for 23rd March 2011 between 12:00 and 12:30 UTC.

The second scenario corresponds to situations of aerosol from a non-local source clearly decoupled from the PBL with an underlying well-mixed PBL. This situation occurred 12% of the dates during the monitoring period. The advection of non-local aerosol particles, especially African dust intrusions, is quite frequent over the site

mainly in spring and summer [*Lyamani et al.*, 2005; *Lyamani et al.*, 2006; *Guerrero-Rascado et al.*, 2009]. When the dust layers are clearly decoupled from the PBL this scenario is similar to the previous one, with satisfactory agreement between methods. Differences in PBL height between 25 m and 235 m were found using $a = 300$ m and a 0.05 WCT-profile threshold. The additional maximum in WCT profile at a higher altitude corresponds to the location of a second aerosol layer over the PBL (Figure 5.5b).

The third and most complex scenario occurs when the PBL presents stratification, as in Figure 5.5c. The WCT method is able to distinguish between the different layers, but it is not feasible to unambiguously identify the PBL height. This situation was quite common during spring 2011, occurring 68% of the dates during the monitoring period. After mixing, when the stratification disappears, the WCT method is able to determine the top of the aerosol layer but it is not always coincident with the top of the PBL if aerosol layers coupled to the PBL exist. This has been already reported by other authors [*Wiegner et al.*, 2006; *Pal et al.*, 2010]. Under these situations, the criteria for the WCT method are not always obvious and objective. A determination of layers is feasible with $a = 300$ m, but in many situations additional information about the daily evolution of the PBL height is needed in order to set the appropriate WCT-profile threshold. Angelini *et al.* [2009] proposed an algorithm that calculates the PBL height in several intervals during a given time frame and takes into account the differences between the obtained values. A similar procedure applied automatically here could improve the results in the presence of stratification. An alternative proposed by Morille *et al.* [2007] uses the maximum found in the WCT profile at different dilations. Moreover, the presence of lofted layers of mineral dust particles also affects the parcel method as the atmospheric temperature profile changes, with lower temperatures near the surface [*Guerrero-Rascado et al.*, 2009; *Santese et al.*, 2010; *Wang et al.*, 2010] leading to an underestimate of the PBL height. Therefore, since the PBL top is not always clearly identified, there is a lack of agreement between both methods and the determination of the PBL height becomes less straightforward.

5.4. One-year statistical analysis of the PBL height over Granada

The WCT-based algorithm was used for PBL height detection using lidar measurements at midday from August 2007 to July 2008. From the total number of measurements (220 days) within this period, an automated PBL height detection using the optimized WCT-based algorithm (a = 300 m and 0.05 WCT-profile threshold) was successful for 178 days (81%). Conversely, the automated procedure fails in 42 days (19%). In 75% of these cases the decrease of the signal was not strong enough to fulfill the requirement of having a maximum in the WCT profile for the established threshold value, preventing the detection of PBL height. Under these conditions, a detailed analysis with ancillary data or a readjustment of the threshold value with an iterative procedure, as explained in section 5.2, is required. The additional 25% failures in the automated PBL height detection occurred in presence of a higher aerosol layer coupled with the PBL, retrieving PBL heights anomalously high. In these latter cases, the WCT method resolves the height of the aerosol layer, but it is not always coincident with the PBL height. The same limitation appears with derivative methods [*Mattis et al.*, 2004] and additional information is needed to correctly identify the PBL height.

Figure 5.6 represents the daily PBL height at midday automatically determined with the WCT-based algorithm for the 178 successful days as well as the mean monthly values at midday from August 2007 to July 2008 over Granada. The mean value for the entire period was 1.7 ± 0.4 km (asl), minimum on 17th January 2008 (1.1 km asl) and maximum on 23rd August (3.1 km asl). Monthly mean values show a PBL height higher in June (2.2 km asl) and lower in January (1.3 km asl).
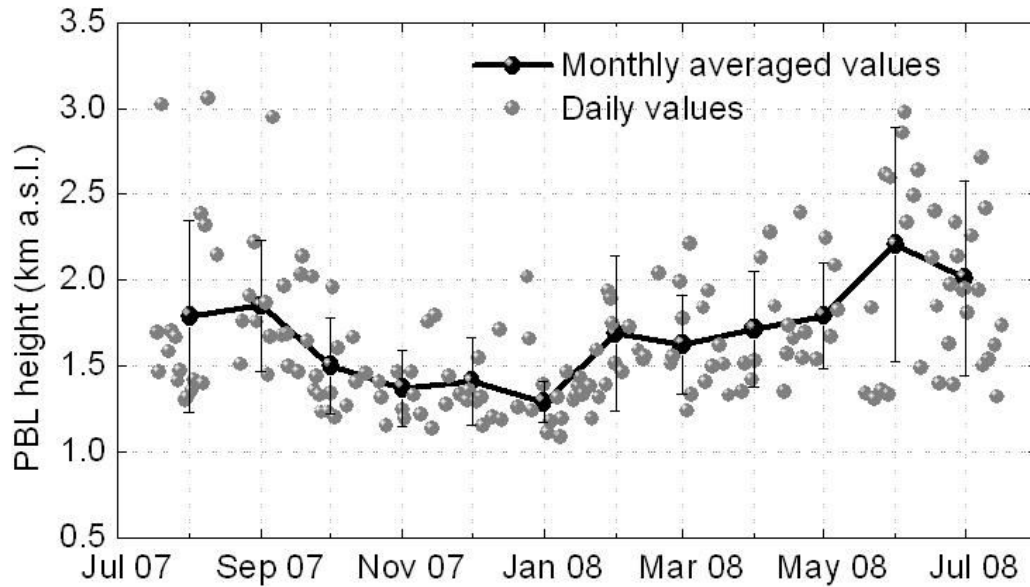
Figure 5.6. Daily PBL heights and mean monthly values at midday from August 2007 and July 2008 at Granada. Error bars indicate ± standard deviation.

The seasonal analysis of the PBL height (Figure 5.7) revealed higher PBL during summer (June-July-August), with larger variability compare to the other seasons. Values ranged from 1.30 to 3.06 km (asl) with a mean value of 2.0 ± 0.6 km (asl). Higher PBL heights in summer are mainly related to the occurrence of thermal lows over the Iberian Peninsula that favors a vigorous growth of the PBL. The higher variability of the PBL height during summer was a result of alternating synoptic conditions during this season. Thus the thermal lows favor deeper PBL than the high pressure systems. Conversely, winter (December-January-February) showed lower PBL heights, with heights from 1.1 to 2.0 km (asl) and a mean value of 1.44 ± 0.24 km (asl). Variability was lower than in summer. Spring (March-April-May) and autumn (September-October-November) were very similar, with mean values of 1.7 ± 0.3 and 1.6 ± 0.4 km (asl), respectively. More than 90% of the values vary from 1.1 to 2.5 km (asl) during both seasons. The seasonal cycle obtained is in agreement with data from central Europe with maximum values in summer and minimum values in winter [*Mattis et al.*, 2004]. Baars *et al.*, [2008] obtained mean values of 1.8 km (asl) in summer and 0.8 km (asl) in winters for a one-year study also over Leipzig (Germany). In Hamburg, about 300 km north of Leipzig and closer to the North Sea, values were 1.8 km (asl) for summer and 1.1 km (asl) for winter [*Matthias and Bosenberg*, 2002]. It is important to note that Granada is at 680 m (asl) while Leipzig and Hamburg are below 100 m (asl),

therefore the PBL depth is larger in these German cities compared to Granada. Meteorological conditions, especially wind regime and humidity, together with orography may also be related with these differences.
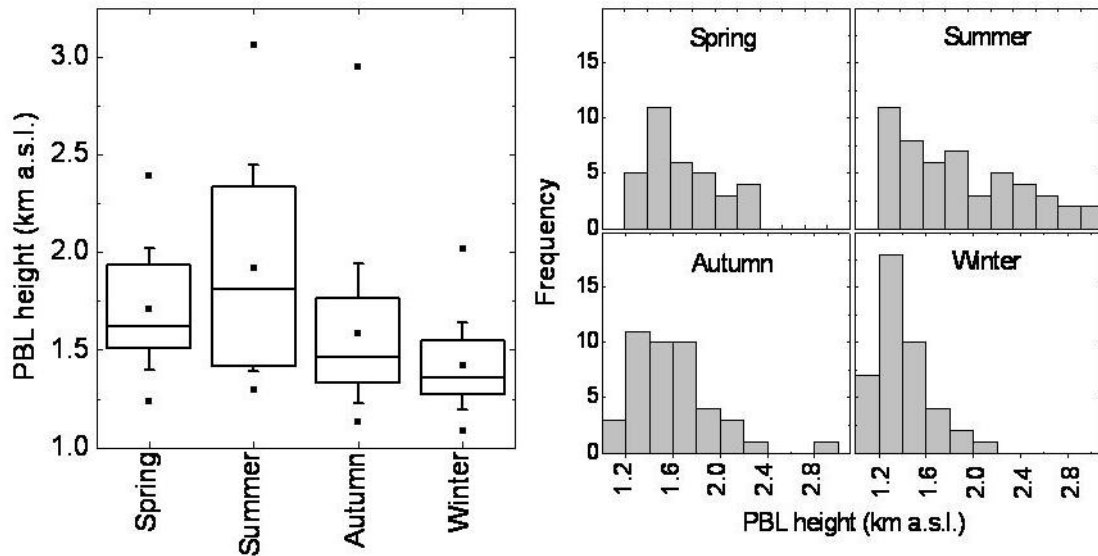

Figure 5.7. a) Box plot of the seasonal variation in the PBL height at Granada for the study period. In each box central line indicates the median and the extent of boxes, 25 and 75 percentiles; whiskers represent the standard deviation. The central point is the mean value and the external points are the maximum and minimum. The horizontal dotted line represents the annual mean. b) Frequency histogram of the PBL height for every season.

5.5. The PBL height and its relation with surface variables

The seasonal cycle of the PBL height is highly related to the seasonal variation of some atmospheric variables at the surface (Figure 5.8). Simultaneous measurements of global radiation obtained with a pyranometer (CM11 pyranometer, Kipp&Zonnen) at midday received at the surface were compared with PBL heights from August 2007 to July 2008 in Figure 5.8a. Global radiation and PBL height show a similar seasonal pattern with higher values in summer and lower in winter; the correlation coefficient was 0.91 during the study period. Radiation received at the surface exerts a strong influence in the growth of the PBL height, since higher values of global radiation favor the convective activity near the surface allowing the PBL to reach higher altitudes. This dependence was also observed by Mattis *et al.* [2004] over Central Europe.

Temperature and barometric pressure at ground level was also monitored during the analyzed period. Temperature was obtained at one-minute time resolution with an

accuracy of 0.6 ºC and 0.01 ºC precision (HMP60, Vaisala) while barometric pressure (PTB101B, Campbell scientific) was also obtained with accuracy between 0.5 and 6 hPa, depending on temperature, and precision of 0.01 hPa.

Surface temperature is also related to global radiation and therefore to PBL height. The correlation coefficient between temperature and global radiation at the surface during the study period was 0.85 while the correlation coefficient between surface temperature and PBL height was 0.79. The seasonal pattern of monthly mean surface temperature and PBL height over Granada at midday during the study period is shown in Figure 5.8b, with maximum values reached in summer and minimum in winter.
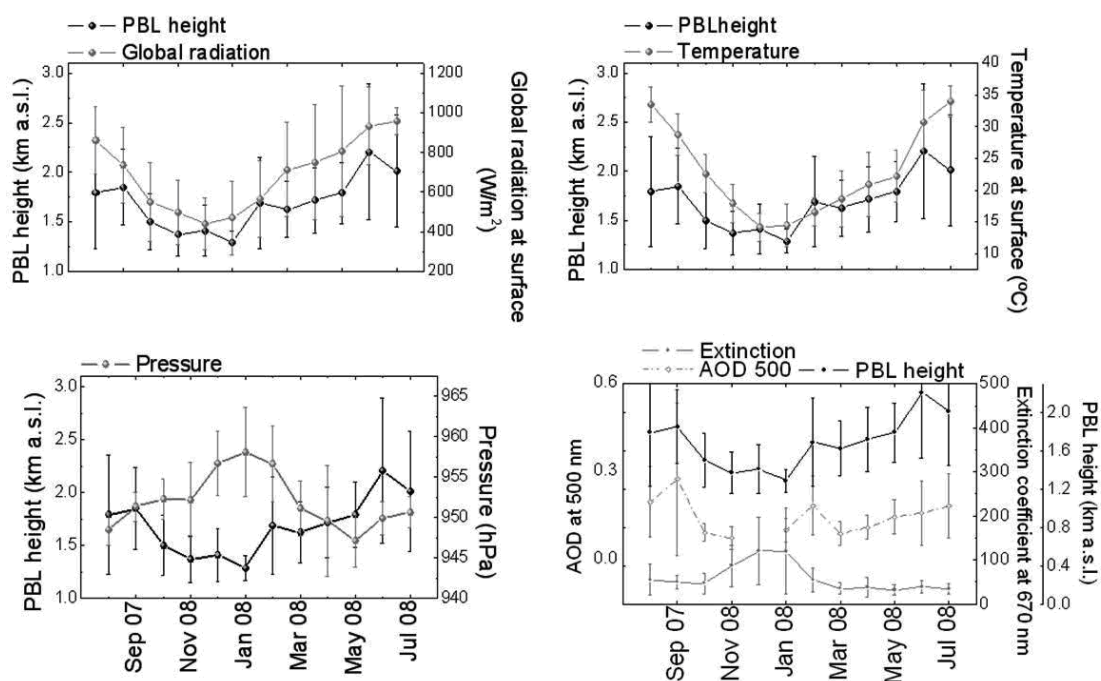

Figure 5.8. a) Monthly mean PBL height (black line) and global radiation at the surface (grey line) at midday from August 2007 to June 2008 at Granada. Error bars indicate ± standard deviation. b) Monthly mean PBL height (black line) and surface temperature (grey line) at midday from August 2007 to June 2008 at Granada. Error bars indicate ± standard deviation. c) Monthly mean PBL height (black line) and surface pressure (grey line) at midday from August 2007 to June 2008 at Granada. Error bars indicate ± standard deviation. d) Monthly mean PBL height (light grey line), aerosol optical depth (AOD) at 550 nm (black line) and surface extinction coefficient (dark grey line) at midday from August 2007 to June 2008 at Granada.

Surface pressure, on the other hand, is in opposite phase with the PBL height. The PBL is higher under low pressure and it reaches lower altitudes with high pressure systems [*Stull*, 1988]. Figure 5.8c illustrates mean monthly values at midday together

with PBL height at Granada during the study period. The correlation coefficient between both variables was -0.57 during the study period.

The relationship of the PBL height with some aerosol optical properties was also analyzed. In previous works a dependence of the seasonal cycle of the extinction coefficient and the PBL height has already been pointed out [*Lyamani et al.*, 2010; *Pereira et al.*, 2011]. Atmospheric extinction coefficient at 637 nm during the monitoring period was computed from aerosol scattering and absorption coefficients.

Aerosol scattering coefficient (σ_{sca}) was measured with an integrating nephelometer (TSI, model 3563) at three wavelengths 450, 550 and 700 nm. This instrument draws the ambient air through at a flow rate of 30 l min^{-1}, illuminates the sample with a halogen lamp and measures scattered light at 450, 550 and 700 nm. Calibration of the nephelometer was carried out every three months using CO_2 and filtered air. In this study, non-idealities due to truncation errors were corrected [*Anderson and Ogren*, 1998].

The aerosol light-absorption coefficient (σ_{abs}) was measured with a MultiAngle Absorption Photometer (MAAP) at 637 nm [*Müller et al.*, 2011]. A detailed description of the method is provided by Petzold and Schönlinner [2004]. The MAAP draws the ambient air at constant flow rate of 16.7 l min^{-1} and provides 1 min values. No corrections were applied to the data.

Moreover, AOD at 500 nm was obtained from sun-photometer measurements (AERONET level 2 data). The extinction coefficient at 637 nm presented an annual cycle opposite to the PBL height (Figure 5.8d), with a correlation coefficient equal to -0.73 during the study period. In fact, during winter the PBL is lower and therefore the available volume for the vertical dispersion of atmospheric particles is smaller. Moreover, the vertical mixing is less efficient, reinforcing the presence of aerosol near the surface in spite of the lower aerosol load in the atmospheric column (lower AOD at 500 nm). In summer, the PBL can reach higher altitudes, allowing additional volume for the dispersion of particles and the vertical mixing of atmospheric aerosol within the PBL. The presence of aerosol near the surface is therefore reduced although the aerosol load in the entire atmospheric column is higher than in winter.

5.6. Conclusions

The present study illustrates the capabilities of an algorithm based on the WCT for automated PBL height detection using lidar measurements. The WCT-based algorithm was optimized by independent measurements using the parcel and the Richardson methods for radiosoundings and the parcel method for simultaneous temperature profiles measured during three months with a ground-based passive microwave radiometer. The analysis of the optimization period showed three types of scenarios: a clean atmosphere over the PBL with the absence of aerosol layers in the FT, aerosol layers in the FT decoupled from the PBL and stratification due to aerosol layers coupled with the PBL or incomplete mixing. For the first two type of scenarios the automated PBL height detection using the WCT method is straightforward and satisfactory with optimal results obtained for a = 300 m and a 0.05 WCT-profile threshold. There was a good agreement between the three methodologies, considering that they are based on different tracers and techniques, with differences below 250 m in the PBL height detection. In the case of multilayering within the PBL, the WCT methodology is likely to fail for detecting the PBL height, requiring therefore additional information and processing for its determination. Methodologies for estimating BPL height under these scenarios include the use of a time frame around the studied interval taking into account the continuity of the PBL height during daytime, as well as an iterative procedure for reducing the WCT-profile threshold when no maximum is found.

The automated PBL height detection using lidar measurements from August 2007 to July 2008 over Granada provided satisfactory results for 81% of the days. The annual mean PBL height was 1.7 ± 0.5 km (asl), with seasonal changes showing higher values in summer (with larger variability) and lower in winter. During spring and autumn mean values are similar with slightly larger variability in autumn.

The correlation of the PBL height with both global radiation and temperature at the surface during the study period confirms the dependence of the PBL height with these surface variables. Surface pressure and aerosol extinction coefficient at 637 nm showed an opposite trend with the PBL height. The lower PBL height in winter reduces the available volume for vertical dispersion, increasing the extinction coefficient at the surface.

5.7. References

Anderson, T. L., and J. A. Ogren (1998), Determining aerosol radiative properties using the TSI 3563 integrating nephelometer, *Aerosol Science and Technology*, *29*(1), 57-69.

Angelini, F., F. Barnaba, T. C. Landi, L. Caporaso, and G. P. Gobbi (2009), Study of atmospheric aerosols and mixing layer by lidar, *Radiation Protection Dosimetry*, *137*(3-4), 275-279.

Baars, H., A. Ansmann, R. Engelmann, and D. Althausen (2008), Continuous monitoring of the boundary-layer top with lidar, *Atmospheric Chemistry and Physics*, *8*(23), 7281-7296.

Bösenberg, J., et al. (2001), EARLINET: a European aerosol research lidar network, laser remote sensing of the atmosphere, Selected Papers of the 20th International Laser Radar Conference, Dabas, A., C. Loth, and J. Pelon, (Eds.), Edition Ecole Polytechnique, Palaiseau, France, pp. 155–158.

Brooks, I. M. (2003), Finding boundary layer top: Application of a wavelet covariance transform to lidar backscatter profiles, *Journal of Atmospheric and Oceanic Technology*, *20*(8), 1092-1105.

Cohn, S. A., and W. M. Angevine (2000), Boundary layer height and entrainment zone thickness measured by lidars and wind-profiling radars, *Journal of Applied Meteorology*, *39*(8), 1233-1247.

Flamant, C., J. Pelon, P. H. Flamant, and P. Durand (1997), Lidar determination of the entrainment zone thickness at the top of the unstable marine atmospheric boundary layer, *Boundary-Layer Meteorology*, *83*(2), 247-284.

Guerrero-Rascado, J. L., F. J. Olmo, I. Aviles-Rodriguez, F. Navas-Guzman, D. Perez-Ramirez, H. Lyamani, and L. A. Arboledas (2009), Extreme Saharan dust event over the southern Iberian Peninsula in september 2007: active and passive remote sensing from surface and satellite, *Atmospheric Chemistry and Physics*, *9*(21), 8453-8469.

Haeffelin, M., et al. (2012), Evaluation of Mixing-Height Retrievals from Automatic Profiling Lidars and Ceilometers in View of Future Integrated Networks in Europe, *Boundary-Layer Meteorology*, *143*(1), 49-75.

Hayden, K. L., K. G. Anlauf, R. M. Hoff, J. W. Strapp, J. W. Bottenheim, H. A. Wiebe, F. A. Froude, J. B. Martin, D. G. Steyn, and I. G. McKendry (1997), The vertical chemical and meteorological structure of the boundary layer in the Lower Fraser Valley during Pacific '93, *Atmospheric Environment*, *31*(14), 2089-2105.

Holzworth, C. G. (1964), Estimates of mean maximum mixing depths in the contiguous United States, *Mon. Weather Rev.*, *92*, 235-242.

Hooper, W. P., and E. W. Eloranta (1985), Lidar measurements of wind in the planetary boundary layer: The method, accuracy, and results from joint measurements with radiosonde and kytoon, *J. Clim. Appl. Meteorol.*, *25*, 990-1000.

Lyamani, H., F. J. Olmo, and L. Alados-Arboledas (2005), Saharan dust outbreak over southeastern Spain as detected by sun photometer, *Atmospheric Environment*, *39*(38), 7276-7284.

Lyamani, H., F. J. Olmo, and L. Alados-Arboledas (2010), Physical and optical properties of aerosols over an urban location in Spain: seasonal and diurnal variability, *Atmospheric Chemistry and Physics*, *10*(1), 239-254.

Lyamani, H., F. J. Olmo, A. Alcantara, and L. Alados-Arboledas (2006), Atmospheric aerosols during the 2003 heat wave in southeastern Spain I: Spectral optical depth, *Atmospheric Environment*, *40*(33), 6453-6464.

Matthias, V., and J. Bosenberg (2002), Aerosol climatology for the planetary boundary layer derived from regular lidar measurements, *Atmospheric Research*, *63*(3-4), 221-245.

Mattis, I., A. Ansmann, D. Muller, U. Wandinger, and D. Althausen (2004), Multiyear aerosol observations with dual-wavelength Raman lidar in the framework of EARLINET, *Journal of Geophysical Research-Atmospheres*, *109*(D13).

Menut, L., C. Flamant, and J. Pelon (1999), Evidence of interaction between synoptic and local scales in the surface layer over the Paris area, *Boundary-Layer Meteorology*, *93*(2), 269-286.

Morille, Y., M. Haeffelin, P. Drobinski, and J. Pelon (2007), STRAT: An automated algorithm to retrieve the vertical structure of the atmosphere from single-channel lidar data, *Journal of Atmospheric and Oceanic Technology*, *24*(5), 761-775.

Müller, T., et al. (2011), Characterization and intercomparison of aerosol absorption photometers: result of two intercomparison workshops, *Atmospheric Measurement Techniques*, *4*(2), 245-268.

Murayama, T., et al. (2001), Ground-based network observation of Asian dust events of April 1998 in east Asia, *Journal of Geophysical Research-Atmospheres*, *106*(D16), 18345-18359.

Pal, S., A. Behrendt, and V. Wulfmeyer (2010), Elastic-backscatter-lidar-based characterization of the convective boundary layer and investigation of related statistics, *Annales Geophysicae*, *28*(3), 825-847.

Pereira, S. N., F. Wagner, and A. M. Silva (2011), Seven years of aerosol scattering properties, near the surface, in the southwestern Iberia Peninsula, *Atmospheric Chemistry and Physics*, *11*, 17-29.

Petzold, A., and M. Schonlinner (2004), Multi-angle absorption photometry - a new method for the measurement of aerosol light absorption and atmospheric black carbon, *J. Aerosol. Sci.*, *35*(4), 421-441.

Santese, M., M. R. Perrone, A. S. Zakey, F. De Tomasi, and F. Giorgi (2010), Modeling of Saharan dust outbreaks over the Mediterranean by RegCM3: case studies, *Atmospheric Chemistry and Physics*, *10*(1), 133-156.

Seibert, P., F. Beyrich, S. E. Gryning, S. Joffre, A. Rasmussen, and P. Tercier (2000), Review and intercomparison of operational methods for the determination of the mixing height, *Atmospheric Environment*, *34*(7), 1001-1027.

Sicard, M., C. Perez, F. Rocadenbosch, J. M. Baldasano, and D. Garcia-Vizcaino (2006), Mixed-layer depth determination in the Barcelona coastal area from regular lidar measurements: Methods, results and limitations, *Boundary-Layer Meteorology*, *119*(1), 135-157.

Steyn, D. G., M. Baldi, and R. M. Hoff (1999), The detection of mixed layer depth and entrainment zone thickness from lidar backscatter profiles, *Journal of Atmospheric and Oceanic Technology*, *16*(7), 953-959.

Stull, R. B. (Ed.) (1988), *An Introduction to Boundary Layer Meteorology*, Dordrecht, Boston, London.

Vogelezang, S. H. P., and A. A. M. Holstlag (1996), Evolution and model impacts of alternative boundary layer formulations, *Boundary-Layer Meteorology*, *81*, 245-269.

Wang, H., X. Zhang, S. Gong, Y. Chen, G. Shi, and W. Li (2010), Radiative feedback of dust aerosols on the East Asian dust storms, *Journal of Geophysical Research-Atmospheres*, *115*.

Welton, E. J., J. R. Campbell, J. D. Spinhirne, and V. S. Scott (2001), Global monitoring of clouds and aerosols using a network of micro-pulse lidar systems. Lidar Remote Sensing for Industry and Environmental Monitoring, paper presented at SPIE.

Wiegner, M., S. Emeis, V. Freudenthaler, B. Heese, W. Junkermann, C. Muenkel, K. Schaefer, M. Seefeldner, and S. Vogt (2006), Mixing layer height over Munich,

Germany: Variability and comparisons of different methodologies, *Journal of Geophysical Research-Atmospheres*, *111*(D13).

Chapter 6

Statistical analysis of aerosol optical properties at Granada (Spain)

In this chapter a statistical study of aerosol optical properties retrieved from Raman lidar in the urban environment of Granada is presented. The measurements were performed during day and night-time in simultaneously with CALIPSO overpasses over our station. Following the EARLINET strategy, regular measurements started in June 2006 and are still ongoing at our station. Here, three years of measurements are presented and analyzed. Mean values and variances of the aerosol extinction and backscatter coefficients in the troposphere have been calculated. Monthly mean AE values have been calculated in the PBL and in the free troposphere (FT) during day and night-time. Moreover, monthly mean LR values at 532 nm have been retrieved from Raman profiles during night-time. These intensive properties have allowed for characterizing the aerosol present in the Granada's atmosphere.

6.1. CALIPSO and measurement strategy

Since mid June 2006, CALIPSO satellite (Cloud-Aerosol Lidar and Infrared Pathfinder Satellite Observations) has provided high vertical resolution profiling of aerosol and clouds on global scale [*Winker et al.*, 2007]. CALIOP, the primary

instrument carried by CALIPSO is the first satellite lidar optimized for aerosol and cloud measurements and is also the first polarization lidar in space. CALIOP is based on a Nd:YAG laser operating at 1064 nm and 532 nm. The outgoing laser beam is linearly polarized and two polarization-sensitive 532 nm channels provide the degree of linear polarization in the return signal. Using the two 532 nm channels and a channel measuring the total 1064 nm return signal, CALIOP offers a detailed insight on the vertical distribution of optical properties for aerosols and clouds. The measurements of sensitive-depolarization signals allow the discrimination between spherical and non-spherical cloud and aerosol particles [*Sassen*, 1991]. The signals at different wavelengths provide qualitative information on particle size and aid in the cloud/aerosol discrimination and the aerosol type identification.

CALIPSO flies as one of 5 satellites in the so-called ''A-train'' constellation of satellites, which provides numerous measurement synergies with the CloudSat cloud profiling radar and the various passive instruments of the A-train, performing cloud and aerosol measurements [*Stephens et al.*, 2002]. All the satellites in the A-train are in a 705 km sun-synchronous polar orbit with an equator-crossing time of about 1:30 PM, local solar time, and a 16-day repeat cycle. The orbit inclination of 98.2º provides global coverage between 82ºN and 82ºS.

Because of its geographical coverage and the deployment of advanced Raman aerosol lidars, EARLINET offers a unique opportunity for the validation and full exploitation of the CALIPSO mission [*Pappalardo et al.*, 2010]. EARLINET provides long-term, quality-assured aerosol data and, because of its geographical distribution over Europe, allows for investigating a large variety of different aerosol situations with respect to layering, aerosol type, mixing state, and properties in the FT and the local PBL. Figure 6.1 shows the geographical distribution of the 27 EARLINET stations.

Figure 6.1. Geographical location of the 27 EARLINET stations

EARLINET started correlative measurements for CALIPSO on 14 June 2006, i.e., at the beginning of the CALIPSO operation. A strategy for correlative measurements has been defined on the basis of the ground track data analysis provided by NASA [*Mattis et al.*, 2008]. While the majority of EARLINET stations contributed on a voluntary basis to this measurement schedule in the first two years of this mission, a funding ESA (European Space Agency) activity has supported correlative EARLINET‐CALIPSO observations at 16 selected EARLINET stations since 1 April 2008 until 1 October 2009. After the completion of this contract, EARLINET members have followed with the same measurement schedule. The EARLINET participating stations perform measurements, as close in time as possible, when CALIPSO overpasses their location within a horizontal radius of 100 km. These measurements are called *case A* measurements and allow a point-to-point comparison between ground-based and satellite-borne lidar measurements. Two types of stations are defined within the frame of the ESA-EARLINET-CALIPSO project: (i) high-performance stations and (ii) contributing stations. High-performance stations are equipped with instruments which measure at least extinction and backscatter coefficients at both 355 and 532 nm (two-wavelength Raman lidars).

The stations are located such that four European core regions are covered (Fig. 6.2): central Europe (Germany and Netherlands), the western Mediterranean (Spain), the central Mediterranean (Italy), and the eastern Mediterranean (Greece). In this way, a broad variety of aerosol types and scenarios can be investigated, which include maritime aerosols (Cabauw), urban aerosols (Leipzig, Napoli), rural aerosols (Maisach,

Potenza), fresh Saharan dust (Mediterranean stations), aged Saharan dust (all stations), fresh forest fire smoke (Mediterranean stations), aged forest fire aerosols (central European stations), photochemical smog (Athens), and long-range transported aerosol in the FT from America and Asia (all stations).
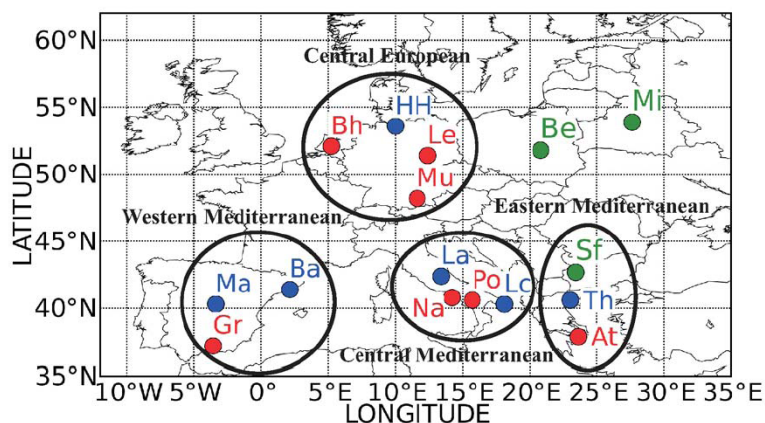

Figure 6.2. Clusters within EARLINET for ESA-CALIPSO strategy. High-performance stations are reported as red dots, green dots represent contributing Raman lidar stations, and blue dots indicate contributing elastic backscatter lidar stations.

The selected contributing stations create clusters around the high-performance stations. All these stations operate Raman lidar instruments as well, but not at several wavelengths. Highly reliable extinction and backscatter coefficients are retrieved at either 355 or 532 nm at these sites. Typical distances of neighbouring stations within a cluster are from 120 to about 800 km. This stations distribution allows for studying the temporal, regional and continental scale representativeness of the observations and comparing these findings with the results of the spaceborne lidar measurements from polar-orbiting satellites [*Pappalardo et al.*, 2010].

The observation strategy schedules additional simultaneous measurements at several EARLINET stations of the same cluster, namely *case B* measurements. Also for the *case B* measurements, 150 min records of measurements (centred on the overpass) are requested, in order to investigate the temporal variability. Further observations, namely *case C* measurements, are performed in conjunction with special events such as Saharan dust outbreaks and forest fire events. The collection of these measurements allows for studying the optical properties of specific aerosol types in detail and investigating the regional and continental scale representativeness of the observations. In summary, the EARLINET observation strategy foresees these measurements: (i) *case*

A (CALIPSO overpass within 100 km); (ii) *case B* (more than one station of the same cluster performs simultaneous measurements); and (iii) *case C* (interesting additional cases such as Saharan dust intrusions, forest fires, etc.).

Since June 2006, Granada station has performed lidar measurements according to the described strategy. The 16-day cycle of CALIPSO observations allows a precise schedule of the case *A* and case *B* measurements over our station, which is reported in Table 6.1.

Cycle's day	1	2	3	4	5	6	7	8	9	10	11	12	13	14	15	16
Noon							X									X
Night									X		X					X

Table 6.1. Schedule measurements for the Granada station corresponding to cases A and B within the ESA-CALIPSO strategy. Black and gray letters indicate measurements correspond to case A and B, respectively.

Data presented in this chapter correspond to the period from January 2008 to December 2010. A total of 68 Raman lidar observations were collected during night-time. Aerosol extinction, backscatter and LR profiles were derived by the Raman technique described in chapter 4 (section 4.2.2). A total of 141 at 532 nm and 77 at 355 nm Raman profiles were satisfactorily inverted. The number of Raman profiles at 355 nm was lower than that at 532 nm due to problems related to the good quality of the nitrogen Raman shifted signal at 387 nm. For those cases, elastic inversions were performed to obtain the backscatter coefficient at 355 nm. Elastic backscatter profiles at 532 nm were also retrieved for those cases in which it was not possible to obtain good quality Raman profiles. During day-time a total of 50 observations were satisfactorily inverted. The inversions were performed with the elastic algorithm described in chapter 4, including a synergetic approach with sun-photometer data to select an appropriated lidar ratio value [*Marenco et al.*, 1997; *Guerrero-Rascado et al.*, 2008].

Table 6.2 shows the number of profiles satisfactorily inverted for the period 2008–2010. Day and night measurements are denoted as "D" and "N", respectively. The profile type (elastic or Raman profile) is labelled as "b" and "e", respectively. The numbers do not reflect the number of measurements performed indeed but the number of quality-assured inversions obtained from the measurements performed.

2008-2010										
	Spring		Summer		Autumn		Winter		Total	
	D	N	D	N	D	N	D	N	**D**	**N**
355b	49	24	53	45	5	25	12	16	**119**	**110**
532b	49	30	89	71	14	24	28	29	**180**	**154**
1064b	42	28	39	62	4	29	11	8	**96**	**127**
355e		38		39		0		0		**77**
532e		41		74		12		14		**141**

Table 6.2. Number of profiles satisfactorily inverted during day and night-time in the period 2008-2010. The profile type, namely elastic or Raman, is labelled as "b" and "e", respectively.

Missing data during these three years were related to bad weather conditions (mainly presence of low clouds) and system maintenance. Figure 6.3 indicates the percentage of non-performed measurement reasons in the analyzed period presented in this chapter.
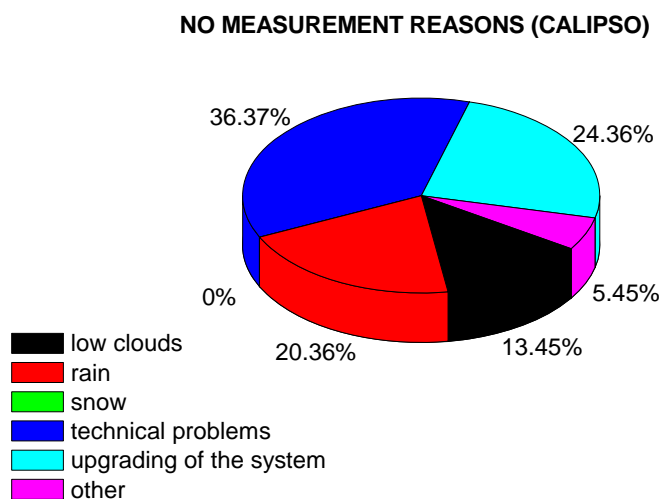
NO MEASUREMENT REASONS (CALIPSO)

Figure 6.3. Information on the causes of missing measurements at Granada station in the CALIPSO program for the period 2008-2010.

6.2. Mean vertical lidar profiles

In this section we present the mean profiles of backscatter from day and night-time measurements and those of extinction and LR at 532 nm from night measurements for the period 2008-2010. For this study, the whole year has been divided in two periods, from October to March (autumn and winter), and from April to September (spring and summer). This division of the year has proved to be the most appropriate to show the seasonal variability of the profiles of optical properties in our station.

Firstly, we present the profiles retrieved from night measurements by applying the Raman algorithm to all night-time measurements when the Raman channel was available. Because of the variability of the height range with reliable data, backscatter and extinction profiles are presented only above the height where all the profiles contributed to the computation of the mean profiles in order to avoid a bias. Backscatter coefficients are given above 1500 m (asl) and the extinction coefficient above 1900 m (asl). It is necessary to remind that our station is located at 680 m (asl). This choice of the start height also avoids any problem related to an incomplete overlap. In other hand, the highest altitude presented for lidar profiles was 6000 m (asl), assuming zero values for those profiles which did not provide aerosol information up to this altitude.

The mean profiles for extinction and backscatter coefficients (thick solid lines) and LRs (black squares) are shown in Figure 6.4. Bars denote the associated standard deviation. For LR, the mean values for layers at different heights have been shown; each value has been calculated as the mean value for a layer of 500 meters. The fraction of time when aerosols were present in each altitude has been indicated for the seven height ranges in the LR plot.

The mean backscatter and extinction profiles for autumn-winter (Fig. 6.4a) indicate that most of the particles are confined to the first few kilometres above surface (below 3500 m asl). The largest values for the extinction and backscatter coefficients are found at altitudes closer to the surface, with values very similar in all seasons. However, it is important to emphasize that the mean profiles during spring-summer (Fig. 6.4b) show larger values at higher altitudes than during autumn-winter. This result is caused by two facts; firstly the PBL height reaches higher values during the warm seasons than during cold seasons as shown in chapter 5, therefore the aerosol reaches higher altitudes. Secondly, during these months (from April to September) the long-range transport of aerosol particles is also more frequent than in the rest of the year. Saharan dust and forest fire smoke are the main aerosol contribution at high altitudes over our station, causing marked particles load in the FT [*Guerrero-Rascado et al.*, 2009; *Alados-Arboledas et al.*, 2011a]. The variability in the frequency of dust events could also be the cause of the large standard deviation associated with extinction and backscatter profiles in spring and summer.
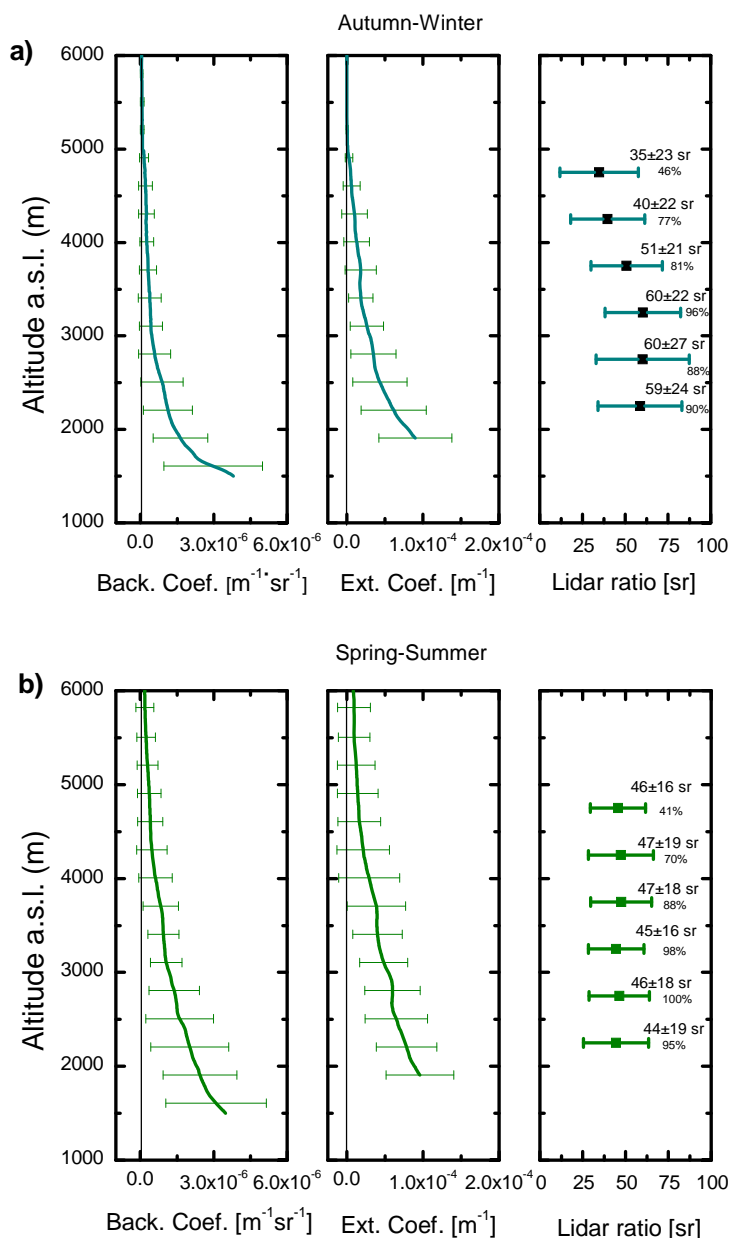
Figure 6.4. (a) Autumn-winter and (b) spring-summer mean vertical profiles for different optical properties during night time at Granada.

The mean LR values in spring-summer show a very constant value around 46 sr for the whole profile although with a large standard deviation. LR is quite dependent on the chemical and morphological aerosol properties, and the mean values found for spring-summer indicate a strong contribution of mineral dust [*Müller et al.*, 2007]. The origin could be, as we mentioned above, the Saharan dust outbreaks that affect our region during these months.

We observe a larger variability of mean LR values in autumn-winter seasons. Mean LRs range between 35 and 60 sr. This variability indicates the presence of

different aerosol types. Large LR values are associated to highly light absorbing particles while low LR values are indicative of particles which present a larger scattering [*Franke et al.*, 2003; *Müller et al.*, 2003]. The highest values, around 60 sr, are observed between 2 and 3 km (asl). These large values suggest an important contribution of absorbing particles at these altitudes and it could be due to local polluted emissions and agricultural biomass burning, which are typical during winter in the south of the Iberian Peninsula. Lower LR values are observed above 3.5 km (asl). The mean LR values at these altitudes ranged between 35 and 50 sr and they are typical of more transparent particles. In our area these values can be associated to long-range transport of mineral dust, marine and polluted marine aerosol particles.
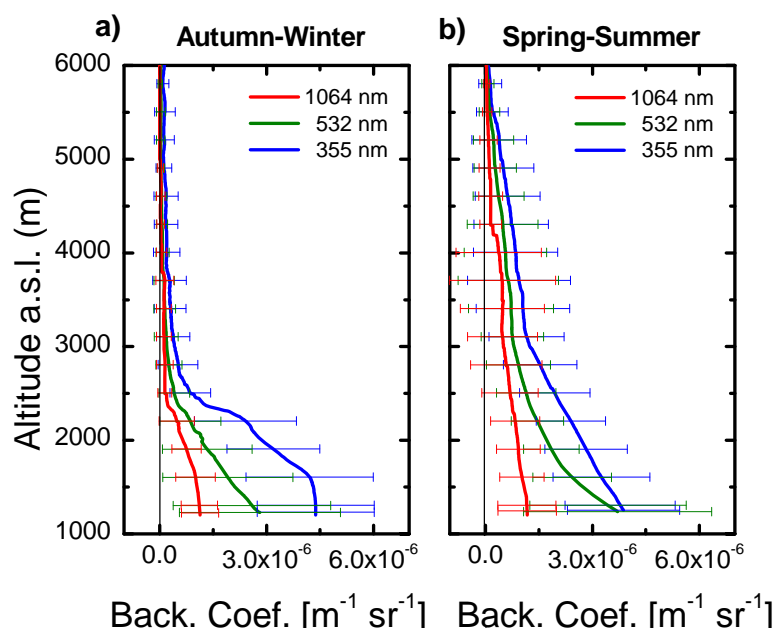

Figure 6.5. (a) Autumn-winter and (b) spring-summer mean backscatter profiles at 355, 532 and 1064 nm for day-time measurements.

Figure 6.5 shows the mean elastic backscatter profiles for autumn-winter and spring-summer at 355, 532 and 1064 nm retrieved from day-time measurements. A seasonal classification similar to that performed in night-time measurements has been carried out. Seasonal differences in the profile shape, similar to those detected at night-time from Raman analysis, are observed in the backscatter profiles at the three wavelengths. In autumn-winter most of the aerosol particles are confined in the first kilometres. In fact, a marked decrease is observed around 2.5 km (asl) at the three wavelengths. Above 3.5 km (asl) the aerosol content is very reduced during these seasons. A strong spectral dependence (i.e. large β-AE) is found in the lower

127

troposphere, indicating an important contribution of small particles (e.g. anthropogenic aerosol). In spring and summer the elastic backscatter profiles present a higher variability in the far height range (above 3 km, asl). It could be due to a higher frequency of Saharan dust intrusions during these seasons, causing a larger variability in the profiles. Moreover, we can see that the spectral dependence is lower than that observed in autumn-winter. It is due to mineral particles present optical properties almost independent on the wavelength [*Guerrero-Rascado et al.*, 2009]. In fact, the spectral dependence in the mean vertical profiles for spring-summer is lower in middle- and upper-troposphere where the contribution of mineral dust could be more relevant.
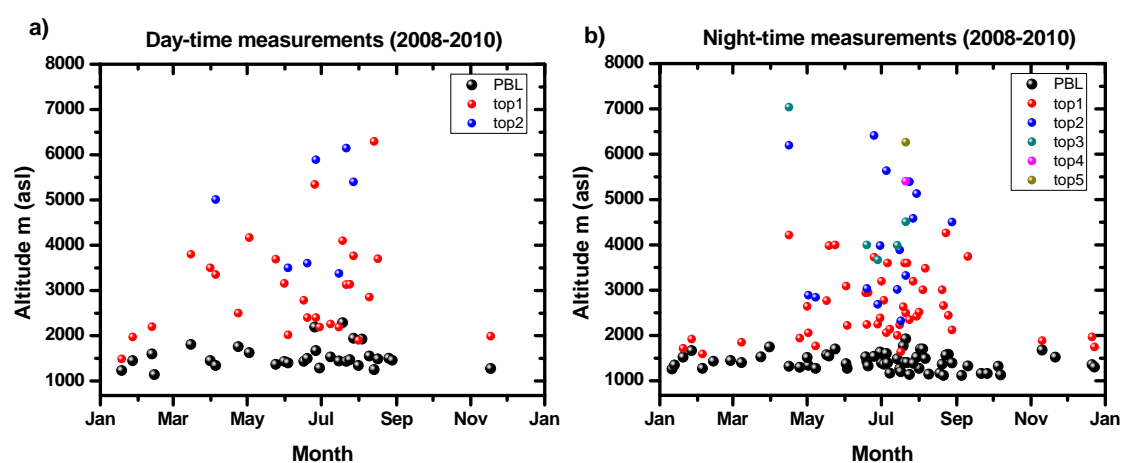

Figure 6.6. PBL heights (black circles) and the top altitude of lofted layers (coloured circles) are reported for (a) daytime measurements and (b) night time measurements.

An analysis of the vertical aerosol layering over our region has been performed. Figure 6.6 shows the PBL height and the residual layer height (black circles) for day and night-time measurements, respectively, for each session during the analyzed period. Moreover, the top heights of lofted layers are presented for those cases which there were presence of aerosol layers above the PBL. These altitudes were retrieved using the WCT-based method described in chapter 5. This figure gives information about the altitudes where the most relevant aerosol load is located. Figure 6.6a shows the results for daytime measurements. We can observe the presence of lofted layers above the PBL for most of the cases between April and September. We see that most of the aerosol layers reach altitudes below 4.5 km (asl) although in some cases they reached almost 7 km (asl). For night-time measurements (fig 6.6b) we note a greater aerosol stratification. Most of the layers above the PBL are found between May and September. As indicated above, the presence of aerosol in the FT, for day and night measurements for these

months, is mainly due to Saharan dust outbreaks and forest-fire smoke [*Guerrero-Rascado et al.*, 2008; *Guerrero-Rascado et al.*, 2009; *Alados-Arboledas et al.*, 2011b].

6.3. Lidar ratio and Angström Exponent seasonal variability

In this section a statistical study of the monthly mean AE and LR values is presented. As mentioned above, LR can only be obtained at night-time. However, AEs are retrieved for both day- and night-time. These two parameters depend on the wavelength, relative humidity and aerosol microphysical properties such as size, chemical composition and shape, but not on the aerosol concentration. Therefore they are appropriate to distinguish between different aerosol types [*Müller et al.*, 2007].

Figure 6.7 shows the monthly mean β-AE in the range 355-532 nm obtained from night-time measurements. The bars correspond to one standard deviation. This figure also shows the number of Saharan dust events that took place in coincidence with lidar measurements during the analyzed period. The identification of Saharan cases was performed by means of backward-trajectory analysis. The mean β-AE was retrieved for two regions, namely inside the PBL and in the FT. This distinction is relevant to identify the variability of aerosol types in the atmosphere column. The monthly mean β-AE values in the PBL and in the FT ranged from 1.7±0.8 (August) to 0.7±0.2 (September) and from 1.9±0.6 (March) to 0.8±0.5 (May), respectively. We observe a clear seasonal behaviour in both regions. In general, the monthly mean β-AE values from May to September are lower than those from October to April. However, an atypically high mean β-AE value was observed in the PBL in August. In this month, several episodes with air masses come from North Africa in the FT and from nearby fires in the PBL took place in our station. This could explain this anomalously high β-AE value in the PBL. In general, the lower β-AE values observed during the warm months evidence a greater presence of larger particles, similar results were observed over other stations [*Mona et al.*, 2006]. In fact, we observe an evident increase in the number of Saharan dust events from May to September (green circles, Fig. 6.7). The larger monthly mean values of β-AE during autumn and winter indicate a predominance of small particles during these seasons. This suggests that anthropogenic particles could be the main contribution to the atmosphere of Granada during these months. This annual cycle in the AOD-related AE has been observed in previous studies for the whole column with sun-photometers in the city of Granada [*Lyamani et al.*, 2010].

Despite the similar β-AE tendency in the PBL and in the FT during the year we can observe some discrepancies between their values. Larger values in the FT than in the PBL are observed from November to March, which indicates a greater contribution of large particles in the PBL during these months. It could be due to a smaller contribution of large particles in the FT due to Saharan dust event is less frequent in these months. Moreover, as we see in Figure 6.6 the FT is cleaner in autumn and winter. On the other hand, an opposite behaviour is observed during the warm months, where the β-AE values in the PBL are larger than in the FT. These results indicate that the contribution of large particles in the FT is more important than in the PBL. It could be mainly to the greater contribution of mineral dust in the FT during these months, while the PBL is also affected by anthropogenic and local sources. Similar observations in the AE have been found by Lyamani *et al*. [2010] from ground based in-situ instrumentation and passive remote sensing. They observed that the contribution of mineral dust (large particle) is more relevant in the whole column, while the scattering-related AE observed in surface is also influenced by anthropogenic aerosol (smaller particles) during spring and summer.
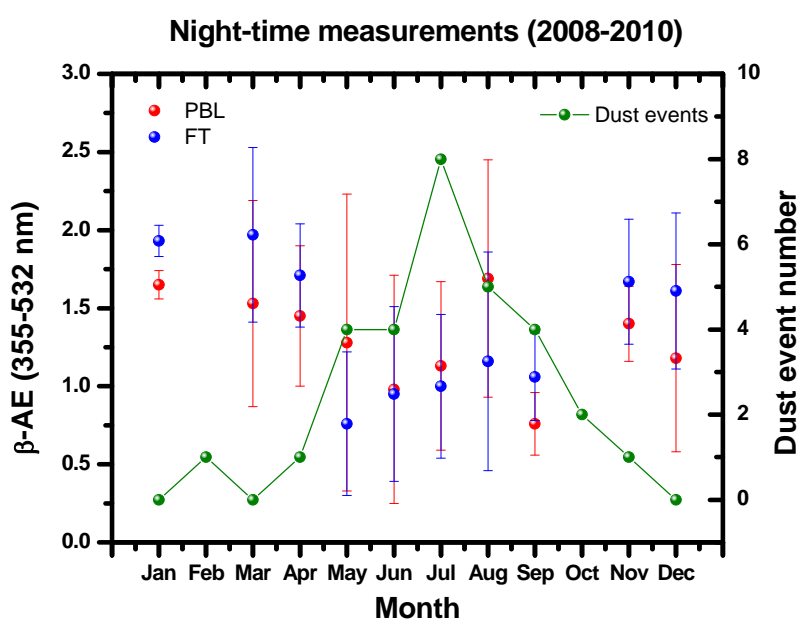

Figure 6.7. Monthly mean β-AE (355-532 nm) retrieved in the PBL (red circles) and in the FT (blue circles) from night time lidar measurements. Number of Saharan dust events in coincident with lidar measurements is also shown (green circles).

In order to take into account the high variability observed for β-AE and LR, a more detailed analysis of these parameters is carried out considering all the data gathered over the three years of measurements. Figure 6.8 shows the frequency

distribution of β-AE in the PBL and in the FT during spring-summer and autumn-winter. For spring-summer we can observe a large variability in the β-AE frequency distribution in the PBL (Fig. 6.8a), with maximum values located at 2.25, 2.0, 1.0 and 0.4. It indicates that aerosol content in the PBL is characterized a wide range of sizes. However, we can observe that for these seasons the β-AE frequency distribution in the FT shows a dominant mode centred 0.75 (Fig 6.8b). It confirms the results observed for the monthly mean β-AE (Fig. 6.7), indicating that coarse particles are dominant in the FT during spring and summer. For autumn and winter seasons we observe two dominant modes in the PBL, a maximum is found around 1.5 and other is observed around 0.6 (Fig 6.8c). It confirms again that PBL is affected by fine and coarse particles. For the FT the maximum frequency is reached for the β-AE values in the range 1.7- 2.2. This range includes 55% of the cases, indicating that fine particles are dominant in the FT during autumn and winter.
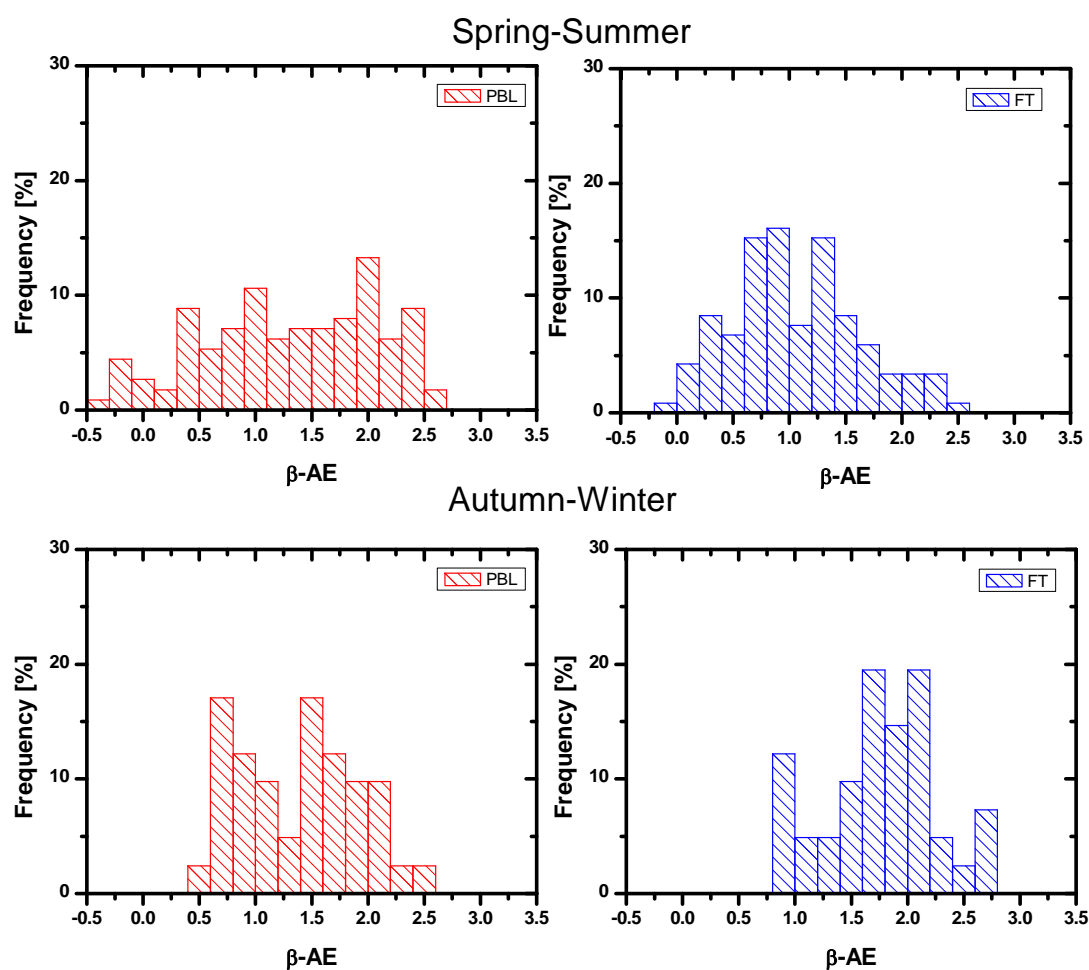

Figure 6.8. Frequency distribution of β-AE for PBL and FT during spring-summer and autumn-winter.

Figure 6.9 shows the monthly mean *β*-AE in the range 355-532 nm obtained from day-time measurements. The number of Saharan dust events in coincidence with lidar measurements is also presented. The monthly mean values in the PBL and in the FT ranged from 1.8±0.2 (March) to 0.6±0.2 (April) and from 2.2±0.1 (October) to 0.5±0.7 (April), respectively. The monthly mean *β*-AE values from April to September are lower than those from October to April. Atypical large *β*-AE values, 1.5±0.5 and 1.3±0.6, are observed in June in the PBL and in the FT, respectively. We identify that for several days air masses come from fire areas in this month. Moreover, we note that a lower number of Saharan dust cases were present during day time in coincidence with lidar measurements in this month. It explains that fine particles were dominant in the lidar measurement. We also observe some discrepancies in the *β*-AE values between the PBL and the FT along the year. As we noted in night-time measurements, larger values or similar values are found in the FT than in the PBL from October to March. However the mean *β*-AE values are lower in the FT than in the PBL from April to September. It evidences again that coarse particles have a greater contribution in the FT during spring and summer while fine particles dominate during autumn and winter. Similar frequency distribution to those observed during night-time was also observed for day-time measurements.
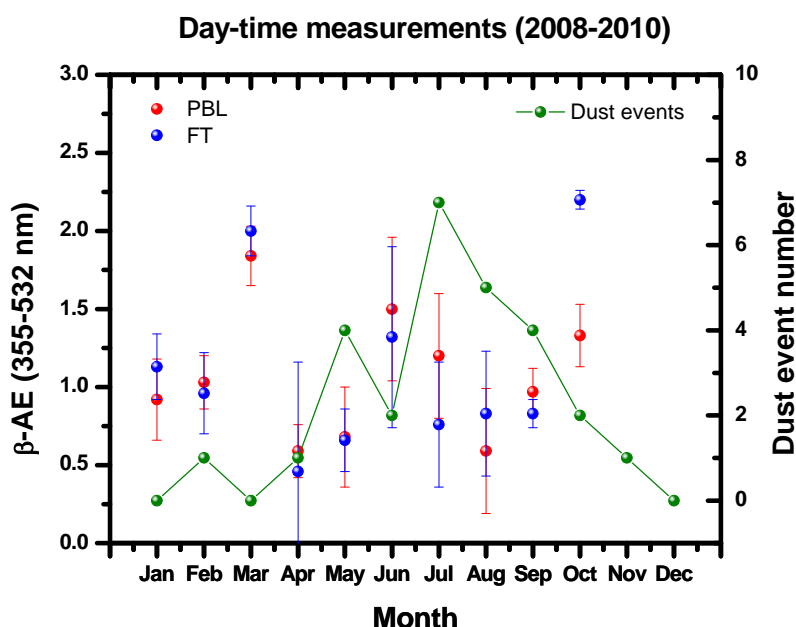

Figure 6.9. Monthly mean β-AE (355-532 nm) retrieved in the PBL (red circles) and in the FT (blue circles) from day-time lidar measurements. Number of Saharan dust events in coincident with lidar measurements is also shown (green circles).

Monthly mean LR values at 532 nm were only retrieved from night time measurements due to the extinction profiles are only available during night time. The LR mean values were only calculated in the FT since in some cases it was not possible to retrieve extinction coefficient inside the PBL. Figure 6.10a shows the monthly evolution of this quantity. Although the annual evolution is not so clear, we can observe the largest LRs during autumn and winter, while lower values are observed in spring and summer. The mean values varied between 36±20 sr (August) and 75±8 sr (November). Large values in LR can be associated to urban and polluted aerosol while values between 40-60 sr are typical of mineral particles [*Ackermann*, 1998; *Matthias and Bosenberg*, 2002; *Müller et al.*, 2007]. No LR data are available in March, since Raman inversions at 532 nm were not possible. Also, there is a gap in the *β*-AE data in October because no reliable 355-nm backscatter profiles were available. During these two months we had technical problems with 607 and 387 nm Raman channels, respectively. Figure 6.10b presents the frequency distribution of LRs. The greatest part of LRs is in the range between 40 and 60 sr (50% of the cases). These LR values are typical for mineral dust and urban-continental particles [*Matthias and Bosenberg*, 2002; *Müller et al.*, 2007]. LRs larger than 60 sr were found for the 20% of the cases, being these values are indicative of highly light absorbing particles [*Franke et al.*, 2003; *Müller et al.*, 2003] and are typically associated to smoke and anthropogenic pollution. The number of cases with lower LR (below 40 sr) was around 25 %, such values are associated to marine and polluted marine particles which present a larger scattering.
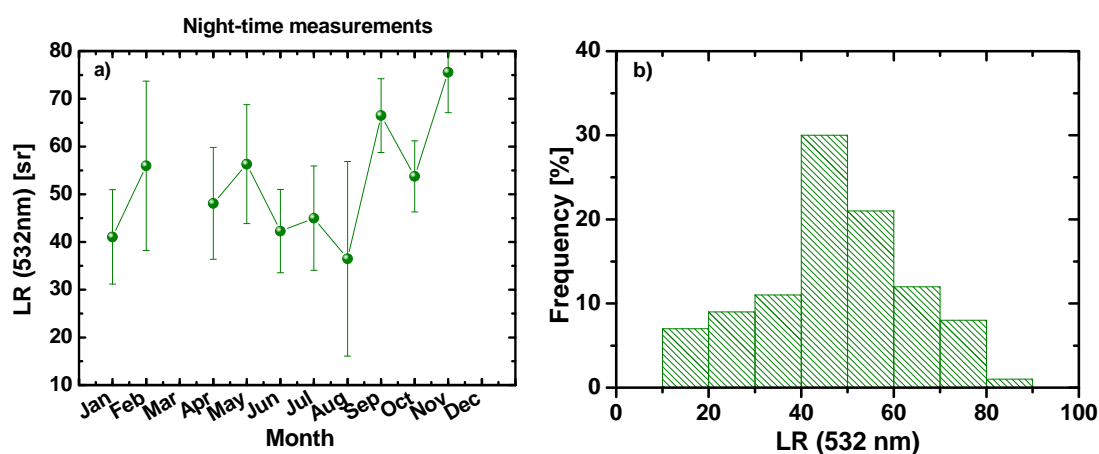

Figure 6.10. a) Monthly mean LR at 532 nm retrieved from night lidar measurements over 3 years, b) frequency distribution of LR at 532 nm.

Night-time measurements of β-AE and LR allowed for correlating these properties in the FT along the three years (Fig. 6.11). A total of 80 pairs of data have been included in this plot. LRs vary between 20 and 85 sr while β-AEs range between 0.18 and 2.3. This wide range of values indicates that different types of aerosol are found in the FT over Granada. Although the coefficient of determination is not so good ($R^2 = 0.45$), a clear positive slope is observed between both properties, indicating that large AEs (smaller particles) are associated to large LRs. This behaviour confirms the expected results since small particles (large AE) usually present a larger absorption and therefore larger LR values (e.g. smoke, anthropogenic pollution) while larger particles (low AE) present a larger scattering (e.g. marine particles).
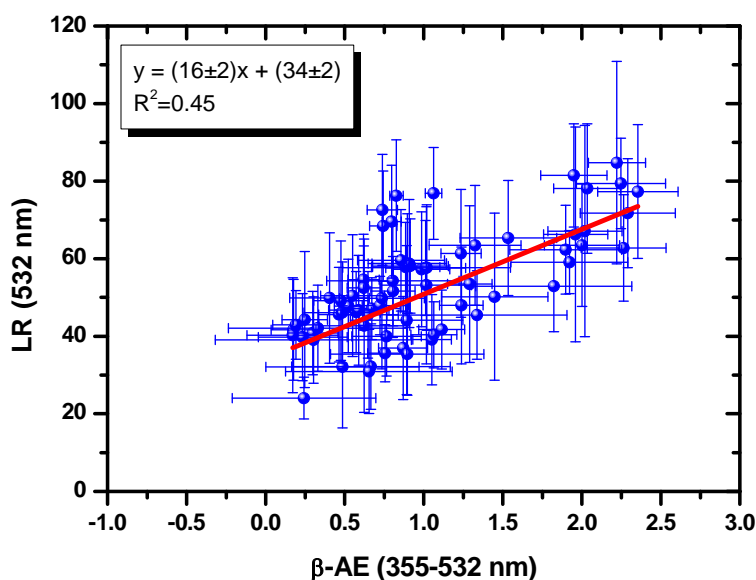
Figure 6.11. β-AE(355-532 nm) versus LR at 532 nm in the FT.

6.4. Conclusions

A characterization of aerosol optical properties has been performed by means of a Raman lidar at Granada, Spain. Seasonal vertical optical profiles showed the largest values for the backscatter and extinction coefficients at altitudes closer to the surface, with values very similar along the year. In the FT we observed larger values during spring-summer than in autumn-winter. This fact can be explained by the impact of lofted aerosol layers associated to Saharan dust outbreaks during the warm season at these heights. For spring-summer the LR profiles presented quite constant mean values (with high standard deviation) in the range typically associated to mineral dust (~46 sr)

while LR profiles are highly variable for autumn-winter. A study of aerosol layering in the whole column indicated that the most of the aerosol particles presented above the PBL is detected during warm months. Moreover, mean monthly integrated β-AE values were obtained in the PBL and in the FT from day and night-time measurements. We observe a clear seasonal behaviour in both atmospheric regions. In general, the monthly mean β-AE values present lower values in warm months than in cold months. It indicates that the presence of large particles is more important in spring and summer. We also observe that β-AE values were larger in the FT than in the PBL in autumn and winter. Opposite tendency was observed in spring and summer. Finally, the annual cycle of LR at 532 nm also suggests a predominance of fine particles during autumn and winter and an increase in the contribution of coarse particles during spring and summer. A moderate correlation was observed between β-AE and LR at 532. The results confirmed that small particles are associated with large absorption while large particles are related with large scattering.

6.5. References

Ackermann, J. (1998), The extinction-to-backscatter ratio of tropospheric aerosol: A numerical study, *Journal of Atmospheric and Oceanic Technology*, *15*(4), 1043-1050.

Alados-Arboledas, L., D. Müller, J. L. Guerrero-Rascado, F. Navas-Guzman, D. Perez-Ramirez, and F. J. Olmo (2011a), Optical and microphysical properties of fresh biomass burning aerosol retrieved by Raman lidar, and star-and sun-photometry, *Geophysical Research Letters*, *38*.

Alados-Arboledas, L., D. Muller, J. L. Guerrero-Rascado, F. Navas-Guzman, D. Perez-Ramirez, and F. J. Olmo (2011b), Optical and microphysical properties of fresh biomass burning aerosol retrieved by Raman lidar, and star-and sun-photometry, *Geophysical Research Letters*, *38*.

Franke, K., A. Ansmann, D. Muller, D. Althausen, C. Venkataraman, M. S. Reddy, F. Wagner, and R. Scheele (2003), Optical properties of the Indo-Asian haze layer over the tropical Indian Ocean, *Journal of Geophysical Research-Atmospheres*, *108*(D2).

Guerrero-Rascado, J. L., B. Ruiz, and L. Alados-Arboledas (2008), Multi-spectral Lidar characterization of the vertical structure of Saharan dust aerosol over southern Spain, *Atmospheric Environment*, *42*(11), 2668-2681.

Guerrero-Rascado, J. L., F. J. Olmo, I. Aviles-Rodriguez, F. Navas-Guzman, D. Perez-Ramirez, H. Lyamani, and L. A. Arboledas (2009), Extreme Saharan dust event over the southern Iberian Peninsula in september 2007: active and passive remote sensing from surface and satellite, *Atmospheric Chemistry and Physics*, *9*(21), 8453-8469.

Lyamani, H., F. J. Olmo, and L. Alados-Arboledas (2010), Physical and optical properties of aerosols over an urban location in Spain: seasonal and diurnal variability, *Atmospheric Chemistry and Physics*, *10*(1), 239-254.

Marenco, F., V. Santacesaria, A. F. Bais, U. Balis, A. diSarra, A. Papayannis, and C. Zerefos (1997), Optical properties of tropospheric aerosols determined by lidar and spectrophotometric measurements (Photochemical Activity and Solar Ultraviolet Radiation campaign), *Applied Optics*, *36*(27), 6875-6886.

Matthias, V., and J. Bosenberg (2002), Aerosol climatology for the planetary boundary layer derived from regular lidar measurements, *Atmospheric Research*, *63*(3-4), 221-245.

Mattis, I., D. Müller, H. Baars, and e. al. (2008), Complementary use of EARLINET, CALIPSO and AERONET observations: case study July 24, 2006, in *Reviewed and revised papers presented at the 24th ILRC*, edited, pp. 1121-1124, Boulder, Colorado.

Mona, L., A. Amodeo, M. Pandolfi, and G. Pappalardo (2006), Saharan dust intrusions in the Mediterranean area: Three years of Raman lidar measurements, *Journal of Geophysical Research-Atmospheres*, *111*(D16).

Müller, D., K. Franke, A. Ansmann, D. Althausen, and F. Wagner (2003), Indo-Asian pollution during INDOEX: Microphysical particle properties and single-scattering albedo inferred from multiwavelength lidar observations, *Journal of Geophysical Research-Atmospheres*, *108*(D19).

Müller, D., A. Ansmann, I. Mattis, M. Tesche, U. Wandinger, D. Althausen, and G. Pisani (2007), Aerosol-type-dependent lidar ratios observed with Raman lidar, *Journal of Geophysical Research-Atmospheres*, *112*(D16).

Pappalardo, G., et al. (2010), EARLINET correlative measurements for CALIPSO: First intercomparison results, *Journal of Geophysical Research-Atmospheres*, *115*.

Sassen, K. (1991), The polarization lidar technique for cloud research - a review and current assessment, *Bulletin of the American Meteorological Society*, *72*(12), 1848-1866.

Stephens, G. L., et al. (2002), The cloudsat mission and the a-train - A new dimension of space-based observations of clouds and precipitation, *Bulletin of the American Meteorological Society*, *83*(12), 1771-1790.

Winker, D. M., W. H. Hunt, and M. J. McGill (2007), Initial performance assessment of CALIOP, *Geophysical Research Letters*, *34*(19).

Chapter 7

Retrieval of water vapour by Raman lidar

In this chapter, we outline a method to obtain water vapour mixing ratio profiles from a Raman lidar. Simultaneous and co-located radio-sounding data are used to calibrate the lidar water vapour measurements and the calibration results obtained during six experiments performed during summer and autumn 2011 are presented. We compare the water vapour profiles measured by the Raman lidar and radiosondes and discuss the differences between the instruments. After that, a comparison of total precipitable water (TPW) obtained from the Raman lidar and the retrieved from a star-photometer is shown. Finally, we present relative humidity profiles derived from the combination of simultaneous profiles of temperature (retrieved from a microwave radiometer) and water vapour mixing ratio (from a Raman lidar).

7.1. Introduction

Water vapour is one of the most important constituents in the Earth's atmosphere and it is characterized by high variability in space and time. It plays a key role in the global radiation budget and in energy transport mechanisms in the atmosphere [*Whiteman et al.*, 1992; *Ferrare et al.*, 2000] as well as in photochemical processes. Moreover, it is the most important gaseous source of infrared opacity in the atmosphere, accounting for about 60% of the natural greenhouse effect for clear skies

[*Kiehl and Trenberth*, 1997], and providing the largest positive feedback in model projections of climate change [*Held and Soden*, 2000]. It also contributes indirectly to the radiative budget by means of microphysical processes leading to the formation and development of clouds, and by affecting the size, shape and chemical composition of aerosol particles [*Reichardt et al.*, 1996], thus modifying the aerosol role in the radiative forcing [*De Tomasi and Perrone*, 2003].

To achieve a comprehensive understanding of the role of the water vapour on local and global scales, systematic observations with high spatial and temporal resolution are required. Among the in-situ techniques, radio-sounding is extensively used due to its high spatial resolution, but the temporal resolution depends on the launch frequency. There are additional disadvantages: it is a costly technique, the verticality of the sounding depends on the wind regime changes with altitude (balloons drift with the wind), and it is difficult to make accurate water vapour measurements in conditions of low relative humidity [*Vaughan et al.*, 1988].

Other measurement techniques have become available to address the need for improved water vapour measurements. These techniques include satellite [*Soden et al.*, 1994], microwave radiometer [*Han et al.*, 1994], DIAL lidar [*Ismail and Browell*, 1994], sun- and star-photometers [*Perez-Ramirez et al.*, 2012] and Raman lidar [*Whiteman et al.*, 1992; *Mattis et al.*, 2002]. By virtue of its ability to provide both high spatial and temporal resolution measurements of water vapour throughout most of the troposphere, Raman lidar has emerged in the last decades as a powerful tool for providing detailed water vapour profiles as required for modelling the complicated processes aforementioned.

7.2. Methodology

Raman analysis can be used in order to obtain gas mixing ratio. The approach is relevant to any Raman-active gas with an appreciable atmospheric concentration, such as water vapour. The Raman method for water vapour mixing ratio profiling involves the detection of two Raman-shifted signals, one corresponding to the water vapour and the other associated to a reference gas, in this case nitrogen. The lidar equation described in section 2.6 can be expressed for the nitrogen and water vapour Raman signals as follows:

7. Retrievals of water vapour measurements by Raman lidar

$$P(R,\lambda_{N_2}) = P(\lambda_0)K_{N_2}\frac{O_{N_2}(R)}{R^2}\beta(R,\lambda_{N_2})\exp\left\{-\int_0^R\left[\alpha(r,\lambda_0)+\alpha(r,\lambda_{N_2})\right]dr\right\} \qquad (7.1)$$

$$P(R,\lambda_{H_2O}) = P(\lambda_0)K_{H_2O}\frac{O_{H_2O}(R)}{R^2}\beta(R,\lambda_{H_2O})\exp\left\{-\int_0^R\left[\alpha(r,\lambda_0)+\alpha(r,\lambda_{H_2O})\right]dr\right\} \qquad (7.2)$$

where $P(R,\lambda_{N2})$ and $P(R,\lambda_{H2O})$ are the backscattered laser power at the Raman-shifted nitrogen and water vapour wavelengths, respectively, from range R; $P(\lambda_0)$ is the emitted laser power at wavelength λ_0; K_{N2} and K_{H2O} are range-independent calibration constants; $O_{N2}(R)$ and $O_{H2O}(R)$ are the overlap functions; $\beta(R,\lambda_{N2})=N_{N2}(R)\cdot\sigma_{N2}(\lambda)$ is backscatter coefficient for nitrogen molecules, where $N_{N2}(R)$ is the number density of nitrogen molecules and $\sigma_{N2}(\lambda)$ is the Raman backscatter cross section at the Raman-shifted nitrogen wavelength; $\beta(R,\lambda_{H2O})=N_{H2O}(R)\cdot\sigma_{H2O}(\lambda)$ represent the magnitudes associated with water vapour molecules; α is the total extinction coefficient at wavelength λ_0, λ_{N2} and λ_{H2O}; and r is the range considered as an integration variable.

Combining equations (7.1) and (7.2) we obtain:

$$\frac{P(R,\lambda_{H_2O})}{P(R,\lambda_{N_2})} = \frac{K_{H_2O}N_{H_2O}(R)\sigma_{H_2O}}{K_{N_2}N_{N_2}(R)\sigma_{N_2}}\exp\left\{\int_0^R\left[\alpha(r,\lambda_{N_2})-\alpha(r,\lambda_{H_2O_2})\right]dr\right\} \qquad (7.3)$$

Equation (7.3) assumes identical overlap factors and range-independent Raman backscatter cross sections for the two signals. The water vapour mixing ratio is defined as the ratio of the mass of water vapour to the mass of dry air in a sample of the atmosphere. From equation (7.3) we can obtain the ratio $N_{H2O}(R)/N_{N2}(R)$ that is proportional to water vapour mixing ratio (w):

$$\frac{N_{H_2O}(R)}{N_{N_2}(R)} = \frac{P(R,\lambda_{H_2O})}{P(R,\lambda_{N_2})}\frac{K_{N_2}\sigma_{N_2}}{K_{H_2O}\sigma_{H_2O}}\exp\left\{-\int_0^R\left[\alpha(r,\lambda_{N_2})-\alpha(r,\lambda_{H_2O_2})\right]dr\right\} \qquad (7.4)$$

and thus

$$w(R) = \frac{P(R,\lambda_{H_2O})}{P(R,\lambda_{N_2})}K\exp\left\{-\int_0^R\left[\alpha(r,\lambda_{N_2})-\alpha(r,\lambda_{H_2O_2})\right]dr\right\} \qquad (7.5)$$

where K takes into account the fractional volume of nitrogen in the atmosphere (78. 08 %), the ratio of molecular masses, the range-independent calibrations constants K_{N2} and K_{H2O}, and range-independent Raman backscatter cross sections σ_{N2} and σ_{H2O}. In

summary, the water vapour mixing ratio profile is obtained by the ratio of water vapour lidar signal to nitrogen lidar signal, a constant calibration factor and an exponential correction due to difference in extinction between the nitrogen shifted and water vapour shifted wavelength. This exponential can be evaluated by radio-sounding or standard atmosphere profile of temperature and pressure but is found to be negligible in most cases [*Mattis et al.*, 2002]. The constant calibration can be determined by comparison with soundings [*Ferrare et al.*, 1995; *Guerrero-Rascado et al.*, 2008].

7.3. Raman lidar water vapour calibration

As we have shown in the previous section, profiles of water vapour mixing ratio are computed from the ratio of Raman water vapour to Raman nitrogen return signals. Whiteman *et al.* [1992] show that a single calibration constant is used to convert these lidar signal ratios into water vapour mixing ratios expressed as the mass of water vapour divided by the mass of dry air. Calibration of water vapour Raman lidar measurements has been extensively discussed in the past [*Vaughan et al.*, 1988; *Whiteman*, 2003; *Leblanc et al.*, 2008]. There are three main approaches to obtain this calibration constant. One approach requires accurate knowledge of the optical transmission characteristics of the lidar system and the ratio of Raman scattering cross sections between water vapour and nitrogen. Leblanc *et al.* [2012] found that the precision of this approach to compute calibration values rarely is better than 10%. Because of the difficulty in reducing the uncertainties in the Raman cross sections and in determining the optical transmission characteristics of the entire lidar detection system, an alternative approach has been developed [*Ferrare et al.*, 1995; *Leblanc et al.*, 2012]. The second approach consists of estimating the constant *C* lidar signal ratios using one (or a set of) well-known water vapour mixing ratio profile(s) measured by another technique. Radiosonde measurement in the troposphere is the most common technique used today. The third common calibration procedure is based on the comparison of TPW obtained through the vertical integration of the water vapour profiles obtained with the Raman lidar and the TPW retrieved from a co-located GPS or microwave radiometer. When using an external measurement, the accuracy of the calibration procedure for the Raman system follows that of the measurement used as reference. Today the accuracy of the best quality radiosoundes, GPS, and microwave

measurements is estimated to be 5%, 7% and 10% respectively [*Miloshevich et al.*, 2009; *Leblanc et al.*, 2012].

In this section we have adopted the second approach where lidar profiles are compared with simultaneous and co-located radiosonde measurements of water vapour. Radiosounding campaigns were performed at our station during summer and autumn 2011. A total of twelve radiosondes (six at midday and six at night) were launched simultaneously with lidar measurements. The radiosounding data were obtained using a GRAW DFM-06 radiosonde (described in chapter 5).

Only the six radiosondes launched at night-time were appropriate for the calibration of the water vapour Raman channel. The radiosonde data were vertically interpolated in order to obtain an equivalent 7.5 m resolution to match the lidar resolution. For calibration purpose, a conventional least square regression is performed between the lidar and radiosonde data. Lidar data between altitude 1.5 and 4.0 km (asl) were used in the calibration regression. This range was chosen in order to use a region with presumably high water vapour mixing ratio (minimizing the error in radiosonde data) and to avoid the large differences that could be found between lidar and radiosonde measurements in the far height range due to the effect of sonde drift. A robust iterative procedure is presented here in order to find the best least square regression. For this purpose after the first fitting, the standard deviation of the data points around the regression line is computed. A scan is then made through the data points, eliminating all points that deviate from the regression line more than one standard deviation. The remaining points are used for a new least-squares regression. These steps are repeated until the lineal regression slope change less than 1%. If the number of remaining points is less than 50% of the initial number the calibration will not be considered as valid. An example of this iterative procedure is shown in Figure 7.1. The case corresponds to the calibration on 25th July 2011. Three iterations were needed to achieve the slope convergence. The figure shows only the first (Fig. 7.1, left) and the last (Fig. 7.1, right) linear regression. Note that for this case the data point deleted after this filtering procedure correspond to low values of water vapour mixing ratio. Radiosondes present larger errors for those situations with low water vapour mixing ratio [*Ferrare et al.*, 1995], this could explain that the largest deviations in our regression were found for these low values. We can observe that for the last iteration

(iteration = 3) the coefficient of determination (R^2) undergoes an improvement. The calibration constant reaches a value of 183 ± 2 g/kg for this case.
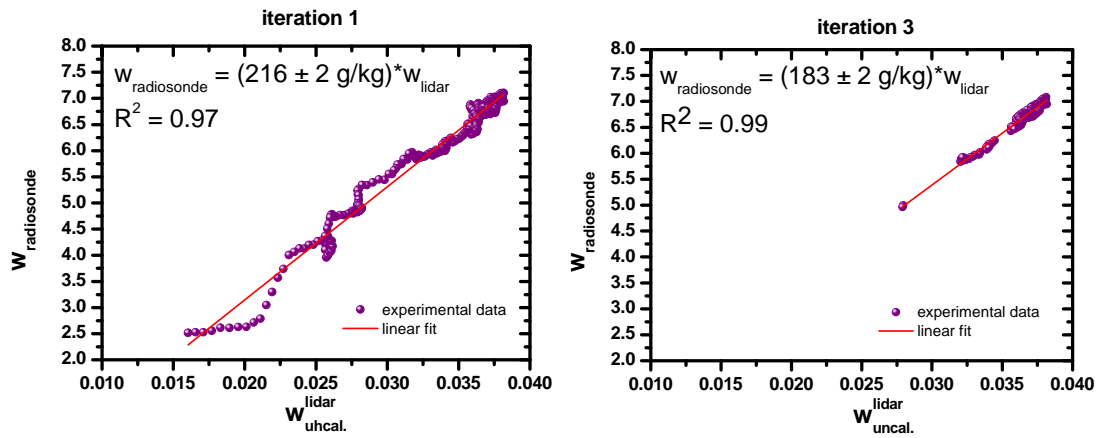

Figure 7.1. Iterative procedure of linear regressions to retrieve lidar calibration constant from the comparison of lidar and radiosonde data: (left) regression for the first iteration, (right) final regression (iteration 3).

For all the cases used in the calibration procedure the number of iterations was less than 5. A good agreement among calibration constants computed for the different cases were observed. Table 7.1 shows the final slope (which corresponds to the calibration constant), R^2 and the standard deviation for the six nights used in the calibration of the lidar water vapour channel.

Date	Slope	R^2	Standard Deviation
18 July 2011	183.7 ± 0.1	0.99	0.06
22 July 2011	185.7 ± 0.2	0.99	0.05
25 July 2011	183.1 ± 0.1	0.99	0.05
28 July 2011	187.0 ± 0.1	0.99	0.13
17 November 2011	182.2 ± 0.2	0.99	0.03
24 November 2011	192.4 ± 0.1	0.99	0.08

Table 7.1. Linear fit between lidar and co-located radiosondes measurements. Calibration of lidar water vapour profiles has been obtained using data in the height range between 1.5 and 4.0 km (asl).

A mean value of 186 ± 4 g/kg was obtained as the calibration coefficient for the whole campaign. The standard deviation around the mean of the calibration coefficient was found to be close to 2%. Previous studies have shown similar standard deviations. Thus, using 15 lidar–radio-sounding comparisons in the IfTP, Leipzig (Germany), the calibration coefficient was computed with an standard deviation around 5% [*Mattis et al.*, 2002]. Moreover, the use of 31 Vaisala RS-80 radiosondes for calibrating the NASA Goddard Space Flight Center Scanning Raman Lidar with the same technique, during

the CAMEX-3 campaign, provided a standard deviation of the calibration constant of the same value [*Whiteman*, 2003]. Therefore, we consider that the calibration constants obtained in our campaign are suitable and reproducible.

Figure 7.2 shows the water vapour mixing ratio profiles obtained from the Raman lidar profiles, using the mean calibration constant calculated above, together with the profiles obtained by radiosondes. The three examples showed correspond to 22nd July, 25th July and 24th November 2011. The cases show different water vapour situations. We observe a good agreement between lidar and radiosonde profiles at all altitudes on 22nd and 25th July. However, larger discrepancies are found above 5 km (asl) for the third case (24th November). This deviation in the far height range could be explained by the large deviation from verticality suffered by the radiosonde during this night.
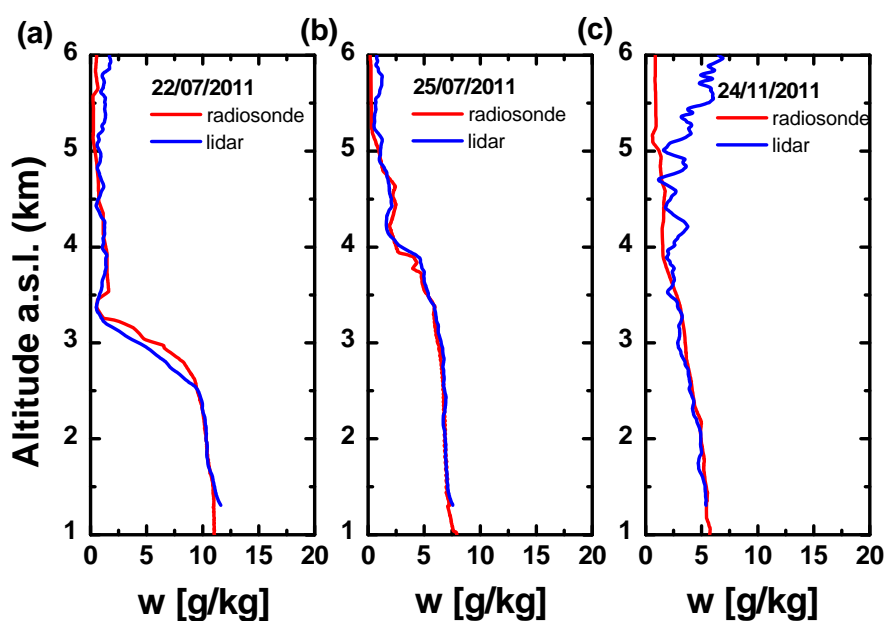
Figure 7.2. Water vapour mixing ratio profiles measured with radiosonde and Raman lidar. The cases correspond to night-time measurements performed on (a) 22nd July, (b) 25th July and (c) 24th November 2011.

Moreover, a statistical analysis in terms of mean absolute deviations and standard deviations between lidar and radiosonde water vapour mixing ratio profiles is presented in Table 7.2. This table shows the discrepancies observed at different height ranges between 1.5 and 5.5 km (asl). We have to keep in mind that the altitude of the station is 0.68 km (asl). We observe that the mean absolute deviation is below 0.5 g/kg

for 55% of the selected ranges. However, larger discrepancies are found between 4.5 and 5.5 km, reaching a maximum mean absolute deviation of 2.2 g/kg on 17th November. The inspection of the RCS temporal evolution allows for identifying that clouds were present at this height range this night. The mean absolute deviation for the whole profile during the six comparisons was 0.6 ± 0.6 g/kg. This low value shows the good agreement between both techniques to retrieve water vapour mixing ratio.

Date	1.5-2.5 km		2.5-3.5 km		3.5-4.5 km		4.5-5.5 km	
	mean	sd	mean	sd	mean	sd	mean	sd
18 July 2011	0.3	0.5	0.2	0.3	0.17	0.11	0.25	0.19
22 July 2011	0.06	0.04	1.0	0.7	0.23	0.18	0.5	0.3
25 July 2011	0.08	0.06	0.17	0.09	0.39	0.22	0.29	0.16
28 July 2011	0.25	0.12	0.7	1.1	0.4	0.3	1.8	0.8
17 November 2011	0.18	0.21	0.27	0.18	1.4	0.5	2.2	0.9
24 November 2011	0.22	0.15	0.29	0.19	0.8	0.6	1.9	1.2

Table 7.2. Mean absolute deviation (mean) and standard deviation (sd) of water vapour mixing ratio (g /kg) between lidar and radiosonde data at different layers.

7.4. Retrieval of total precipitable water using Raman lidar: assessment against a star photometer

In this section a comparison of TPW retrieved with a Raman lidar and a co-located star-photometer is presented [*Perez-Ramirez et al.*, 2012]. The measurements used were performed at the CEAMA from March to May 2007. The calibration constant to retrieve water vapour profiles from Raman lidar was obtained during an experimental campaign at "El Arenosillo" (37.11º N, 6.73º W, 0 m asl), Huelva (Spain). All details about this calibration are given by Guerrero-Rascado et *al*. [2008].

Star photometer was routinely operated during the selected period even though only cloud-free data are actually used; nevertheless lidar measurements were only limited to operational protocols of the EARLINET network. Measurements taken by the lidar system during the study period are summarized in Table 7.3. Mean profiles of water vapour mixing ratio were computed by averaging one hour of lidar measurements, then TPW is calculated by integrating $w(R)$ for the entire atmospheric profile. To deal

with the region where the overlap between the laser beam and the receiver field of view is null (see Figure 4.3), it is assumed a constant $w(R)$ from 150 m (agl) down to ground. Differences between the water vapour mixing ratios independently determined at ground level, using data from a meteorological station, and those obtained from the lidar system at the lowest available altitude were between 10-20%. The water vapour mixing ratios determined at surface are used to reconstruct the lowermost lidar profile through a linear interpolation between the surface and the lowest level where we can derive a realistic value from the lidar system. Nevertheless, the TPW values computed in this way are only 1.5% larger than those obtained assuming a constant mixing ratio for the first 150 m (agl). These differences are within the uncertainty of the star-photometer and the Raman lidar system.

Date	Hour (UTC)
8 March 2007	20:03-22:03
22 March 2007	01:00-02:00
17 April 2007	19:30-22:30
19 April 2007	21:45-22:45
30 April 2007	01:30-02:30 and 20:00-22:00
7 May 2007	20:00-22:00
8 May 2007	20:00-23:59
9 May 2007	00:00-04:00
10 May 2007	20:00-22:00
14 May 2007	20:00-22:00
16 May 2007	01:30-03:30
17 May 2007	20:00:22:00

Table 7.3. Measurements taken with the Raman lidar system between March and May 2007.

In total, there were 28 lidar measurements of TPW allowing for direct comparison with values obtained from star-photometry (Figure 7.3). The range of TPW values goes from 0.43 to 1.80 cm. It is evident a strong correlation between both instruments (R = 0.938). The proximity of the data points to the 1:1 line as well as the slope (0.91 ± 0.06) and intercept (0.12 ± 0.06 cm) of the linear fit reflect the agreement between both instruments. In spite of the slope, star-photometer data are only 3% lower on average than those from lidar due to the non-zero intercept. This bias between the

instruments is lower than the systematic uncertainties associated with the methodology used for derived TPW from the star-photometer (6%, [*Perez-Ramirez et al.*, 2012]) and the uncertainty of the lidar system (6.5% as stated by [*Whiteman et al.*, 2006]). Furthermore, differences in the techniques must be taken into account. In this sense, retrievals of TPW during day-time using different techniques have been widely discussed in the literature, reporting uncertainties up to 5% between sun-photometry and radiosounding data [*Schmid et al.*, 2001], and remarking systematic underestimation of microwave radiometer data over multifilter rotating shadowband radiometers [*Alexandrov et al.*, 2009].

As can be observed from Figure 7.3, there is an agreement between both techniques for the entire range of TPWs. Saturated vapour pressure increases with temperature and so it does the amount of water vapour that can be stored without reaching saturation, therefore larger temperatures allow for larger TPW. In this case, the atmosphere was colder in March than in May, therefore TPW had usually lower values in March. Moreover, the night-to-night fluctuations of TPW are associated with changes in the air masses reaching the site.
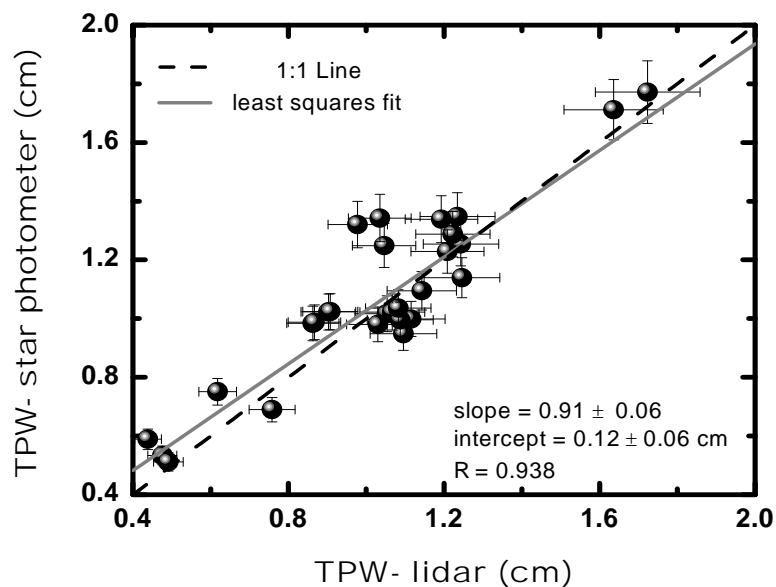

Figure 7.3. Comparison between TPW retrieved by the lidar system and the star-photometer from March 2007 to May 2007. Bars correspond to the experimental errors on measurements.

Figure 7.4 shows a detailed analysis of TPW measurements for one night, 8 to 9 May 2007, as an example of the results corresponding to a better time resolution. Data from both instruments agree and show a similar trend with a maximum difference in

TPW close to 5%; the slight decrease in TPW through the night is evidenced by both instruments. For the star-photometer, the mean value of TPW corresponding to this night was 1.01 ± 0.04 cm, with maximum and minimum values of 1.12 and 0.93 cm, respectively. The mean value obtained from the lidar system was 1.01 ± 0.11 cm, with maximum and minimum values of 1.14 and 0.86 cm, respectively. Air masses reaching the city of Granada were identified using five-day backward-trajectories computed by the aforementioned HYSPLIT model [*Draxler and Rolph*, 2003] at 500, 1500 and 3500 m (agl). Particularly, during this night backward trajectories at all the altitudes were coming from the North-Atlantic and the Iberian Peninsula, bringing warm air masses with considerable water vapour content.
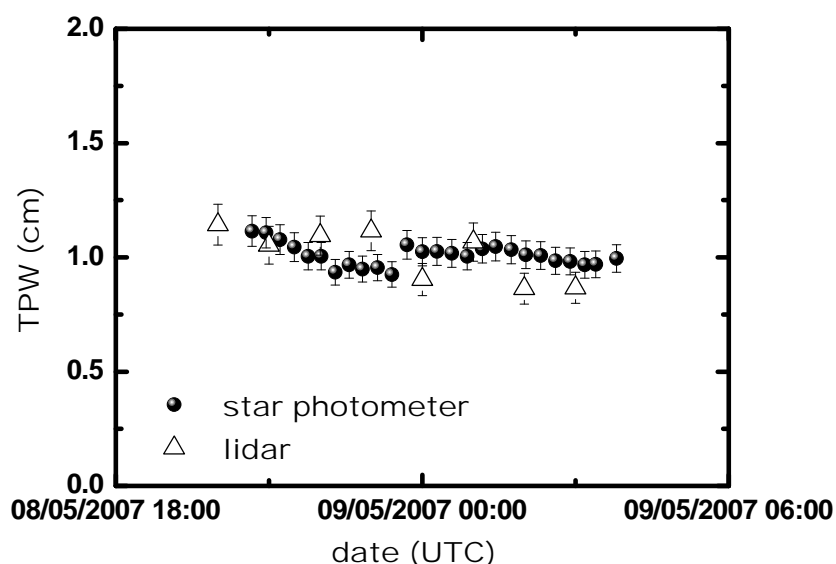

Figure 7.4. Precipitable water vapour retrieved during the night from 8th to 9th May 2007 using both the star-photometer and the lidar system. Bars correspond to the experimental errors on measurements.

7.5. Retrieval of relative humidity using Raman lidar and microwave radiometer

In this last section the retrieval of relative humidity profiles by mean of a Raman lidar and a microwave radiometer is discussed. Relative humidity (*RH*) is an important variable in the description of aerosol-cloud interaction and hygroscopic growth studies. Global radiosonde observations provide most of the *RH* information required as input in weather-forecast models [*Mattis et al.*, 2002]. But as we have indicated in previous sections the temporal resolution of routine observations performed by weather services

is rather low, typically with one or two radiosounding launches per day. Therefore important weather phenomena such as the development of the convective boundary layer and the passage of cold and warm fronts are not appropriately monitored.

On the other hand, the use of Raman lidars for the acquisition of information on aerosol and water vapour, which permits the study of the same air volume, is a powerful and attractive approach to studying aerosol-climate interactions, because the optical properties of particles strongly depend on relative humidity [*Hanel*, 1981]. At present, the rotational Raman lidar technology allows simultaneous measurements of temperature and water vapour mixing ratio profiles to retrieve *RH* profiles [*Di Girolamo et al.*, 2004]. The main problem is that the use of such system is not broadly used and the most common lidar systems only provide water vapour mixing ratio profiles. In this section we present *RH* profiles obtained from the combination of two instruments, namely microwave radiometer (described in section 3.2.3) and Raman lidar. As we have described in the previous section, Raman lidar technique is a powerful tool to retrieve mixing ratio profiles during night time. This information combined with continuous temperature profile observations obtained from a co-located microwave radiometer, allows for obtaining RH profiles.

Next, the main equations to retrieve *RH* from temperature and water vapour mixing ratio profiles are presented. *RH* is defined as the ratio of the actual amount of water vapour in the air compared to the equilibrium amount (saturation) at that temperature, and it can be calculated as

$$RH(z) = \frac{e(z)}{e_w(z)} \times 100 \tag{7.6}$$

where $e(z)$ is the water vapour pressure and $e_w(z)$ is the saturation pressure. The water vapour pressure is related to the water vapour mixing ratio as follows

$$e(z) = \frac{p(z)w(z)}{0.622 + w(z)} \tag{7.7}$$

where $p(z)$ is the air pressure and must be estimated from profiles of routine radiosounding measurements or by assuming standard atmospheric conditions. The use of an air pressure profile assuming a standard atmosphere (US 1976) scaled to a surface value measured at ground level in equation 7.7 leads to negligible errors in the computation of the water vapour pressure; therefore it will be used in our retrievals. On

the other hand, *RH* depends on the temperature as a function of the saturation vapour pressure according to [*List*, 1951]

$$e_w(z) = 6.107 \exp\left[\frac{M_A[T(z) - 273]}{M_B + [T(z) - 273]}\right]$$ (7.8)

with the constants $M_A = 17.84$ (17.08) and $M_B = 245.4$ (234.2) for T below (above) 273 K. The constant are taken from the 6th edition of the *Smithsonian Meteorological Tables* [*List*, 1951].

Figure 7.5 shows an example of comparison between *RH* profiles retrieved from combination of a Raman lidar and microwave radiometer and from radiosondes. The figure also shows the water vapour mixing ratio profiles retrieved from lidar and radisonde (7.5a) and the temperature profiles obtained from radiosonde and microwave radiometer (7.5b). The results correspond to night time measurements performed on 25th July 2011. Radiosonde was launched at 20:40 UTC and microwave radiometer and Raman lidar measurements were operating during time period 20:30-21:30 UTC. A water vapour mixing ratio profile from Raman lidar was computed following the procedure described in section 7.2. We can see a very good agreement in the water vapour mixing ratio retrieved from lidar and radiosonde (Fig. 7.5, a). The differences were lower than 5% below 3.5 km asl although they slightly increase (up to 8 %) above this altitude.

In Figure 7.5c, the *RH* profile (red line) was computed using the water vapor mixing ratio profile (Fig 7.5a) from lidar and the temperature profile from microwave radiometer (Fig. 7.5b) as we described in this section. The result shows a good agreement between both profiles. The largest discrepancies are found around 3.4 km (asl), where radiosonde reaches *RH* values around 15% larger than those retrieved from Raman lidar and microwave radiometer. These larger differences in *RH* are due to the deviation between the temperature measured with the radiosonde and those retrieved from microwave radiometer (Fig. 7.5b). The discrepancies between both temperatures profiles reached maximum values of 30% in these altitudes. However, the agreement in the rest of the RH profiles is quite good with relative differences below 10 %.
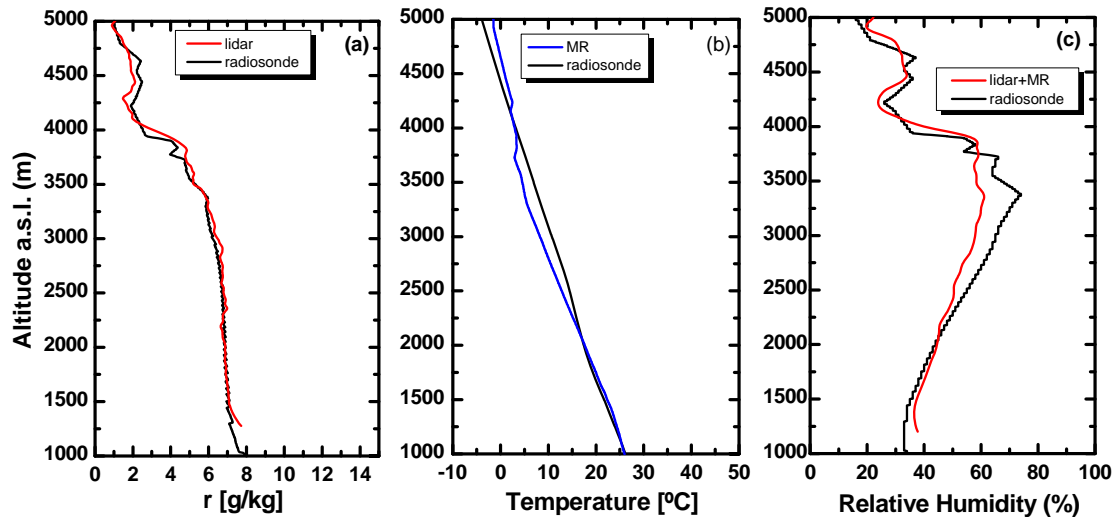
Figure 7.5. Night-time measurements performed on 25th July 2011. (a) Water vapour mixing ratio profiles retrieved from Raman lidar and radiosonde, (b) temperature profiles from microwave radiometer and radiosonde, and. (c) RH profile obtained from Raman lidar and microwave radiometer (MR) and from radiosonde.

RH profiles have been also obtained for the rest of the nights with coincident radiosoundings, therefore a total of six profiles were retrieved. A statistical analysis for the temperature and *RH* variables has been performed for these cases. Table 7.4 shows the mean absolute deviation between the temperatures obtained from microwave radiometer and from radiosondes at different height ranges. A mean absolute deviation of 1.2 ± 0.7 ºC is found for the whole column (0-5 km, agl). It can be seen that the absolute deviation of the temperature is lower than 1.0 ºC for the height range below 2 km (agl). We can observe that the discrepancies increase with the altitude reaching a maximum value of 2.1 ± 1.5 ºC between 4 and 5 km (agl). This increase in the temperature deviations with altitude could be explained by the loss of verticality in the radiosonde data. Moreover, the lower resolution of microwave radiometer in the far height range (see section 3.2.3) causes an increase in the errors for these regions. In fact, the largest deviations are found for those regions where there is a strong gradient in the temperature profile (e. g. inversions) since the microwave radiometer vertical resolution produces some artificial smoothing in the profile.

range [km]	mean (T) [ºC]	range [km]	mean (RH) [%]
0-1	0.3 ± 0.1	0.5-1	3.1 ± 1.4
1-2	0.8 ± 0.1	1-2	4.9 ± 2.2
2-3	1.4 ± 0.8	2-3	6 ± 3
3-4	1.5 ± 1.1	3-4	5.4 ± 2.2
4-5	2.1 ± 1.5	4-5	19 ± 12

Table 7.4. Mean absolute deviation (mean) for temperature and relative humidity profiles at different altitude ranges.

Table 7.4 also shows the absolute deviation between the *RH* profiles. The range selected for the comparison was 0.5-5 km (agl). The first 0.5 km closest to surface has not been taken into account in order to avoid a potential non-cancelation of the overlap functions at the nitrogen and water vapour channels. The mean absolute deviation in the *RH* between 0.5 and 5 km (agl) was 7 ± 6 %. The RH deviations change with altitude in a similar way as the temperature deviations. A loss of verticality of the radiosonde and the lower resolution of the microwave radiometer in the far height range could explain again theses discrepancies. Nevertheless, we can observe a low mean absolute deviation (below 6 % in RH) for *RH* profiles between 0.5 and 4 km (agl). These results show the capability to obtain *RH* profiles from the combination of Raman lidar and microwave radiometer with a high temporal and spatial resolution that is very useful in hygroscopic growth studies and allows for better understanding of other important phenomena related to water vapour in the lower troposphere.

7.6. Conclusions

This chapter presented the water vapour measurements performed with Raman lidar, star-photometer and radiosondes at the Granada station. Firstly, the methodology for obtaining water vapour mixing ratio profiles from Raman lidar was presented. A radiosonde field campaign was performed in order to retrieve the calibration constant for the lidar water vapour channel. Linear regression between the lidar and radiosonde data at the range 1.5-4.0 km (asl) was used to retrieve this constant. A robust iterative approach to obtain the best linear regression was introduced. A mean value of 186 ± 4 g/kg was obtained as the calibration coefficient for the whole campaign. The standard deviations in the calibration coefficient were found to be close to 2%. A good

agreement between radiosonde- and lidar-derived profiles was achieved. The mean absolute deviation between the lidar and sounding data was about 0.6 ± 0.6 g/kg in the altitude range 1.5-5.5 km (asl).

Moreover, a comparison of the TPW retrieved with a Raman lidar and a co-located star-photometer is presented. A strong correlation between both instruments (R^2 = 0.880) was obtained. The proximity of the data points to the 1:1 line as well as the slope (0.91 ± 0.06) and intercept (0.12 ± 0.06 cm) of the linear fit reflects the agreement between both datasets. This bias between the instruments is lower than the systematic uncertainties associated with the methodology.

Finally, mixing ratio water vapour profiles retrieved from Raman lidar combined with temperature profiles from a microwave radiometer allowed for obtaining RH profiles in the lower troposphere. A statistical analysis in terms of mean absolute deviation found that the mean absolute deviation for the temperature in the lower troposphere (0-5 km, agl) is around 1.2 ± 0.7 ºC. The discrepancies in the relative humidity were found around 7 ± 6 %. The errors were smaller (below 1.0ºC in the temperature and 5 % in the RH) for the first two kilometers of the atmosphere.

7.7. References

Alexandrov, M. D., B. Schmid, D. D. Turner, B. Cairns, V. Oinas, A. A. Lacis, S. I. Gutman, E. R. Westwater, A. Smirnov, and J. Eilers (2009), Columnar water vapor retrievals from multifilter rotating shadowband radiometer data, *Journal of Geophysical Research-Atmospheres*, *114*.

De Tomasi, F., and M. R. Perrone (2003), Lidar measurements of tropospheric water vapor and aerosol profiles over southeastern Italy, *Journal of Geophysical Research-Atmospheres*, *108*(D9).

Di Girolamo, P., R. Marchese, D. N. Whiteman, and B. B. Demoz (2004), Rotational Raman Lidar measurements of atmospheric temperature in the UV, *Geophysical Research Letters*, *31*(1).

Draxler, R. R., and G. D. Rolph (2003), http://www.arl.noaa.gov/ready/hysplit4.html*, Silver Spring, MD*.

Ferrare, R., et al. (2000), Comparison of aerosol optical properties and water vapor among ground and airborne lidars and Sun photometers during TARFOX, *Journal of Geophysical Research-Atmospheres*, *105*(D8), 9917-9933.

Ferrare, R. A., S. H. Melfi, D. N. Whiteman, K. D. Evans, F. J. Schmidlin, and D. O. Starr (1995), A comparison of water-vapor measurements made by Raman lidar and radiosondes, *Journal of Atmospheric and Oceanic Technology*, *12*(6), 1177-1195.

Guerrero-Rascado, J. L., B. Ruiz, G. Chourdakis, G. Georgoussis, and L. Alados-Arboledas (2008), One year of water vapour Raman Lidar measurements at the Andalusian Centre for Environmental Studies (CEAMA), *International Journal of Remote Sensing*, *29*(17-18), 5437-5453.

Han, Y., J. B. Snider, E. R. Westwater, S. H. Melfi, and R. A. Ferrare (1994), Observations of water-vapor by ground-based microwave radiometers and Raman lidar, *Journal of Geophysical Research-Atmospheres*, *99*(D9), 18695-18702.

Hanel, G. (1981), An attempt to interpret the humidity dependencies of the aerosol extinction and scattering coefficients, *Atmospheric Environment*, *15*(3), 403-406.

Held, I. M., and B. J. Soden (2000), Water vapor feedback and global warming, *Annual Review of Energy and the Environment*, *25*, 441-475.

Ismail, S., and E. V. Browell (1994), Recent lidar technology developments and their influence on measurements of tropospheric water-vapor, *Journal of Atmospheric and Oceanic Technology*, *11*(1), 76-84.

Kiehl, J. T., and K. E. Trenberth (1997), Earth's annual global mean energy budget, *Bulletin of the American Meteorological Society*, *78*(2), 197-208.

Leblanc, T., I. S. McDermid, and R. A. Aspey (2008), First-year operation of a new water vapor Raman lidar at the JPL table mountain facility, California, *Journal of Atmospheric and Oceanic Technology*, *25*(8), 1454-1462.

Leblanc, T., I. S. McDermid, and T. D. Walsh (2012), Ground-based water vapor raman lidar measurements up to the upper troposphere and lower stratosphere for long-term monitoring, *Atmospheric Measurement Techniques*, *5*.

List, R. J. (Ed.) (1951), *Smithsonian Meteorological Tables* Washington, D.C.

Mattis, I., A. Ansmann, D. Althausen, V. Jaenisch, U. Wandinger, D. Muller, Y. F. Arshinov, S. M. Bobrovnikov, and I. B. Serikov (2002), Relative-humidity profiling in the troposphere with a Raman lidar, *Applied Optics*, *41*(30), 6451-6462.

Miloshevich, L. M., A. Paukkunen, H. Voemel, and S. J. Oltmans (2009), Development and Validation of a Time-Lag Correction for Vaisala Radiosonde Humidity Measurements (vol 21, pg 1305, 2004), *Journal of Atmospheric and Oceanic Technology*, *26*(5), 1020-1020.

Perez-Ramirez, D., F. Navas-Guzman, H. Lyamani, J. Fernandez-Galvez, F. J. Olmo, and L. Alados-Arboledas (2012), Retrievals of precipitable water vapor using star photometry: assessment with Raman lidar and link to sun photometry, *Journal of Geophysical Research-Atmospheres*, *117*, D05202.

Reichardt, J., U. Wandinger, M. Serwazi, and C. Weitkamp (1996), Combined Raman lidar for aerosol, ozone, and moisture measurements, *Optical Engineering*, *35*(5), 1457-1465.

Schmid, B., et al. (2001), Comparison of columnar water-vapor measurements from solar transmittance methods, *Applied Optics*, *40*(12), 1886-1896.

Soden, B. J., S. A. Ackerman, D. O. Starr, S. H. Melfi, and R. A. Ferrare (1994), Comparison of upper-tropospheric water-vapor from GOES, Raman lidar, and cross-chain Loran atmospheric sounding system measurements, *Journal of Geophysical Research-Atmospheres*, *99*(D10), 21005-21016.

Vaughan, G., D. P. Wareing, L. Thomas, and V. Mitev (1988), Humidity measurements in the free troposphere using Raman backscatter, *Quarterly Journal of the Royal Meteorological Society*, *114*(484), 1471-1484.

Whiteman, D. N. (2003), Examination of the traditional Raman lidar technique. II. Evaluating the ratios for water vapor and aerosols, *Applied Optics*, *42*(15), 2593-2608.

Whiteman, D. N., S. H. Melfi, and R. A. Ferrare (1992), Raman lidar systems for the measurement of water vapor and aerosols in the Earth's atmosphere, *Applied Optics*, *31*(16), 3068-3082.

Whiteman, D. N., et al. (2006), Raman lidar measurements during the International H2O Project. Part I: Instrumentation and analysis techniques, *Journal of Atmospheric and Oceanic Technology*, *23*(2), 157-169.

7. Retrievals of water vapour measurements by Raman lidar

Chapter 8

Retrieval of microphysical aerosol properties from extinction and backscatter lidar data

This chapter focuses on the retrieval of atmospheric aerosol microphysical properties by means of Raman lidar measurements. A brief description of the methodology used to retrieve microphysical properties of spherical aerosol particles is presented. The retrieval procedure is applied to two special situations. The first one corresponds to a fresh biomass burning episode; it was the first comprehensive study of optical and microphysical properties of particulate pollution that describes rather fresh biomass burning aerosol. The second case corresponds to the detection of volcanic particles originated from Eyjafjallajökull volcanic eruption, this is the first study based on Raman lidar retrieval approaching the characterization of volcanic sulphate particles in the lower troposphere, including optical and microphysical properties.

8.1. Introduction

A better understanding of the importance of atmospheric aerosol particles in atmospheric processes requires an investigation of the spatio-temporal variability of their chemical and physical properties. These properties include their mean size, their volume or mass, surface-area and number concentrations, and their complex refractive index. A detailed knowledge of the role of particles in the atmosphere can only achieved by an adequate vertical profiling of these properties. For this purpose, a variety of methods have been proposed since the early 1970s, being multiwavelength Raman lidar a promising technique for determining the atmospheric aerosol microphysical properties. These methods can basically be classified into three distinct groups. The first group deals with the combinations of a monostatic lidar with some other instruments, e.g., in situ instruments carried aboard an aircraft [*Grams et al.*, 1972] or balloon [*Wandinger et al.*, 1995]. The second one is the combined use of lidar with a sun-photometer [*Reagan et al.*, 1977; *Chaikovsky et al.*, 2010]. The drawback for both cases is that two co-located instruments are needed simultaneously in order to provide reliable data on the same particles. Moreover, the different observational geometry of the involved instrumentation has to be deemed. In particular, the lidar and sun-photometer point in different directions, i.e., away from the sun and into the sun, respectively. For that reason, the constraint of observations of the same ensemble of particles cannot be strictly fulfilled, and thus represents an additional source of error. Finally, the third group is a rigorous mathematical approach on the basis of multiwavelength lidar observations [*Uthe*, 1982]. In that respect the technically robust setup of monostatic Raman lidars is almost exclusively considered.

The method of inversion with regularization is the standard application for the retrieval of particle microphysical properties from multiwavelength aerosol lidar measurements [*Müller et al.*, 1999b; a; *Veselovskii et al.*, 2002; *Ansmann and Müller*, 2005a]. The method uses the spectral information contained in the backscatter and extinction profiles at several wavelengths and its change with the particle size [*Müller et al.*, 1999a; *Veselovskii et al.*, 2002]. A set of two extinction and three backscatter coefficients can be considered as the optimum choice for the specifications of an aerosol lidar [*Veselovskii et al.*, 2002], if simplifications like wavelength- and size–independence for the complex refractive index of tropospheric particles are considered.

The three standard wavelengths of a Nd:YAG laser, i.e., 355, 532, and 1064 nm, are the minimum number of wavelengths for particle characterization [*Bockmann*, 2001; *Müller et al.*, 2001; *Veselovskii et al.*, 2002], under the above-mentioned simplifications for the complex refractive index. The high requirement for the Raman lidar specifications along with the need of high quality optical properties profiles justifies the absence of systematic aerosol microphysical studies. Moreover, the method is designed to be applied to optical data of spherical particles, therefore preventing its application to the study of highly non-spherical particles such as mineral dust. The basic properties of the successful algorithms used for the retrieval of microphysical particle properties will be discussed below. From our lidar profiles database, two special events with different particle types have been selected to illustrate the reliable application of this method. The first one corresponds to fresh biomass burning aerosol [Alados-Arboledas et al., 2011] and the second one to volcano sulphate particles. Both cases are presented and discussed along this chapter.

8.2. Microphysical inversion algorithm

The inversion method of regularization with constraints [*Tikhnonov and Arsenin*, 1977] is the standard method for the retrieval of particle microphysical properties from multiwavelength Raman lidar observations [*Müller et al.*, 1999a; *Wandinger et al.*, 2002]. Profiles of particle microphysical properties follow from the numerical inversion of the vertically and spectrally resolved particle backscatter and extinction coefficients. The optical data are related to the physical quantities by the Fredholm integral equations of the first kind:

$$g_i(\lambda_k) = \int_{r_{\min}}^{r_{\max}} K_i(r,m,\lambda_k,s)v(r)dr + \varepsilon_i^{\exp}(\lambda_k)$$

$$i = \beta_{aer}, \ \alpha_{aer}, \quad k = 1, \ldots, n \tag{8.1}$$

The term $g_i(\lambda_i)$ denotes the optical data at wavelengths λ_k in a specific height R. For the sake of simplicity, references to height R will be omitted in the following discussion. The subscript i denotes the kind of information, i.e., whether it is the particle backscatter (β_{aer}) or extinction (α_{aer}) coefficient. Data have an error $\varepsilon_i^{exp}(\lambda_k)$. The expression $K_i(r,m,\lambda_k,s)$ describes the kernel efficiencies for backscatter and extinction, respectively. They depend on the radius r of the particles, their complex refractive index

m, the wavelength λ_k of the interacting light, as well as the shape s of the particles. For spherical particle geometry, the kernel functions $K_i(r,m,\lambda_k,s)$ are calculated from the respective extinction and backscatter efficiencies $Q_i(r,m,\lambda_k)$ for individual particles [*Bohren and Huffman*, 1983] weighted with their geometrical cross section πr^2:

$$K_i(r,m,\lambda_k) = \pi r^2 Q_i(r,m,\lambda_k) \tag{8.2}$$

The term $v(r)$ describes the volume concentration of particles per radius interval dr. The lower integration limit is defined by r_{min}, the radius down to which particles are optically efficient.

With the subscript $p = (i, \lambda_k)$ summarizing the kind and wavelength of optical data, Equation (8.1) is rewritten into the following form:

$$g_p = \int_{r_{min}}^{r_{max}} K_p(r,m)v(r)dr + \varepsilon_p^{exp} \tag{8.3}$$

Equation (8.3) can not be solved analytically [*Twomey*, 1977]. The numerical solution process leads to the so-called ill-posed inverse problem [*Bockmann*, 2001], which is characterized by the incompleteness of the available information, the non-uniqueness of the solutions, and the non-continuous dependence of the solutions on the input data. Even uncertainties as small as round-off errors in the input data lead to disproportionately large changes in the final solution.

The instability of the solutions can only be controlled by introducing meaningful boundary conditions. To minimize the number of *a priori* assumptions in the retrieval, $v(r)$ is composed of a linear combination of triangular base functions $B_j(r)$ and weight factors w_j as

$$v(r) = \sum_j w_j B_j(r) + \varepsilon^{math}(r) \tag{8.4}$$

The right-hand side of Eq. (8.4) contains the mathematical residual error $\varepsilon^{math}(r)$ that is caused by the approximation with base functions. The index j denotes the number of the applied base functions which is typically set to 8 [*Müller et al.*, 1999b] [*Veselovskii et al.*, 2002].

In general the exact position of the investigated particle size distribution along the size range used by Eq. (8.3) is not known. The problem is overcome by the use of a

so-called inversion window of variable width and variable position along the investigated size range [*Müller et al.*, 1999b]. No sensible solutions are obtained if the inversion window does not cover the position of the investigated particle size distribution. In that respect, the sliding inversion window can be regarded as a filter function. Currently 50 different inversion windows within the particle size range from 0.01 to 10 μm are used to obtain an estimate of the position of the particle size distribution [*Müller et al.*, 1999b; *Veselovskii et al.*, 2002].

The weight factors follows from inserting Eq. (8.4) into (8.3), and rewriting it into a vector-matrix equation:

$$\mathbf{g} = \mathbf{Aw} + \boldsymbol{\varepsilon} \tag{8.5}$$

The optical data are written as vector $\mathbf{g} = [g_p]$, the weight factors are denoted by $\mathbf{w} = [w_j]$, and the errors are described by $\boldsymbol{\varepsilon} = [\varepsilon_p]$. $\varepsilon_p = \varepsilon_p^{exp} + \varepsilon_p^{math}$ is the sum of experimental and mathematical errors. The matrix $\mathbf{A} = [A_{pj}]$ is called weight matrix [*Twomey*, 1977]. Its elements are given by

$$A_{pj}(m) = \int_{r_{min}}^{r_{max}} K_p(r,m)B_j(r)dr \tag{8.6}$$

The simple solution of Eq. (8.5) for the weight factors,

$$\mathbf{w} = \mathbf{A^{-1}}\,\mathbf{g} + \boldsymbol{\varepsilon'} \tag{8.7}$$

fails to provide reasonable results [*Twomey*, 1977] although the optical data can be reproduced within the error limits $\boldsymbol{\varepsilon}$. It is explained by the high dynamic range of several orders of magnitude of the elements of $\mathbf{A}$ and $\mathbf{A^{-1}}$ [*Twomey*, 1977; *Müller et al.*, 1999a]. Therefore the term $\boldsymbol{\varepsilon'} = -\mathbf{A^{-1}}\,\boldsymbol{\varepsilon}$, which describes the respective errors, and $\mathbf{A^{-1}}$, which denotes the inverse of the matrix $\mathbf{A}$, lead to error amplification and discontinuity of the solutions.

Therefore, a procedure called regularization is introduced. It is used to reduce the number of solutions by restricting the highest acceptable difference between the vector $\mathbf{Aw}$ and $\mathbf{g}$ to

$$e^2 \geq \left\| \varepsilon \right\|^2 = \left\| Aw - g \right\|^2 + \gamma \Gamma(v) \tag{8.8}$$

Only solutions that minimize $\boldsymbol{\varepsilon}$ are accepted. The penalty term $\Gamma(v)$ is controlled by the Lagrange multiplier γ and suppresses oscillations in the resulting particle size distribution. It is defined as

$$\Gamma(v) = \mathbf{w}^{\mathrm{T}}\mathbf{H}\mathbf{w} \tag{8.9}$$

$\mathbf{w}^{\mathrm{T}}$ is the transposed vector $\mathbf{w}$. The matrix $\mathbf{H}$ contains the demand for smoothness which stretches over three base functions. Finally, the weight factor is retrieved as

$$\mathbf{w} = (\mathbf{A}^{\mathrm{T}}\mathbf{A} + \gamma\,\mathbf{H})^{-1}\mathbf{A}^{\mathrm{T}}\mathbf{g} \tag{8.10}$$

For one input data set only a fraction of the solutions of the inversion algorithm represents trustworthy results. This needs a careful analysis of the inversion output. At the end, several hundred trustworthy solutions out of hundreds of thousands of mathematical inversion results are averaged. A mean aerosol number concentration and a mean complex refractive index are obtained. The surface-weighted (effective) mean radius is calculated as the ratio of surface–area and volume concentrations as

$$r_{eff} = \frac{\int v(r)r^3\,dr}{\int v(r)r^2\,dr} \tag{8.11}$$

and used as a measure of mean particle size. Finally, the single scattering albedo is calculated from the retrieved parameters by means of Mie calculations.

Simulations with monomodal and bimodal logarithmic-normal size distributions show that it is possible to derive effective radius, volume, and surface-area concentrations to an accuracy of ±50%, the real part of the complex refractive index to ±0.05, and the imaginary part to ±50%. Number concentrations may have errors larger than ±50% [*Müller et al.*, 1999b].

Currently only cases of spherical particles are considered for this inversion scheme. Any non-sphericity effect will be another source of error. For a description of these errors, models are necessary that permit us to calculate the backscattering and the extinction behaviour and the difference with respect to spherical scatterers. At present, lidar microphysical algorithms developers are working on these issues to improve the current capabilities.

8.3. Case studies

In this section two examples of optical and microphysical retrievals from Raman lidar measurements are presented. Optical properties were retrieved by means of the methodology described in chapter 4 while the microphysical properties were obtained using the algorithm with regularization described in the previous section. Fresh biomass burning aerosol and volcano sulphate particles will be analyzed below.

8.3.1 Fresh biomass burning episode

Knowledge on smoke particles from fires has attained specific interest in recent years. Smoke is an important source of black carbon that is a key component in atmospheric heating by aerosol pollution. Smoke particles can experience medium-to long-range transport and only scarce information is available on particle transformation processes such as particle growth during transcontinental transport. Despite its importance observations of vertically resolved optical and microphysical properties of smoke are still few and scarce. Lidar active remote sensing can overcome this gap in our understanding of the impact of these aerosol particles as it provides vertical profiles of aerosol properties. Several authors [*Ferrare et al.*, 1990; *Radke et al.*, 1995; *Müller et al.*, 2007a] present some evidences of particle growth on the basis of height-resolved lidar measurements of forest-fire smoke in the FT. However, an important gap in these studies is the observation of smoke plumes near the sources of forest fires (fresh smoke) in mid-latitudes. In this section, a fresh biomass burning plume is characterized by means of a multiwavelength Raman lidar, a star- and a sun-photometer very close to the source region, i.e., transport time was about 24-36 hours. This was the first time that such observations were carried out. This study contributes to previous studies on aged smoke particle, in particular concerning the first stages of the smoke transport and the vertical changes of some smoke-related properties. Furthermore, this measurement case shows the merit of such type of combined instrument observations. We may derive a better interpretation on the basis of an analysis of combined data set, which may not be possible if we had only data sets from a single instrument. Furthermore data from one instrument may compensate for a loss of data from another instrument.

The observations presented in this section were made with the Raman lidar, star- and sun-photometer located at the CEAMA. Multiwavelength Raman lidar was used for

vertically resolved measurements of particle optical properties of the biomass-burning plume discussed in this section.

AOD was measured at night-time with the star-photometer Excalibur (section 3.2.2). At daytime AOD was measured with an AERONET Cimel radiometer CE-318-4 [*Holben et al.*, 1998] (section 3.2.1). Level 2.0 data from AERONET are available for the measurements presented here. Optical data were used to retrieve microphysical properties by means of the inversion algorithm described in section 8.2. For the lidar retrievals, we computed mean backscatter and extinction coefficients for layers of 500 m geometrical thickness. We derive particle size and complex refractive index from which we compute single scattering albedo from the Mie-scattering algorithm, i.e. the fresh smoke particles are assumed to be spheres. The same inversion algorithm is used for the analysis of the AOD data from sun- and star- photometer. In that case we can only retrieve particle size [*Pahlow et al.*, 2006]. The error bars of the microphysical properties follow from the errors of the input optical data and the uncertainties that are generated by the inversion algorithm. We apply a search grid of complex refractive indices (from 1.3 to 1.8 in real part and from 0i to 0.1i in imaginary part) and particle size parameters (from 10 nm to 5 μm in particle radius) which automatically causes approximation errors [*Ansmann and Müller*, 2005b]. The uncertainties of single scattering albedo follow from the uncertainties of the retrieved particle size distributions and the complex refractive indices.

Next we present the results observed on 24th September, 2007. Figure 8.1a shows that AOD and AE evolution retrieved from sun- and star-photometer during night and day-time on 24th and 25th September. It shows that AOD increased on 24th September, with maximum values around sunset, in coincidence with AE around 1.3.
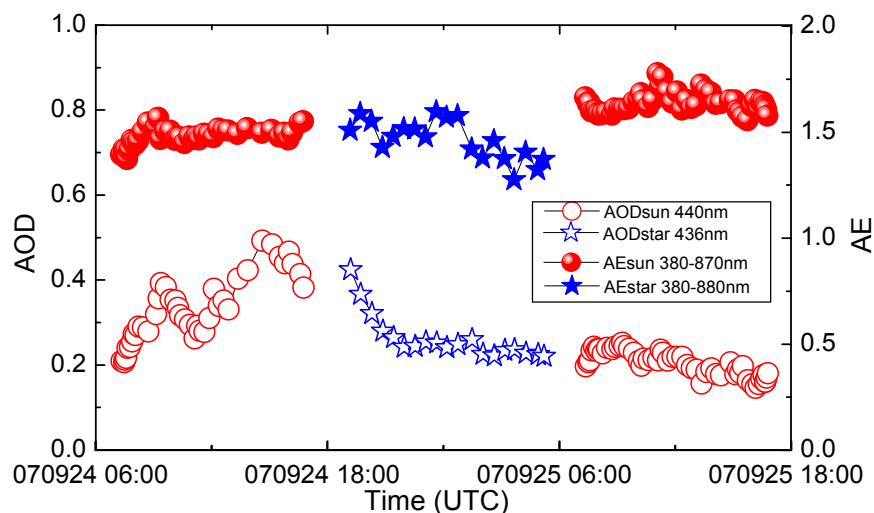
Figure 8.1. Series of AOD and AE measured with sun- and star-photometer in Granada on 24th -25th September 2007.

According to weather maps and backward-trajectory (Fig. 8.2a), it is evident that the synoptic conditions over our station favoured recirculation of air and air mass stagnation below 2 km (asl). Air flow was from westerly to northerly direction at least up to 5 km (asl). Simulations with NAAPS model predicted the presence of smoke plumes with particle concentrations up to 4mg/m^3 over Granada and up to 16 mg/m^3 over the western Iberian Peninsula (Fig. 8.2b). Fire MODIS Products (http://firms.modaps.eosdis.nasa.gov/firemap/) indicated a hot spot (at 37.798°N and 3.787°W) around 70 km from Granada in the period from 22nd -24th September. Using the coordinates of these fires at the early stages, obtained from satellite images, and our remote sensing data we estimated the approximate time when the plume arrived over Granada. This information suggests around 24–36 hours of transport time of the fresh biomass burning particles. AOD again decreases in the early evening (Fig. 8.1). On the basis of our remote sensing data we believe that this decrease was in part caused by inhomogeneities of the smoke plume. We do not have enough information to judge if this decrease in AOD is also caused by local effects related to the pollution loading in the PBL.
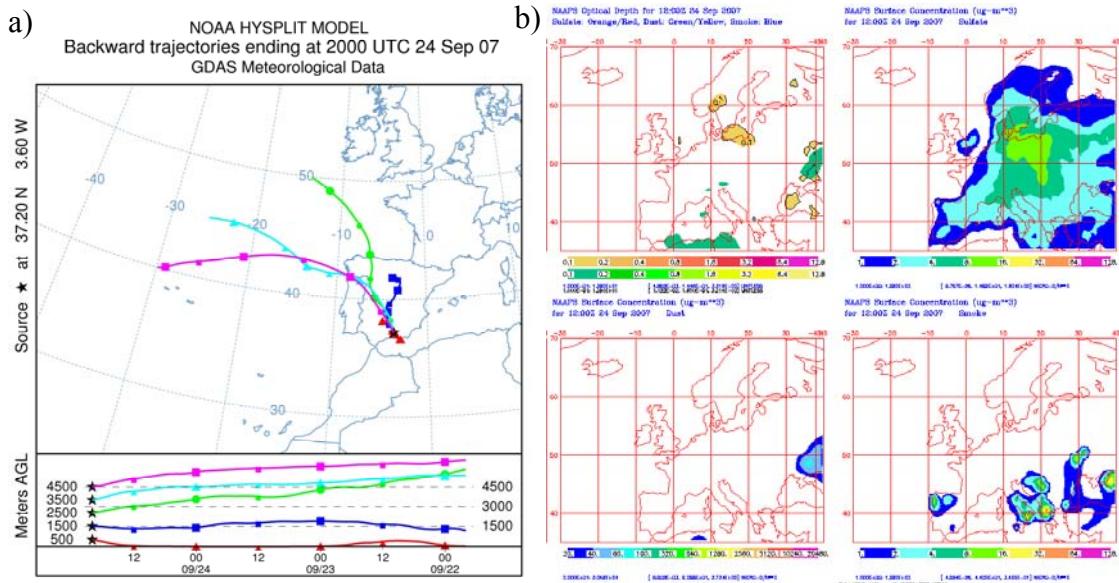
Figure 8.2. a) Backward trajectories analysis from NOAA HYSPLIT model ending at Granada (20 UTC, 24th September 2007), b) Naaps model prediction for AOD, sulphate concentration, dust concentration and smoke concentration.

Figure 8.3 shows in more detail the spectral dependence of AOD measured with the three instruments. Measurement times are around 16:45 UTC for the sun-photometer, around 19:42 UTC for the star-photometer and between 19:03-20:03 UTC for the lidar. AOD from lidar in the overlap region was computed assuming a constant extinction from the minimum height (around 970 m agl) where Raman retrieval is possible down to the surface. A good agreement is observed among these data. Due to the different features of the instruments we do not have a temporal overlap of the measurements provided by the three instruments. Temporal evolutions of the RCS do not indicate any significant change of the plume properties during the measurement period that was used for this comparison of spectral dependencies. For comparison Figure 8.3 also shows the mean spectral optical depth from sun-photometer measurements (red bullets) for September 2004–2008. The mean AE at 440-870 nm for this period is 1.1 ± 0.5.
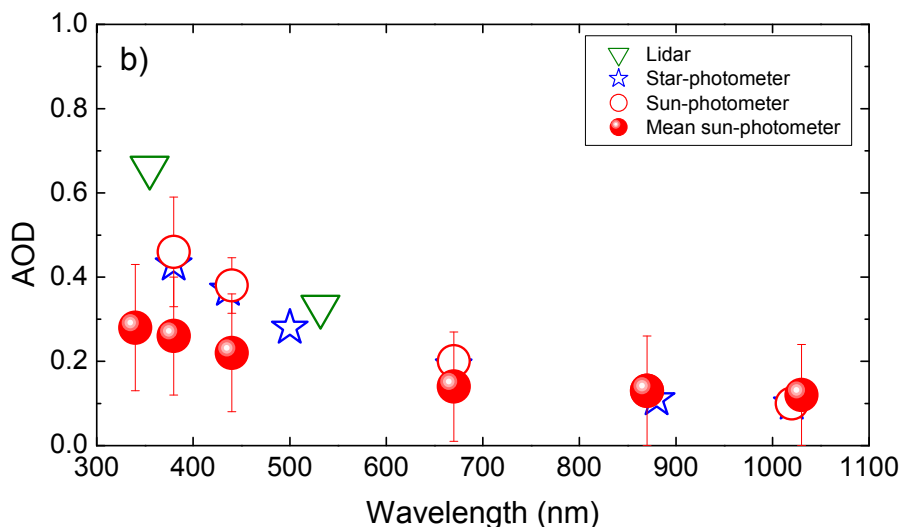
Figure 8.3. Spectral dependence of aerosol optical depth derived from lidar, sun- and star-photometer measurements.

Figure 8.4 shows the aerosol layering on 24th September. The optical profiles show the presence of aerosol particles up to 4 km asl. About 50% of AOD at 532 nm is contributed by the aerosol layer above 2 km asl; cf. AOD shown in Figure 8.1. In the following we discuss our results for the height range from 2.0 to 3.5 km. In that height range extinction and backscatter coefficients are not negligible (>1 $Mm^{-1} \cdot sr^{-1}$ at 532 nm) and lidar misalignment effects are negligible.

The LR are around 60–65 sr at 355 and 532 nm. For comparison, Amiridis *et al.* [2009], reporting on biomass burning smoke produced over East Europe, find increasing LR from 40 sr to nearly 100 sr (at 355 nm) for smoke plumes that increase in age from 7 days to 16 days. Values between 21 and 67 sr at 355 nm are reported by Müller *et al.* [2005] for biomass burning smoke advected from North America and Siberia to Germany after up to 2.5 weeks of transport time. LRs of 40 sr and 65 sr at 355 nm and 532 nm, respectively, were observed for Siberian forest fire smoke over Japan after approximately 4 days of transport time [*Murayama et al.*, 2004]. LR depends on size, shape and chemical composition of the particles, which in turn depend on kind of burned biomass, intensity of the fire, and many other additional factors. The complex influence of various parameters may be the reason that there is no clear pattern of LR change at a given wavelength with the age of the smoke plume. More interestingly the ratio of the LR (value at 355 nm to value at 532 nm) for the case of fresh smoke presented here is around unity, whereas the ratio for aged fire smoke is less than one

[*Murayama et al.*, 2004; *Müller et al.*, 2005]. The differences in this ratio confirm the initial assumption that we observe comparably fresh smoke over Granada. Up to now it was observed ratios less than unity for aged, long-range-transported smoke [*Müller et al.*, 2007b].
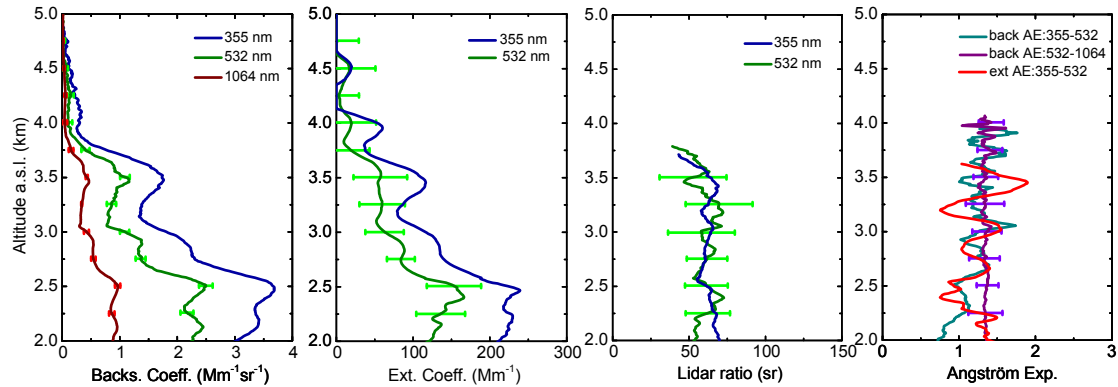

Figure 8.4. Mean profiles of aerosol optical properties (extinction coefficients, backscatter coefficients, LR, β-AE and α-AE for the measurement from 19:03 to 20:03 UTC on 24th September 2007. Error bars denote one-standard deviation.

β-AEs and α-AEs in the spectral range 355-532 nm are between 1.0 and 1.5. These numbers indicate that particles in the accumulation mode are dominant, which is a typical feature of smoke particles from fires. For comparison, aged smoke particles (after long-range transport of several days) show α-AE close to zero and β-AE of approximately one [*Wandinger et al.*, 2002; *Müller et al.*, 2005].

Table 8.1 presents effective radius (r_{eff}), real (m_{real}) and imaginary (m_{imag}) part of the complex refractive index, and single scattering albedo (ω) for several 500-m layers. We also show column-integrated values of effective radius obtained from the inversion of AOD measured with star- and sun-photometer. Table 8.1 shows excellent agreement of effective radius derived from the active and passive remote sensing data. The columnar-integrated effective radii tend to be slightly higher than those retrieved from lidar although all retrieved radii are below 0.2 μm. At our station, typical values of effective radius retrieved from sun-photometer for total, fine and coarse mode are 0.40 ± 0.17 μm, 0.13 ± 0.02 μm, and 2.2 ± 0.4 μm, respectively. The numbers describe the period from 2004 to 2008 (AERONET level 2 data).

	Range (km asl)	α-AE (355-532)	r_{eff} (μm)	m_{real}	m_{imag}	ω_{355}	ω_{532}	ω_{1064}
Lidar	2.0-2.5	1.16±0.22	0.17±0.06	1.49±0.12	0.022±0.018	0.76±0.14	0.80±0.13	0.86±0.11
	2.5-3.0	1.20±0.16	0.15±0.05	1.53±0.13	0.023±0.017	0.78±0.13	0.83±0.12	0.87±0.11
	3.0-3.5	1.3 ± 0.4	0.13±0.03	1.53±0.14	0.022±0.017	0.83±0.10	0.87±0.08	0.90±0.07
StP	column	1.61± 0.10	0.19±0.05					
SPM	column	1.34± 0.08	0.20±0.05					

Table 8.1. Mean aerosol microphysical properties derived from the lidar profiles, and columnar-integrated microphysical properties. Shown are effective radius (r_{eff}), real (m_{real}) and imaginary (m_{imag}) part of the complex refractive index and single scattering albedo at 355, 532 and 1064 nm (ω_{355}, ω_{532}, ω_{1064}). Also shown is the AE from the extinction measurements with lidar (355/532 nm) and from AOD measured with sun-photometer (380/500 nm). The lidar results hold for the measurement from 19:03 to 20:03 UTC on 24th September 2007. Results for star- and sun-photometer hold for the measurement around 19:42 UTC and 16:45 UTC, respectively.

Effective radii found in this study are lower than those obtained for long-range transport of aged Siberian forest fire smoke over Japan, i.e., 0.22 ± 0.04 μm [*Murayama et al.*, 2004]. An effective radius of around 0.25 μm was determined during LACE98 for a long-range transported biomass burning plume that originated from forest fires in northwestern Canada [*Wandinger et al.*, 2002]. O'Neill *et al.* [2002] presents optical and microphysical properties of fire smoke observed with sun-photometer close to the source region in Canada. These authors report on effective radii around 0.14 μm. Our values for particle effective radius fall within this broad range of numbers. Müller *et al.* [2007a] present a study of particle growth during long-range transport of forest-fire smoke derived from Raman lidar and sun-photometry observations. The authors find a parameterization which describes particle growth with transport time. Interestingly our results on particle size fall onto this particle growth curve. However, AE from Granada results shows slightly lower values than the curve fit presented for this property (Fig. 8.5).
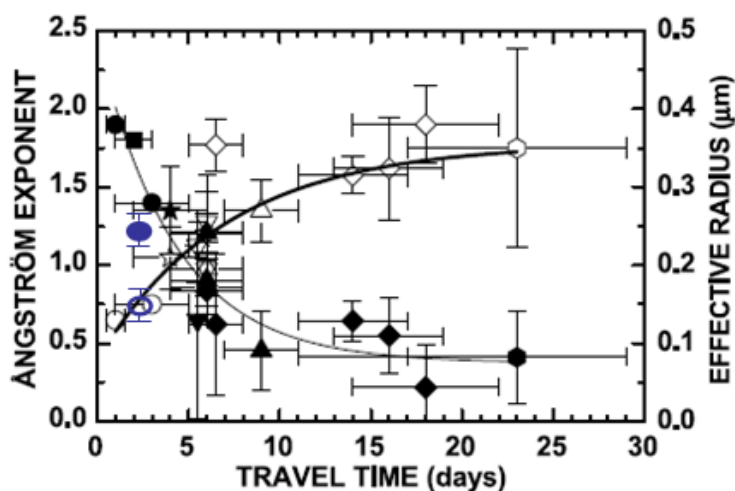
Figure 8.5. AE (closed symbols and thin trace from curve fit) and effective radius (open symbols and thick trace from curve fit) of forest-fire smoke versus transport time. These results were published by Müller et al. [2007]. Granada lidar results are shown as blue symbols in this plot.

Physical and chemical processes like particle coagulation and particle-size specific sedimentation, as well as gas-to-particle condensation processes may be responsible for the observed particle size. Also the specific properties of the burnt material and the burning processes (flaming versus smoldering fire) may generate different particle sizes at the source of the fires. However, we know too little of this processes and the causes of particle size modification during atmospheric transport, and thus an explanation on why particle size reported here fits to this parameterization must be left open for future studies.

Table 8.1 also presents the complex refractive index. The real part varies between 1.49 and 1.53. The imaginary part is 0.02i. Both real and imaginary parts are quite constant with altitude, given the comparably large uncertainties. For comparison a summary of highly absorbing smoke particles for different regions on the globe (South America, South India) is given by Müller *et al.* [2005]. Real parts range from 1.5 to 1.66 at visible wavelengths. Imaginary parts cover values from 0.01i to 0.07i. The complex refractive indices reported in these references do not show a clear pattern of change of imaginary part with transport time. Crucial information such as air mass transport times, as well as kind of burnt material and type of fires is missing. For this reason any further interpretation of our results regarding change of particle light-absorption with age of particles cannot be done.

172

The single scattering albedo slightly increases with altitude (Table 8.1). The values vary between 0.76 and 0.90 with a slightly positive spectral dependence. These values are in the range of those encountered in the literature. Murayama *et al.* [2004] reported a single scattering albedo of 0.95 ± 0.06 at 532 nm around the peak of a Siberian forest fire smoke event over Japan. O'Neill *et al.* [2002] retrieved single scattering albedo in the range 0.97 to 0.99, 32 km away from the biomass burning aerosol sources. Alados-Arboledas *et al.* [2007] obtained single scattering albedoes ranging from 0.80 to 0.87 (in the spectral range 440–1020 nm) for a lofted smoke plume monitored at a high mountain station with sun-photometer. Wandinger *et al.* [2002] found single scattering albedoes of 0.76 ± 0.06 and 0.81 ± 0.05 at 355 and 532 nm, respectively, for forest-fire smoke transported from western Canada. Eck *et al.* [2009] found values above 0.95 at visible wavelengths for smoke from smoldering forest fires observed with sun-photometer in Alaska. Reid *et al.* [2005] reported that single scattering albedo of biomass-burning aerosols typically decreases with increasing measurement wavelength. We are cautious though with a respective interpretation of our results for single scattering albedo. The inversion procedure applied to the lidar profiles does not consider any spectral dependence of the refractive index. Thus, the spectral dependence of single scattering albedo is only driven by the effect of the particle size distribution.

8.3.2 Eyjafjallajökull volcanic plume case

The Eyjafjallajökull volcano in southern Iceland (63.63° N, 19.61° W) started to erupt on 20th March 2010. The first phase was characterized by an effusive eruption that produced lava flows on the ground and only minor emissions into the atmosphere. On 14th April an explosive eruption started a period with major activity that lasted until 22nd May 2010 [*Emeis et al.*, 2011]. After 14th April the volcanic plume drifted from Iceland to Central Europe due to strong westerly winds, causing the closure of most of the European airspace with the subsequent economic impact. The synoptic conditions did not favour the arrival of the volcanic plume over the Iberian Peninsula until 5th May [*Sicard et al.*, 2012].

Volcanic eruptions emit ash, water vapour, and other gases into the atmosphere. Furthermore, water vapour and sulphur dioxide injected into the stratosphere during

particularly explosive events can produce global veils of sulphuric acid droplets that affect the Earth's climate [*Robock*, 2000]. On the other hand, volcanic ash is composed of non-spherical mineral particles with a large range of sizes [*Gislason et al.*, 2010]. In the troposphere these particles can cause hazard to humans and machinery on the ground, as well as damage to aircraft that fly through ash plumes [*Miller and Casadevall*, 2000].

The Eyjafjallajökull volcanic aerosol plume has been characterized with remote sensing techniques at different locations in Europe [*Ansmann et al.*, 2010; *Ansmann et al.*, 2011; *Emeis et al.*, 2011; *Mona et al.*, 2011]. A unique combination of Raman lidar, sun- and star-photometer allowed us to characterize the optical and microphysical properties of the volcanic plume that was observed over Granada from 5th to 8th May 2010.

As we mentioned above the volcanic plume arrived over the Iberian Peninsula for the first time on 5th May 2010. During this time a high-pressure system located over southern Iceland and western Ireland and a low-pressure system over southern France caused the flow of the volcanic plume towards the Iberian Peninsula [*Sicard et al.*, 2012]. Volcanic particles were observed with different instrumentation at Granada (Spain) during the period from 5th to 13th May. In this study we focus on optical and microphysical properties of the volcanic plume in the lower troposphere retrieved during the night from 7th to 8th May in Granada.

Figure 8.6 shows the evolution of AOD at 440 and 436 nm measured by the sun- and star- photometers, respectively. The same figure shows the AE values calculated in the wavelength ranges 440-870 nm and 440-880 nm for the sun- and star- photometers, respectively. Sun-photometer data correspond to AERONET level 2 data. There was an evident increase of AOD after 09:00 UTC on 7th May 2010. Night-time values were about 0.42-0.45. The AE was in the range of 1.2-1.3, indicating a predominance of fine-mode particles. After sunrise on 8th May, AOD decreased and the AE showed large variability (ranging from 1.4 to 0.6).
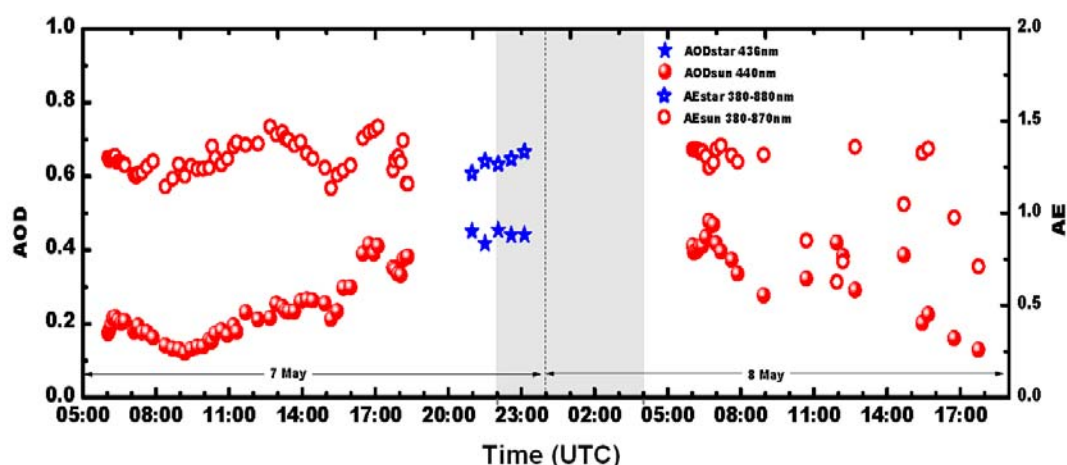
Figure 8.6. Time series of AOD (wavelength are given in the legend) and AE measured with sun- and star-photometer at Granada on 7th -8th May 2010.

Column-integrated volume size distributions retrieved using AERONET inversion algorithm [*Dubovik and King*, 2000; *Dubovik et al.*, 2006] show a clear increase in the fine-mode volume concentration between the morning of 7th May and the morning of 8th May. However, the coarse-mode volume concentration shows only a slight increase, indicating that there is no significant change in the presence of large particles during this period (Fig. 8.7a). Similar behaviour in the size distribution was observed at ground level in Madrid during this volcanic event, being this increase in the aerosol fine-mode coincident with an increase in ambient sulphate concentration [*Revuelta et al.*, 2012].

Figure 8.7. a) Columnar integrated size distributions retrieved by Cimel CE 318-4. Two size distributions for 7th and 8th of May are presented. b) Back-trajectories ending at Granada at different levels (500, 2500, 3500, 4500 m agl) at 22:00 UTC, 7 May 2010.

175

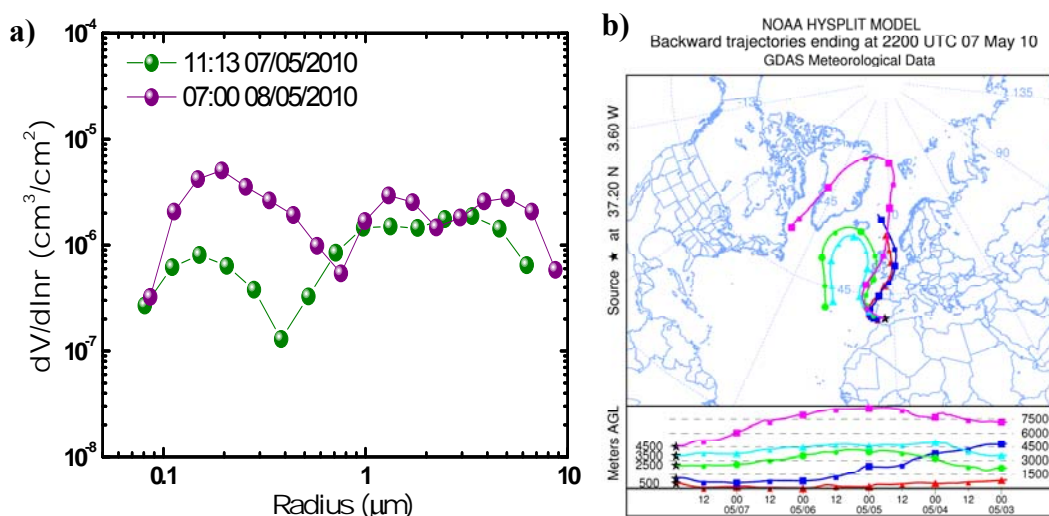Figure 8.8 provides an overview of the lidar observations performed during the night from 7th to 8th May in Granada. A multilayered structure is evident. A decoupled lofted aerosol layer was observed around 3 km (asl). According to backward trajectory analyses [*Draxler and Rolph*, 2003] the air mass at these levels comes from the volcano area (Fig. 8.7b). This layer descended during the night without being mixed with the aerosol in the PBL. Another aerosol layer underneath subsided and was mixed into the residual aerosol layer during the night. Patches of low clouds were present during some intervals perturbing the lidar observations at heights above 2 km asl.
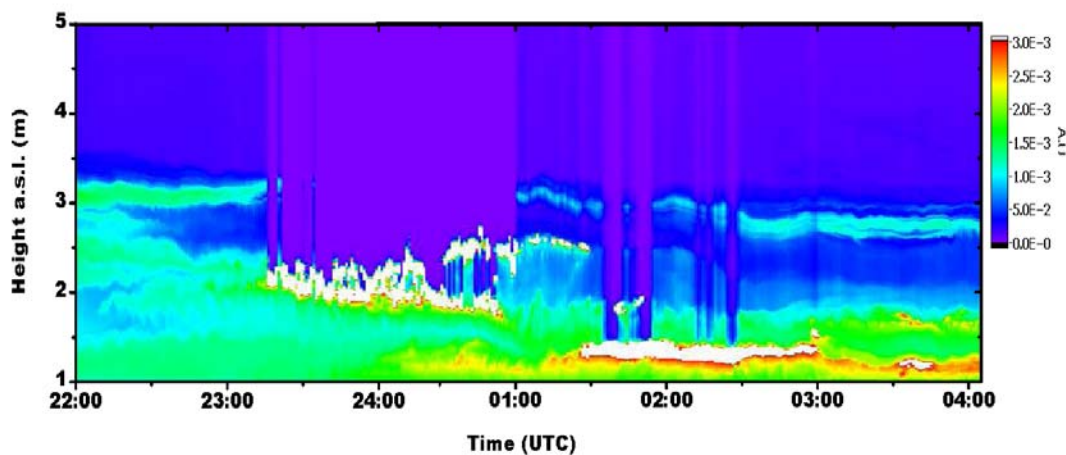
Figure 8.8. Temporal evolution of lidar RCS at 532 nm during night-time (7th -8th May, 2010).

Extensive and intensive vertically resolved aerosol optical properties changed during the night indicating a temporal evolution of the vertical distribution of the aerosol load and a possible change in chemical composition. Figure 8.9 shows aerosol optical properties at the beginning and the end of the night-time lidar observations. During the first measurement period (22:30-23:20 UTC on 7th May) the backscatter and extinction profiles show the presence of aerosol particles up to 3.5 km height (asl), with a decoupled layer between 2.7 and 3.5 km asl. Values of approximately $1 \cdot 10^{-5}$ m^{-1}sr^{-1} and $3.8 \cdot 10^{-4}$ m^{-1} for the backscatter and extinction coefficients, respectively, were retrieved in the centre of this layer. LRs are very similar at both wavelengths (355 and 532 nm), reaching values around 50 sr in the centre of the layer. These values are in agreement with values observed for stratospheric particles during other volcanic eruptions [*Mattis et al.*, 2010]. Similar values were also found at other stations during this volcanic event.
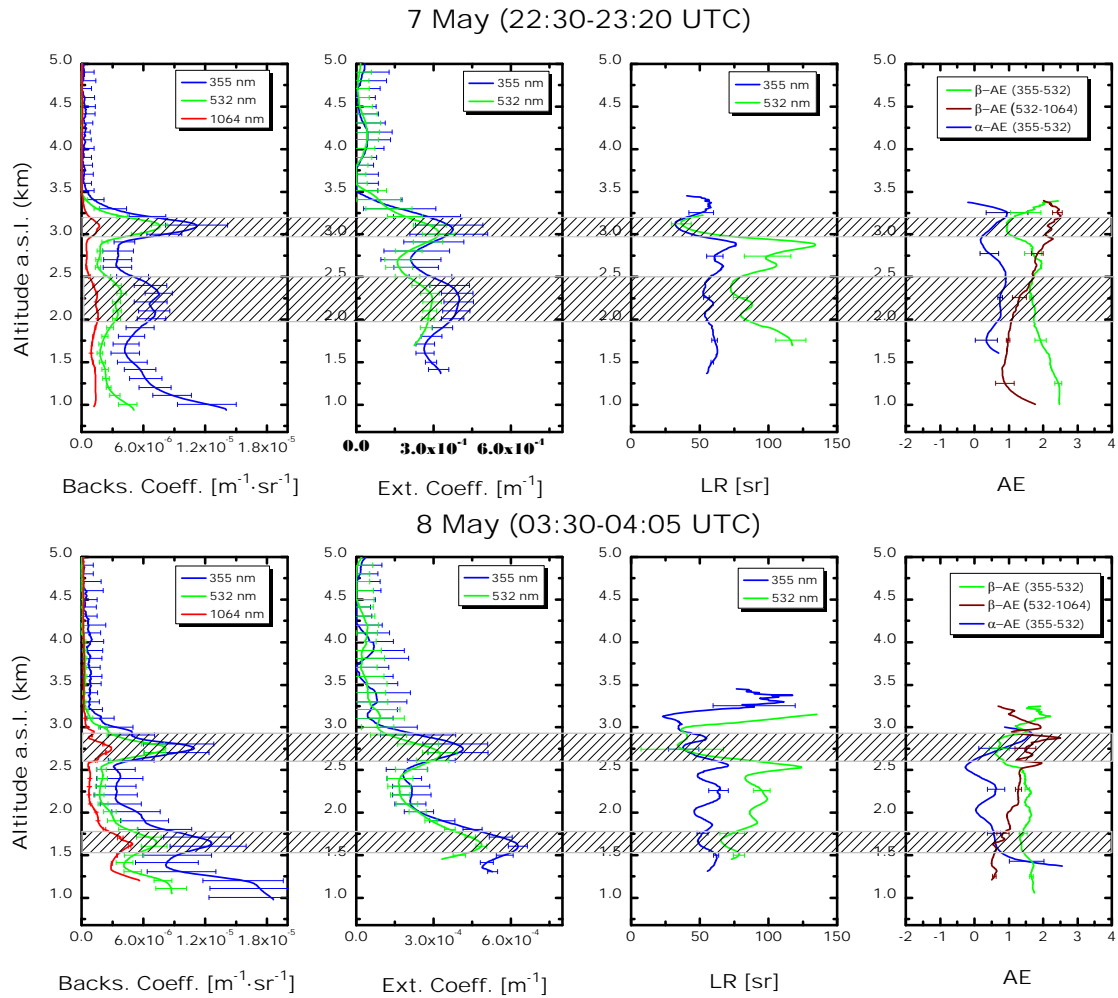
Figure 8.9. Mean profiles of aerosol optical properties (backscatter coefficient, extinction coefficient, LR and AE), for the measurement from 22:30 to 23:20 UTC on 7th May (top) and from 03:30-04:05 on 8th May 2010 (bottom). Experimental error bars are shown for backscatter and extinction coefficients derived from Monte Carlo techniques, whereas for lidar ratio and Ångström exponent the error bars denote one-standard deviation for the 500-meter layers.

Linear particle depolarization ratios (δ_p) were calculated from the signals cross-polarized with respect to the state of polarization of the light emitted at 532 nm [*Cairo et al.*, 1999; *Freudenthaler et al.*, 2009; *Bravo-Aranda et al.*, in press]. δ_p reached values of 5.0 % (±0.1 %), which is much lower than the one observed at other EARLINET stations in central and south Europe during this volcanic outbreak [*Ansmann et al.*, 2010; *Emeis et al.*, 2011; *Mona et al.*, 2011], suggests a dominance of spherical particles over our station. Using the depolarization information was possible to obtain the contributions of non-ash (fine fraction) and ash particles (coarse fraction) to total particle backscatter and extinction coefficients [*Ansmann et al.*, 2011]. The method makes use of lidar observations of the particle backscatter coefficient and the linear

particle depolarization ratio at 532 nm in order to separate the backscatter contributions of the weakly light depolarizing non-ash aerosol components from the contribution of strongly light depolarizing ash particles. This separation method is based on the work by Tesche *et al*. outlined in detail by Tesche *et al*. [2009] and refined recently for ash and fine-mode particles by Ansmann *et al*. [2011]. These results indicated that almost 82% of the particles in this plume correspond to the fine-mode aerosol fraction. The α-AE (355-532 nm) reached values around 0.7±0.1 whereas larger values around 1.1±0.2 were observed for β-AE (355-532nm). The β-AE at 532-1064 nm in this layer is 2.1±0.1 indicating that the backscatter coefficient changes more sensitively at larger wavelengths. A similar behaviour has been observed in other stations located in the Iberian Peninsula as at Évora (Portugal) [*Sicard et al.*, 2011]. All these results support the results obtained with the sun-photometer and suggest that the volcanic aerosol plume arriving at our station was mainly composed of fine-mode particles, namely volcanic sulphuric acid droplets and sulphates.

Figure 8.8 shows that the lofted layer subsided during the night, although it remained decoupled from the aerosol layers in the PBL. The values of backscatter and extinction coefficients observed for this layer at the end of the night (Fig. 8.9, bottom) are similar to those registered during the previous period. A similar behaviour was observed for the LR. However, some changes were observed in the AEs. The values of α-AE (355-532nm) showed a slight increase (0.8±0.5) while β-AE (355-532, 532-1064) showed a slight decrease (0.7±0.1 and 1.7±0.3, respectively) which suggests an increase in the particle size.

According to the large AEs and the low δ_p of this aerosol layer, which indicate a predominance of fine fraction particles with spherical shapes, it was feasible to retrieve microphysical aerosol properties using the retrieval scheme proposed by Ansmann and Müller [2005a]. Wandinger *et al*. [2002] for example show that trustworthy values of effective radius can be derived using the inversion algorithm described in section 8.2 even if δ_p values are as large as 7%. Particle effective radius was retrieved for this lofted aerosol layer in the two intervals marked in Figure 8.9. Effective radius was 0.32±0.14 μm at the beginning of the observational period and 0.55±0.13 μm at the end. This result is in agreement with the changes detected in β-AE. These findings together with the negligible changes in δ_p (from 6 to 7%) suggest that the increase in the size of the

178

dominant particles was not a result of increasing contribution by coarse-mode particles of volcanic origin but likely an increase of the size of particles in the accumulation mode. These results are confirmed by the sun-photometer columnar retrieval that evidences a broadening of the particle size distribution towards large particles in the accumulation mode (Fig 8.7a). An unusually large accumulation mode was also observed during the low-explosive phase of this volcanic event at the Mace Head Atmospheric Research Station, Ireland (53.3º N, 54.2º W), in this phase, a very important increase in non-sea-salt sulphate mass was observed by in-situ instrumentation at this station [*O'Dowd et al.*, 2011]. Similar results were also obtained in the vertical column from AERONET measurements in 1993 when Mt. Pinatubo volcanic sulphate aerosols were present in the stratosphere. Size distribution retrievals showed an unexpected middle mode peak at ~0.6 μm radius [*Eck et al.*, 2009]. All these observations are in agreement with our results and support that mainly volcanic sulphate particles arrived to our station.

The effective radii determined for the lofted aerosol layer are larger than the values of around 0.2 μm observed with Raman lidar for stratospheric aerosol layers 1.5 years after the eruption of Mt. Pinatubo [*Wandinger et al.*, 1995]. This difference could be explained by the fact the particles found in the stratosphere after the Mt. Pinatubo eruption were mainly sulphuric acid droplets while in our case we expect a mixture of sulphuric acid droplets and sulphates that additionally are exposed to high relative humidity which favours hygroscopic growth.

A second lofted aerosol layer has been studied. This layer presents a stronger subsidence than the previous layer descending from 2.0 to 1.5 km (asl) during the observational period (Fig. 8.9). Associated to this subsidence process, the layer became narrower and the peak values of the backscatter and extinction coefficients increased. Some additional features differentiate this layer from the upper one. For the period from 22:30-23:20 UTC, β-AE (355-532 nm) and α-AE are 1.7±0.1 and 0.8±0.1, respectively, which are larger than the values we found for the upper layer. However, an opposite tendency was observed for β-AE (532-1064 nm) that reached a value of 1.4 ±0.2 in the lower layer. Lower δ_p (around 4%) than those measured in the upper layer were also detected, suggesting an even lower contribution of non-spherical particles. There were some changes in the mentioned properties during the night, which was likely associated to the subsidence of the aerosol layer. We find a negligible decrease in α-AE and an

evident decrease in β-AE (at 355-532 nm and 532-1064 nm), especially for the latter pair of wavelengths. In spite of these changes the LRs were rather constant during the night (around 55 sr at 355 nm and 75 sr at 532 nm). The effective radius at the beginning of the night (0.30±0.11 μm) was slightly lower than the value retrieved for the upper layer. It showed an increase (up to 0.39±0.10 μm) during the night which was clearly lower than the increase occurring in the upper layer. The following information is relevant to explain these results.

An unexpected increase of scattering coefficient was measured in the surface boundary layer during the night from 7th to 8th May with an integrating nephelometer (TSI, model 3563, described in section 5.5) (Fig 8.10, bottom). Large scattering-related AE (~2) was observed for these measurements. According to the single scattering albedo retrievals (Fig 8.10, bottom), this aerosol was less absorbent than the typical aerosol in our urban station [*Lyamani et al.*, 2010]. An increase in fine-mode particles (Fig. 8.10 top) was also observed with an Aerodynamic Aerosol Sizer (APS-3321, TSI, described in section 5.5).

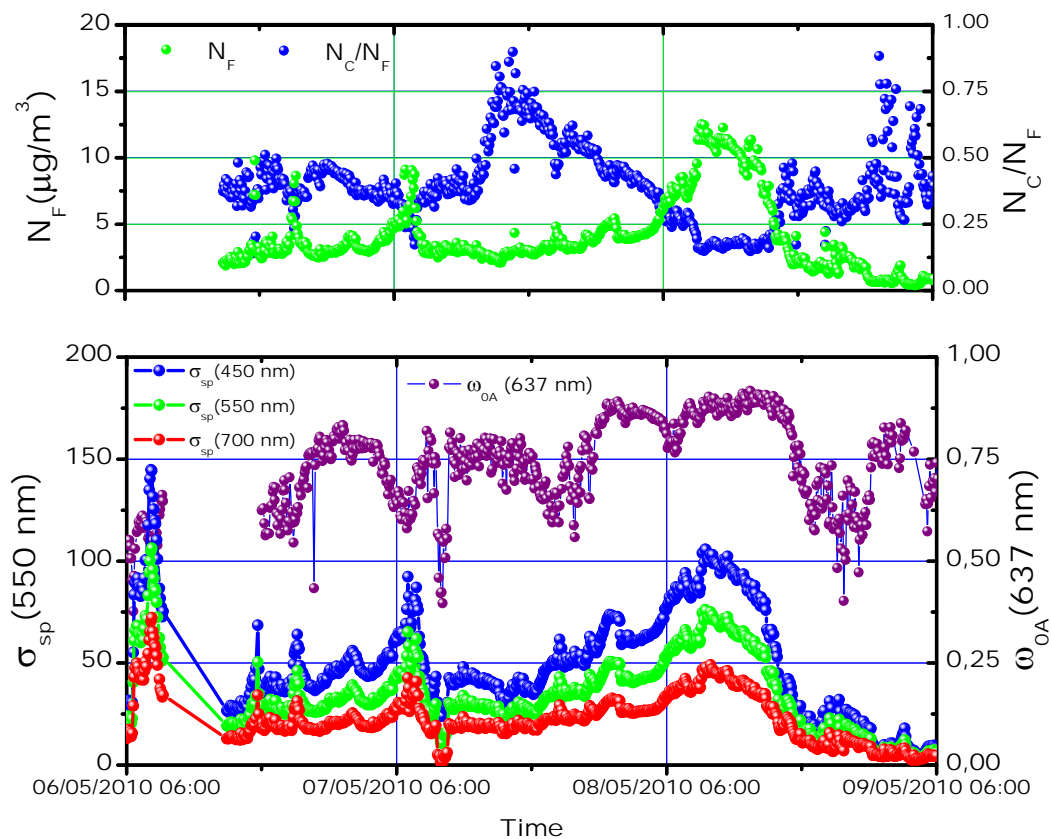**Figure 8.10.** Evolution of (top) number density for fine and coarse particles and of (bottom) aerosol scattering coefficient at 450, 550 and 700 nm and single scattering albedo at 637 nm, obtained at Granada from 6th to 9th May, 2010.

On other hand, chemical analysis performed with a high-volume samplers (flow rate 30 m^3 h^{-1} for sampling PM$_{10}$ (CAV-A/MSb) using quartz fiber filters. PM$_{10}$ high-volume sampler showed a significant increase of non-marine sulphate particles (SO$_4$$^{2-}$) during the period from 6-8 May. The concentration of sulphate particles changed from 2.9 μg/m^3 on 6 May to values as large as 4.8 μg/m^3 on 8 May. This increase was combined with a decrease of nitrates and organic and elemental carbon, thus suggesting the non-anthropogenic origin of these sulphates (Fig. 8.11a). The observed value of sulphate concentration on 8th May (Sunday) is significantly higher than the mean value (3 μg/m^3) obtained at our station in the period 2006 to 2010 from available chemical analysis during weekends [G. Titos, personal communication]. It is interesting to note that the increase of the sulphate particle concentration was also observed in the remote regional background EMEP station Víznar (37º 14'N, 03º 28' W and 1260 m asl) which is located 6 km northeast of the city of Granada (Fig. 8.11b). The sulphate concentration for this background station ranged from 0.34 μg/m^3 on 5th May to a value as high as 1.22 μg/m^3 on 8th May. Low values were observed again on the following days (0.29 μg/m^3 on 9th May).
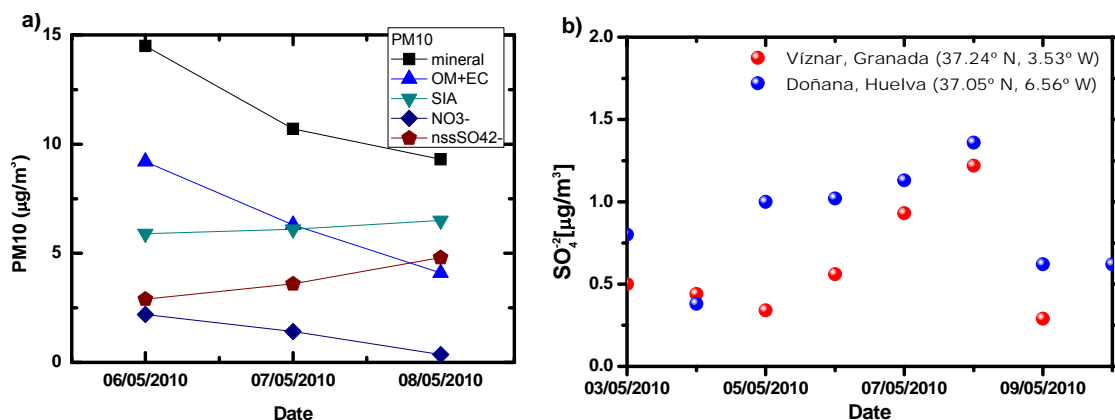
Figure 8.11. a) 24h mean mineral, OM+EC (Organic matter and elemental carbon), SIA (Secondary Inorganic aerosols), nitrates and non sea salt sulphates mass concentration in PM10 measured at CEAMA.

This last information from in-situ measurements offers additional insight into the nature of the lofted aerosol layers. In principle the slight differences in their optical and microphysical properties and the corresponding evolution can be explained by the fact that the upper layer was likely composed of a mixture of sulphuric acid droplets and sulphates. However, in the lower layer the sulphuric acid droplets were neutralized when the layer descended and reacted with anthropogenic particles contained in the

residual nocturnal layer. As a result of this reaction the composition of this layer was mainly of sulphates. This could explain the differences in the increase of effective radius during the night. On the one hand, the effective radius of the particles in the upper layer was almost two times larger than the one determined for the lower layer. This could have been caused by the RH. Forecast of RH on the basis of model analysis data issued by the National Oceanic and Atmospheric Administration (NOAA, http://ready.arl.noaa.gov/READYcmet.php) shows values close to 80% in the upper level. The absence of sulphuric acid droplets could be the reason for the smaller increase of the effective radius of around 50% in the lower aerosol layer [*Biskos et al.*, 2009].

Scatter plots of intensive aerosol properties are presented in Fig. 8.12. Intensive properties are appropriate to distinguish different types of aerosols [*Groß et al.*, 2011]. Fig. 8.12a shows effective radius versus the LR at 355 nm retrieved for different layers. A total of 18 inversions of optical data into microphysical particle properties were successfully performed. Until now just a few studies relating microphysical and optical properties of volcanic sulphuric droplet particles have been performed. For comparison our results are presented together with the values for fresh smoke particles presented in section 8.3.1 and stratospheric volcanic particles observed after the Mt. Pinatubo eruption [*Wandinger et al.*, 1995]. We can see that effective radii of the volcanic particles observed at our station are larger than the effective radii of fresh smoke and stratospheric volcanic particles. A large variability of the LR at 355 nm is observed for the volcanic particles observed at Granada, ranging from 34 to 67 sr. The LRs of the sulphate particles measured at the Granada station are larger than the LRs of the Mt. Pinatubo sulphate particles. The larger values could be explained by the fact that the sulphate particles measured at Granada are mixed with anthropogenic particles. Fig. 8.12b presents the scatter plot δ_p versus LR at 355 nm for our measurement of the volcanic event and the volcanic ash observed over central Europe. For comparison we also show results of measurements of marine aerosols, Saharan dust and biomass burning aerosols observed during the SAMUM field experiments in 2006 and 2008 [*Groß et al.*, 2011]. The volcanic sulphate particles are clearly distinguishable from other aerosol types; particularly remarkable are the large differences between the ash particles observed in central Europe and the sulphate particles measured in our station. The sulphate particles show much lower δ_p values indicating a more spherical particle

shape compared to the other aerosol types. However, the lidar ratio is not so useful to differentiate the sulphates from the other types of particles. The values of the volcanic sulphate particles observed at Granada overlap with the values measured for the other aerosols displayed in Figure 8.12.
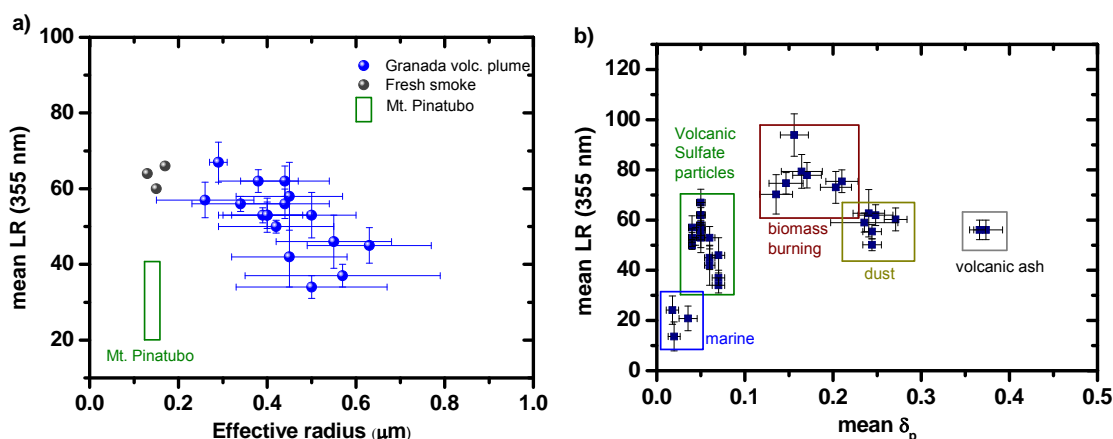
Figure 8.12. a) Effective radius and (b) linear particle depolarization ratio versus the lidar ratio at 355 nm for different aerosol types.

8.4. Conclusions

In this chapter an inversion method to retrieve microphysical properties from Raman lidar measurements has been applied to our lidar data. As study cases we have selected two special situations, a fresh biomass burning episode and the arrival of a volcanic plume over our station.

For the biomass burning episode the results allow for extending previous studies on ageing of biomass burning aerosols due to the relatively short transport time of this event. The lidar observations on 24th September 2007 showed that up to 50% of AOD at 532 nm was contributed by this fresh smoke layer. β-AE for the wavelength range from 355 to 532 nm were up to 1.3 and thus on average larger than what is usually observed for aged smoke particles. Column-averaged AE derived from sun-photometer measurements were rather close to those values, both, before and after the night-time Raman lidar observations. Star-photometer measurements, simultaneously with the lidar observations, provided similar results. The column-averaged LRs range between 60 and 65 sr at 355 nm and 532 nm, respectively. In contrast, aged long-range-transported smoke particles show LRs which are larger at 532 nm compared to the values at 355

nm. There is reasonable agreement for the microphysical parameters, i.e., effective radius and the complex refractive index. The particle radius of the fresh fire smoke particles was below 0.2 μm, which is less than the typical values found for long-range transported, aged smoke particles in boreal areas of the Northern Hemisphere. The imaginary part varied around 0.02i, indicating comparably strong light-absorption of the smoke particles. The single scattering albedo ranged between 0.76 and 0.90 depending on wavelength.

The volcanic episode allowed us to study optical and microphysical properties of sulphate and sulphuric-acid particles which originated from the Eyjafjallajökull volcanic eruption in Iceland in 2010. This is the first time that optical and microphysical characterizations of these particles have been performed in the lower troposphere by a multiwavelength Raman lidar. The observations were complemented with star- and sun-photometers operated at the lidar site. On 7th May, an increase in the AOD at 440 nm was observed, reaching maximum values (around 0.45) during night time. The corresponding AE was in the range of 1.2-1.3, indicating a predominance of the fine-mode particles. An increase in the accumulation mode was also observed between the morning of 7th May and the morning of 8th May. Lidar observations allowed for characterizing two volcanic layers during the night from 7th to 8th May 2010. An upper lofted layer subsided during the night without being mixed with the aerosol in the PBL, while a lower layer presented a stronger subsidence and reached the nocturnal boundary layer. No significant changes in the LRs were observed during the night for both layers. The values were around 55 and 75 sr at 355 and 532 nm, respectively, for the lower layer; and around 55 sr at both wavelengths for the upper lofted layer. However, a decrease of the β-AE in both layers was evident. The particle effective radius for the upper lofted layer changed from 0.32±0.14 μm at the beginning of the night to 0.55±0.13 μm at the end of the night. For the lower layer the values changed from 0.30±0.11 μm to 0.39±0.10 μm. The increase of effective radius during the night could be due to hygroscopic growth since RH was forecasted to be comparably high (close to 80 %) in both layers. The larger increase in the upper lofted layer could be explained by the fact that this layer contained a higher concentration of sulphuric acid droplets which have stronger hygroscopic growth, whereas the lower layer may have contained a larger fraction of sulphate particles. The increase of sulphates at ground level was observed by in-situ instruments. The volcanic layers had a rather low δ_p value (4-7 %) which

indicates the presence of spherical particles. These values are clearly lower than the depolarization ratios observed for other aerosol types.

8.5. References

Alados-Arboledas, L., J. L. Guerrero-Rascado, H. Lyamani, F. Navas-Guzman, and F. J. Olmo (2007), Characterization of the atmospheric aerosol by combination of Lidar and sun-photometry, *Proc. SPIE*, 6750,67500J, doi:67510.61117/67512.737557.

Amiridis, V., D. S. Balis, E. Giannakaki, A. Stohl, S. Kazadzis, M. E. Koukouli, and P. Zanis (2009), Optical characteristics of biomass burning aerosols over Southeastern Europe determined from UV-Raman lidar measurements, *Atmospheric Chemistry and Physics*, *9*(7), 2431-2440.

Ansmann, A., and D. Müller (2005a), Lidar and atmospheric aerosol particles, in Lidar, in *Range-Resolved Optical Remote Sensing of the Atmosphere*, edited by C. Weitkamp, Springer, Singapore.

Ansmann, A., and D. Müller (Eds.) (2005b), *Lidar and atmospheric aerosol particles, in Lidar. Range-Resolved Optical Remote Sensing of the Atmosphere*, 105-114 pp., Springer, Singapore.

Ansmann, A., et al. (2010), The 16 April 2010 major volcanic ash plume over central Europe: EARLINET lidar and AERONET photometer observations at Leipzig and Munich, Germany, *Geophysical Research Letters*, *37*.

Ansmann, A., et al. (2011), Ash and fine-mode particle mass profiles from EARLINET-AERONET observations over central Europe after the eruptions of the Eyjafjallajokull volcano in 2010, *Journal of Geophysical Research-Atmospheres*, *116*.

Biskos, G., P. R. Buseck, and S. T. Martin (2009), Hygroscopic growth of nucleation-mode acidic sulfate particles, *J. Aerosol. Sci.*, *40*(4), 338-347.

Bockmann, C. (2001), Hybrid regularization method for the ill-posed inversion of multiwavelength lidar data in the retrieval of aerosol size distributions, *Applied Optics*, *40*(9), 1329-1342.

Bohren, C. F., and D. R. Huffman (1983), Absorption and scattering of light by small particles, *Nature*, *306*(5943), 625-625.

Bravo-Aranda, J. A., F. Navas-Guzman, J. L. Guerrero Rascado, D. Perez-Ramirez, M. J. Granados-Muñoz, and L. Alados Arboledas (in press), Analysis of lidar depolarization calibration procedure and application to the atmospheric aerosol characterization, *International Journal of Remote Sensing, in press*.

Cairo, F., G. Di Donfrancesco, A. Adriani, L. Pulvirenti, and F. Fierli (1999), Comparison of various linear depolarization parameters measured by lidar, *Applied Optics*, *38*(21), 4425-4432.

Chaikovsky, A., O. Dubovik, P. Goloub, D. Tanre, A. Lopatsin, S. Denisov, T. Lapyonok, and Y. Karol (2010), The retrieval of aerosol microphysical properties in the vertical column using combined lidar/photometer data: a step to integrating photometer and lidar networks, paper presented at 25th International Laser Radar Conference, St. Petersburg.

Draxler, R. R., and G. D. Rolph (2003), http://www.arl.noaa.gov/ready/hysplit4.html, *Silver Spring, MD*.

Dubovik, O., and M. D. King (2000), A flexible inversion algorithm for retrieval of aerosol optical properties from Sun and sky radiance measurements, *Journal of Geophysical Research-Atmospheres*, *105*(D16), 20673-20696.

Dubovik, O., et al. (2006), Application of spheroid models to account for aerosol particle nonsphericity in remote sensing of desert dust, *Journal of Geophysical Research-Atmospheres*, *111*(D11).

Eck, T. F., et al. (2009), Optical properties of boreal region biomass burning aerosols in central Alaska and seasonal variation of aerosol optical depth at an Arctic coastal site, *Journal of Geophysical Research-Atmospheres*, *114*.

Emeis, S., et al. (2011), Measurement and simulation of the 16/17 April 2010 Eyjafjallajokull volcanic ash layer dispersion in the northern Alpine region, *Atmospheric Chemistry and Physics*, *11*(6), 2689-2701.

Ferrare, R. A., R. S. Fraser, and Y. J. Kaufman (1990), Satellite measurements of large-scale air-pollution - measurements of forest fire smoke, *Journal of Geophysical Research-Atmospheres*, *95*(D7), 9911-9925.

Freudenthaler, V., et al. (2009), Depolarization ratio profiling at several wavelengths in pure Saharan dust during SAMUM 2006, *Tellus Series B-Chemical and Physical Meteorology*, *61*(1), 165-179.

Gislason, S. R., et al. (Eds.) (2010), *Characterization of Eyjafjallajökull volcanic ash particles and a protocol for rapid risk assessment*, Robert A. Berner, New Haven.

Grams, G. W., B. G. Schuster, I. H. Blifford, and J. J. Deluisi (1972), Complex index of refraction of airborne fly ash determined by laser radar and collection of particles at 13 km, *J. Atmos. Sci.*, *29*(5), 900-&.

Groß, S., V. Freudenthaler, M. Wiegner, J. Gasteiger, A. Geiß, and F. Schnell (2011), Dual-wavelength linear depolarization ratio of volcanic aerosols: lidar measurements of the Eyjafjallajökull plume over Maisach, Germany, *Atmospheric Environment, 10.1016/j.atmosenv.2011.06.017.*

Holben, B. N., et al. (1998), AERONET - A federated instrument network and data archive for aerosol characterization, *Remote Sensing of Environment*, *66*(1), 1-16.

Lyamani, H., F. J. Olmo, and L. Alados-Arboledas (2010), Physical and optical properties of aerosols over an urban location in Spain: seasonal and diurnal variability, *Atmospheric Chemistry and Physics*, *10*(1), 239-254.

Mattis, I., P. Seifert, D. Müller, M. Tesche, A. Hiebsch, T. Kanitz, J. Schmidt, F. Finger, U. Wandinger, and A. Ansmann (2010), Volcanic aerosol layers observed with multiwavelength Raman lidar over central Europe in 2008-2009 (vol 24, D00L04, 2010), *Journal of Geophysical Research-Atmospheres*, *115*.

Miller, T. P., and T. J. Casadevall (2000), Volcanic ash hazards to aviation, in *Encyclopedia of Volcanoes*, edited by H. Sigurdsson, pp. 915-930, Elsevier, New York.

Mona, L., A. Amodeo, G. D'Amico, A. Giunta, F. Madonna, and G. Pappalardo (2011), Multi-wavelength Raman lidar observations of the Eyjafjallajökull volcanic cloud over Potenza, Southern Italy, *Atmospheric Chemistry and Physics Discussion*, *11*, 12763-12803.

Müller, D., U. Wandinger, and A. Ansmann (1999a), Microphysical particle parameters from extinction and backscatter lidar data by inversion with regularization: simulation, *Applied Optics*, *38*(12), 2358-2368.

Müller, D., U. Wandinger, and A. Ansmann (1999b), Microphysical particle parameters from extinction and backscatter lidar data by inversion with regularization: theory, *Applied Optics*, *38*(12), 2346-2357.

Müller, D., U. Wandinger, D. Althausen, and M. Fiebig (2001), Comprehensive particle characterization from three-wavelength Raman-lidar observations: case study, *Applied Optics*, *40*(27), 4863-4869.

Müller, D., I. Mattis, U. Wandinger, A. Ansmann, D. Althausen, and A. Stohl (2005), Raman lidar observations of aged Siberian and Canadian forest fire smoke in the free troposphere over Germany in 2003: Microphysical particle characterization, *Journal of Geophysical Research-Atmospheres*, *110*(D17).

Müller, D., I. Mattis, A. Ansmann, U. Wandinger, C. Ritter, and D. Kaiser (2007a), Multiwavelength Raman lidar observations of particle growth during long-range transport of forest-fire smoke in the free troposphere, *Geophysical Research Letters*, *34*(5).

Müller, D., A. Ansmann, I. Mattis, M. Tesche, U. Wandinger, D. Althausen, and G. Pisani (2007b), Aerosol-type-dependent lidar ratios observed with Raman lidar, *Journal of Geophysical Research-Atmospheres*, *112*(D16).

Murayama, T., D. Muller, K. Wada, A. Shimizu, M. Sekiguchi, and T. Tsukamoto (2004), Characterization of Asian dust and Siberian smoke with multiwavelength Raman lidar over Tokyo, Japan in spring 2003, *Geophysical Research Letters*, *31*(23).

O'Dowd, C., et al. (2011), The Eyjafjallajökull ash plume e Part I: Physical, chemical and optical characteristics, *Atmospheric Environment, doi:10.1016/j.atmosenv.2011.07.004*.

O'Neill, N. T., T. F. Eck, B. N. Holben, A. Smirnov, A. Royer, and Z. Li (2002), Optical properties of boreal forest fire smoke derived from Sun photometry, *Journal of Geophysical Research-Atmospheres*, *107*(D11).

Pahlow, M., D. Muller, M. Tesche, H. Eichler, G. Feingold, W. L. Eberhard, and Y. F. Cheng (2006), Retrieval of aerosol properties from combined multiwavelength lidar and sunphotometer measurements, *Applied Optics*, *45*(28), 7429-7442.

Radke, L. F., A. S. Hegg, P. V. Hobbs, and J. E. Penner (1995), Effects of aging on the smoke from a large forest-fire, *Atmospheric Research*, *38*(1-4), 315-332.

Reagan, J. A., J. D. Spinhirne, D. M. Byrne, D. W. Thomson, R. G. Depena, and Y. Mamane (1977), Atmospheric particulate properties inferred from lidar and solar radiometer observations compared with simultaneous insitu aircraft measurements - case-study, *Journal of Applied Meteorology*, *16*(9), 911-928.

Reid, J. S., T. F. Eck, S. A. Christopher, R. Koppmann, O. Dubovik, D. P. Eleuterio, B. N. Holben, E. A. Reid, and J. Zhang (2005), A review of biomass burning emissions part III: intensive optical properties of biomass burning particles, *Atmospheric Chemistry and Physics*, *5*, 827-849.

Revuelta, M. A., M. Sastre, A. J. Fernández, L. Martín, R. García, F. J. Gómez-Moreno, B. Artíñano, M. Pujadas, and F. Molero (2012), Characterization of the Eyjafjallajökull volcanic plume over the Iberian Peninsula by lidar remote sensing and ground-level data collection, *Atmospheric Environment*, *48*, 46-55.

Robock, A. (2000), Volcanic eruptions and climate, *Reviews of Geophysics*, *38*(2), 191-219.

Sicard, M., et al. (2012), Monitoring of the Eyjafjallajökull volcanic aerosol plume over the Iberian Peninsula by means of four EARLINET lidar stations, *Atmospheric Chemistry and Physics 12*, 3115-3130.

Tesche, M., A. Ansmann, D. Müller, D. Althausen, R. Engelmann, V. Freudenthaler, and S. Gross (2009), Vertically resolved separation of dust and smoke over Cape Verde using multiwavelength Raman and polarization lidars during Saharan Mineral Dust Experiment 2008, *Journal of Geophysical Research-Atmospheres*, *114*.

Tikhnonov, A. N., and V. Y. Arsenin (1977), *Solutions of ill posed problems*, V. H. Winston and Sons, New York.

Twomey, S. (1977), *Introduction to the Mathematics of Inversion in Remote Sensing and Indirect Measurements*, Elsevier ed., Amsterdam.

Uthe, E. E. (1982), Particle-size evaluations using multiwavelength extinction measurements, *Applied Optics*, *21*(3), 454-459.

Veselovskii, I., A. Kolgotin, V. Griaznov, D. Muller, U. Wandinger, and D. N. Whiteman (2002), Inversion with regularization for the retrieval of tropospheric aerosol parameters from multiwavelength lidar sounding, *Applied Optics*, *41*(18), 3685-3699.

Wandinger, U., A. Ansmann, J. Reichardt, and T. Deshler (1995), Determination of stratospheric aerosol microphysical properties from independent extinction and backscattering measurements with a Raman lidar, *Applied Optics*, *34*(36), 8315-8329.

Wandinger, U., et al. (2002), Optical and microphysical characterization of biomass-burning and industrial-pollution aerosols from multiwavelength lidar and aircraft measurements, *Journal of Geophysical Research-Atmospheres*, *107*(D21).

Conclusions and outlook

A significant part of the research of this dissertation concerns methodological developments. Implementation of the previous steps (pre-processing) to be applied to raw lidar signals, before using the inversion algorithms, was carried out in order to guarantee the quality of the lidar products. In this sense, the overlap features of the lidar system were analyzed to properly correct for the incomplete overlap between fields of view for the laser beam and the receiver. We found that below 500 m (agl) our system deviates from perfect overlap more than 40 %, so any study of the Planetary Boundary Layer (PBL) requires the appropriate overlap correction. The implementation of an elastic algorithm to retrieve profiles of aerosol optical properties was performed and checked in an algorithm intercomparsion that took place in the framework of SPALINET. This intercomparison showed that the elastic algorithm implemented in this thesis provides a reliable retrieval of aerosol optical profiles. The discrepancies observed between our retrievals and the solutions were smaller than those obtained for other stations in a previous intercomparison developed in the frame of EARLINET. Another important aspect of methodological issues was the development and implementation of alternative calibration procedures for the infrared lidar channel. This channel usually presents a low signal-to-noise ratio in the molecular height range where the lidar signals are usually calibrated. Two alternative calibration methods for the infrared channel were presented. The first is based on the use of cloud base for calibrating and requires the presence of cirrus clouds in the lidar profile. The second method uses the near height range to calibrate the infrared channel, where the contribution of aerosol is non-negligible. For this purpose, the infrared backscatter coefficient at this reference level is derived from the backscatter coefficient profiles at other wavelengths, namely 355 and 532 nm. Both methods show significant

improvement in the infrared backscatter coefficient profiles when these calibrations were applied.

Another major aspect of the research conducted in this dissertation concerns the capacity of the lidar technique to retrieve PBL heights. An algorithm based on the Wavelet Covariance Transform (WCT) for automated PBL height detection using lidar measurements was implemented. The WCT-based algorithm was optimized by using independent measurements of PBL height, estimated using the parcel and Richardson methods for a set of thermodynamic radiosondes. Additionally, the parcel method was used for temperature profiles measured during three months with a ground-based microwave radiometer near the lidar. Analysis of the optimization period showed three types of scenarios: (i) clean atmosphere over the PBL with an absence of aerosol layers in the Free Troposphere (FT), (ii) aerosol layers in the FT decoupled from the PBL and (iii) stratification due to aerosol layers coupled with the PBL or incomplete mixing. For the first two types of scenarios the automated PBL height detection using the WCT-based method is straightforward and satisfactory, with optimal results obtained for $a = 300$ m and a 0.05 WCT-profile threshold. For these, there was good agreement with the radiosonde-based methods despite the differences in tracers and techniques, with differences below 250 m. In the case of multilayering within the PBL, the WCT-based methodology is likely to fail to detect the PBL height; this signals the need either for additional information and processing for its determination (e.g., interpolation based on prior and posterior estimates, supposing continuity of the PBL height during daytime), or for an iterative procedure based on reducing the WCT-profile threshold.

Automated PBL height detection using lidar measurements from August 2007 to July 2008 over Granada provided satisfactory results for 81% of all days. The annual mean PBL height was 1.7 ± 0.5 km (asl), with seasonal changes showing higher values in summer (with larger variability) and lower in winter. During spring and autumn mean values are similar with slightly larger variability in autumn. The correlation of the PBL height with both global solar irradiance and air temperature at ground level during the study period confirms the dependence of PBL height on these variables measured at the ground. The aerosol extinction coefficient in the surface boundary layer is anti-correlated with PBL height, while aerosol optical depth presents a certain degree of correlation. Therefore, we can state that the lower PBL height in winter reduces the

available volume for vertical dispersion, increasing the extinction coefficient at the surface in spite of the lower aerosol load in the vertical column during this season.

Raman lidar profiles were used to characterize aerosol optical properties for the urban area of Granada. Vertical profiles of optical properties showed the largest values for both the backscatter and extinction coefficients at low altitudes, i.e. closer to the surface, with similar values throughout the year. In the FT we observed larger values during spring-summer than in autumn-winter. This fact can be explained by the impact of lofted aerosol layers associated with Saharan dust outbreaks during the warm season at these heights. For spring-summer the LR profiles presented quite constant mean values (with high standard deviation) in the range typically associated with mineral dust (~46 sr) while LR profiles are highly variable during autumn-winter. A study of aerosol layering in the whole column indicated that most aerosol particles detected above the PBL occur during warm months. Moreover, mean monthly integrated β-AE values were obtained in the PBL and in the FT from day- and night-time measurements, showing clear seasonal behaviour in both atmospheric layers. In general, the monthly mean β-AE values were lower in warm months than in cold months, indicating more relevant presence of large particles in spring and summer. We also observed that β-AE values were lower in the FT than in the PBL in spring and summer, while the opposite behaviour was observed in autumn and winter. Finally, the annual cycle of LR at 532 nm suggests a predominance of fine particles during autumn and winter and an increase in the contribution of coarse particles during spring and summer. Moderate correlation was observed between β-AE and LR at 532 nm. The results confirmed that small particles are associated with large absorption, while large particles are related with large scattering.

Aspects related to water vapour have also been addressed in this thesis. Water vapour measurements performed with Raman lidar, star-photometer and radiosondes were presented. The methodology for obtaining water vapour mixing ratio profiles from Raman lidar was presented and discussed. A radiosonde field campaign was performed in order to retrieve the calibration constant for the lidar water vapour channel. Linear regressions between the lidar and radiosonde data in the range 1.5-4.0 km (asl) were used to retrieve this constant. A robust iterative approach to obtain the best linear regression was introduced. A mean value of 186 ± 4 g/kg was obtained as the calibration coefficient for the whole campaign (standard deviations close to 2%). Good

agreement between radiosonde- and lidar-derived profiles was achieved, with mean absolute deviation about 0.6 ± 0.6 g/kg in the altitude range 1.5-5.5 km (asl). A comparison of the Total Precipitable Water retrieved with the Raman lidar and the co-located star-photometer showed good agreement between both instruments and methodologies (R^2 = 0.880). Moreover, the combination of water vapour mixing ratio profiles retrieved from the Raman lidar and temperature profiles from a microwave radiometer allowed obtaining relative humidity (RH) profiles in the lower troposphere. A comparison with radiosonde products was carried out. Statistical analysis found that the mean absolute deviation for the temperature in the lower troposphere (0-5 km, agl) is around 1.2 ± 0.7 ºC. The discrepancies in RH were found around 7 ± 6 %. The errors were smaller (below 1.0ºC in temperature and 5 % in RH) for the first two kilometers of the atmosphere.

In the last part of this thesis, the retrieval of microphysical properties from Raman lidar measurements is addressed. The inversion method of regularization with constraints was presented and applied to two special cases, namely fresh biomass burning and volcanic episodes. For the biomass burning episode the results expanded upon those from previous studies regarding ageing of biomass burning aerosols for this fresh smoke event. The lidar observations showed that up to 50% of AOD at 532 nm was contributed by this fresh smoke layer. β-AE (355-532 nm) were up to 1.3 and thus on average larger than what is usually observed for aged smoke particles. The column-averaged LRs range between 60 and 65 sr at 355 nm and 532 nm, respectively. In contrast, aged smoke particles from long-range-transport showed larger LRs at 532 nm compared to the values at 355 nm. The particle radius of the fresh smoke particles was below 0.2 μm, is less than typical values found for long-range transported, aged smoke particles in boreal areas of the Northern Hemisphere. The imaginary part varied around 0.02i, indicating comparably strong light-absorption of the smoke particles. The single scattering albedo ranged between 0.76 and 0.90 depending on wavelength.

On the other hand, the volcanic episode allowed studying optical and microphysical properties of particles from the Eyjafjallajökull volcanic eruption in Iceland in 2010. The observations demonstrated that the main components of this plume were sulphate and sulphuric-acid particles. This is the first study of optical properties and microphysical properties of volcanic sulphate particles in the lower troposphere/boundary layer based on multiwavelength Raman lidar measurements. A

remarkable increase in the particle number concentration in the accumulation mode was determined from inversion of the aerosol optical properties. The large β-AE (larger than 1.0) indicated the presence of small particles. The particle effective radii ranged between 0.30-0.55 μm. The volcanic layers had a rather low linear particle depolarization ratio (δ_p) (4-7 %) which indicates the presence of spherical particles. These values are clearly lower than the δ_p observed for other types of aerosols. In situ instrumentation confirmed an increase of sulphate particles at ground level during this period.

Future research will be necessary to continue advancement in the aspects developed in this thesis:

- One of the aims for the future will be to evaluate the WCT-based algorithm to retrieve the PBL height not beyond convective conditions only, and thus this parameter will be obtained for the whole day. This will allow continuous monitoring of PBL height. .

- Continuing the routine analysis of optical lidar profiles will extend the analysis of vertically resolved aerosol optical properties. Thus, better understanding of the urban environment of Granada will be achieved.

- On the other hand, the possibility of performing more radiosonde campaigns will allow checking the robustness of the RH retrievals from lidar and the microwave radiometer. Moreover, the knowledge of optical and microphysical aerosol properties along with the RH profile will permit the use of lidar data to study aerosol hygroscopic growth.

Conclusiones y perspectivas

Una parte importante del trabajo de investigación desarrollado en esta tesis está relacionado con el desarrollo metodológico. Con el objetivo de garantizar la calidad de los productos lidar se implementaron una serie de pre-procesados que hay que aplicar a las señales lidar antes de utilizar cualquier algoritmo de inversión. En este sentido se analizaron las características de solapamiento del sistema lidar con el objetivo de corregir el solapamiento incompleto existente entre el haz laser y el campo de visión del sistema receptor. Se encontró que por debajo de 500 m (sobre el nivel del terreno) el sistema lidar se desvía más de un 40 % del solapamiento completo, por lo que se concluye que cualquier estudio dentro de la Capa Límite Planetaria (PBL) requiere de una apropiada corrección de solapamiento. Además, se implementó un algoritmo elástico para la obtención de perfiles de propiedades ópticas del aerosol que fue validado en una intercomparación de algoritmos realizada en la red SPALINET. Esta comparación mostró que el algoritmo elástico implementado en esta tesis proporciona perfiles fiables de propiedades ópticas. Las discrepancias observadas entre los resultados obtenidos con nuestro algoritmo y las soluciones fueron más pequeñas que las obtenidas por otras estaciones dentro de una intercomparación previa realizada en la red EARLINET. Otro aspecto metodológico importante tratado en la tesis fue el desarrollo e implementación de dos procedimientos alternativos para la calibración del canal infrarrojo del sistema lidar. Este canal suele presentar una valor bajo de razón señal ruido en el denominado rango molecular, donde típicamente se calibran las señales lidar. Se han presentado dos métodos alternativos de calibración para dicho canal. El primero utiliza como referencia de calibrado la base de una nube. Esto requiere

la presencia de nubes tipo cirro en el perfil lidar. El segundo método utiliza el rango cercano para calibrar el canal de infrarrojo, pese a que en este rango la contribución de aerosol no es despreciable. De este modo, el valor del coeficiente de retrodispersión del canal infrarrojo en la altura de referencia es obtenido a partir de los perfiles de los coeficientes de retrodispersión en 355 y 532 nm. Ambos métodos de calibración mostraron una mejora significativa en el coeficiente de retrodispersión del canal infrarrojo.

Otro importante aspecto abordado en el desarrollo de esta tesis concierne a la capacidad de la técnica lidar para obtener la altura de la PBL. Con este fin se implementó un algoritmo basado en la transformada de covarianza wavelet (WCT) para detectar de un modo automático la altura de la PBL usando medidas lidar. El algoritmo basado en WCT fue optimizado usando medidas independientes de la altura de la PBL. Estos valores de referencia de alturas de la PBL se estimaron usando los métodos de la burbuja y el de Richardson para un conjunto de radiosondeos. Por otra parte, el método de la burbuja también se aplicó a un conjunto de tres meses de medidas de perfiles de temperatura obtenidos con un radiómetro de microondas situado junto al sistema lidar. El análisis del periodo de optimización mostró tres tipos de escenarios posibles: (i) una atmósfera limpia sobre la PBL con ausencia de capas de aerosol en la trosposfera libre, (ii) capas de aerosol en la troposfera libre desacopladas de la PBL y (iii) estratificación debida a capas de aerosol acopladas con la capa límite o mezcladas parcialmente. Para los primeros dos escenarios la detección de la altura de la PBL usando el método basado en WCT fue directa y satisfactoria con resultados óptimos obtenidos para una dilación a = 300 m y un valor umbral pare el perfil de WCT de 0.05. Para ambos se encontró un buen acuerdo con los métodos basados en radiosondeos a pesar de usar trazadores y técnicas distintas, con diferencias por debajo de 250 m. En el caso de multicapas dentro de la PBL, la metodología basada en WCT falló al detectar la altura de la PBL, por lo que requiere información y procesado adicional para su determinación comoel uso de un intervalo de tiempo alrededor del periodo analizado en el que se tenga en cuenta la continuidad de la altura de la PBL durante el día, o un procedimiento iterativo para reducir el valor umbral para el perfil de WCT.

La detección automática de la altura de la PBL usando medidas lidar desde Agosto de 2007 a Julio de 2008 sobre Granada proporcionó resultados satisfactorios para el 81% de los días. El valor medio anual de la altura de la PBL fue 1.7 ± 0.5 km

(sobre el nivel del mar), mostrando cambios estacionales con valores más altos en verano (con mayor variabilidad) y más bajos en invierno. Durante la primavera y el otoño los valores medios fueron similares con una variabilidad ligeramente mayor en otoño. La correlación entre la altura de la PBL con la irradiancia solar global y la temperatura del aire en superficie durante el periodo estudiado confirmó una dependencia de la altura de la PBL con estas variables medidas a nivel de suelo. Además, se encontró que el coeficiente de extinción de aerosol en la capa límite superficial está anticorrelacionado con la altura de la PBL, mientras que el espesor óptico de aerosol presenta cierto grado de correlación. Por lo tanto, es posible afirmar que una altura de la PBL más baja en invierno reduce el volumen disponible para la dispersión vertical, aumentando el coeficiente de extinción en la superficie a pesar de la menor carga de aerosol en la columna durante esta estación.

Los perfiles lidar Raman fueron usados para caracterizar las propiedades ópticas del aerosol en el entorno urbano de Granada. Los perfiles verticales de propiedades ópticas mostraron valores más altos para los coeficientes de retrodispersión y extinción en las alturas más próximas a la superficie, con valores similares a lo largo del año. En la troposfera libre se observaron valores más altos durante primavera-verano que en otoño-invierno. Esto se explica por una mayor presencia de capas de aerosol de origen sahariano en la troposfera libre durante la estación cálida. En primavera-verano los perfiles de razón lidar presentan valores medios muy constantes (con una alta desviación estándar) en el rango de valores típicamente asociado a polvo mineral (~46 sr) mientras que son altamente variables para el otoño-invierno. Un estudio de la estratificación de las capas de aerosol en la columna atmosférica indicó que la mayoría del aerosol presente por encima de la PBL se detecta durante las estaciones cálidas. Además, se obtuvieron los valores medios del exponente de Angström obtenido a partir del perfil de retrodispersión (β-AE) en la PBL y en la trosposfera libre a partir de medidas diurnas y nocturnas. Se observó un claro comportamiento estacional para este parámetro en ambas regiones de la atmósfera. En general, los valores medios mensuales de β-AE presentan valores más bajos en los meses cálidos que en los meses más fríos, lo que evidencia una mayor presencia de partículas gruesas en primavera y verano. También se observó que los valores de β-AE son más pequeños en la troposfera libre que en la PBL en primavera y verano, mientras que se observó una tendencia opuesta en otoño y en invierno. Finalmente, el ciclo anual de razón lidar en 532 nm también sugirió

un predominio de partículas finas durante el otoño e inverno y un aumento en la contribución de partículas gruesas durante la primavera y el verano. Además, se observó una correlación moderada entre β-AE y la razón lidar en 532 nm. Los resultados confirmaron que las partículas pequeñas están caracterizadas por una mayor absorción mientras las gruesas presentan una mayor dispersión.

Otro aspecto relevante abordado en esta tesis es el relacionado con medidas de vapor de agua. Las medidas presentadas aquí han sido realizadas con el lidar Raman, el fotómetro estelar y radiosondeos. Uno de los temas fundamentales tratados ha sido la presentación y discusión de la metodología necesaria para obtener perfiles de razón de mezcla de vapor de agua a partir del sistema lidar. Con el fin de obtener la constante de calibración para el canal lidar de vapor de agua se realizó una campaña de radiosondeos. Para obtener dicha constante se realizaron regresiones lineales entre los datos obtenidos con lidar y radiosondeos en el rango 1.5-4.0 km (asl). Se implementó una aproximación iterativa con el objetivo de obtener la mejor regresión lineal que nos proporcionara una constante de calibración robusta. Se obtuvo un valor medio de 186 ± 4 g/kg como constante de calibración representativa de todos los calibrados realizados durante la campaña (con desviación estándar entre las constantes próxima a un 2 %). Con esta constante de calibración se consiguió un buen acuerdo entre los perfiles de razón de mezcla de vapor de agua lidar y los obtenidos con radiosondeos, con una desviación media absoluta de 0.6 ± 0.6 g/kg en el rango de alturas de 1.5-5.5 km (sobre el nivel del mar). La comparación del agua total precipitable obtenida a partir del sistema lidar y el fotómetro estelar mostró un buen acuerdo entre ambos instrumentos y metodologías (R^2 = 0.880). Además, la combinación de perfiles de razón de mezcla de vapor de agua obtenidos con el lidar Raman y de perfiles de temperatura obtenidos con un radiómetro de microondas permitió la obtención de perfiles de humedad relativa en la troposfera baja. Los perfiles obtenidos con el lidar Raman y el radiómetro de microondas fueron comparados con los proporcionados con los radiosondeos. Un análisis estadístico en términos de desviación media absoluta encontró que para los perfiles de temperatura la desviación media absoluta en la troposfera baja (0-5 km, sobre el nivel del suelo) era alrededor de 1.2 ± 0.7 ºC, mientras que las discrepancias en la humedad relativa fueron alrededor de 7 ± 6 %. Los errores fueron más pequeños (por debajo de 1ºC en temperatura y 5% en humedad relativa) para los primeros dos kilómetros de la atmósfera.

La última parte de la tesis abordó la obtención de propiedades microfísicas a partir de medidas con el lidar Raman. El método de inversión de regularización con condiciones de contorno fue presentado y aplicado a dos casos especiales, un episodio de humo fresco procedente de quema de biomasa y un episodio volcánico. En el episodio de quema de biomasa, dado el tiempo relativamente corto entre la generación del evento y su detección ha sido posible estudiar las propiedades de humo reciente. De este modo los resultados obtenidos han permitido extender los resultados de estudios previos centrados en el análisis de humo envejecido. Las observaciones lidar mostraron que esta capa de humo reciente contribuye del espesor óptico del aerosol hasta un 50% en 532 nm . El valor del β-AE (355-532 nm) llegó hasta 1.3 siendo en promedio más alto que los valores usualmente observados para partículas de humo más envejecidas. Los valores promedio en columna de razón lidar variaron entre 60 y 65 sr en 355 nm y 532 nm, respectivamente. En contraste, las partículas de humo envejecidas, que viajan largas distancias, muestran valores de razón lidar más altos en 532 nm comparados con los observados en 355 nm. El radio efectivo de estas partículas de humo reciente alcanzó valores por debajo de 0.2 μm, siendo más bajo que los valores típicos encontrados en humo envejecido. La parte imaginaria del índice de refracción varió entorno a 0.02i, indicando una fuerte absorción de la luz para estas partículas. El albedo de dispersión simple varió entre 0.76 y 0.90 dependiendo de la longitud de onda.

Por otro lado, el episodio volcánico permitió estudiar las propiedades ópticas y microfísicas de las partículas originadas en la erupción volcánica del Eyjafjallajökull en Islandia en 2010. Las observaciones mostraron que sobre nuestra estación la principal contribución de este penacho de aerosol fue debido a partículas de sulfatos y gotas de ácido sulfúrico. Este es el primer estudio de propiedades ópticas y microfísicas de sulfatos volcánicos en la baja troposfera realizado con un sistema lidar Raman. Durante el evento volcánico se observó un destacable aumento en la concentración numérica de partículas en el modo de acumulación. Los valores altos de β-AE (mayores que 1.0) obtenidos a partir de los perfiles lidar indicaron la presencia de partículas pequeñas. El radio efectivo en el penacho volcánico varió entre 0.30-0.55 μm. Estas partículas presentaron una baja razón de despolarización lineal (δ_p) (4-7 %) lo cual es una evidencia de su relativamente alta esfericidad. Estos valores son claramente más bajos que los valores de δ_p observados para otros tipos de aerosol. La instrumentación in situ confirmó un aumento de sulfatos a nivel del suelo durante el periodo estudiado.

El desarrollo de la tesis ha dado lugar a avances en la investigación al tiempo que ha sugerido nuevas líneas en las que desarrollar la futura investigación:

- Uno de los objetivos para el futuro será evaluar el método de WCT para obtener la altura de la capa límite no sólo bajo condiciones convectivas y de esta forma poder obtener este parámetro en cualquier momento del día. Esto permitirá una monitorización continua de la altura de la PBL.

- Una continuación del análisis de perfiles lidar de propiedades ópticas permitirá extender el análisis realizado hasta el momento. De esta forma será posible lograr un mayor conocimiento de las propiedades ópticas de la atmósfera urbana en el entorno Granada.

- Por otro lado, la posibilidad de realizar más campañas con radiosondeos permitirá comprobar la robustez del método descrito para obtener perfiles de humedad relativa a partir del lidar y del radiómetro de microondas. Además, el conocimiento de propiedades ópticas y microfísicas del aerosol junto con los perfiles de humedad relativa permitirá el uso de datos lidar en el desarrollo de estudios de crecimiento por higroscopicidad.

- Otra reto motivador a realizar en los próximos años vendrá de la colaboración con los desarrolladores de algoritmos microfísicos con el fin de poder obtener propiedades físicas de partículas no esféricas, como pueden ser las partículas de polvo mineral.

List of abbreviations

Abbreviation	Definition
ADNET	Asian Dust NETwork
AE	Angström Exponent
AERONET	Aerosol Robotic Network
agl	above ground level
AN	analog
AOD	Aerosol Optical Depth
APD	Avalanche Photodiode Detector
asl	above see level
BC	Black Carbon
CALIPSO	Cloud-Aerosol Lidar and Infrared Pathfinder Satellite Observation
CEAMA	Centro Andaluz de Medio Ambiente
CNN	Cloud Condensation Nuclei
DREAM	Dust Regional Atmospheric Model
EARLINET	European Aerosol Research Lidar Network
FWHM	Full Width at Half Maximum
GFAT	Atmospheric Physics Group
HYSPLIT	Hybrid single-particle Lagrangian integrated trajectories model
IPCC	Intergovernmental Panel on Climate Change
lidar	light detection and ranging
LR	Lidar Ratio
LWP	Liquid Water Path
MPLNET	Micro-Pulsed Lidar NETwork
Nd:YAG	Neodymium-doped yttrium-aluminium-garnet
OD	Optical Depth
OU	Optical Unit

List of abbreviations

PBL	Planetary Boundary Layer
PC	Photon Counting
PMT	Photomultiplier tube
RCS	Range Corrected Signal
RF	Radiative Forcing
RFOV	Receiver Field Of View
RH	Relative Humidity
SAU	Signal Adquisition Unit
SNR	Signal-to-Noise-Ratio
SPALINET	Spanish and Portuguese Aerosol Lidar Network
TOA	Top of the atmosphere
TPW	Total precipitable water
W	Precipitable water vapour
WCT	Wavelet Covariance Transform
WSU	Wavelet Separation Unit

List of abbreviations

List of abbreviations

List of publications

Parts of this work have been published in:

Peer reviewed journals:

Guerrero-Rascado, J. L., F. J. Olmo, I. Aviles-Rodriguez, **F. Navas-Guzmán**, D. Perez-Ramirez, H. Lyamani, and L. A. Arboledas (2009), Extreme Saharan dust over the southern Iberian Peninsula in september 2007: active and passive remote sensing from surface and satellite, *Atmospheric Chemistry and Physics*, *9*(21), 8453-8469.

Guerrero-Rascado, J. L., F. J. Olmo, I. Aviles-Rodriguez, **F. Navas-Guzmán**, D. Perez-Ramirez, H. Lyamani, and L. A. Arboledas (2009), Extreme Saharan dust over the southern Iberian Peninsula in september 2007: active and passive remote sensing from surface and satellite, *Atmospheric Chemistry and Physics Discussion*, 9, 15673-15723.

Sicard, M., F. Molero, J. L. Guerrero-Rascado, R. Pedrós, F. J. Expósito, C. Córdoba-Jabonero, J. M. Bolarín, A. Comerón, F. Rocandenbosch, M. Pujadas, L. Alados-Arboledas, J. A. Martínez-Lozano, J. P. Díaz, M. Gil, A. Requena, **F. Navas-Guzmán** and J. M. Moreno (2009), Aerosol Lidar Intercomparison in the Framework of SPALINET-The Spanish Lidar Network: Methodology and Results, *IEEE Transactions on Geoscience and Remote Sensing*, *47*(10), 3547-3559.

Alados-Arboledas, L., D. Müller, J. L. Guerrero-Rascado, **F. Navas-Guzmán**, D. Pérez-Ramírez, and F. J. Olmo (2011), Optical and microphysical properties of fresh biomass burning aerosol retrieved by Raman lidar, and star-and sun-photometry, *Geophysical Research Letters*, *38*.

Guerrero-Rascado, J. L., J. Andrey, M. Sicard, F. Molero, A. Comeron, M. Pujadas, F. Rocadenbosch, R. Pedros, O. Serrano-Vargas, M. Gil, F. J., Olmo, H. Lyamani, **F. Navas-Guzmán** and L. Alados-Arboledas (2011), Aerosol closure study by lidar, Sun photometry, and airborne optical counters during DAMOCLES field campaign at El Arenosillo sounding station, Spain, *Journal of Geophysical Research-Atmospheres*, *116*.

Guerrero Rascado, J. L., **F. Navas-Guzmán**, J. A. Díaz, J. A. Bravo-Aranda, and L. Alados Arboledas (2011), Quality assurance at the EARLINET Granada station: characterization of the optical subsystem for a multichannel Raman lidar, *Óptica Pura y Aplicada*, *44*(1), 19-23.

Guerrero-Rascado, J. L., D. Müller, **F. Navas-Guzmán**, D. Perez-Ramirez, and L. Alados-Arboledas (2011), First results of aerosol microphysical properties by 3+2 Raman lidar at EARLINET Granada station, *Romanian Journal of Physics*, *56*(3-4), 467-475.

Navas-Guzmán, F., J. L. Guerrero-Rascado, J. A. Bravo-Aranda, and L. Alados-Arboledas (2011), Calibration of 1064 nm-backscatter profiles with a multiwavelength Raman lidar, *Romanian Journal of Physics*, *56*(3-4), 460-466.

Navas-Guzmán, F., J. L. Guerrero Rascado, and L. Alados Arboledas (2011), Retrieval of the lidar overlap function using Raman signals, *Óptica Pura y Aplicada*, 44(1), 71-75.

Navas-Guzmán, F., J. L. Guerrero-Rascado, J. A. Bravo-Aranda, and L. Alados Arboledas (2011), On the use cirrus clouds for ground-based elastic lidar calibration, *Óptica Pura y Aplicada*, 44 (1), 49-53.

Sicard, M., J. L. Guerrero-Rascado, **F. Navas-Guzmán**, J. Preißler, F. Molero, S. Tomás, J. A. Bravo-Aranda, A. Comerón, F. Rocadenbosch, F. Wagner, M. Pujadas, and L. Alados-Arboledas (2011), Monitoring of the Eyjafjallajökull volcanic aerosol plume over the Iberian Peninsula by means of four EARLINET lidar stations, *Atmospheric Chemistry and Physics Discussion*, *11*, 29681-29721.

Navas-Guzmán, F., D. Müller, J. A. Bravo-Aranda, D. Perez-Ramirez, F. J. Olmo, J. L. Guerrero-Rascado, and L. alados-Arboledas (2012), Eruption of the Eyjafjallajökull volcano in spring 2010: multiwavelength Raman lidar measurements of sulphate particles in the lower troposphere, *Geophysical Research Letters*, *submitted*.

Molero, F., A. J. Fernández, M. Pujadas, M. Sicard, S. Tomás, A. Comerón, D. Lange, D. Kumar, J. Giner, C. Muñoz, F. Rocadenbosh, **F. Navas-Guzman**, M. J. Granados-Muñoz, L. Alados-Arboledas, J. A. Bravo-Aranda, J. Preißler, F. Wagner, and J. L. Guerrero-Rascado (2011), Study on aerosol properties over Madrid (Spain) by multiple instrumentation during SPALI10 lidar campaign, *Revista Boliviana de Física*, *20s*, 16-18.

Pérez-Ramírez, D., **F. Navas-Guzmán**, H. Lyamani, J. Fernandez-Galvez, F. J. Olmo, and L. Alados-Arboledas (2012), Retrievals of precipitable water vapor using star photometry: assessment with Raman lidar and link to sun photometry, *Journal of Geophysical Research-Atmospheres*, *117*, D05202.

Pérez-Ramírez, D., H. Lyamani, F. J. Olmo, D. N. Whiteman, **F. Navas-Guzmán**, and L. Alados Arboledas (2012), Cloud screening and quality control algorithm for star

photometer data: assessment with lidar measurements and with all-sky-images, *Atmospheric Measurement Techniques Discussion*, *5*(1657-2693).

Sicard, M., J. L. Guerrero-Rascado, **F. Navas-Guzmán**, J. Preißler, F. Molero, S. Tomás, J. A. Bravo-Aranda, A. Comerón, F. Rocadenbosch, F. Wagner, M. Pujadas, and L. Alados-Arboledas (2012), Monitoring of the Eyjafjallajökull volcanic aerosol plume over the Iberian Peninsula by means of four EARLINET lidar stations, *Atmospheric Chemistry and Physics 12*, 3115-3130.

Granados-Muñoz, M. J., **F. Navas-Guzman**, J. A. Bravo-Aranda, J. L. Guerrero-Rascado, H. Lyamani, J. Fernández-Gálvez, and L. Alados-Arboledas (2012), Automatic determination of the planetary boundary layer height using lidar: one year analysis over South Spain, *Journal of Geophysical Research-Atmospheres,* accepted.

Bravo-Aranda, J. A., **F. Navas-Guzmán**, J. L. Guerrero-Rascado, D. Pérez-Ramírez, M. J. Granados-Muñoz, and L. Alados Arboledas Analysis of lidar depolarization calibration procedure and application to the atmospheric aerosol characterization, *International Journal of Remote Sensing, in press*.

Book chapters:

Alados-Arboledas,L., J. L. Guerrero-Rascado, H. Lyamani, **F. Navas-Guzmán**, and F. J. Olmo (2007), Characterization of the atmospheric aerosol by combination of Lidar and sun-photometry*, Proceedings of SPIE 2007*, vol. 6750, 67500J-1—67500J-8, ISBN 0277-786X-07.

Costa, M.J., D. Bortoli, S. Pereira, A. M. Silva, F. Wagner, N. Belo, J. L. Guerrero-Rascado, **F. Navas-Guzmán**, and L. Alados-Arboledas (2007), Analysis of the measurements taken by a ceilometer installed in the South of Portugal, *Proceedings of SPIE 2007*, vol. 6745, 674523-1—674523-8, ISBN 0277-786X-07.

Navas-Guzmán,F., J. L. Guerrero-Rascado, and L. Alados-Arboledas (2007), Determinación de la altura de la capa límite planetaria (PBL) a partir de medidas Lidar y radiosondeos, *XXXI Reunión bienal de la real sociedad española de Física. Comunicaciones científicas*, 198-1 – 198-4, ISBN: 978-84-690-7298.

Navas-Guzmán, F., Determinación de la altura de la capa limite atmosférica a partir de medidas lidar y radiosondeos (2008), ISBN: 978-84-691-6420-4.

Alados-Arboledas, L., H. Horvath, X. Querol, F. J. Olmo, J. L. Guerrero-Rascado, H. Lyamani, **F. Navas-Guzmán**, J. A. Bravo-Aranda, M. Gangl, S. Castillo, and A. Alastuey (2009), Atmospheric aerosol properties in an urban atmosphere: ESTIO2005, *Proceedings of the 8th International Symposium on Tropospheric Profiling: Integration of Needs, Technologies and Applications*, S12-P04-1 -- S12-P04-4, ISBN: 978-90-6960-233-2.

Guerrero-Rascado,J. L., H. Lyamani, A. M. Silva, F. Wagner, S. N. Pereira, **F. Navas-Guzmán**, J. A. Bravo-Aranda, and L. Alados-Arboledas (2009), Airborne and ground

based instrumentation comparison: closure study during CAPEX project, *Proceedings of the 8ᵗʰ International Symposium on Tropospheric Profiling: Integration of Needs, Technologies and Applications*, S12-P03-1 -- S12-P03-4, ISBN: 978-90-6960-233-2.

Alados-Arboledas, L., D. Müller, **F. Navas-Guzmán**, D. Pérez-Ramírez, J. L. Guerrero-Rascado, and F. J. Olmo (2010), Use of ground based passive and active remote sensing for the retrieval of aerosol microphysical properties, *Book of extended abstracts of Cuarta Reunión Española de Ciencia y Tecnología de Aerosoles*, C2-1-6, ISBN: 978-84-693-4839-0.

Guerrero-Rascado, J. L., F. J. Olmo, F. Molero, **F. Navas-Guzmán**, M. J. Costa, A. M. Silva, M. Pujadas, M. Sicard, and L. Alados-Arboledas (2010), Characterization of atmospheric aerosols for a long-range transport of biomass-burning from North America over the Iberian Peninsula, *Proceedings of the 25ᵗʰ International Laser Radar Conference,* 580-583, ISBN: 978-5-94458-109-9.

Guerrero-Rascado, J. L., M. Sicard, F. Molero, **F. Navas-Guzmán**, J. Preißler, D. Kumar, J. A. Bravo-Aranda, S. Tomás, M. N. Reba, L. Alados-Arboledas, A. Comerón, M. Pujadas, F. Rocadenbosch, F. Wagner, and A. M. Silva (2010), Monitoring of the Eyjafjallajökull ash plume at four lidar stations over the Iberian Peninsula: 6 to 8 May 2010, *Book of extended abstracts of Cuarta Reunión Española de Ciencia y Tecnología de Aerosoles*, C15-1-6, ISBN: 978-84-693-4839-0.

Guerrero-Rascado, J. L., F. J. Olmo, F. Molero, **F. Navas-Guzmán**, M. J. Costa, A. M. Silva, M. Pujadas, M. Sicard, and L. Alados-Arboledas (2010), Aerosol direct radiative effects of a transatlantic biomass burning plume over Granada, Spain, *Book of extended abstracts of Cuarta Reunión Española de Ciencia y Tecnología de Aerosoles*, C7-1-7, ISBN: 978-84-693-4839-0.

Navas-Guzmán,F., J. A. Bravo-Aranda, M. J. Granados, J. L. Guerrero-Rascado, and L. Alados-Arboledas (2010), Study on the planetary boundary layer top with Raman lidar, *Book of extended abstracts of Cuarta Reunión Española de Ciencia y Tecnología de Aerosoles*, C9-1-6, ISBN: 978-84-693-4839-0.

Olmo, F. J., **F. Navas-Guzmán**, H. Lyamani, J. A. Bravo-Aranda, A. Valenzuela, J. L. Guerrero-Rascado, and L. Alados-Arboledas (2010), Monitoring of lofted aerosol layers of mineral desert dust with Raman Lidar and a set of photometers at different altitudes, *Book of extended abstracts of Cuarta Reunión Española de Ciencia y Tecnología de Aerosoles*, C11-1-6, ISBN: 978-84-693-4839-0.

Navas-Guzmán, F., D. Pérez-Ramírez, F. J. Olmo, H. Lyamani, J. L. Guerrero-Rascado, J. A. Bravo-Aranda, and L. Alados-Arboledas (2010), On the synergetic use of passive and active remote sensing for atmospheric aerosol radiative effect computations, *Proceedings of the 25ᵗʰ International Laser Radar Conference*, 1146-1149, ISBN: 978-5-94458-109-9.

Bravo-Aranda, J. A., **F. Navas-Guzman**, M. J. Granados-Muñoz, J. L. Guerrero-Rascado, and L. Alados-Arboledas (2011), Atmospheric aerosol characterization by

dual lidar depolarization, *Book of extended abstracts of Quinta Reunión Española de Ciencia y Tecnología de Aerosoles*, H2-1-H2-5, ISBN: 978-84-7834-662-2.

Fernández-Gálvez, J., J. L. Guerrero-Rascado, F. Molero, H. Lyamani, M. A. Revuelta, **F. Navas-Guzman**, M. Sastre, J. A. Bravo-Aranda, A. J. Fernández, M. J. Granados-Muñoz, F. J. Gómez-Moreno, F. J. Olmo-Reyes, M. Pujadas, and L. Alados-Arboledas (2011), Aerosol size distribution from inversion of solar radiances and measured at ground-level during SPALI10 campaign, *Proceedings of the global conference on global warming 2011*, ISBN: 978-989-95091-3-9.

Granados-Muñoz, M. J., **F. Navas-Guzmán**, J. A. Bravo-Aranda, J. L. Guerrero-Rascado, J. Fernández-Gálvez and L. Alados-Arboledas (2011), Multi-instrumental detection of the mixing layer height over Granada, Book of extended abstracts of Quinta Reunión Española de Ciencia y Tecnología de Aerosoles, B5-1- B5-6, ISBN: 978-84-7834-662-2

Molero, F., A. Amodeo, M. Sicard, J. Preißler, **F. Navas-Guzmán**, V. Freudenthaler, A. J. Fernández, A. Giunta, S. Tomás, F. Wagner, M. J. Granados-Muñoz, I. Mattis, M. Pujadas, G. D'amico, A. Comerón, J. L. Guerrero-Rascado, L. Alados-Arboledas, D. Lange, J. A. Bravo-Aranda, D. Kumar, G. Pappalardo, J. Giner, C. Muñoz, and F. Rocadenbosch (2011), Study on aerosol properties over Madrid (Spain) by multiple instrumentation during EARLINET lidar intercomparison campaign: SPALI10, *Book of extended abstracts of Quinta Reunión Española de Ciencia y Tecnología de Aerosoles,* B4-1- B4-6, ISBN: 978-84-7834-662-2.

Navas-Guzmán, F., J. A. Bravo-Aranda, J. L. Guerrero-Rascado, M. J. Granados-Muñoz, and L. Alados-Arboledas, Study of ground-based vertical profiles of tropospheric aerosol in coincidence with CALIPSO overpasses at Granada, Spain (2011), *Book of extended abstracts of Quinta Reunión Española de Ciencia y Tecnología de Aerosoles*, D3-1-D3-6, ISBN: 978-84-7834-662-2.

Participation in national and international conferences

Navas-Guzmán, F., J. L. Guerrero-Rascado, A. B. Fernandez-Medina, J. A. Adame, and L. Alados-Arboledas (2007), Mixing layer height determination by lidar and radiosounding data, *European Aerosol Conference,* Salzburg (Austria).

Alados-Arboledas, L., J. L. Guerrero-Rascado, H. Lyamani, D. Pérez-Ramírez, **F. Navas-Guzmán**, and F. J. Olmo-Reyes (2008), Multi-instrumental approach for the monitoring of Saharan outbreaks, *3rd International Workshop on Mineral Dust,* Leipzig (Germany).

Guerrero-Rascado, J. L., **F. Navas-Guzmán,** and L. Alados-Arboledas (2008), Eighteen months lidar measurements in coincidence with CALIPSO overpasses at Granada, Spain, *European Aerosol Conference,* Thessaloniki (Greece).

Navas-Guzmán, F., L. Guerrero-Rascado,D. Pérez-Ramírez, and L. Alados-Arboledas

(2008), Overlap correction technique for Raman lidar, *European Aerosol Conference,* Thessaloniki (Greece).

Pérez-Ramírez, D., **F. Navas-Guzmán**, J. L. Guerrero-Rascado, F. J. Olmo-Reyes, and L. Alados-Arboledas (2008), Precipitable water vapour characterisation with passive and active remote sensing, *European Aerosol Conference,* Thessaloniki (Greece).
Alados-Arboledas, L., J. L. Guerrero-Rascado, **F. Navas-Guzmán**, D. Pérez-Ramírez, H. Lyamani, and F. J. Olmo-Reyes (2008), Monitoring the daily evolution of the atmospheric aerosol in an urban environment by means of remote sensing and in-situ methodologies, *European Aerosol Conference,* Thessaloniki (Greece).

Alados-Arboledas, L., H. Horvath, X. Querol, F. J. Olmo-Reyes, J. L. Guerrero-Rascado, H. Lyamani, **F. Navas-Guzmán**, J. A. Bravo-Aranda, M. Gang, and A. Alastuey (2009), Atmospheric aerosol properties in an urban atmosphere, ESTIO2005, *8th International Symposium on Tropospheric Profiling: Integration of Needs, Technologies and Applications*, Delft (Holland).

Guerrero-Rascado, J. L., F. J. Olmo-Reyes, **F. Navas-Guzmán**, D. Pérez-Ramírez, H. Lyamani, and L. Alados-Arboledas (2009), Active and passive remote sensing, analysis of an extreme over Southern Iberian Peninsula, *European Aerosol Conference,* Karlsruhe (Germany).

Guerrero-Rascado, J. L., **F. Navas-Guzmán**, J. A. Díaz-Navas, J. A. Bravo-Aranda, and L. Alados-Arboledas (2009), Quality assurance at the EARLINET Granada station, characterization of the optical subsystem for a multichannel Raman lidar, *5th Workshop on Lidar Measurements in Latin America,* Buenos Aires (Argentina).

Guerrero-Rascado, J. L., H. Lyamani, A. M. Silva, F. Wagner, S Pereira, **F. Navas-Guzmán**, J. A. Bravo-Aranda, and L. Alados-Arboledas (2009), Airborne and ground based instrumentation comparison, closure study during CAPEX project, *8th International Symposium on Tropospheric Profiling: Integration of Needs, Technologies and Applications*, Delft (Holland).

Guerrero-Rascado, J. L., D. Müller, **F. Navas-Guzmán**, D. Pérez-Ramírez, and L. Alados-Arboledas (2009), First results of aerosol microphysical properties by 3+2 Raman lidar at EARLINET Granada station, *Optoelectronics Techniques for Environmental Monitoring,* Bucarest (Romania).

Navas-Guzmán, F., J. L. Guerrero-Rascado, J. A. Bravo-Aranda, and L. Alados-Arboledas (2009), On the use cirrus clouds for elastic lidar calibration, *5th Workshop on Lidar Measurements in Latin America,* Buenos Aires (Argentina).

Navas-Guzmán, F., J. L. Guerrero-Rascado, J. A. Bravo-Aranda, H. Lyamani, and L. Alados-Arboledas (2009), Calibration of 1064nm-backscatter profiles with cirrus clouds for a multiwavelength Raman lidar, *5th Workshop on Lidar Measurements in Latin America,* Buenos Aires (Argentina).

Navas-Guzmán, J. L. Guerrero-Rascado, and L. Alados-Arboledas (2009), Retrieval of the lidar overlap function using Raman signals, *5th Workshop on Lidar Measurements in Latin America,* Buenos Aires (Argentina).

Navas-Guzmán, F., J. L. Guerrero-Rascado, and L. Alados-Arboledas (2009), Calibration of 1064nm-backscatter profiles with a multiwavelength Raman lidar, *Optoelectronics Techniques for Environmental Monitoring,* Bucarest (Romania).
Alados-Arboledas, L., D. Müller, **F. Navas-Guzmán**, D. Pérez-Ramírez, J. L. Guerrero-Rascado, and F. J. Olmo-Reyes (2010), Retrieval of aerosol microphysical properties by Raman lidar, and star- and sun-photometry, *International Aerosol Conference,* Helsinki, Finland.

Alados-Arboledas, L., **F. Navas-Guzmán**, J. A. Bravo-Aranda, H. Lyamani, D. Pérez-Ramírez, J. L. Guerrero-Rascado, and F. J. Olmo-Reyes (2010), Monitoring of the Eyjafjallajökull volcanic ash plume at Granada, Spain, in the framework of EARLINET and AERONET, *International Aerosol Conference,* Helsinki, Finland.

Alados-Arboledas, L., **F. Navas-Guzmán**, J. A. Bravo-Aranda, , H. Lyamani, D. Pérez-Ramírez, J. L. Guerrero-Rascado, M. Antón-Martínez, and F. J. Olmo-Reyes (2010), Ground-based active and passive remote sensing of the Eyjafjallajökull volcanic aerosols at Granada, Spain, *25th International Laser Radar Conference,* San Petersburg (Russia).

Bravo-Aranda, J. A., **F. Navas-Guzmán**, M. J. Granados-Muñoz, and L. Alados-Arboledas (2010), Atmospheric aerosol characterization by lidar depolarization profiles, *3RD International Symposium on Recent Advances in Quantitative Remote Sensing*, Torrent (Spain).

Guerrero-Rascado, J. L., F. J. Olmo-Reyes, F. Molero, **F. Navas-Guzmán**, M. J. Costa, A. M. Silva, M. Pujadas, M. Sicard, L. Alados-Arboledas (2010), Characterization of atmospheric aerosols for a long-range transport of biomass-burning from North America over the Iberian Peninsula, *25th International Laser Radar Conference,* San Petersburg (Russia).

Molero, F., M. Sicard, J. L. Guerrero-Rascado, **F. Navas-Guzmán**, S. Tomas, J. Preissler, D. Kumar, F. Rocadenbosch, L. Alados-Arboledas, F. Wagner, A. Comeron, and M. Pujadas (2010), Comparison of SPALINET network lidar measurements with models forecasts during the Eyjafjalla, *25th International Laser Radar Conference,* San Petersburg (Russia).

Navas-Guzmán, F., D. Pérez-Ramírez, F. J. Olmo-Reyes, H. Lyamani, J. L. Guerrero-Rascado, J. A. Bravo-Aranda, and L. Alados-Arboledas (2010), On the synergetic use of passive and active remote sensing for atmospheric aerosol radiative effect computations, *25th International Laser Radar Conference,* San Petersburg (Russia).

Navas-Guzmán, F., D. Müller, D. Pérez-Ramírez, J. L. Guerrero-Rascado, J. A. Bravo-Aranda, and L. Alados-Arboledas (2010), Optical and microphysical properties of tropospheric aerosol from Raman lidar, *3RD International Symposium on Recent Advances in Quantitative Remote Sensing,* Torrent (Spain).

Navas-Guzmán, F., F. J. Olmo-Reyes, J. L. Guerrero-Rascado, H. Lyamani, J. A. Bravo-Aranda, and L. Alados-Arboledas (2010), Study on the assumption of using a range-independent lidar ratio in elastic lidar, *3RD International Symposium on Recent Advances in Quantitative Remote Sensing*, Torrent (Spain).

Olmo-Reyes, F. J.**, F. Navas-Guzmán**, H. Lyamani, J. A. Bravo-Aranda, J. L. Guerrero-Rascado, and L. Alados-Arboledas (2010), Vertical structure of the atmospheric aerosol derived from Raman lidar and a set of photometers at different altitudes, *International Aerosol Conference,* Helsinki, Finland.

Pérez-Ramírez, D., H. Lyamani, F. J. Olmo-Reyes, **F. Navas-Guzmán**, and L. Alados-Arboledas (2010), Star photometer for aerosol characterization, improvements on calibration procedures by astronomic Langley, *3RD International Symposium on Recent Advances in Quantitative Remote Sensing*, Torrent (Spain).

Pérez-Ramírez, D., H. Lyamani, F. J. Olmo-Reyes, **F. Navas-Guzmán**, and L. Alados-Arboledas (2010), Aerosol size distributions retrieved from starphotometry by King inversion method, *3RD International Symposium on Recent Advances in Quantitative Remote Sensing*, Torrent (Spain).

Sicard, M., A. Comeron, F. Molero, J. L. Guerrero-Rascado, **F. Navas-Guzmán**, J. M. Bolarín, F. Rocadenbosh, S. Tomas, D. Kumar, M. Pujadas, J. Preissler, F. Wagner, J. A. Bravo-Aranda, L. Alados-Arboledas, A. Requena, and A. Silva (2010), Seguimiento de las cenizas del Eyjafjalla sobre la península ibérica por la red de lidares Hispano-Portuguesa SPALINET, *X Congreso Nacional del Medio Ambiente,* Madrid (Spain).

Alados-Arboledas, L., **F. Navas-Guzmán**, J. A. Bravo-Aranda, H. Lyamani, D. Pérez-Ramírez, J. L. Guerrero-Rascado, I. Foyo-Moreno, I. Alados-Arboledas, M. J. Granados-Muñoz, G. Titos-Vela, J. Fernández-Gálvez, A. Valenzuela-Gutierrez, M. Anton-Martínez, A. Quirantes-Sierra, X. Querol-Carceller, A. Alastuey-Urós, and F. J. Olmo-Reyes (2011), Multi-instrumental characterization of the mixing of Eyjafjallajökull volcanic aerosols and boundary layer aerosols at Granada, Spain, *European Aerosol Conference*, Manchester (England).

Molero, F., J. Andrey, J. Preissler, **F. Navas-Guzmán**, A. Giunta, M. Sicard, A. J. Fernández, M. Parrondo, F. Wagner, M. J. Granados-Muñoz, G. D'Amico, S. Tomas, M. Pujadas, C. Córdoba-Jabonero, J. L. Guerrero-Rascado, L. Alados-Arboledas, A. Amodeo, A. Comeron, J. A. Bravo-Aranda, G. Pappalardo, D. Kumar, I. Mattis, V. Freudenthaler, D. Lange, C. Muñoz, and F. Rocadenbosch (2011), Aerosol size distribution study by airborne and ground-level in-situ measurements and remote sensing during EARLINET lidar intercomparison campaign, SPALI10, *European Aerosol Conference*, Manchester (England).

Molero, F., A. J. Fernández, M. Pujada, M. Sicard, S. Tomas, A. Comeron, D. Lange, D. Kumar, C. Muñoz, F. Rocadenbosh, **F. Navas-Guzmán**, M. J. Granados-Muñoz, L. Alados-Arboledas, J. A. Bravo-Aranda, J. Preissler, F. Wagner, and J. L. Guerrero-Rascado (2011), Study on aerosol properties over madrid (Spain) by multiple

instrumentation during SPALI10 lidar campaign, *VI Workshop on Lidar Measurements in Latin America*, La Paz (Bolivia).

Navas-Guzmán, **F.**, J. A. Bravo-Aranda, J. L. Guerrero-Rascado, M. J. Granados-Muñoz, and L. Alados-Arboledas (2011), Three years of Raman lidar measurements in correspondence with CALIPSO overpasses over the south of the Iberian Peninsula, *European Aerosol Conference*, Manchester (England).

Pappalardo, G., L. Alados-Arboledas, Lucas; **F. Navas-Guzmán,** and Earlinet team. (2011), 4D distribution of the 2010 Eyjafjallajökull ash plume over Europe observed by the European Lidar network EARLINET, *EGU General Assembly*, Vienna (Austria).